

TECHNISCHE UNIVERSITÄT MÜNCHEN  
Lehrstuhl für Carbon Composites

# **A Multiphysics Simulation Toolkit Developed to Address Scale-up Challenges of Out-of-Autoclave Composites Manufacturing**

**Theodosia Kourkoutsaki**

Vollständiger Abdruck der von der Fakultät für Maschinenwesen der Technischen Universität München zur Erlangung des akademischen Grades eines

**Doktor-Ingenieurs**

genehmigten Dissertation.

Vorsitzender: Prof. Dr. Oliver Lieleg

Prüfer der Dissertation: 1. Prof. Dr.-Ing. Klaus Drechsler  
2. Prof. Dr. Sebastien Comas-Cardona

Die Dissertation wurde am 19.01.2017 bei der Technischen Universität München eingereicht und durch die Fakultät für Maschinenwesen am 12.06.2017 angenommen.

Technische Universität München  
Fakultät für Maschinenwesen  
Lehrstuhl für Carbon Composites  
Boltzmannstraße 15  
D-85748 Garching bei München

Tel.: +49 (0) 89 / 289 – 15092

Fax.: +49 (0) 89 / 289 – 15097

Email: [info@lcc.mw.tum.de](mailto:info@lcc.mw.tum.de)

Web: [www.lcc.mw.tum.de](http://www.lcc.mw.tum.de)



*'The noblest pleasure is the joy of understanding'.  
Leonardo da Vinci*

*This thesis is dedicated to my cousin Nikos who left us early & to all young people  
around the world who were not fortunate enough to receive an education.*



# ACKNOWLEDGEMENTS

This thesis was realized in the context of my work as a Research Assistant at the Chair of Carbon Composites, in the years 2012-2016. I would like to thank my Institute, GE Global Research and TUM for providing the means and financial support to perform this work. Multiple people contributed in making this opportunity possible and supported me throughout this endeavor, whom I would like to acknowledge here.

Professor Drechsler and Elisabeth, thank you for offering me the possibility to join your team at the LCC, for your flexibility and for ensuring we have the means to do the best work we can at all times. Professor Hinterhölzl, Roland, thank you for supporting my travels to France when necessary for the progress of this work and for staying positive no matter the situation. Many thanks goes to Cigdem, Mrs. Uruk, Annetta and Diana who helped me navigate through all administrative aspects, always with a smile and helpful attitude. Also a great thank you goes to Clemens, Daniel A., Luciano, Rainer and Christian L. for supporting several lab activities over the years.

I would like to greatly thank my second supervisor, Prof. Comas-Cardona from GeM at Ecole Centrale de Nantes, for being such a great scientist, teacher and inspiration for me in both a professional and personal level. Without your devotion to this project, the numerous discussions, competency, optimism and interpersonal skills, this work would not have been completed. Thanks for believing in me and doing above and beyond what was necessary to keep me motivated at all times! Furthermore I would like to thank Christophe Binetruy, the head of the Materials, Processes and Technology of Composites Team of the GeM Lab in Nantes for bringing me in contact with Sebastien, for hosting me several times in Nantes and for happily discussing and providing his feedback and technical support whenever necessary. Thanks also goes to Andrien Leygue for his tips in efficient Matlab programming and Jean-Michel, Pierrick and Yiannick for assisting with setting-up various experiments in the lab during my stay in Nantes.

This project was made possible thanks to GE's support, therefore I would particularly like to thank my Manager Shridhar Nath as well as the Director of GE Global Research in Germany Carlos Haertel and my HR Manager Mike Smith who enabled me to take an extended leave from my position for the purpose of this thesis. Shridhar, thank you for the trust over the years!

The Laura Bassi Award of TUM, which I received at the end of 2015 enabled me to concentrate on my writing during the last six months of my stay at the LCC, therefore I am very grateful to TUM and particularly Dr. Sandmann, Mrs. Schneider and Mrs. Reichenberger for offering me this opportunity. Furthermore I would like to acknowledge the funding of the Bavarian-French center for cooperation (BFHZ), which enabled scientific exchanges with GeM in Nantes in the context of this work.

I would like to thank my mentor Ram Upadhyay as well as my colleagues Thomas, Martin, and Mathias from the Composites Manufacturing Lab in Munich for providing

the means to perform my validation work, Anjali Singhal from GRC Niskayuna for performing CT measurements and finally Mark Vermilyea and Jorge Carretero Benignos for always being available for a deep dive in a range of technical topics covered in this work! A great thanks goes to John Savage from GE Aviation Systems for providing the material used in this work and for systematically reviewing my written work! Furthermore I am grateful to Mike Smith and Chris Wade from GE Aviation Systems for providing material systems for screening purposes and technical support.

Professor Clemens Dransfeld, Professor Kunal Masania and Andre Keller from the Fachhochschule Nordwestschweiz, thank you for collaborating on rheology modeling. I am very grateful to Nikos Pantelidis from Synthesites for offering technical support and his DC monitoring system free of charge for the duration of this work. Furthermore I would like to thank Professor Pissis, Professor Kyritsis and Dr. Roula Kryptou from the Physics Department of the National Technical University of Athens for undertaking dielectric measurements of some samples and for discussing several aspects of thermal analysis and cure monitoring since 2005. I am also thankful to all students I have supervised for their engagement and technical contribution in different aspects of this work.

Last but not least I would like to thank my colleagues for the good collaboration in lecturing and lecture organization and for taking the time to offer advice and expertise. Thank you Alexane, Elinor, Thorsten, Uli, Robin, Jonathan, Tobias WR, Stefan, Jakob from LCC and Arthur, Adrien, Benedikt and the ‘Spanish office’ from GeM. Alexane, Thorsten and Uli, thank you for helping out in the preparation of this manuscript. A very special thanks goes to Alexane and Elinor for offering numerous tips and tricks in any topic possible which made my life easier and mostly for being good friends and sharing the ups and downs of the PhD life! Thank you Kosta, Michaela, Gianni K, my ‘Dr. friends’ and best academic mentors one could ask for, for demystifying academia, for taking the time to review parts of the manuscript and just hanging in there with me when needed.

On a personal note I would like to thank my parents, my sister and my good friends around the globe for their unconditional love and friendship, for believing in me and supporting everything I choose to do - even if it comes at a cost of our quality time together. Mom, I cannot thank you enough for enabling me to follow my dreams and develop a career and life abroad, sacrificing your own convenience! A big thank you for supporting me at every step of the way! Finally this thesis would not have been possible without the continuous support and encouragement of Jens. Thank you very much for being there and grounding me down to earth by reminding me that the pleasures in life are hidden in the smallest everyday moments!

# KURZFASSUNG

Wachsende Produktionsvolumen und steigende Bauteilgrößen von Faserverbundstrukturen führten zur Entwicklung der sogenannten Out-of-Autoclave Verfahren (OoA), mit dem Ziel die kostenintensive Konsolidierung im Autoklav zu ersetzen. Kennzeichnend für OoA-Verfahren ist, dass die Konsolidierung allein unter Vakuum und ohne externe Druckbeaufschlagung erfolgt. Zur Gewährleistung der Bauteilqualität sind speziell für OoA-Verfahren optimierte Prepregs erhältlich. Diese sogenannten Semi-prepregs sind im Ausgangszustand teilimprägniert und ermöglichen so eine homogene Vakuumverteilung und weitere Konsolidierung. Allerdings besteht die Gefahr, dass inhomogene Druck- und Temperaturverteilungen während des Aushärtezyklus zu Porositäten im Bauteil führen.

Die Komplexität des OoA-Verfahrens beruht auf der zeitgleichen Evakuierung und Imprägnierung des konsolidierenden Fasermaterials unter nicht isothermen Bedingungen, weshalb Wärmeübertragung und chemo-rheologische Effekte ebenfalls in Betracht gezogen werden müssen. Aufgrund der Verteilung des Vakuums im trockenen Bereich des Semi-Prepregs hängen die idealen Prozessrandbedingungen stark von der Bauteilgröße ab. Diese Herausforderung wird im Rahmen dieser Arbeit adressiert. Es werden Simulationsmodelle entwickelt, welche die virtuelle Optimierung eines Materialsystems und des Aushärtezyklus ermöglichen. Die vorgestellte Methodik fokussiert sich auf die Modellierung der zeitabhängigen Luftströmung durch das trockene Fasermaterial und die Kopplung des lokalen Luftdrucks an der makroskopischen Harzfront, welche auf Basis der Druckrandbedingungen ermittelt werden. Eine unidirektionale Kopplung des zeitabhängigen Luftdrucks (in der Bauteilebene) und dem Druck an der Harzfront (in Dickenrichtung) in einem unkonsolidierten Faserbündel bei isothermen Randbedingungen wird in Matlab implementiert. Das Modell bildet den Einfluss der verzögerten Vakuumverteilung auf die Imprägnierungszeit des Garns gut ab. Eine bilaterale Kopplung von Luft- und Harzdruck bei temperaturabhängigen Bedingungen in Längen- und Dickenrichtung eines Bauteils mit mehreren Prepreg-Lagen wird in COMSOL Multiphysics implementiert. Dieses Modell berücksichtigt zusätzlich die gegenseitige Beeinflussung der zeitgleichen Strömung der Gas- sowie der Flüssigphase. Die zeitabhängige Luft-Permeabilität eines Semi-Prepregs und die chemisch-rheologischen Eigenschaften des enthaltenen Harzfilms werden experimentell charakterisiert und dienen als Eingangsgrößen der Simulation. Hierzu wird ein kommerziell verfügbares OoA Prepreg (MTM 44-1, basierend auf einem 2x2 Gewebe) verwendet.

Zu Validierungszwecken wird aus dem gleichen Material ein monolithischer Demonstrator in einem Heißluftofen gefertigt. Die experimentell gewonnenen Temperaturprofile entsprechen in hohem Grad den Simulationsergebnissen. Direkt im Laminat durchgeführte Leitfähigkeitsmessungen korrelieren unmittelbar mit der berechneten Entwicklung der Viskosität. Weiterhin stimmen gemessene und simulierte minimale Luftdrücke

an zwei Positionen entlang der Längsachse des Bauteils gut überein. Die Druckentwicklung vom Minimal- bis zum Umgebungsdruck, die durch die graduelle Verschließung der Luftkanäle dominiert wird, wird vom Modell akkurat abgebildet. Während die zuvor erwähnten physikalischen Prozesse sehr genau von der Simulation abgebildet werden, ist bei den Endwerten der Bauteilporosität eine Abweichung zu beobachten, welche auf die fehlende Kompaktierung sowie die makroskopische Auflösung im simulierten Bauteil zurückgeführt werden können.

Die durchgeführten Sensitivitätsstudien unter Verwendung des genannten Prepregs liefern eine Anleitung zur Material- und Aushärtezyklusoptimierung. Eine Erhöhung der Harzviskosität bei Raumtemperatur oder Absenkung der Permeabilität in Dickenrichtung des Textils verbessert die Vakuumverteilung während der Evakuierung bei Raumtemperatur (vor dem Aushärtezyklus) signifikant. Reduzierte Heizraten während des Aushärtens sind vorteilhaft, da diese zu einem langsameren Anstieg des Luftdrucks im Laminat führen, vorausgesetzt, der Aushärtungsprozess setzt erst nach vollständiger Imprägnierung des Prepregs ein.

## ABSTRACT

Increasing dimensions and production volumes of composite parts led to the development of an alternative process known as Out-of-Autoclave manufacturing (OoA), which aims at replacing the expensive prepreg consolidation in an Autoclave. The primary characteristic of composite processing OoA is that the parts are consolidated solely under vacuum pressure. To enable the production of components with acceptable quality, material manufacturers developed optimized prepregs for OoA processing. These materials are partially wetted at their initial state (semi-prepregs), enabling homogeneous vacuum distribution and further consolidation during the cure cycle. However, during the cure cycle, transient, inhomogeneous pressure and temperature conditions may lead to residual porosity formation. OoA manufacturing is a rather complex process which combines air and resin flow in a consolidating fibrous (porous) medium (i.e. prepreg) under non-isothermal conditions, therefore heat transfer and chemo-rheological effects have to also be taken into consideration. Since the vacuum is distributed via the dry fiber tows, modifications of the part dimensions affect directly the boundary conditions.

To address these challenges, a multi-physics simulation framework which enables material down-selection and virtual testing of production cycles is developed in this thesis. The proposed simulation focuses on modeling the transient air flow through the dry tows and coupling the predicted local gas pressure on the macroscopic resin flow via pressure boundary conditions. A one-way coupling of the transient gas pressure (distributed in-plane) on the resin flow front in a non-consolidating tow (through its thickness), at isothermal conditions is implemented in Matlab. The model accurately depicts the impact of a delayed vacuum distribution on the impregnation time of the prepreg tows. A two-way, 2D coupling (part thickness and length) between the air and resin pressure at non-isothermal conditions is implemented in COMSOL Multiphysics. This model additionally captures the gas pressure development inside the prepreg, even when there is an interaction between the time-scales of air and resin flow. The transient air-permeability of a commercially available OoA prepreg (MTM 44-1, based on a 2x2 twill weave fabric) and the chemo-rheology of the prepreg resin are characterized and used as input for the simulation.

A monolithic demonstrator made of the same prepreg is manufactured in a convection oven for validation purposes. The sensor data collected during this experiment show a close match between the monitored and predicted temperatures. The measured electrical resistance of the laminate correlates directly with the resin viscosity development and is in very good agreement with the simulated viscosity evolution. Furthermore the minimum gas pressure obtained in two locations of the laminate along the part's length closely agrees with the minimum simulated gas pressure. From this point onwards the gradual locking of the air-pathways and the temperature increase lead to an equalization of the laminate pressure with the atmospheric pressure, a behavior successfully depicted

in the simulation. While the model accurately depicts the above mentioned physical phenomena, the deviation of the predicted from the experimentally determined residual porosity may be primarily attributed to the absence of the laminate's compaction and the macroscopic resolution of the developed model.

Sensitivity studies using as a basis the MTM 44-1 prepreg provide a guidance for material or cure cycle optimization. An increase of the resin's viscosity at room temperature or a decrease of the textile's through thickness permeability significantly improves the vacuum distribution during debulking. During the cure cycle reduced heating rates are preferred since they lead to a slower increase of the gas pressure inside the laminate. Nevertheless it should be ensured that curing takes place only after full wetting of the prepreg is achieved.



# Table of Contents

<b>Table of Contents</b> .....	<b>xi</b>
<b>Nomenclature</b> .....	<b>xv</b>
<b>Abbreviations</b> .....	<b>xxv</b>
<b>List of Figures</b> .....	<b>xxvii</b>
<b>List of Tables</b> .....	<b>xxxv</b>
<b>1 Introduction</b> .....	<b>1</b>
1.1 Composites Manufacturing using Prepregs .....	1
1.2 Autoclave versus Out-of-Autoclave .....	2
1.3 Key Out-of-Autoclave Applications .....	5
1.4 Out-of-Autoclave Prepregs – A Review .....	5
1.5 Voids in Out-of-Autoclave Manufacturing.....	9
1.6 Voids and Structural Performance OoA .....	11
1.7 Thesis Motivation and Objectives .....	13
1.8 Outline.....	14
<b>2 A Review of the Governing Physics in Out-of-Autoclave Processing</b> .....	<b>17</b>
2.1 Introduction.....	17
2.2 Resin Flow through a Porous Medium .....	18
2.2.1 Conservation of Mass .....	18
2.2.2 Conservation of Momentum.....	19
2.2.3 Compaction and Percolation Flow .....	22
2.2.4 Constitutive Laws .....	23
2.3 Air Flow through a Porous Medium .....	31
2.3.1 Mechanisms of Gas Transport.....	31
2.3.2 Ideal Gas Law .....	33
2.3.3 Governing Equations .....	34
2.3.4 Constitutive Laws .....	38
2.4 Coupling Air and Resin Flow .....	39
2.4.1 State of the Art.....	39

2.4.2	Resin Front Propagation .....	42
2.5	Heat Transfer through a Porous Medium.....	43
2.6	Summary and Discussion .....	45
<b>3</b>	<b>Characterization of the MTM 44-1 Prepreg.....</b>	<b>47</b>
3.1	Morphological Characterization.....	47
3.1.1	Microscopy and Computed Tomography .....	48
3.1.2	Geometry Definition .....	50
3.2	Quantification of the Volume Fraction of all Prepreg Constituents at the Initial State .....	51
3.2.1	Determination of Global Volume Fractions .....	51
3.2.2	Determination of Local Volume Fractions .....	60
3.3	Prepreg Characterization .....	63
3.3.1	Permeability to Air.....	63
3.3.2	Tow Permeability to Resin.....	72
3.4	Resin Film Characterization.....	73
3.4.1	Cure Kinetics .....	73
3.4.2	Rheometry.....	84
3.4.3	Rheological Modeling.....	89
3.5	Summary and Discussion .....	98
<b>4</b>	<b>The Impact of Air Evacuation on the Impregnation of OoA Prepregs.....</b>	<b>101</b>
4.1	Isothermal Tow Impregnation.....	102
4.1.1	Domain and Assumptions.....	102
4.1.2	Modeling Approach .....	103
4.1.3	Sensitivity Studies.....	110
4.2	Non-Isothermal Prepreg Impregnation.....	116
4.2.1	Domain and Assumptions .....	117
4.2.2	Modeling Approach .....	118
4.2.3	Coupling Scheme .....	122
4.2.4	Sensitivity Studies.....	124
4.3	Summary and Discussion .....	153

<b>5</b>	<b>Validation of the OoA Simulation.....</b>	<b>157</b>
5.1	Experimental Test Bench.....	157
5.2	Process Monitoring.....	158
5.2.1	Pressure Gauges.....	159
5.2.2	Temperature and Viscosity Sensors.....	160
5.2.3	Displacement Sensors.....	160
5.3	Room Temperature Debulking.....	161
5.4	Manufacturing a CFRP Demonstrator OoA.....	162
5.5	Simulation and Experimental Verification.....	163
5.5.1	Simulation Domain and Assumptions.....	163
5.5.2	Temperature and Viscosity Evolution.....	164
5.5.3	Gas Pressure Development.....	171
5.5.4	Laminate Consolidation.....	177
5.6	Laminate Quality Evaluation.....	179
5.7	Summary and Discussion.....	181
<b>6</b>	<b>Conclusions and Outlook.....</b>	<b>183</b>
6.1	OoA Process Simulation.....	183
6.2	Material Characterization, Process Monitoring and Quality Evaluation... 186	
6.3	Recommendations for Manufacturing Monolithic Parts Out-of-Autoclave.....	188
	<b>References.....</b>	<b>191</b>
<b>A</b>	<b>Appendix.....</b>	<b>211</b>
a	OoA Applications and a Review of Commercially Available Prepregs (Chapter 1).....	211
b	Image Analysis of the MTM 44-1 Prepreg (Section 3.2.1.2).....	213
c	Raw Data from the Air Permeability Measurements of the MTM 44-1 Prepreg (Section 3.3.1).....	214
d	Dynamic Oscillatory Testing of Resins using Parallel Plate Rheometry (Section 3.4.2).....	215
e	Linear Visco-Elastic Domain Definition (LVE) of the MTM 44-1 Resin (Section 3.4.2).....	218
f	Inputs for the Isothermal Tow Impregnation Models (Section 4.1).....	221

g	Sensor and Probe Locations in the CFRP Demonstrator used for Validation (Chapter 5).....	223
h	Temperature Homogeneity Measurements on the Tool used for Validation (Chapter 5).....	224
<b>B</b>	<b>Publications</b> .....	<b>227</b>
<b>C</b>	<b>Supervised Student Theses</b> .....	<b>229</b>

# Nomenclature

Symbol	Unit	Description
<b>General symbols and representations</b>		
$x, X$		Scalar quantities
$\mathbf{x}, \mathbf{X}$		Tensors (1 <sup>st</sup> and 2 <sup>nd</sup> order)
$\langle x \rangle$		Volume average of a quantity $x$ (scalar/tensor)
$\hat{x}$		Estimated/predicted value of a quantity $x$ (scalar/tensor)
$\bar{x}$		Average value of a quantity $x$ (scalar/tensor)
$\dot{x}$		Rate of evolution of a quantity $x$ (scalar/tensor)
$x^*$		Dimensionless quantity (scalar/tensor)
$i$		Index
$N, M$		Scalars denoting number/amount of a quantity $x$
$R^2$		Coefficient of determination
$R_{adj}^2$		Adjusted coefficient of determination
$d_x$		Standard deviation of a quantity $x$ in subscript
$e_x$		Standard error of the mean for a quantity $x$ in subscript
<b>Subscripts and superscripts</b>		
$i$		Subscripts used for porous domain definition $p$ : prepreg $t$ : tow
$j$		Subscripts used for wetting fluid definition $a$ : air $r$ : resin
$n_i, m_i$		Superscripts used for cure reaction orders
$xx$		In-plane contribution of a quantity
$zz$		Through-thickness contribution of a quantity
<b>Greek Symbols</b>		
<b>Tensors (1<sup>st</sup> and 2<sup>nd</sup> order)</b>		
$\bar{\mathbf{v}}_a$	$\text{m}\cdot\text{s}^{-1}$	Mean velocity of the gas through the porous (fibrous) medium during sliding flow
$\boldsymbol{\sigma}$	Pa	Applied stress tensor (on porous/fibrous medium)

Symbol	Unit	Description
$\sigma_f$	Pa	Effective stress tensor of the fiber bed
$\tau_v$	Pa	Viscous stress tensor of a fluid's motion through a porous/fibrous medium
<b>Scalars</b>		
$\alpha$	-	Degree of cure
$\alpha_{c0}$	-	Critical degree of cure at $t=0$
$\alpha_{cT}$	K <sup>-1</sup>	Critical degree of cure at temperature T
$\alpha_g$	-	Degree of cure at gel-point
$\gamma$	N·m <sup>-1</sup>	Surface tension of mercury
$\gamma_s$	-	Shear strain of the resin during an oscillatory test
$\dot{\gamma}_{sr}$	s <sup>-1</sup>	Maximum shear strain rate measured at distance $r = R$ from the shaft of the rheometer during a parallel plate test
$\delta$	rad	Phase difference between the stress and strain response during a parallel plate oscillatory test
$\Delta H_t$	J·g <sup>-1</sup>	Heat or enthalpy of reaction released from 1g of resin at time t during cross-linking
$\Delta H_R$	J·g <sup>-1</sup>	Total heat or enthalpy of reaction released from 1g of resin until complete curing of a thermoset resin
$\Delta T_{avg}$	°C	Temperature difference between the average and local tool temperatures
$\Delta T_p$	°C	Difference between the sample and reference temperature in DSC
$\Delta T_{Op}$	°C	Difference between the sample and furnace temperature in DSC
$\Delta P_f$	Pa	Pressure difference developed in the resin impregnated fibrous domain of the prepreg or tow
$\vartheta$	°	Contact angle between mercury and the material characterized via mercury porosimetry
$\lambda$	m	Mean free path (8·10 <sup>-8</sup> m for air at 25°C and 1atm)
$\lambda_n$	-	Coefficient in the analytical solution of the 1D gas pressure developed in a porous medium
$\mu_j$	Pa·s	Fluid viscosity
$\mu_0$	Pa·s	Initial air viscosity at absolute temperature (Sutherland's equation)
$\rho_b$	kg·m <sup>-3</sup>	Bulk prepreg density measured using mercury porosimetry
$\langle \rho C_p \rangle_j$	J·m <sup>-3</sup> ·K <sup>-1</sup>	Effective volumetric heat capacity of the porous medium (fibrous) filled with a fluid

<b>Symbol</b>	<b>Unit</b>	<b>Description</b>
$\rho_f$	$\text{kg}\cdot\text{m}^{-3}$	Fiber density
$\rho_j$	$\text{kg}\cdot\text{m}^{-3}$	Fluid density
$\sigma_s$	Pa	Shear stress applied on the resin (during sinusoidal oscillatory testing in the rheometer )
$\sigma_{s0}$	Pa	Shear stress amplitude of the resin (during sinusoidal oscillatory testing in the rheometer )
$\tau$	-	Dimensionless elapsed cure time (Kiuna et al.)
$\tau_a$	-	Dimensionless time for air flow out of a prepreg
$\phi$	- or %	Porosity
$\phi_i$	- or %	Porosity (global -ply/local-tow)
$\phi_j$	- or %	Local volume fraction of fluids (air/resin)
$\langle\Phi_v\rangle$	$\text{J}\cdot\text{m}^{-3}$	Viscous dissipation per unit volume
$\omega$	$\text{rad}\cdot\text{s}^{-1}$	Angular frequency (rheometer)
$\Omega$	mrad	Scanning angle (rheometer)

### Latin Symbols

#### Tensors (1<sup>st</sup> and 2<sup>nd</sup> order)

$\mathbf{g}$	$\text{m}\cdot\text{s}^{-2}$	Gravitational acceleration
$\mathbf{I}$	-	Unit tensor
$\mathbf{k}_f$	$\text{W}\cdot\text{m}^{-1}\cdot\text{K}^{-1}$	Thermal conductivity tensor of the fibers
$\langle\mathbf{k}\rangle_j$	$\text{W}\cdot\text{m}^{-1}\cdot\text{K}^{-1}$	Effective thermal conductivity of the porous medium impregnated with a fluid
$\mathbf{K}$	$\text{m}^2$	Intrinsic or viscous flow permeability tensor
$\mathbf{K}_j$	$\text{m}^2$	Permeability tensor of the prepreg or tow to fluid
$\mathbf{K}_{a,eq}$	$\text{m}^2$	Equivalent permeability of a sandwich panel
$\mathbf{u}_{jf}$	$\text{m}\cdot\text{s}^{-1}$	Fluid velocity vector at the flow-front
$\mathbf{v}_j$	$\text{m}\cdot\text{s}^{-1}$	Local fluid velocity vector
$\mathbf{v}_{jD} = \langle\mathbf{v}_j\rangle$	$\text{m}\cdot\text{s}^{-1}$	Volume averaged fluid velocity or Darcy's velocity vector in the porous (fibrous) medium

#### Scalars

$a$	-	Dimensionless viscosity as a function of time (Kiuna's model)
$a_b$	-	Biot's effective stress coefficient
$a_f$	-	Correction factor in the definition of a sandwich panel permeability

<b>Symbol</b>	<b>Unit</b>	<b>Description</b>
$aw_p$	$\text{g}\cdot\text{m}^{-2}$	Prepreg areal weight
$aw_f$	$\text{g}\cdot\text{m}^{-2}$	Textile areal weight
$aw_r$	$\text{g}\cdot\text{m}^{-2}$	Resin areal weight
$A, B, C$	-	Rate constants in the resin viscosity evolution
$A_c$	$\text{m}^2$	Cross-sectional area
$A_i$	$\text{m}^2$	Cross-sectional area of prepreg ply or tow
$A_j$	$\text{m}^2$	Cross-sectional area impregnated with a fluid $j$
$A_m$	$\text{m}^2$	Area of the cavity used for air permeability determination of the MTM 44-1 prepreg
$A_{n,1}, A_{n,i}$	$\text{Pa}\cdot\text{s}$	Pre-exponential coefficients in $n_0(T)$ and $n_i(T)$
$A_{n,2}, A_{k,i}$	$\text{s}^{-1}$	Pre-exponential coefficient in $k(T)$ and $k_i(T)$
$A_{n,3}$	-	Coefficient correlating the dimensionless viscosity with the dimensionless time (Kiuna et al.)
$A_{n,4}$	$\text{K}^{-1}$	Coefficient of the viscosity factor $S_f$ (Keller et al.)
$AR_f$	-	Air resistance to filling
$b$	-	Klinkenberg factor
$c$	-	Coefficient defined in Gebart's permeability equations, a weak function of the fiber volume fraction
$C_G$	-	Coefficient characteristic of the fiber arrangement type in Gebart's permeability
$C_i$	-	Coefficients in the Williams-Landel-Ferry model
$c_k$	-	Coefficient accounting for chemical reaction effects on the viscosity
$C_{p_f}$	$\text{J}\cdot\text{kg}^{-1}\cdot\text{K}^{-1}$	Specific heat capacity of fiber at constant pressure
$C_{p_j}$	$\text{J}\cdot\text{kg}^{-1}\cdot\text{K}^{-1}$	Specific heat capacity of fluid at constant pressure
$C_{p_{Rev}}$	$\text{J}\cdot\text{g}^{-1}\cdot^\circ\text{C}^{-1}$	Reversing specific heat capacity measured via MDSC
$C_{p_r}$	$\text{J}\cdot\text{g}^{-1}\cdot^\circ\text{C}^{-1}$	Specific heat capacity of reference pan measured via DSC/MDSC
$C_{p_s}$	$\text{J}\cdot\text{g}^{-1}\cdot^\circ\text{C}^{-1}$	Specific heat of the pan containing a sample measured via DSC/MDSC
$C_s$	-	Sutherland's coefficient
$\frac{d\alpha}{dt}$	$\text{s}^{-1}$	Cure reaction rate
$\frac{dH_t}{dt}$	mW	Differential heat flow rate measured at time $t$ during cross-linking of a thermoset resin
$\frac{dH_{iso}}{dt}$	mW	Isothermal heat flow rate measured via DSC



<b>Symbol</b>	<b>Unit</b>	<b>Description</b>
$\frac{dH_{res}}{dt}$	mW	Residual heat flow rate measured with a dynamic MDSC sweep on a sample previously tested with isothermal DSC
$\frac{dH_{Rev}}{dt}$	mW	Reversible heat flow rate measured with MDSC
$\frac{dH_{Non_Rev}}{dt}$	mW	Non-reversible heat flow rate measured with MDSC
$\frac{dn}{dt}$	Pa	Non isothermal resin viscosity rate (complex)
$dt_0$	s	Solver initialization time used in the delayed air evacuation model
$\frac{dT_{dyn}}{dt}$	°C·min <sup>-1</sup>	Heating ramp rate for first sweep in MDSC
$dt_{fill}$	s	Difference between the impregnation time of an OoA tow predicted by the instantaneous and the delayed air evacuation model
$\frac{dT_{iso}}{dt}$	°C·min <sup>-1</sup>	Heating rate up to the dwell temperature in isothermal DSC
$\frac{dT_{res}}{dt}$	°C·min <sup>-1</sup>	Heating ramp rate of the second temperature sweep in MDSC
$\frac{dT_{sp}}{dt}$	°C·min <sup>-1</sup>	Heating ramp rate of a sample in DSC/MDSC
$\frac{dQ}{dt}$	mW	Heat flow rate introduced to or emitted by the sample in DSC/MDSC
$D$	-	Coefficient accounting for the rate of a resin's reaction shift from kinetic to diffusion controlled
$E_k, E_{n,2}$	J·mol <sup>-1</sup>	Kinetic analogue of the activation energy
$E_n, E_{n,1}$	J·mol <sup>-1</sup>	Resin activation energy
$E_{n,3}$	-	Coefficient correlating the dimensionless viscosity with dimensionless time (Keller et al.)
$E_{n,4}$	-	Coefficient of the viscosity factor $S_f$ (Keller et al.)
$f$	Hz	Frequency
$F_N$	N	Normal force
$G^*$	Pa	Complex shear modulus
$G'$	Pa	Storage modulus
$G''$	Pa	Loss modulus
$G_1$	s	Pre-exponential coefficient used in the determination of the resin's gel-time
$G_2$	°C <sup>-1</sup>	Coefficient used in the determination of the resin's gel-time at various temperatures

<b>Symbol</b>	<b>Unit</b>	<b>Description</b>
$h_e$	m	Minor axis of tow fitted with an ellipse
$\frac{h_c}{2h_s}$	-	Ratio of the core dimensions of a sandwich panel
$H$	mm	Distance between the two parallel plates of the rheometer
$H_i$	m	Thickness of the prepreg ply or tow
$H_{iso}$	J·g <sup>-1</sup>	Heat of reaction of 1g of resin, measured via isothermal DSC
$H_{min}$	mm	Position where gas equilibrates with atmospheric pressure (compromised vacuum connection)
$H_r$	m	Resin film thickness
$H_{res}$	J·g <sup>-1</sup>	Residual heat of reaction in 1g of resin measured with a dynamic MDSC measurement sweep on a sample previously tested via isothermal DSC
$H_{t,j}$	m	Local thickness of the tow saturated with a fluid
$I_j$	-	Degree of impregnation of the prepreg with fluid
$k(T), k_i(T)$	s <sup>-1</sup>	Kinetic parameter expressing cure-rate advancement
$k_{\infty}$	s <sup>-1</sup>	Direct kinetic analogue of the viscosity ( $n_{\infty}$ ) for a fully cured resin undergoing a single reaction
$k_{f,xx}, k_{f,zz}$	W·m <sup>-1</sup> ·K <sup>-1</sup>	Thermal conductivity of the fibers in-plane and through thickness
$k_j$	W·m <sup>-1</sup> ·K <sup>-1</sup>	Thermal conductivity of the fluid
$K_{j,xx}, K_{j,zz}$	m <sup>2</sup>	In-plane ( $K_{j,xx}$ ) and through-thickness permeability ( $K_{j,zz}$ ) of a prepreg or tow
$K_m$	m	Knudsen flow parameter related to pore geometry (sliding flow)
$K_n$	-	Knudsen number
$K_{rel}(S_j)$	-	Relative permeability - scalar varying from zero to one with the saturation of the porous domain
$l$	m	Characteristic length of pores in a fibrous medium
$l_e$	m	Major axis of tow ellipse
$L$	m	Part length
$m_{a0}, m_a$	g	Mass of air at t=0 and at every t
$m_b$	g	Prepreg mass measured with mercury porosimetry
$m_{c0}$	g	Mass of penetrometer (mercury porosimetry)
$m_{Hg}$	g	Mass of mercury (mercury porosimetry)
$m_{tot}$	g	Mass of penetrometer (mercury and prepreg)

<b>Symbol</b>	<b>Unit</b>	<b>Description</b>
$M$	N·m	Torque of the rheometer's shaft
$M_n$	$\text{g}\cdot\text{mol}^{-1}$	Molar mass (for dry air $\sim 28.96$ )
$n, n^*$	Pa·s	Resin viscosity (complex)
$n'$	Pa·s	Viscous component of the complex resin viscosity
$n''$	Pa·s	Elastic or out-of-phase component of the complex viscosity
$n_{gas}$	mol	Amount of substance in the gas
$n_{max}, n_{min}$	Pa·s	Maximum/minimum viscosity of the resin
$n_0$	Pa·s	Initial resin viscosity (at $t=0$ )
$n_i(T)$	Pa·s	Viscosity evolution as a function of temperature
$n_\infty$	Pa·s	Viscosity of a fully cured resin system
$n_{gel}$	Pa·s	Resin viscosity at the gel-point, $t_{gel}$
$n_s$	Pa·s	Resin viscosity at temperature $T_s$
$n_{min}$	Pa·s	Minimum resin viscosity
$p_1 - p_6$	-	In-plane air permeability coefficients
$P_i, PS_i$	mm x mm	Sensor coordinates denoting position inside part
$P_a = \langle P \rangle^a = P_{gas}$	Pa	Air/gas pressure in the porous/fibrous medium
$P_{atm}$	Pa	Atmospheric pressure
$P_c$	Pa	Capillary pressure
$P_{gas\_min}$	Pa	Minimum gas pressure developed within the time-scale of resin flow (delayed air evacuation model)
$P_{max}$	Pa	Maximum applied pressure (mercury porosimetry)
$P_r = \langle P \rangle^r = P_f$	Pa	Resin/fluid pressure in the porous/fibrous medium
$P_s$	Pa	'Pseudo' or 'slip' pressure
$P_{vac}$ $P_{vac\_min}, P_{vac\_max}$	Pa	Vacuum pressure (maximum and minimum)
$Q$	$\text{m}^3\cdot\text{s}^{-1}$	Rate of volumetric discharge (Darcy)
$\langle Q \rangle_j$	$\text{J}\cdot\text{m}^{-3}$	Energy dissipation of the fluid per unit volume
$r_i$	$\mu\text{m}$	Curvature of mercury's interface to the pore
$r_{pore}$	$\mu\text{m}$	Pore radius measured via mercury porosimetry
$R$	$\text{J}\cdot\text{K}^{-1}\cdot\text{mol}^{-1}$	Universal gas constant (dry air $\sim 8.3144$ )
$R(t)$	M $\Omega$	Electrical resistance of the prepreg
$\langle \dot{R} \rangle$	$\text{J}\cdot\text{m}^{-3}$	Energy generation per unit volume due to curing
$Re$	-	Reynolds number
$R_f$	$\mu\text{m}$	Fiber radius
$R_{max}, R_{min}$	M $\Omega$	Minimum/maximum electrical prepreg resistance

<b>Symbol</b>	<b>Unit</b>	<b>Description</b>
$R_{norm}$	M $\Omega$	Normalized electrical resistance of the prepreg
$R_p$	mm	Radius of plate used in parallel plate rheometry
$R_r$	$^{\circ}\text{C}\cdot\text{W}^{-1}$	Thermal resistance between the heat source and reference pan during DSC/MDSC measurements
$R_s$	$^{\circ}\text{C}\cdot\text{W}^{-1}$	Thermal resistance between the heat source and sample pan during a DSC/MDSC measurements
$R_{sp}$	$\text{J}\cdot\text{kg}^{-1}\cdot\text{K}^{-1}$	Specific gas constant (for dry air $\sim 287.06$ )
$s$	$\text{g}\cdot\text{m}^{-3}\text{s}^{-1}$	Sink term (Volume averaged rate of mass per unit area of the porous medium)
$S_f$	-	Viscosity shifting factor (Keller et al.)
$S_j$	-	Degree of saturation of a fibrous medium with a fluid $j$
$t$	s or min	Time (units as reported in the text/graphs)
$t_c$	s	Characteristic time for air flow
$t_{fill}$	s	Impregnation time of tow with resin
$t_{fill_{96.9\%}}$	s	Impregnation time of 96.9% of tow area with resin
$t_{gel}$	s	Time at gel-point of the resin
$t_{min}$	s	Time at minimum viscosity of the resin
$t_p$	s	Modulation period of an MDSC
$t_{PSi}$	s	Prepreg/ply locking time
$t_s$	s	Sampling time
$\tan \delta$	-	Loss factor
$T_j$	$^{\circ}\text{C}$	Temperature of the fluid saturated porous medium
$T, T(t)$ $T_{top}(t), T_{tool}(t)$	$^{\circ}\text{C}$ or K	Temperature and temperature boundary conditions (units as reported in the text/graphs)
$T_0$	K	Absolute temperature in Sutherland's equation (273.15K)
$T_{0p}$	$^{\circ}\text{C}$	DSC furnace temperature
$T_A$	$^{\circ}\text{C}$	Temperature amplitude in a modulated DSC
$T_{dyn}$	$^{\circ}\text{C}$	Temperature range used for the first MDSC sweep
$T_g, T_{g\infty}$	$^{\circ}\text{C}$	Glass transition temperature of cured material
$T_{g0}$	$^{\circ}\text{C}$	Glass transition temperature of uncured material
$T_{iso}$	$^{\circ}\text{C}$	Dwell temperature in isothermal DSC
$T_{res}$	$^{\circ}\text{C}$	Temperature range of the second sweep in MDSC
$T_{rp}$	$^{\circ}\text{C}$	Reference pan temperature in DSC
$T_s$	$^{\circ}\text{C}$	Reference temperature

<b>Symbol</b>	<b>Unit</b>	<b>Description</b>
$T_{sp}$	°C	Sample pan temperature in DSC
TC i	mm x mm	Thermocouple positions in the laminate
$TC_{avg\_m}$	°C	Difference between the average experimental and the average simulated temperature
$v_{jD,xx}, v_{jD,zz}$	$m \cdot s^{-1}$	In-plane and out-of-plane Darcy velocity
$u_{jf,xx}, u_{jf,zz}$	$m \cdot s^{-1}$	In-plane and out-of-plane flow-front velocity of the fluid in the porous (fibrous) medium
$V_{a,p}$	$m^3$	Air volume in the prepreg (mercury porosimetry)
$V_B$	$m^3$	Bulk prepreg volume (mercury porosimetry)
$V_{f,i}$	$m^3$	Fiber volume (mercury porosimetry)
$V_I$	$m^3$	Cumulative intrusion volume (mercury porosimetry)
$V_{j,i}$	$m^3$	Fluid volume (mercury porosimetry)
$V_S$	$m^3$	Skeletal volume (mercury porosimetry)
$V_f$	- or %	Fiber volume fraction
$V_{f,i}$	- or %	Fiber volume fraction of prepreg or tow
$V_{f,j}$	- or %	Local fiber volume fraction (in sub-domain saturated with a single fluid)
$V_{gas}$	$m^3$	Volume of gas
$V_m$	$m^3$	Volume of air trapped in the cavity prior to air permeability determination of the MTM 44-1 prepreg
$V_{f,max}$	- or %	Maximum fiber volume fraction (Gebart)
$V_{r,p}$	- or %	Global resin volume fraction
$V_t$	$m^3$	Tank volume – referring to the tank used for air permeability measurements of a sandwich panel
$W_r$	- or %	Weight fraction of the resin
$\gamma_0$	-	Coefficient correlating the dimensionless viscosity with the dimensionless time (Kiuna et al.)
$z_f$	m	Resin front position through tow/prepreg thickness
$z_{min}$	m	Position where 96.9% of the tow thickness impregnated with resin (compromised vacuum connection)



# Abbreviations

<b>Abbreviation</b>	<b>Description</b>
AC	Alternating Current
BC	Boundary Conditions
CCD	Charge Coupled Device (in the context of this work refers to CCD microscopy)
CFRP	Carbon Fiber Reinforced Polymer
CI	Confidence Interval
c-RIO	Compact Rio Data logging platform from National Instruments
CT, $\mu$ CT	Computed Tomography, micro Computed Tomography
DC	Direct current
DCB	Double Cantilever Beam (ref. to mechanical testing procedure)
DEA	Dielectric Analysis
DGEBA	Diglycidyl Ether of Bisphenol A
DoD	Department of Defense
DPM	Dropping Pressure Method to measure air permeability
DSC	Dynamic Scanning Calorimetry
DVRT/DVDT	Differential Variable Reluctance Transducer
EVAC's	Evacuation Channels inside an Out-of-Autoclave prepreg
FEA	Finite Element Approach
FT	Fourier Transform
GMT	Glass Mat Thermoplastic material
IC	Initial Condition
IDoI	Initial Degree of Impregnation
ILSS	Interfacial Shear Strength (ref. to mechanical testing procedure)
LB	Lower Bound
LCM	Liquid Composite Molding
MDSC	Modulated Dynamic Scanning Calorimetry
NCF	Non Crimp Fabric
NMR	Nuclear Magnetic Resonance
OoA	Out-of-Autoclave Processing
OHC	Open Hole Compression (ref. to test procedure)
PW	Plain Weave (ref. to textile architecture)
RPM	Raising Pressure Method to measure air permeability
RT	Room Temperature

---

<b>Abbreviation</b>	<b>Description</b>
RVE	Reference Volume Element
SEM	Scanning Electron Microscope
SSE	Sum of Squares due to Errors
TBA	Torsional Braid Analysis
TGMDA/TGGDM	Tetraglycidyl 4,4' Diaminodiphenylsulphone
TMA	Thermal Mechanical Analysis
UB	Upper Bound
UD	Unidirectional Fabric
VARI	Vacuum Assisted Resin Infusion
VBO	Vacuum Bag Only Processing
V-RTM	Vacuum Assisted Resin Transfer Molding
WLF	Williams-Landel-Ferry
5HS	Five harness satin (ref. to textile architecture)

---



# List of Figures

Fig. 1-1:	Process steps involved in manufacturing of composite parts with prepregs .....	1
Fig. 1-2:	Manufacturing set-ups and typical cure cycles utilized when processing prepregs in and Out-of-Autoclave .....	3
Fig. 1-3:	Cross-sections of two Out-of-Autoclave prepregs and their impregnation schemes .....	6
Fig. 1-4:	Boeing quality targets for the third generation of Vacuum-Bag-Only Prepregs compared against Autoclave performance [25] .....	8
Fig. 1-5:	Porosity development in an Out-of-Autoclave prepreg stack (MTM 44-1, 2x2 TW) .....	10
Fig. 1-6:	Graphical representation of the PhD thesis content and structure .....	15
Fig. 2-1:	Interacting physics during Out-of-Autoclave processing .....	17
Fig. 3-1:	Planar views of (a) a 2x2 twill weave textile, consisting the basis of the MTM44-1 prepreg [216] (b) top side and (c) bottom side of the MTM44-1 prepreg .....	48
Fig. 3-2:	Cross-sectional views of the MTM44-1 prepreg at different locations and magnifications .....	49
Fig. 3-3:	(a) Zoom of the ‘tow equivalent’ domain of the MTM 44-1 prepreg [S1] (b) cross-section of an MTM44-1 prepreg stack [S2] (c) simplified domain used as a basis for modeling .....	50
Fig. 3-4:	Image analysis process used for global porosity determination .....	55
Fig. 3-5:	(a) sketch of a mercury penetrometer and (b) typical curve acquired during porosity measurements of a prepreg using mercury porosimetry .....	57
Fig. 3-6:	Mercury porosimetry curves for all OoA prepregs .....	58
Fig. 3-7:	SEM picture of the proprietary PW OoA prepreg .....	59
Fig. 3-8:	Porosity of an MTM 44-1 ply determined via image segmentation and porosimetry .....	60
Fig. 3-9:	Microscopy images of the MTM 44-1 prepreg and image analysis .....	62
Fig. 3-10:	Experimental test-bench used for the determination of the in-plane air permeability .....	64
Fig. 3-11:	Schematic of the approach used to determine the MTM 44-1 air permeability .....	65

Fig. 3-12: Conditioning of the prepreg stack before testing its air permeability [SN1] .....	66
Fig. 3-13: Air permeability of the MTM 44-1 prepreg for a range of porosities .....	67
Fig. 3-14: Experimental versus simulated pressures and resulting microstructures imaged with $\mu$ CT after conditioning the MTM 44-1 prepreg for 10min at (a) 80°C (b) 100°C .....	70
Fig. 3-15: MTM 44-1 permeability vs. porosity of samples conditioned at various temperatures and times .....	70
Fig. 3-16: Through thickness permeability of the MTM 44-1 tow for a quadratic and a hexagonal distribution of fibers in the tow and their average.....	72
Fig. 3-17: MDSC thermogram of the MTM 44-1 resin depicting two consecutive scans performed at 1°C/min on the same sample .....	76
Fig. 3-18: Total enthalpy of the MTM 44-1 resin determined via non-isothermal measurements .....	77
Fig. 3-19: (a) Isothermal heat flow of the MTM 44-1 resin measured between 100 °C-200 °C and (b) residual heat flow determined via a subsequent dynamic scan .....	79
Fig. 3-20: Total enthalpy of the MTM 44-1 resin determined at isothermal temperatures .....	79
Fig. 3-21: MTM 44-1 cure rate vs. degree of cure and global fitting error .....	83
Fig. 3-22: Rheological properties of the MTM 44-1 resin generated between 110-180°C using isothermal oscillatory parallel plate rheometry (see Appendix d).....	86
Fig. 3-23: Non-isothermal oscillatory measurements of MTM 44-1 resin at three heating rates generated using a parallel plate rheometer (see Appendix d).....	88
Fig. 3-24: Predicted gel time of the MTM 44-1 resin ( $t_{gel}$ ) at isothermal temperatures between 100-200 °C .....	89
Fig. 3-25: Dimensionless MTM 44-1 resin viscosity (a) vs dimensionless time ( $\tau$ ).....	91
Fig. 3-26: Determination of viscosity coefficients $A_{n,1}$ , $A_{n,2}$ , $E_{n,1}$ , $E_{n,2}$ using linear regression .....	92
Fig. 3-27: Determination of the shifting factor $S_f$ using linear regression.....	93
Fig. 3-28: Comparison between the experimental and modeled isothermal resin viscosity.....	94

Fig. 3-29: Comparison of the experimental and modeled MTM 44-1 resin viscosity resulting from the analytical (3-51) and pde (3-49) expressions at a heating rate of 2°C/min.....	96
Fig. 3-30: Comparison of the experimentally measured and modeled MTM 44-1 viscosity of Equation (3-49) implemented in COMSOL Multiphysics at 1 and 2 °C/min.....	97
Fig. 4-1: ‘tow equivalent’ used as a basis for the development of isothermal tow impregnation models in Matlab .....	102
Fig. 4-2: Boundary conditions used in isothermal tow impregnation model development .....	103
Fig. 4-3: Resin and gas pressure evolution – Instantaneous air evacuation .....	105
Fig. 4-4: Resin and gas pressure evolution – Compromised vacuum connection .....	106
Fig. 4-5: Modeling scheme of the delayed air evacuation out of the Out-of-Autoclave tows.....	108
Fig. 4-6: Resin and gas pressure evolution – Delayed air evacuation .....	109
Fig. 4-7: Impregnation time of a Material 1 tow, for a range of lengths and permeability ratios.....	112
Fig. 4-8: The impact of the air resistance to flow $AR_f$ on the tow impregnation time difference $dt_{fill}$ between the instantaneous and delayed air evacuation models.....	113
Fig. 4-9: Impregnation time of three tows (Materials 1-3) at 130°C for a range of lengths and permeability ratios.....	114
Fig. 4-10: The impact of the air resistance to flow $AR_f$ on the impregnation time difference between the instantaneous and delayed air evacuation models $dt_{fill}$ at 130°C.....	115
Fig. 4-11: Prepreg domain used as a basis for non-isothermal impregnation modeling using COMSOL Multiphysics .....	117
Fig. 4-12: Boundary conditions for air and resin flow .....	119
Fig. 4-13: Coupling scheme utilized in modeling the non-isothermal impregnation of the OoA prepreg in COMSOL Multiphysics .....	123
Fig. 4-14: (a) Domain geometry and (b) meshing concept used to perform sensitivity studies .....	125
Fig. 4-15: (a) Boundary conditions for air flow and (b) vacuum application via a step function .....	126

Fig. 4-16: Gas pressure evolution over time at three locations along the part length, for the materials with permeabilities of Cases 1-4 (Fig. 4-3).....	127
Fig. 4-17: Influence of the through thickness air permeability reduction $K_{a,zz}$ (Cases 1-4) on the in-plane versus out-of-plane air velocity ratio $v_{aD,xx}/v_{aD,zz}$ .....	128
Fig. 4-18: The influence of the in-plane air permeability reduction from Cases 1 to Case 5, on the gas pressure evolution at three locations along the part length.....	128
Fig. 4-19: Gas pressure distribution in the air saturated prepreg sub-domain .....	129
Fig. 4-20: Temperature development on the tool surface during three OoA cure cycles.....	130
Fig. 4-21: Gas pressure evolution along the length of the air-saturated prepreg domain in the material of Case 1 and for cure cycles shown in Fig. 4-20.....	130
Fig. 4-22: Air density evolution along the length of the air-saturated prepreg of Case 1 and for cure cycles shown in Fig. 4-20.....	131
Fig. 4-23: (a) Prepreg porosity evolution over time and (b) resulting in-plane air permeability evolution over time for Cases 1, 3 and 6 (see Tab. 4-4) .....	132
Fig. 4-24: Gas pressure evolution along the length of the air-saturated prepreg domain for prepregs with the properties of Cases 1, 3 and 6 (see Tab. 4-4) at 291.9K (~19°C) .....	133
Fig. 4-25: 2D plots depicting the pressure difference developed along the length and thickness of the part at 20s and 10000s, for the prepregs of Cases 1, 3 and 6 (see Tab. 4-4).....	134
Fig. 4-26: Gas pressure evolution over time along the length of the air-saturated prepreg domain, for the prepregs of Cases 1 and 6 (see Tab. 4-4) at 291.9K (~19°C).....	135
Fig. 4-27: Development of pressure difference after 10000s in the prepreg of Case 1 and 6 .....	136
Fig. 4-28: Influence of the increased initial resin viscosity on the prepreg porosity and the resulting in-plane air permeability evolution over time for Cases 1 and 6 .....	137
Fig. 4-29: (a) Resin viscosity (b) prepreg porosity (c) impregnation state (d) in-plane air permeability as a function of porosity for three temperature profiles depicted in Fig. 4-20 .....	139
Fig. 4-30: The influence of various physical phenomena on the gas pressure development inside the air saturated prepreg domain .....	140

Fig. 4-31: (a) Gas pressure (b) air density along the length of the air-saturated prepreg domain for the prepreg of Case 1 (Tab. 4-4) and three temperature profiles (Fig. 4-20) .....	141
Fig. 4-32: Gas pressure evolution inside the dry prepreg sub-domain of Case 1 at selected times during two cure cycles with a heating rate of 0.5 and 3 °C/min .....	142
Fig. 4-33: (a) Domain and probe locations (b) spatial discretization (meshing) .....	144
Fig. 4-34: (a) Temperature development inside the resin impregnated sub-domain of the prepreg (b) resin viscosity at P 1, P 7, P 10 for the cure cycles depicted in (a).....	145
Fig. 4-35: Gas pressure at three positions along the length of the air-saturated sub-domain for the material of Case 1 (see Tab. 4-4) at room temperature (at 291.9K ~19°C) and for three cure cycles at 0.5, 3°C/min and with zone heating (see Tab. 4-5).....	145
Fig. 4-36: 2D Temperature and gas pressure development inside the domain of Fig. 4-33 at three selected times when the zone heating concept presented in Tab. 4-5 is utilized .....	146
Fig. 4-37: (a) Porosity evolution in the prepreg of Case 1 processed at room temperature and three cure cycles at 0.5, 3°C/min and with zone heating (Tab. 4-5) (b) air permeability as a function of porosity (c) impregnation state - air (d) impregnation state –resin .....	147
Fig. 4-38: Domain used as a basis for studying the effects of out-of-plane temperature gradients .....	148
Fig. 4-39: (a) Temperature boundary conditions and (b) spatial discretization (meshing) .....	148
Fig. 4-40: Temperature and gas pressure distribution in the part of Fig. 4-38 at selected times .....	149
Fig. 4-41: (a) Resin temperature development utilizing the local and global porosity to describe the in-plane air evacuation (b) resin viscosity at three positions through the part thickness (P 7, P 7.1, P 7.2) .....	150
Fig. 4-42: (a) Gas pressure at three positions at the mid-span of the part, through its thickness (P 7, P 7.1, P 7.2) considering air evacuation based on the local and global porosity development and (b) zoom on the locking time of the three plies concerned (# 1, 11, 20).....	151
Fig. 4-43: Comparison of (a) the prepreg porosity of the material of Case 1 during processing with a rate of 0.5°C/min (Fig. 4-20) (b) the air	

	permeability as a function of the prepreg porosity (c) the impregnation state - air (d) the impregnation state –resin.....	152
Fig. 5-1:	(a) Aluminum tool used in the manufacturing of the CFRP demonstrator (b) data-acquisition scheme.....	158
Fig. 5-2:	Fully instrumented demonstrator part before undergoing OoA processing.....	158
Fig. 5-3:	Pressure sensor and tool-part integration .....	159
Fig. 5-4:	(a) Displacement measurement sensors (DVDTs) (b) real-time viscosity measurement via a measurement of the DC Resistance – provided by Synthesites (Optimold).....	160
Fig. 5-5:	Set-up used to perform debulking experiments at room temperature .....	161
Fig. 5-6:	(a) Measurement of the gas pressure at PS 1 and PS 2 during room temperature debulking ( $T_{avg}$ ) (b) sketch of the expected versus measured gas pressure at PS 2.....	161
Fig. 5-7:	Bagging and instrumentation scheme used for manufacturing of the demonstrator .....	163
Fig. 5-8:	(a) CFRP demonstrator geometry in COMSOL Multiphysics (b) spatial discretization .....	164
Fig. 5-9:	(a) Temperature boundary conditions (b) experimental and virtual sensor positions .....	164
Fig. 5-10:	(a) Temperature cycles applied at the top and bottom of the part (b) difference between the average and local temperatures, measured at the top and bottom plane .....	165
Fig. 5-11:	Simulated temperature and resin viscosity development in the demonstrator part.....	166
Fig. 5-12:	Comparison of experimentally measured and simulated temperatures at the mid-plane of the CFRP demonstrator (between the tenth and eleventh ply) .....	167
Fig. 5-13:	(a) Resistance measured in the material at positions DC 1 and DC 2, in the mid-plane of the laminate (b) comparison of the measured and simulated temperatures as well as normalized viscosity and resistance signals at position DC 1 in the laminate.....	169
Fig. 5-14:	Locations of the pressure sensors and simulation probes inside the demonstrator.....	171
Fig. 5-15:	(a) Simulated gas pressures at the inlet and ten more locations along the length of the demonstrator (P 1-P 10, at positions depicted in Fig.	

5-14) (b) tool temperature and the air volume evolution as depicted in the bottom ply of the part during the cycle .....	172
Fig. 5-16: Comparison of the measured and simulated pressure at the inlet and at two positions along the part length (P 5/ PS 1 and P 8/ PS 2, see Fig. 5-14 for sensor locations) .....	173
Fig. 5-17: Interaction between the simulated temperature, pressure and air volume in the bottom ply of the demonstrator at the inlet and three locations along the part length .....	174
Fig. 5-18: Domain deformation and gas pressure development at three selected times .....	175
Fig. 5-19: (a) Local porosity evolution in three plies located through the thickness of the part (ply #1,11, 20) (b) air permeability as a function of the local porosity evolution (c) gas pressure at the mid-span of the part (d) degree of impregnation - resin .....	176
Fig. 5-20: Part thickness evolution during OoA processing plotted along (a) the pressure development and (b) the local difference between measured and simulated temperature .....	177
Fig. 5-21: Porosity of parts with 0.59 and 1.2m length at three locations along the part length and pictures depicting (a) front side of part with L=0.59m (b) back side of part with L=0.59m (c) front side of part with L=1.2m (d) back side of part with L=1.2m [S5].....	179
Fig. 5-22: Intra-tow porosity summary and indicative worst case porosities observed at the back side of each part for (a) 0.59m long part (b) 1.2m long part .....	180
Fig. A- 1: Shear stress and strain of a viscoelastic fluid during an oscillatory test ( $0 < \delta < \pi/2$ ).....	215
Fig. A- 2: (a) The Anton Paar MCR 302 Rheometer and (b) schematic of the parallel plate set-up utilized for testing the MTM 44-1 resin film.....	216
Fig. A- 3: Amplitude sweep of the MTM 44-1 resin at 1Hz, for four isothermal temperatures .....	218
Fig. A- 4: Evolution of the MTM 44-1 storage modulus during the isothermal amplitude sweep at 1Hz for a range of temperatures.....	219
Fig. A- 5: Evolution of the storage and loss modulus of the MTM 44-1 resin during a frequency sweep at 0.1% deformation, for a range of temperatures .....	219

Fig. A- 6: Position and installation of thermocouples used to evaluate tool homogeneity .....	224
Fig. A- 7: (a) Tool and air temperature inside the oven ( $T_m$ ) versus time and (b) temperature difference between the front and middle/back of the tool and the two ends of the tool area where the validation parts are placed ( $\Delta T_m$ ) versus time, during the cure cycle .....	224
Fig. A- 8: Temperature homogeneity monitoring during cool-down, via an IR camera .....	225



# List of Tables

Tab. 1-1: Advantages and disadvantages of processing prepregs inside and outside the Autoclave [2, 4, 14, 18, 23] .....	4
Tab. 1-2: Key Features of Out-of-Autoclave Prepregs.....	9
Tab. 2-1: Numerical values used in Gebart’s model for the two idealized fiber distributions.....	25
Tab. 3-1: MTM 44-1 ply thickness and measurement error (using a range of methods).....	52
Tab. 3-2: Summarized properties of three MTM 44-1 prepreg batches .....	53
Tab. 3-3: Theoretical volume content of the MTM 44-1 prepreg constituents (via Method 1).....	53
Tab. 3-4: MTM 44-1 ply porosity determined via segmentation of the $\mu$ CT images .....	55
Tab. 3-5: Area and dimensions of MTM44-1 tows fitted to an ellipse .....	61
Tab. 3-6: Local fiber volume fraction of the MTM 44-1 tows.....	62
Tab. 3-7: Fitting coefficients of the MTM 44-1 in-plane air permeability as a function of the prepreg’s porosity and regression quality attained (see Equation (3 23)) .....	68
Tab. 3-8: Non-isothermal MDSC settings used for the measurement of the MTM44-1 resin .....	76
Tab. 3-9: Glass transition temperatures of the MTM 44-1 resin and method of calculation .....	77
Tab. 3-10: Settings used for isothermal DSC measurements on the MTM44-1 resin, followed with an MDSC scan for the quantification of the total enthalpy of the material.....	78
Tab. 3-11: Activation energy of the MTM 44-1 for a range of temperatures and degrees of cure .....	81
Tab. 3-12: Fitting coefficients of the cure rate versus degree of cure model proposed by Kratz and Shahkarami et al. [159, 167] (Equation (3-34)) adapted for the MTM 44-1 resin.....	82
Tab. 3-13: Minimum viscosity $n_0$ , gel time $t_{gel}$ and viscosity at the gel point $n_{gel}$ , measured at a range of temperatures during isothermal characterization of the MTM 44-1 resin .....	87

Tab. 3-14: Minimum viscosity $n_{min}$ , time at minimum viscosity $t_{min}$ , gel time $t_{gel}$ and viscosity $n_{gel}$ of the MTM 44-1 resin, for three cure cycles with heating rates between 1-3 °C/min .....	88
Tab. 3-15: Coefficients of Equation (3-42), determined through the best fit of the normalized viscosity vs normalized time for the MTM 44-1 resin (95% Confidence Interval) .....	91
Tab. 3-16: Coefficients determined via linear regression of the viscosity $n_o(T)$ and cure rate advancement $k(T)$ functions of the MTM 44-1 resin.....	92
Tab. 3-17: Simulated MTM 44-1 resin gel time and time interval used for determining the fitting quality (Equation (3-46)).....	94
Tab. 4-1: Material properties used to model heat transfer in COMSOL Multiphysics .....	122
Tab. 4-2: Part dimensions, probe coordinates and miscellaneous inputs for sensitivity studies .....	125
Tab. 4-3: Permeability characteristics of the air saturated prepreg domain.....	127
Tab. 4-4: Permeability characteristics of the materials from Case 1, 3, 6 under investigation .....	132
Tab. 4-5: Temperature cycles applied in the three Zones of the part and probe locations.....	144
Tab. 4-6: Part dimensions and probe locations inside the part of Fig. 4-38 .....	150
Tab. 5-1: Time at which the minimum DC Resistance and viscosity is measured.....	170
Tab. 6-1: OoA process simulation tool and quality of predicted outputs .....	186
Tab. 6-2: Review of the governing physics and constitutive laws implemented in COMSOL Multiphysics, used as a basis for the OoA simulation and suggestions for future work .....	187
Tab. A- 1: A list of commercial products manufactured Out-of-Autoclave.....	211
Tab. A-2: A review of available commercial OoA prepregs, key features and their applications .....	212
Tab. A- 3: Global Porosity Determination via image segmentation of $\mu$ CT images of single plies .....	213
Tab. A- 4: List of measurement points used to define the in-plane air permeability of the MTM 44-1 prepreg as a function of its porosity (see Chapter 3, Section 3.3).....	214

Tab. A- 5: Inputs used in the calculation of the tow impregnation times and pressure profiles at isothermal conditions during instantaneous air evacuation (Fig. 4-3), compromised vacuum connection (Fig. 4-4) and delayed air evacuation (Fig. 4-5).....	221
Tab. A- 6: Inputs used in sensitivity studies summarized in Section 4.1, Fig. 4-7 to Fig. 4-10 .....	222
Tab. A- 7: Sensors (experimental) and probe (simulation) locations in the CFRP demonstrator part presented in Chapter 5 .....	223



# 1 Introduction

The first Chapter of this thesis introduces the Out-of-Autoclave manufacturing methodology, commonly referred to as OoA, comparing it against the traditional Autoclave manufacturing of composite parts, utilizing prepregs (Sections 1.1 and 1.2). An overview of products currently manufactured outside the Autoclave, as well as the most common commercial prepregs specifically designed for Out-of-Autoclave processing and their key characteristics are summarized in Sections 1.3 and 1.4. Main concerns around replacing Autoclave with OoA manufacturing arise from the reduced pressure available in the later during the cure cycle. This may lead to an increased amount of voids and often to unacceptable material properties of the produced part. An overview of the void formation problematic with focus on OoA processing is given in Section 1.5, while a brief summary of the performance of composite parts manufactured OoA for a range of applications is given in Section 1.6. The Chapter closes with a presentation of the motivation and objectives of the work (Section 1.7), while an outline lays-out the structure and main content of each Chapter (Section 1.8).

## 1.1 Composites Manufacturing using Prepregs

The most established method to produce composite parts for the aerospace sector is via the use of high performance fibers, made into fabric sheets after pre-impregnating them with a resin system. These pre-impregnated sheets are known as prepregs.

Prepregs have been widely introduced in the production of Aerospace parts for military or civil aircrafts. Primary aim of the replacement of metallic parts of aircrafts with composites was the reduction of weight and therefore fuel consumption, while maintaining equivalent mechanical performance and prolonging the aircraft's service time.

The major steps followed during prepreg processing are depicted in Fig. 1-1.

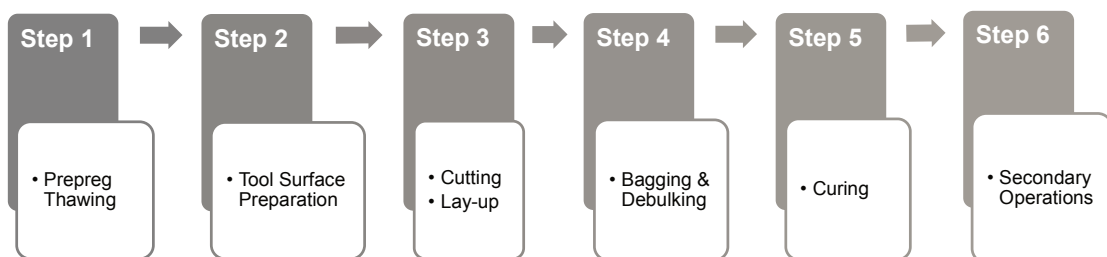


**Fig. 1-1: Process steps involved in manufacturing of composite parts with prepregs**

Since the resin is deposited on the prepreg during the material manufacturing stage, the prepreg has a limited shelf life and should be stored cold to limit the resin ageing before being used to manufacture a part. Prepreg rolls shall be removed from the freezer a few hours before processing, in order to allow the resin to reach viscosity and tackiness required for handling (Step 1) [1–3]. While the tool surface is cleaned and prepared for lay-up (Step 2), prepreg is cut into layers according to mold shape and part design. These layers are finally placed or formed to the required shape (either in a manual or automated fashion, Step 3). At this stage air can become entrapped between the prepreg plies of the laminate, which can eventually transition into residual intra-ply porosity. In order to reduce this effect, short vacuum cycles can be introduced at this stage (debulking cycles), after a certain amount of plies has been placed on the tool (Step 4). Finally, the part is packaged using auxiliary consumables (release film, breather, bleeder etc.) inside a flexible membrane or a vacuum bag [4] and undertakes the curing cycle; a predefined temperature and pressure schedule after which the part obtains its final shape and structural capacity (Step 5). Once the cure cycle is completed, it may be painted, cut to shape or prepared for joining, or undergo other secondary operations (Step 6) [1, 5].

The benefits of using prepreg materials for the production of composite parts are three-fold: the good control over the dimensional tolerance of the resulting part and the production of parts with high strength and consistent material properties. Nevertheless, a few challenges are associated with their processing. According to Hubert et al. [6], the tool design and the design of the bagging and curing procedure shall enable the production of ‘a fully cured, void free and undistorted part in the shortest time and the most economical fashion’ [6]. Residual stresses can built-up during the cure cycle and lead to deformations or warpage, due to a mismatch between the heat transfer coefficients of the tooling and the part [6]. Non-optimized cure cycle temperature can lead to the production of parts with reduced performance and temperature capability ( $T_g$ ). Manufacturing heavily contoured parts is a challenge for the drapability of a prepreg. Its incorrect placement may lead to wrinkle formation on the finished part [3], with negative consequences on its mechanical performance [7, 8].

## 1.2 Autoclave versus Out-of-Autoclave

The traditional route for processing thermoset prepreps is via the application of external pressure in a large heated pressure vessel, the Autoclave. As the composites application space expands towards the high volume and economically sensitive industrial markets (automotive, wind energy, consumer goods) while the parts become increasingly larger, the availability of autoclave facilities has become scarce [4, 9]. This has led to the development of flexible, scalable and cost effective manufacturing processes in the last decade. Replacing the Autoclave is economically interesting, primarily for manufacturing larger structures where an appropriately sized Autoclave would not be available or would be costly to access [10–12].

An example of an alternative to the Autoclave processing is the Out-of-Autoclave (OoA) or otherwise known as Vacuum Bag Only (VBO) manufacturing, which is the focus of this work. OoA or VBO processing aims to offer production flexibility and reduce processing costs of thermoset prepregs [9–11, 13]. OoA curing typically takes place in an oven, with the part placed on a single sided tool, closed under vacuum, with the use of a flexible membrane or vacuum bag. Other forms of Out-of-Autoclave manufacturing are consolidation on heated tools (i.e. Quickstep process), microwave heating and press forming, primarily used for processing thermoplastic prepregs.

The main difference in processing prepregs inside the autoclave lies in the ability to apply high external pressure to the laminate during cure, up to  $7 \cdot 10^5$  Pa (7bar). While both in the Autoclave and in the oven it is possible to heat-up the part and apply vacuum, Out-of-Autoclave processing is performed solely under vacuum pressure ( $10^5$  Pa or 1bar). Heating takes place in both cases via convection, though the inert gas atmosphere of the autoclave (nitrogen -  $N_2$ ), is generally more efficient in the application and maintenance of the temperature, while it can better suppress heat generated by exothermic reactions [14]. A schematic of the operation principal of both methods is given in Fig. 1-2.

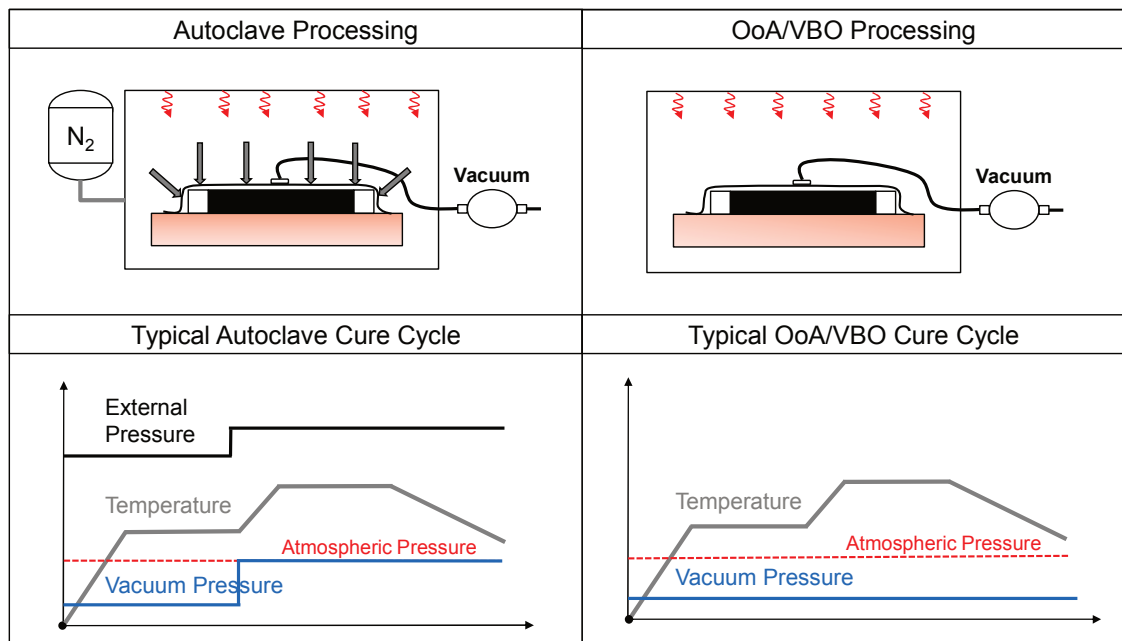


**Fig. 1-2: Manufacturing set-ups and typical cure cycles utilized when processing prepregs in and Out-of-Autoclave**

The curing schedule of the Autoclave is designed to maintain gas and volatiles into solution through balancing the hydrostatic and void pressure [2, 15, 16]. Though vacuum assists in volatile removal from the resin at the early stages of the cycle [2], bubbles or voids formed during the process can only collapse by applying a high pressure gradient before resin gelation takes place [2, 15, 16]. Due to the limited pressure available during Out-of-Autoclave cure, a good laminate quality cannot be achieved via balancing the hydrostatic with void pressure and maintaining gas and volatiles into solution [2, 15]. In

order to circumvent this limitation, the reinforcement used as a basis for the prepreg is intentionally left partially impregnated, to assist with vacuum distribution through the dry fibers inside the laminate [9, 17, 18]. While the laminate processed OoA is heated, the resin transitions from a solid to a liquid state completing the prepreg impregnation. At this stage both air and resin flow takes place through the same fibrous domain. Hence the impregnation quality is a result of the balance between the rate of air transport out of the part, its expansion during heating and the evolution of resin viscosity before cure [9, 12].

However, since the final impregnation of the prepregs takes place during the cure cycle [9], transient, non-homogeneous vacuum pressure and temperature conditions are present. This creates a greater risk for residual porosity in the part compared to Autoclave processing [9, 12, 18]. Local pressure and temperature inhomogeneity primarily encountered in large parts, can lead to formation of local air pockets inside the impregnating tows, essentially by cutting them off from the vacuum supply [12, 19].

Choosing the appropriate processing avenue for manufacturing a specific part, requires striking a good balance between the ultimate part quality and part features required and techno-economic factors, such as cost, productivity and equipment availability. Several researchers have proposed cost-models to assist in the decision making process of the most suitable production process selection [20, 21]. Centea et al. [22] applied the model proposed by Gutowski et al. [21] to develop a generic cost model for OoA manufacturing, demonstrating the dominating influence of the raw material cost when manufacturing using prepregs [22]. The main advantages and disadvantages as a basis for decision making between Autoclave and OoA manufacturing are synthesized in Tab. 1-1.

**Tab. 1-1: Advantages and disadvantages of processing prepregs in and outside the Autoclave [2, 4, 14, 18, 23]**

	<b>Autoclave Processing</b>	<b>OoA/VBO Processing</b>
<b>Advantages</b>	High Performance Stable & Repeatable Good geometric tolerances Significant data-pool of Aerospace qualified materials	Reduced tooling cost Reduced part warpage/tool re-work Higher process adaptability/flexibility Closer to net-shape manufacturing compared to LCM Increased process flexibility compared to Autoclave
<b>Disadvantages</b>	Energy Intensive High tooling costs High Capital Investment Large footprint Medium/Low production Volumes	Reduced geometrical stability Long tool occupation for reduced porosity Lower heat transfer/Slower cycles Part/Material specific process development Lower automation potential Limited Aerospace qualified materials



### 1.3 Key Out-of-Autoclave Applications

Out-of-Autoclave manufacturing has its roots in applications where a high structural performance would not be essential, such as: tooling, model airplanes, boat-hull manufacturing or manufacturing small ‘niche’ parts for industrial applications, the interest in expanding towards high performance applications is growing. It is nevertheless evident that the Out-of-Autoclave processing of prepregs is an attractive option due to its reduced investment cost and flexibility even in high-end space and aerospace applications.

According to Gardiner [11], US Department of Defense advisories (DoD) indicated that future military aircraft programs will be produced in small volumes with very small budgets [11]. The US Air Force has identified OoA prepregs as vital to achieving the fast and affordable manufacturing that the DoD will require [11], while future NASA programs are expected to be cost-constrained to an even greater degree [11]. Publically funded programs, mainly led by the USA and UK governments, focused on research and development efforts addressing primarily the high performance, automation and productivity/accelerated insertion aspects in order to mature the VBO/OoA technologies [11, 18, 24]. Key Aerospace manufacturers have also included Out-of-Autoclave technologies in their growth strategies for high volume commercial aircraft production [25]. Airbus has qualified the first OoA prepreg for use in secondary aircraft applications (Solvay MTM 44-1), while GE is already producing secondary wing structures for the Airbus A350 XWB aircraft, manufactured outside the Autoclave. Some of the most commonly known, high performance applications for Out-of-Autoclave materials are summarized in Appendix a, Tab. A- 1. As the experience with OoA materials leads to performance improvements, an increased process reliability and the development of a robust material database will assist the qualification process, expansion of the OoA processing is meant to continue [10]. The manufacturing interchangeability between Autoclave and oven would maximize resource utilization, promote significant cost savings and minimize material and process qualification effort. Ultimate goal for the production of parts Out-of-Autoclave is to achieve increased productivity at a reduced cost, with a performance competing that of the Autoclave.

### 1.4 Out-of-Autoclave Prepregs – A Review

Due to the lack of external pressure available outside the Autoclave, Out-of-Autoclave material suppliers have concentrated their efforts in developing material systems which enable manufacturing of good quality parts using alternative strategies. The presence of dry fiber tows attracts most attention as the key feature differentiating Out-of-Autoclave from conventional prepregs [9, 18]. The initial degree of impregnation (IDoI) of the prepreg and its impregnation pattern can vary depending on the fiber bed substrate and the manufacturing method used for their production [9].

Several researchers captured this characteristic in a range of commercially available OoA systems [17–19, 26–29]. Centea et al. [17] characterized an MTM45-1 prepreg produced by Solvay (Advanced Composites Group at the time), based on a 5-harness satin weave carbon fabric. The prepreg is partially impregnated by a resin film applied on both sides of the textile [17]. Kourkoutsaki et al. [19] characterized the MTM 44-1 prepreg, based on a 2x2 twill weave (Solvay) and observed single sided impregnation achieved through a film deposition process [19]. Kratz et al. [26] quantified the initial degree of impregnation of three types of textile architectures based on carbon fibers of the Cycom 5320 prepreg (Solvay), all impregnated with resin between 23 - 47% [26]. Both Helmus et al. [28] and Kratz et al. [26] observed a double sided impregnation pattern on the unidirectional Cycom 5320 prepreg (Solvay), while the unidirectional reinforcement had the highest degree of impregnation of all Cycom 5320 prepregs measured [26]. Cender et al. [27] monitored the evolution of the impregnation state of two OoA prepregs during processing, manufactured by Gurit based on twill weave carbon fabrics with resin layer deposited on one side of the fabric (ST94-RC200T and ST94-RC303T) [27]. The resin film is deposited on top of the fiber bed without significantly impregnating the tow in both aforementioned prepregs [27]. Tavares et al. [29] characterized the air permeability of semi-prepregs made of alternating dry and impregnated areas along the surface of a two layered Non-Crimp Fabric (NCF) [29]. In this case the resin is deposited on one side of the fabric with a pattern which leaves an amount gaps or dry fibers [29].

The presence of dry fibers in each ply, attained via a partial surface impregnation, assists in the distribution of the vacuum everywhere inside the laminate [30]. A partially impregnated prepreg ensures a homogeneous vacuum distribution inside the part [19, 30]. At the same time, the dry fibers form a network allowing the transport of entrapped gasses, moisture and volatiles outside the laminate [18]. As the type of reinforcement makes a difference in the extraction process, different degree and type of impregnation is chosen for different textile architectures [9]. For example tight weave materials with small tow size need to have impregnation levels close to zero for the materials to achieve acceptable OoA processability as noted by Ridgard et al. [9].

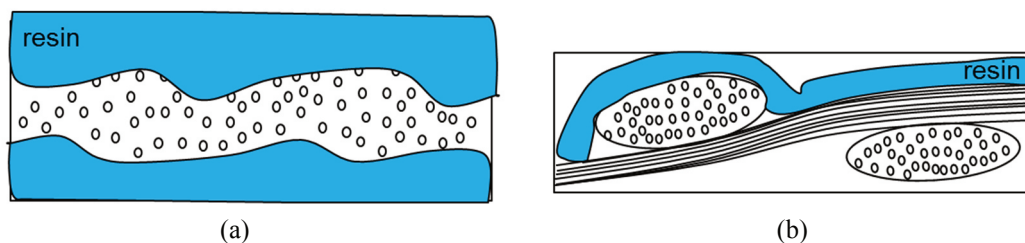


**Fig. 1-3: Cross-sections of two Out-of-Autoclave prepregs and their impregnation schemes**  
 (a) Prepreg based on a unidirectional reinforcement and (b) prepreg based on a textile.

Since the Out-of-Autoclave prepregs are highly permeable to air at the initial processing conditions, characterizing the prepreg permeability to air at the initial state and during processing has attracted significant attention in the literature [12, 19, 31–39]. A sketch

of two typical Out-of-Autoclave prepregs and their impregnation pattern is given in Fig. 1-3. Since void collapse is no longer possible, the preemptive removal of volatiles and entrapped gasses from the laminate and the use of resin systems with reduced solvent content [40] are measures for reducing the risk of void growth at higher temperatures.

In order to enable an efficient air transport and gas extraction, it is critical to design an efficient laminate breathing strategy around the part with breathable dams (using fabric tows or thick breather material), avoiding unnecessary bleeding [9, 41]. Particular care shall be taken to enable air flow out of areas with ply drop-offs, tight curvature [42, 43] or thick monolithic sections, by applying pressure intensification schemes and modifying the contact of consumables on the laminate [42, 43]. Leaks shall be avoided throughout the cure cycle. The allowable pressure drop and maximum pressure requirements are specified by the material supplier, along with material bagging and cure cycle details [41].

It is evident that maintaining the air evacuation channels open for as long as possible is beneficial for both the transport of unwanted species out of the laminate [9], as well as for the homogeneity of the prepreg impregnation. To achieve this, a balance has to be struck between the initial degree of impregnation and impregnation pattern of the prepreg, the laminate 'breathing' or venting strategy used and the selection of resin characteristics at room temperature, during the debulking temperature as well as during processing. A high resin viscosity at low temperatures for as long as necessary inhibits cold flow [9] and enables mobilization of entrapped gases and extraction of unwanted species out of the laminate. At the same time the rate of decrease of the viscosity with increasing temperature and the rate of crosslinking which is causing the viscosity to rise should enable full impregnation of the tows before gelation takes place [44]. The load carrying capability of the resin shall be maximized via an optimized prepreg consolidation process and controlled laminate bleeding [2, 13, 18]. The resin viscosity at room temperature also affects the tackiness of the prepreg. Very tacky prepregs tend to be more prone to air entrapment between plies [2, 18, 40] while not tacky enough seem to have a similar effect [45, 46]. In any case, the tackiness of the prepreg shall be maintained at the initial levels for at least a month at room temperature (under controlled conditions) in order to enable reliable processing, preventing significant variability and reduction in mechanical properties [46, 47]. Surface roughness may have an effect on the inter-ply porosity formation during processing of prepregs [2], though no systematic study has quantified this effect nor addressed the void formation physics to the knowledge of the author. A detailed list of the available commercial Out-of-Autoclave prepregs are summarized in Appendix a, Tab. A-2, while a summary of their key properties is given in Tab. 1-2.

According to Ridgard et al. [9], for each combination of resin and reinforcement, the required prepreg structure including impregnation level is defined in a process control document (PCD), which specifies how the prepreg material itself needs to be made [9]. As stretched by both Hexcel and Solvay, for each prepreg combination and format, there are corresponding OoA cure cycles, which produce acceptable results [9, 13]. While all

fiber architectures could in theory be used to produce an OoA prepreg, their selection should be carefully considered in light of the part and process constraints [9, 18].

The incorporation of honeycomb cores in parts produced OoA parts poses further challenges, due to the air circulation between the face-sheets and the honeycomb itself. This interaction mainly depends on: textile type, resin impregnation pattern, laminate lay-up and honeycomb material as well the cell structure of the honeycomb itself [34, 48–50]. Another critical aspect of manufacturing Out-of-Autoclave using honeycomb is the generation of volatiles at high temperatures, caused by vaporization of moisture or solvents included either in the organic cores or at the adhesive films used at the bonding line [51, 52]. Drying the cores and the adhesive before processing and generally avoiding moisture ingress and ensuring appropriate adhesive film selection are measures, which reduce the influence of such defects on the bonding and part quality.

The first generation of OoA prepreps seemed to have significant shortcomings compared to Autoclave prepreps [9], mainly related to out-life [46] and tackiness [45] and their negative impact on the residual porosity and material performance reliability [9, 13, 45–47]. The need to make processing and performance of OoA prepreps comparably stable to that of an Autoclave prepreg, led to the development of the second and third generation materials. Continuous improvements of the OoA prepreps focused on the reduction of the entrapped porosity and parallel improvement of handlability and reliable mechanical performance [45, 46]. Airbus and Boeing Companies paved the way towards the qualification of such material systems for use in Aerospace applications. The forecast of Boeing for the evolution of OoA prepreps in terms of performance and basic processing features is presented in Fig. 1-4.

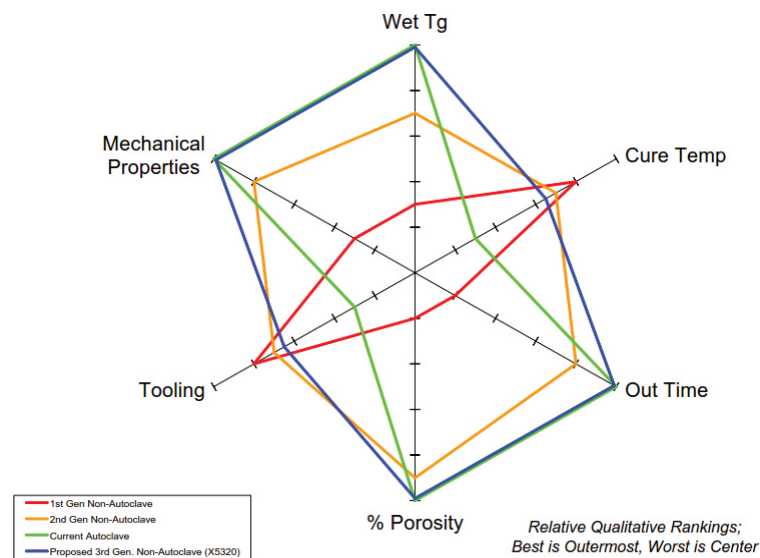


**Fig. 1-4: Boeing quality targets for the third generation of Vacuum-Bag-Only Prepreps compared against Autoclave performance [25]**

**Tab. 1-2: Key Features of Out-of-Autoclave Prepregs**

<b>Characteristics</b>	<b>Features</b>	<b>Comments</b>
<b>Reinforcement</b>	UD Woven fabrics Multiaxial fabrics (NCFs)	Available in a range of areal weights, tow count & fiber types
<b>Epoxy type</b>	Hot-melt systems	Preferred due to their latency
	Addition reaction	Reduced volatile content
	Low reactivity	Reduced outgassing
<b>Resin viscosity</b>	High at RT, low during processing	Allows gas distribution, volatile extraction, prevents cold flow
	Gel point reached at low temperatures compared to Autoclave	Prohibits void growth due to increasing volatile pressure with increasing temperature
<b>Degree of impregnation</b>	Partial impregnation Dry fibrous network	Enables gas transport outside the part and homogeneous vacuum distribution inside the laminate
<b>Impregnation pattern</b>	Single / Double sided Partial surface impregnation	
<b>Tack</b>	Medium tackiness preferred	High or Low tack can entrap porosity
	Shall be stable at RT	For reliable processing

## 1.5 Voids in Out-of-Autoclave Manufacturing

One of the most commonly encountered defects in composites processing are voids or porosity. In order to maximize the structural performance of composite parts, the presence of voids in the finished part has to be reduced to an absolute minimum. Though zero residual porosity is essentially required, the target is typically set to a maximum allowable 2% porosity inside parts used in the Aerospace field.

Voids can be classified in three major categories based on the mechanisms driving their formation [15, 16, 18, 53, 54]:

- Flow induced voids, caused by incomplete wetting of tows and interstitial spaces.
- Voids created due to reaction or dissolution of various chemical species (moisture, solvents, volatiles or gases) at increased temperatures, under vacuum.
- Voids formed or enlarged due to diffusion, transport and agglomeration of air bubbles.

Fahrhang et al. [53] has classified voids based on their origin, referring to them as ‘sources’, when these are included in the laminate since the beginning of the process and ‘sinks’, when they are generated during the process. The voids formed or entrapped inside a prepreg ply are referred to as intra-ply voids or intra-laminar porosity, while the voids located at the interface between two plies are referred to as inter-ply or inter-laminar porosity [54]. This classification has been extended further to describe porosity in complex textile architectures. In this case porosity located in the interstices between fiber tows is referred to as inter-tow porosity, while porosity located inside the fiber tows is referred to as intra-tow porosity or fiber-tow porosity. When the pores are entrapped inside the resin, they can also be referred to as resin voids. The main types of porosity encountered in an OoA prepreg are presented in Fig. 1-5, using  $\mu$ CT images of a partially impregnated woven textile. The location, size and morphology of voids is influenced by the mechanisms driving their formation and can therefore be used to deduce information about the origin or formation mechanism which led to their formation.

Several researchers have studied factors affecting porosity formation in OoA prepregs. As synthesized by the author, [19] main drivers of porosity formation are considered to be: the length of the part or its distance from the vacuum source [35, 55, 56], the vacuum level during processing [18, 43], material characteristics such as the percentage and pattern of initial tow impregnation [17, 18, 31, 39], the textile architecture and its air permeability, in combination with resin characteristics such as latency/cure kinetics (rheokinetics) and prepreg tack [18, 53, 57, 58]. Other factors, such as high moisture uptake [18, 54], prepreg out time [18, 59] and local defects (fuzz balls, broken tows or particle clusters [15, 46] ) can also influence the final porosity content of a part produced OoA. Apart from OoA specific porosity sources, air can be entrapped between the prepreg layers during the lay-up process, or even be included in the raw materials (i.e. resin).

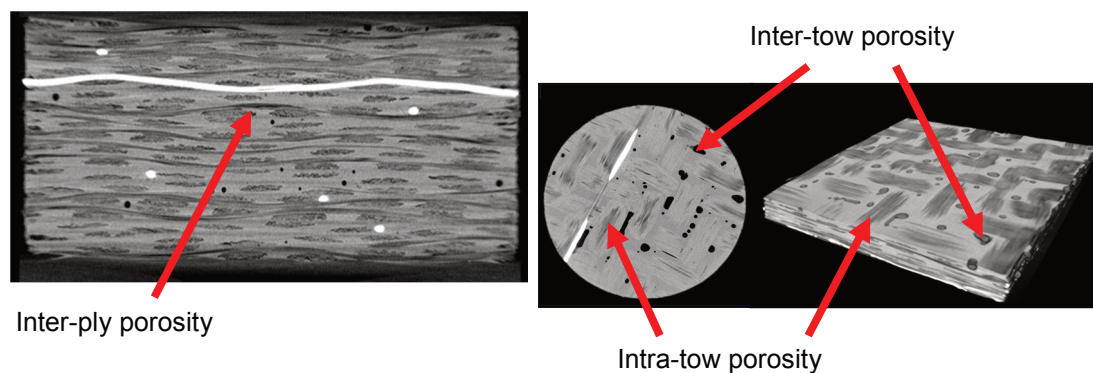


**Fig. 1-5: Porosity development in an Out-of-Autoclave prepreg stack (MTM 44-1, 2x2 TW)**  
The light grey color represents the resin, the darker the fibers while the black the voids.

Assuming that voids are entrapped inside the laminate prior to processing initiation. Inside the vacuum bag the pressure of voids increases with increasing temperature, reaching a point where the hydrostatic pressure of the resin will be smaller than the void



pressure [2, 15, 16]. This condition marks the initiation of void growth and volatile dissolution inside the laminate. In a typical Autoclave cycle at this stage the vacuum bag shall be vented to atmospheric pressure, while a high external pressure shall be applied to assist in bubble collapse [2]. Since this is not possible in oven processing, material manufacturers achieve the reduction of the potential for void growth due to outgassing by utilizing low reactivity epoxies, with reduced solvent content, produced via addition reaction [9]. Lengthy out-times and exposure to humidity shall be avoided, in order to avoid void nucleation and growth taking place at temperatures above 80°C and at 45% relative humidity or higher [54].

To address void formation related to incomplete, non-optimized flow, the resin chemistry shall provide minimal flow during debulking, ensure good wetting of the laminate and gel right after this is achieved [9, 40, 44]. Long debulking times at room temperature ensure volatile removal out of the part and reduce the risk of air entrapment between plies. A very good quality of vacuum with limited leaks and a prepreg permeable to air is essential for producing porosity free parts Out-of-Autoclave. Moreover the geometry of the part as well as the tool and oven details contributing to the heat transfer have to be taken into account in order to optimize the temperature schedule and achieve homogeneous heating [43, 58, 60, 61]. Homogeneous heat transfer in the part, combined with high, homogeneous vacuum distribution will enable full wetting of the initially dry tows and the manufacturing of a part with a limited void content. It is therefore clear that care has to be taken at all steps of an OoA process, in order to avoid the incorporation of porosity sources in the laminate which cannot be removed during the cure cycle. Careful control of the material storage and out time, repeatability of the bagging and debulking processes along with an optimized cure schedule are the enablers for producing a part with limited porosity outside the Autoclave.

## 1.6 Voids and Structural Performance OoA

Before the introduction of a new material in the market, a significant amount of studies needs to be performed to guarantee its reliable performance. Along with the development of the Out-of-Autoclave process, focus is given in investigating the quality of the resulting products and benchmarking their mechanical performance against the Autoclave quality. As discussed in Section 1.2, reducing the processing pressure when transitioning from Autoclave to OoA processing, raised concerns for increased porosity in the finished parts. In the last few years, several Out-of-Autoclave materials are undergoing official or research qualification for various applications. A brief summary of the coupon level mechanical performance obtainable with commercially available Out-of-Autoclave prepregs, based on open literature, is given here.

Mortimer et al. [13] presented a benchmark study of three baseline material systems manufactured by Hexcel for Autoclave cure (M36/914 & 8552 matrix/5HS fabric) and compared against the M56 OoA prepreg based on a UD and two woven textiles (PW &

5HS) [13]. The tensile and compressive strength and moduli as well as the interlaminar shear strength were measured at both dry/RT and wet/elevated temperature conditions for all material systems. The in-plane tensile strength ( $0^\circ$ ) of both Out-of-Autoclave materials was found to be higher than the Autoclave cured materials, with a comparable tensile modulus [13]. At the same time the in-plane compressive strength and the interlaminar shear strength of the Out-of-Autoclave materials at RT/dry as well as elevated temperature/wet conditions were found to be 10-20% lower than those of the Autoclave cured material [13], potentially due to the presence of higher porosity OoA.

The three most commonly encountered OoA material systems in the literature are produced by Solvay: Cycom 5320, Cycom 5320-1, and MTM 45-1. These OoA systems (based on several textile formats) have been primarily tested by NASA against typical Autoclave materials (Cycom 977-3, 8552-1). Lucas et al. [46] presented test results of the Cycom 5320/IM7 and 5320-1/T40-800B in compression after impact, which show a superior performance of the OoA prepregs, while both the open-hole compressive strength and tensile strength were equivalent to the Autoclave cured baseline systems [46]. Sutter et al. [47] and Grunenfelder et al. [59] reported an exponential reduction of the interfacial shear strength (ILSS) of the Cycom 5320 prepreg for increasing out-time. Beyond 21 days out-time, the material is losing from 40% up to 80% of its initial performance for a maximum of two months investigated. The Cycom 5320 material has a comparable interfacial shear strength (ILSS), fracture toughness (DCB) and open hole compressive strength (OHC) to the two Autoclave systems [47]. Grimsley et al. [62] measured the notched compressive strength of the same materials at dry room temperature conditions, as well as at elevated temperatures and moisture. At room temperature the open hole compressive strength of the panels (OHC) produced with the Cycom 5320-1/T40-800b OoA material was higher than the one from the Cytec 977-3/IM7 prepreg produced in an Autoclave, while at elevated temperature/wet conditions both systems had equivalent performance. In both processes, the wet/elevated temperature conditions reduced the open-hole compressive strength of the panels by almost 50% of the one at RT/dry conditions [62]. Kellas et al. tested sandwich panels consisted of 8ply quasi-isotropic face-sheets with an aluminum core [63]. The 5320-1/T40-800B OoA prepreg and the 977-3/IM7 prepregs were used for the manufacturing of the face-sheets, while the test coupons produced were tested under flat-wise tension, face-sheet tension and edgewise compression. In all cases, the OoA prepreg was stronger but less stiff, while an almost identical response of both the Autoclave and OoA material to buckling was observed.

The MTM 45-1 prepreg was found to have approximately 20% reduced interfacial shear strength compared to the baseline coupons manufactured using an Autoclave (Cycom 977-3). The performance reduction was caused by the presence of tow voids and cracks observed after failure [47]. The same material had only about 50% of the average compressive strength measured in the Autoclave processed materials [47]. Czarnocki et al. [64] tested the delamination resistance of a laminate made with the MTM 46/HTS OoA



prepreg. Its Mode I and Mode II fracture toughness was found to be equivalent to un-toughened Autoclave cured systems, such as the 977-3/IM/ or 914C/T300 [64]. Suhot et al. [65] investigated the flexural fatigue performance of laminates produced under various curing pressures outside the Autoclave using the UD SPRINT prepreg as a basis [65]. He observed that the coupons with increased amount of voids had reduced fatigue strength with damage initiation mostly, but not necessarily, originating from voids [65].

In principal, it is therefore possible to produce coupons with Autoclave quality or better without an Autoclave. The transferability of the quality from a coupon level to a scaled part requires a very good understanding of the complex, transient process physics, which take place during processing and are responsible for void formation. For a review on manufacturing demonstrators built with OoA materials and the resulting quality, the reader is encouraged to refer to the review paper by Centea et al. [18].

## 1.7 Thesis Motivation and Objectives

In the following Chapters light is shed on the mechanisms of flow induced intra-tow/intra-ply porosity formation. A Multiphysics modeling framework is developed to enable the design and virtual testing of OoA cycles. This framework can be used as a basis for selecting the optimum cure-cycle parameters, which will enable the production of parts with minimum porosity outside the Autoclave (OoA).

While the partially impregnated tows of OoA prepregs assist in volatile transport and vacuum distribution, their impregnation is only meant to be completed during the cure cycle. This poses a risk for residual porosity due to incomplete tow impregnation caused by transient, non-homogeneous pressure and temperature conditions developed during the cycle. Once the access of the initially unsaturated tows to vacuum is disrupted, there is no pressure available to enable further saturation, resulting in the development of air pockets inside the tow. The air pockets will remain unsaturated and will develop into residual intra-tow porosity once the resin gels.

Modifications of the part dimensions affect the flow and heat transfer boundary conditions directly. This makes experimental investigations through costly prototyping trials of little use for processing risk retirement purposes, due to the limited scalability of the phenomena involved [11, 12]. Scaling-up an OoA process from a lab prototype to a significantly thicker or longer part is not possible a priori for any material, part and process combination [9, 11]. The proposed simulation tool can be used to guide material down-selection and to test the effect of various cure cycles and bagging schemes on the part quality and to enable a cost-efficient transition to prototyping large parts OoA.

The main focus is placed on the incorporation of the physics of air flow through the prepreg during debulking and cure, coupled to resin flow and prepreg consolidation at non-isothermal conditions. The MTM 44-1 prepreg, based on a 2x2 twill weave textile is thoroughly characterized and used as a basis for this development. A test-bench with

integrated sensors is developed for validating the physics captured in the model against experiments. The primary objectives of this work fit into the following four categories:

- **1D and 2D Multiphysics simulation of the OoA process**  
Development of a macroscopic simulation model, which will couple the air and resin flow through the tow or prepreg ply. This model shall enable studying the impact of material characteristics and processing parameters to the porosity formation within a tow or ply, at isothermal and non-isothermal conditions.
- **Material characterization**  
Definition of a material characterization matrix, entailing all inputs required for simulating the OoA process physics. Development of new characterization methods where required, with focus on air-permeability measurements. Material characterization of a model system (MTM 44-1) and empirical model development from generated data.
- **Validation of the OoA process simulation**  
Experimental validation of the modeling results against experiments performed using monolithic CFRP parts produced OoA.
- **Sensitivity studies and process recommendations**  
Identification of processing parameters, with the highest influence on the impregnation time of a tow during OoA processing. Providing guidelines for improving the quality of a produced part in terms of intra-tow/intra-ply porosity.

## 1.8 Outline

The thesis is divided into six Chapters, with the following content:

**Chapter 1** introduces the topic of Out-of-Autoclave manufacturing (OoA). The motivation and key objectives of this work are highlighted in this Chapter.

**Chapter 2** presents the theoretical foundations of the principal physics involved in OoA processing. A literature review of the state of the art simulation approaches addressing the flow through fibrous media, heat and consolidation is included. The developments required to sufficiently address the needs of OoA simulation are discussed.

**Chapter 3** summarizes the MTM 44-1 material characterization and model development, used as a basis and providing inputs for the OoA simulation. The characterization entails the use of microscopy and image analysis of the prepreg and tows, resin viscosity and cure kinetics and measurement of the prepreg's air permeability at various processing states. The characterization results and empirical models resulting from the derived data are presented, while each method is accompanied by a brief literature review section on the state of the art methods used to characterize similar material systems.

**Chapter 4** introduces the simulation tools developed in the context of this work. The Chapter is split into two sections. The first section concentrates on the development of a numerical model which couples weakly resin and air flow isothermally through an

initially dry tow of the MTM 44-1 prepreg, in a non-consolidating medium via pressure boundary conditions (Matlab), with the aim to predict its impregnation time. The impact of various pressure boundary conditions on the tow impregnation time is presented, while sensitivity studies demonstrate the impact of processing conditions and material characteristics on the tow filling time. The second section addresses the implementation of the two-way coupled air and resin flow approach in COMSOL Multiphysics, expanding the air-resin flow coupling towards non-isothermal conditions, depicting the impregnation of each prepreg ply in 2D (length and thickness) during the cure cycle.

**Chapter 5** concentrates on the presentation of experimental results from the production of a monolithic demonstrator part OoA. The development of an instrumented test-bench for capturing all processing parameters during the cure cycle is included. The predicted OoA simulation outputs, such as pressure, temperature, viscosity etc. are compared against experimental results acquired during OoA manufacturing of the demonstrator.

**Chapter 6** summarizes the most significant findings and key contributions made in the context of this thesis, provides guidelines for improved OoA manufacturing of monolithic parts, while it concludes with recommendations for future research.

The content of the thesis is graphically depicted in Fig. 1-6.

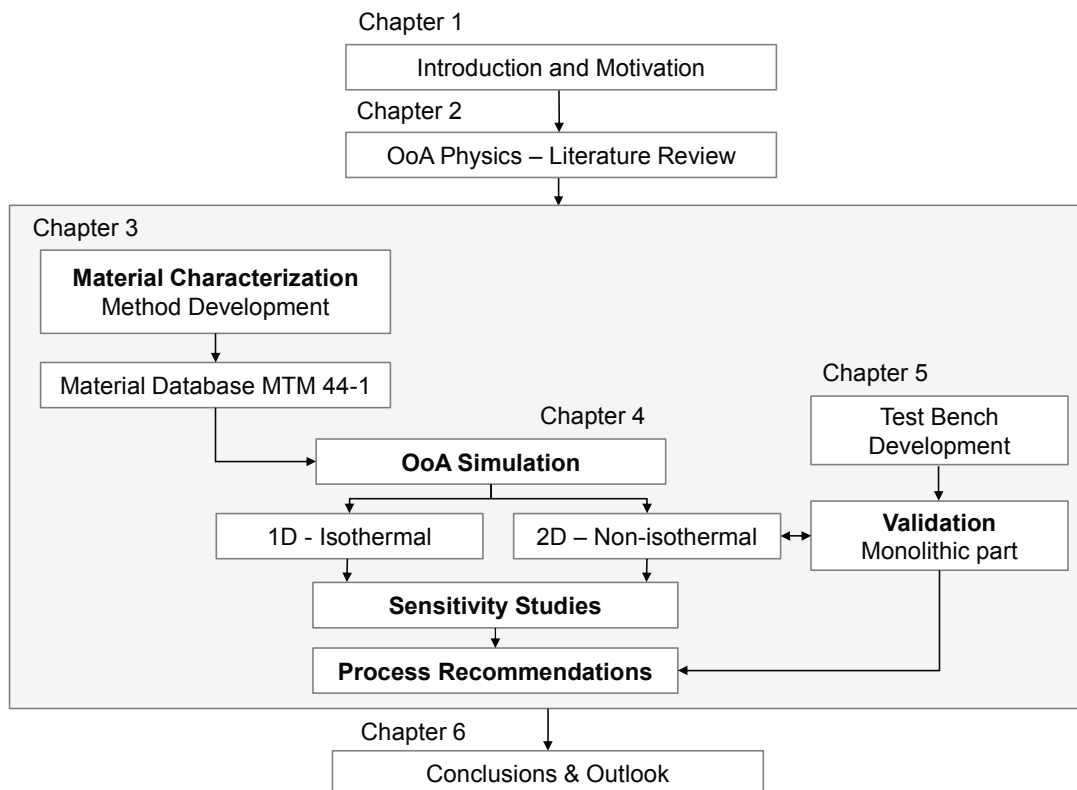


**Fig. 1-6:** Graphical representation of the PhD thesis content and structure



## 2 A Review of the Governing Physics in Out-of-Autoclave Processing

A range of phenomena takes place simultaneously during processing outside the Autoclave: air flow and vacuum distribution through the partially saturated fiber tows, transient heat development, viscosity evolution, resin flow, compaction and finally curing of the matrix, as depicted in Fig. 2-1. Optimization of the composite manufacturing process outside the autoclave requires a good understanding of all the involved physics and their interactions.

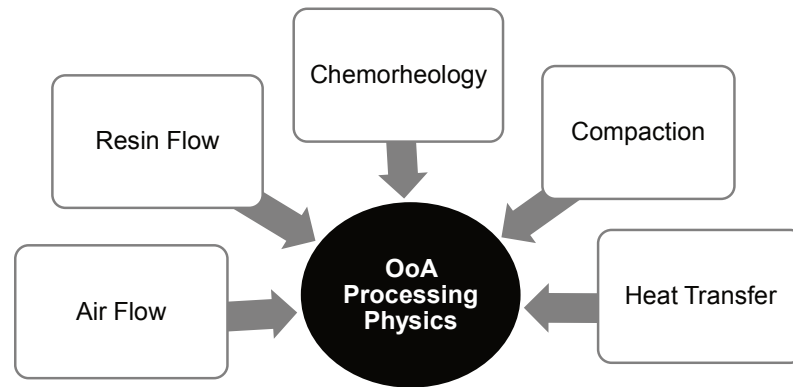


**Fig. 2-1: Interacting physics during Out-of-Autoclave processing**

In this work, emphasis is particularly given in the aspects related to the air flow (either isothermal or non-isothermal) and coupling it to the resin flow inside the tows during processing, without taking into account the compaction of the fibrous medium. The physics taking place during processing of composite parts OoA are reviewed. The state-of-the-art process modeling approaches used to couple the flow of two immiscible fluids in the field of composites are presented. Finally, the key differences between OoA processing physics and the state-of-the-art modeling approaches of conventional composite manufacturing methods (liquid composite molding or autoclave) are highlighted.

### 2.1 Introduction

The theory of porous media is used to describe the physics of fluid flow and heat transfer through a fibrous domain. A porous medium consists of a porous and a solid or stationary phase. The stationary phase is typically called the skeleton, while the open space through which fluid flow can take place is the porosity.

The general equation used to correlate the volume fractions of the two phases in a porous medium writes:

$$V_s + \phi = 1 \quad (2-1)$$

The volume fraction of the skeleton writes as  $V_s$ , while  $\phi$  is the porosity volume content.

If the porous medium is a fibrous tow, its volume fraction is written as  $V_f$  and its porosity is calculated via Equation (2-2). In this context, the porosity characterizes the volume fraction of the tow initially filled with air, later saturated with resin.

$$\phi = 1 - V_f \quad (2-2)$$

Equation (2-2) can be modified according to Equation (2-3), to reflect the simultaneous presence of more than one fluid in the volume of a fibrous medium [66].

$$V_f + \frac{\phi_1 + \phi_2}{\phi} = 1 \quad (2-3)$$

If one of the two fluids present in the tow moves significantly faster than the other one in a stationary fibrous medium, the sum of the fibers and the slow moving fluid form the skeleton. In this case Equation (2-3) can be reformulated into Equation (2-4).

$$\phi_1 + \frac{V_f + \phi_2}{V_s} = 1 \quad (2-4)$$

Volume averaging is used to express the properties of interest within a selected volume of the porous medium. Conservation equations can therefore be expressed at different levels of the porous microstructure, if the volume fraction of the concerned phase is known.

## 2.2 Resin Flow through a Porous Medium

The equations for mass and momentum conservation and the phenomenological laws, which describe the behavior of the constituents are presented in this Section.

### 2.2.1 Conservation of Mass

The continuity, or mass balance Equation (2-5), expresses the mass conservation of the resin with density  $\rho_r$  and velocity  $\mathbf{v}_r$ , through the porous medium [4].

$$\left\langle \frac{\partial \rho_r}{\partial t} \right\rangle + \langle \nabla \cdot (\rho_r \mathbf{v}_r) \rangle = -s \quad (2-5)$$

The local difference in the kinetics of microscopic and mesoscopic impregnation present in a multiscale porous medium is depicted by a mass  $s$  included in Equation (2-5). For

a fluid flowing through a non-consolidating medium with small density variations compared to its velocity variations, Equation (2-5) is simplified into Equation (2-6).

$$\frac{\partial \langle \rho_r \rangle}{\partial t} + \nabla \cdot (\rho_r \langle \mathbf{v}_r \rangle) = 0 \quad (2-6)$$

Where  $\langle \rho_r \rangle$  and  $\langle \mathbf{v}_r \rangle$  stand for the volume-averaged density and velocity of the fluid respectively inside the porous/fibrous domain of interest.

If the resin flow is laminar, takes place quasi-statically ( $\partial \langle \rho_r \rangle / \partial t = 0$ ) and the fluid is incompressible ( $\rho_r = \text{constant}$ ), the conservation of mass of Equation (2-5) can be simplified into Equation (2-7) or even into Equation (2-8) if no resin sinks are present [4].

$$\nabla \cdot \langle \mathbf{v}_r \rangle = -s \quad (2-7)$$

$$\nabla \cdot \langle \mathbf{v}_r \rangle = 0 \rightarrow \frac{\partial \langle v_{r,x} \rangle}{\partial x} + \frac{\partial \langle v_{r,y} \rangle}{\partial y} + \frac{\partial \langle v_{r,z} \rangle}{\partial z} = 0 \quad (2-8)$$

Various researchers have developed analytical expressions for sink terms. Indicatively, the most commonly utilized expressions are:

- Constant and On/Off sink terms which capture the difference in the impregnation rate of simplified tow or gap geometries in woven fiber mats [67]. The sink term involves an average pressure dependent saturation rate [67–73].
- Phenomenological intra-tow sink term derived by curve fitting of pressure or saturation curves using volume averaging [74–76].
- Sink developed by a detailed FEA analysis of a repeating unit cell of the textile architecture [77–80].

## 2.2.2 Conservation of Momentum

The momentum conservation of Equation (2-9) relates the forces encountered during the flow of resin through a porous medium with its acceleration [4, 81, 82].

$$\underbrace{\rho_r \frac{D\mathbf{v}_r}{Dt}}_{\text{Inertia Force}} = \underbrace{-\phi \nabla \langle P \rangle^r}_{\text{Hydrodynamic Force}} + \underbrace{\nabla \cdot \langle \boldsymbol{\tau}_v \rangle}_{\text{Viscous Stress Force}} + \underbrace{\rho_r \mathbf{g}}_{\text{Gravitational Force}} \quad (2-9)$$

This is the expression of second Newton's law for the flow of a fluid through a porous medium. The  $\rho_r$  stands for the resin density,  $\mathbf{v}_r$  is the resin velocity,  $P^r$  is the fluid pressure,  $\boldsymbol{\tau}_v$  is the viscous stresses developed due to the fluid's motion through the porous medium and  $\mathbf{g}$  represents the body force per unit mass.

The general momentum equation for the flow of a fluid through a fully saturated, stationary fiber bed is expressed using local volume averaging on a Representative Volume Element (RVE) according to Equation (2-10) [82].

$$\underbrace{\rho_r \frac{\partial \langle \mathbf{v}_r \rangle}{\partial t} + \rho_r \nabla \cdot \langle \mathbf{v}_r \mathbf{v}_r \rangle}_{\text{Inertia Force}} = \underbrace{-\phi \nabla \langle P \rangle^r}_{\text{Hydrodynamic Force}} + \underbrace{n \nabla \cdot \nabla \langle \mathbf{v}_r \rangle}_{\text{Viscous Stress Force}} - \underbrace{\phi n \mathbf{K}_r^{-1} \cdot \langle \mathbf{v}_r \rangle}_{\text{Viscous Drag Force}} \quad (2-10)$$

The symbol  $\langle P \rangle^r$  stands for the intrinsic pressure, applied on the fluid inside the porous medium and  $n$  its viscosity, while  $\mathbf{K}_r$  is the permeability of the porous medium. The viscosity and permeability are discussed in more detail in Section 2.2.4. To derive Equation (2-10) from (2-9), Tucker and Dessenberger [82] considered a fully saturated porous medium with uniform porosity without mass exchanges between the solid and fluid phase. The fluid is considered Newtonian, with a constant density, while its flow is laminar ( $Re < 1$ ) [82]. Equation (2-10) is applicable when the fluid flows through a porous medium under isothermal conditions and no surface tension develops [82].

When the flow of a fluid with a constant viscosity and negligible inertia is concerned, the general form of Equation (2-10) is simplified into Brinkman's Equation (2-11).

$$-\phi \nabla \langle P \rangle^r + n \nabla \cdot \nabla \langle \mathbf{v}_r \rangle - \phi n \mathbf{K}_r^{-1} \cdot \langle \mathbf{v}_r \rangle = 0 \quad (2-11)$$

Under the assumption that the volume-averaged viscous stress can be neglected [81–83], the momentum balance equation reduces to Darcy's law, Equation (2-12) [84].

$$\nabla \langle P \rangle^r + n \mathbf{K}_r^{-1} \cdot \langle \mathbf{v}_r \rangle = 0 \quad (2-12)$$

Darcy's law was developed in 1856 by the French physicist, with the aim to correlate the flow rate of water in a column of water saturated sand with the applied pressure [84]. The law states that the volumetric discharge rate  $Q$ , divided by the cross-sectional area  $A$  through which flow takes place, is proportional to the pressure gradient  $\Delta P_r$  present across the length of the medium,  $L$ . The constant of proportionality is the permeability of the medium in the direction of flow  $K_{r,zz}$ , divided by the viscosity of the fluid  $n$ , according to Equation (2-13).

$$\frac{Q}{A} = -\frac{K_{r,zz} \Delta P_r}{n L} \quad (2-13)$$

Equation (2-13) correlates linearly the pressure gradient in the material, with the average velocity of the fluid, also known as Darcy's Flux or Darcy's velocity [83, 84]. Equations (2-12) and (2-14) are equivalent and describe the volume averaged velocity of a fluid  $\mathbf{v}_{rD}$  through a reference volume of the porous medium [83, 84].

$$\mathbf{v}_{rD} = \langle \mathbf{v}_r \rangle = -\frac{\mathbf{K}_r}{n} \nabla \langle P \rangle^r \quad (2-14)$$

Once Darcy's velocity is known, the local velocity  $\mathbf{u}_{rf}$  is calculated via Equation (2-15).



$$\mathbf{u}_{rf} = \frac{\mathbf{v}_{rD}}{\phi} \quad (2-15)$$

Coupling Darcy's law with the mass conservation of an incompressible medium leads to the development of the Laplace Equation (2-16), which can be used to calculate the fluid pressure in a domain permeated by the fluid, via the application of selected boundary conditions. The intrinsic fluid pressure  $\langle P \rangle^r$  is simplified to  $P_r$  or  $P_f$  in this work.

$$\nabla \cdot \left( \frac{\mathbf{K}_r}{n} \nabla \langle P \rangle^r \right) = 0 \rightarrow \nabla \cdot \left( \frac{\mathbf{K}_r}{n} \nabla P_r \right) = 0 \quad (2-16)$$

Different formulations of the momentum conservation equation, can be applied to describe the flow at different levels of the fibrous medium. Darcy's law is invoked to model phenomena related to the macroscopic flow of resin through a fibrous domain [4, 85–89]. In this case it is typically assumed that the resin and air saturated phases of a textile are separated by a flat resin front. More details on methods used to track the position of the resin front are given in Section 2.4.2. Darcy's law and the mass conservation are typically used in Liquid Composite Molding processes to calculate the mold filling time, determine the pressure distribution and optimize the injection and venting schemes or predict the occurrence of dry spots [90]. Advani, Brusckke and Parnas [90] point out that 'practice has converged on the use of Darcy's law to describe the physics of flow in fibrous media'. Nevertheless, the impregnation of heterogeneous fibrous media with dual scale porosity is shown to deviate from the linear pressure evolution described by Darcy's law [67, 89–98]. When the flow of resin through textile preforms [67, 89–93, 96–98], or preforms consisting of plies with different permeabilities are concerned [67, 90, 99], the assumption of a fully saturated flow is not fulfilled close to the impregnation front [91]. A partially saturated zone separates the fully impregnated and dry region due to the difference between the intra and inter-tow resin velocity. The most commonly encountered approaches accounting for the coexistence of the two flow types are:

1. Combination of the Navier–Stokes equation used to describe the macro/inter-tow flow and Brinkman's equation to describe the micro/intra-tow flow [100, 101]. This approach captures the flow in a multi-scale porous medium very accurately, at a high computational cost. Therefore utilizing this method is typically restricted to permeability computations in a unit cell.
2. Modification of Darcy's Law to include a variable, unsaturated permeability and a capillary pressure as a function of the saturation [66, 98, 102, 103].
3. Application of Darcy's law at the macroscopic (textile) and microscopic (tow) level. Introduction of a sink/source term in the macroscopic conservation of mass, couples the two effects together ensuring a global mass conservation (see Equation (2-7) and References in Section 2.2.1). Approaches 1 and 3 are discussed in more detail in Section 2.4.

### 2.2.3 Compaction and Percolation Flow

The impregnation of a fibrous medium, accompanied by a movement of the resin through the fiber is defined as Percolation flow.

When an external pressure is applied to the composite, it results to an increase of the fiber volume fraction, up to a theoretical maximum defined by the spatial distribution of the fibers. During the compaction, the fibrous network takes up an increasing amount of the applied load which is initially taken by the resin. This is accompanied by a reduction of the part thickness and a local fiber rearrangement, also known as nesting [104]. Dave et al. [105] describes the effect with a piston (resin), spring (fibrous network) analogy.

According to Comas-Cardona et al. [106] the resin pressure and the effective stresses of the fiber bed can be correlated through Biot's Equation (2-17) [107], where  $\sigma$  the applied stress,  $\sigma_f$  the effective stress of the fiber bed,  $P_r$  the resin pressure,  $a_b$  Biot's coefficient representing the ratio of stress relief due to pore pressure and  $\mathbf{I}$  the unit tensor [107].

$$\sigma = \sigma_f + a_b P_r \mathbf{I} \quad (2-17)$$

Most studies in the field of composites use Terzaghi's equation [108] to correlate the stresses in the laminate with the externally applied stress, which can be derived by Biot's equation when  $a_b = 1$  [106, 107]. Complementary to the flow and stress equilibrium equations, constitutive laws for the through thickness compression of the material are used to describe the evolution of the effective stress and deformation or fiber volume fraction. The constitutive laws can be derived from micromechanics models, based on textiles RVEs [109, 110], empirical relationships which correlate the effective stress to the volume fraction [111] or the void ratio [105, 112, 113] and finally fitting experimental data from compression tests performed in textiles [106, 114–119] or saturated materials [37, 106, 118, 120–124]. The models developed to describe the consolidation process of Autoclave prepregs, consider a coupled saturated flow of resin towards the bleeder using Darcy's law which leads to an elastic fiber bed compaction.

Predicting the loss of resin mass out of the laminate is a typical output of such simulations. Loos and Springer [125], Dave et al. [105, 112, 113], Gutowski et al. [104] and collaborators, derived equations to describe the coupled resin flow and compaction problem in laminates during autoclave processing. Hubert et al. [126] amongst others, extended these approaches towards complex part geometries, using FEA approaches. A detailed discussion on the various features of the above mentioned models can be found in the review paper by Hubert and Poursartip [127].

The compaction behavior of textiles is investigated in the context of several Liquid Composite Molding processes. When processing with vacuum is concerned (VARI, V-RTM), the goal is to develop models which capture the influence of the flow front progression on the local fiber volume fraction, the thickness and the impregnation time of the part [69, 73, 128, 129]. In processes which involve high compaction forces in a

closed rigid tooling, interest mostly lies on quantifying the fiber bed deformation in order to predict a part's thickness, residual stress distribution and the stresses applied on the tooling during processing [114, 115, 117].

Michaud et al. [66, 123, 130] addressed aspects of parallel impregnation and compaction of a reinforcement with thermoplastic matrices (Glass Mat Thermoplastics – GMT), using a coupled model based on the approach developed by Sommer et al. [131]. Helmus et al. [132], applied the same theory to model the simultaneous consolidation and air evacuation of OoA prepregs. The effective stress of the fiber bed is modeled as a function of the fiber volume fraction according to the relationship developed by Gutowski et al. [104]. The approach by Sommer et al. [131], is extended further to include relaxation effects during deconsolidation in GMTs [102, 133]. Finally, Larsson, Wysocki, Rouhi and collaborators [134–137], developed a ‘unified finite-strain continuum framework’ for modeling consolidation and flow of partially impregnated fibrous media, such as OoA prepregs. The formulation considers a nonlinear reversibly compressible fibrous network, saturated with an incompressible fluid including the presence of voids.

## 2.2.4 Constitutive Laws

Since Darcy's law (Equation (2-14)) is the basis of most studies relating to macroscopic flow in Composites Processing [4, 90], the fibrous medium permeability and the resin viscosity directly involved in the relationship are discussed.

### 2.2.4.1 Permeability

Permeability expresses the ease of a fluid to flow through a porous medium [4]. The permeability characterizes the textile or preform and it is primarily a function of the fiber network architecture [93, 99] and the fiber volume fraction [4, 88, 138]. Darcy's law (Equations (2-13) and (2-14)) lumps in the permeability term all interactions which take place between the fluid and the fibrous medium [4]. Permeability is anisotropic and direction dependent in orthotropic media such as fiber reinforcements [4, 139] and it is described by a second order tensor [139].

Three approaches used to determine the permeability of a textile are summarized below.

1. Use of simplified analytical equations to calculate the permeability of idealized unidirectional fiber distributions.

This category entails models, such as the isotropic model proposed by Kozeny-Carman [138], based on the adaptation of the capillary model from soil mechanics. This approach is later expanded to include the effect of through thickness permeability reduction to zero, once the fibers are in contact. The three most commonly known modifications are performed by introducing further experimental constants as done by Gutowski [104] or in the case of Gebart [140] and Brusckie and Advani [85], using lubrication theory.

2. Modeling of the flow through a unit cell of a textile architecture, using analytical or FE simulation approaches.

Since the analytical formulations can address flows through unidirectional fibrous domains, models that are more complex are used to model the interaction of the flow inside and outside the yarns. Once the textile architecture is captured with the required detail and the boundary conditions for the flow are applied, the macroscopic flow or the coupled macroscopic and tow flow can be predicted. The most detailed modeling approach captures the resin flow inside the tow as Darcian, while the flow through the channels of a textile is captured using Stokes flow [68, 141]. For simplification the yarns are occasionally treated as impermeable, since their permeability is typically at least two orders of magnitude lower than the channel permeability [142, 143].

3. Experimental determination of the permeability through saturated or unsaturated measurements.

A summary of the most widely used permeability measurements for characterizing fibrous reinforcements, are given in the review paper by Sharma and Siginer [139]. The experimental determination of a textile reinforcement's permeability is a source of significant variability and a field of continuous developments and attempts for standardization [144]. Particularly challenging is the determination of the through thickness permeability of dry consolidating textiles [118, 145–147] and lubricated, consolidating fibrous media [118, 146].

Characterizing the permeability of a prepreg is not as straightforward to pursue experimentally. In a prepreg, the amount of resin necessary to impregnate each ply is deposited on top of it or partially impregnating it, as a high viscosity layer of a constant thickness. As the fibrous medium is sandwiched between two, almost impermeable layers of resin [18], the procedure of pumping a fluid through the thickness of the stack and measuring its mass flow and the developed pressure gradient is not possible. To acquire the through thickness permeability information, a possibility would be to characterize the fiber bed permeability used as a basis for the prepreg by itself. In this case the liquid used for the measurement has to be selected carefully to match the viscosity of a hot-melt resin system. This imposes significant difficulties in practice, since the viscosity of those resins at room temperature is much higher than that of oils typically used for this purpose in infusion applications ( $10^4$ - $10^5$  Pa·s). The standard post-processing procedure to determine the permeability would have to be adjusted to consider the material as a three phase medium, of which the solid part consists of the fibers and the resin. Since the prepreg is at a partially saturated state, the direct comparison of the prepreg's permeability to the textile permeability is not meaningful.

A promising approach to characterize the dual scale permeability of partially impregnated woven prepreps was proposed by Cender et al. [27]. The experimental technique uses a CCD camera to track the flow front propagation of the resin through a glass tool,

under the application of pressure and heat [27]. The resin flow is modeled as longitudinal, one dimensional flow into two porous media in series in order to capture the permeability change between intra and inter-tow regions. The model is used to fit the experimental curve of the area filled with resin and its evolution in time, for up to approximately 65% filling of the tow, which is the limit of this method.

The simplified constitutive equations developed by Gebart [140] describe the flow along (Equation (2-18)) and perpendicular to the fiber bed (Equation (2-19)) as Darcian, driven by an imposed pressure gradient [104, 140]. The through-thickness permeability of a prepreg tow saturated with resin is calculated in this work via Equation (2-19).

$$K_{r,xx} = \frac{8R_f^2 (1 - V_f)^3}{c V_f^2} \quad (2-18)$$

$$K_{r,zz} = C_G \left( \sqrt{\frac{V_{f,max}}{V_f}} - 1 \right)^{\frac{5}{2}} R_f^2 \quad (2-19)$$

Where, the parameters  $C_G$  and  $V_{f,max}$  are characteristics of the fiber arrangement type,  $c$  is a weak function of the fiber volume fractions equivalent to the Kozeny constant, depending on both the fiber arrangement type and the fiber volume fraction. The symbol  $R_f$  refers to the radii of the fibers used, while  $V_f$  reflects the fiber volume fraction of the medium. The model parameters used in Equations (2-18) and (2-19) for the two characteristic fiber distributions, are given in Tab. 2-1, where it is shown that a much higher packing is possible with a hexagonal fiber distribution.

**Tab. 2-1: Numerical values used in Gebart's model for the two idealized fiber distributions**

Fiber Arrangement	$C_G$	$V_{f,max}$	$c$
Quadratic	$\frac{16}{9\pi\sqrt{2}}$	0.785	57
Hexagonal	$\frac{16}{9\pi\sqrt{6}}$	0.906	53

The application of Gebart's model [140] for the definition of the through thickness permeability of the MTM 44-1 prepreg is discussed further in Chapter 3.3.2.

### 2.2.4.2 Rheokinetics

Resin viscosity plays a dominant role in the impregnation quality of a fibrous medium, as it is inversely proportional to its velocity. Since the resin viscosity ultimately evolves as a result of temperature application and the degree of cure, both aspects are discussed with the focus placed on epoxy resin systems.

#### Epoxy Resin

Epoxyes are the most commonly utilized thermosetting resin systems in the field of high performance composites. Typical features making them attractive are their low shrinkage, good chemical resistance and mechanical properties. The primary disadvantage of epoxyes is their brittleness due to their high cross-linking density. Most commonly used systems are either based on DGEBA (Diglycidyl Ether of Bisphenol A) or the TGMDA/TGGDM epoxy (Tetraglycidyl 4,4' Diaminodiphenylsulphone) [2].

The epoxy polymer is formed irreversibly by linking monomers or oligomers into a network via a step reaction process. The basic reaction that takes place is between the epoxide and a curing agent, also known as hardener. According to Campbell [2] the most common types of curing agents used in epoxyes are amines (aliphatic or aromatic), hydroxyl and anhydrides. Halides of metals and their fluoroborates can also be used as catalytic agents, though typically in a small percentage in combination with the main curing agents [2]. The curing process of epoxyes depends on the reactivity characteristics of the involved functional groups, their molecular structure and spatial distribution [148–150]. The resulting material after cure is chemically and thermally stable, insoluble and rigid [148].

Commercial systems usually consist of a mix of different epoxy types and curing agents and occasionally initiators and inhibitors. Addition of different chemical groups in the primary epoxy system assists in tuning the crosslinking process, which has an impact on the cure reaction rates and the resin viscosity development. At the same time various molecules can be incorporated in the polymer as tougheners (second phase toughening, network alteration or interlayering) reducing the brittleness of epoxy resins [2].

#### Cure Kinetics

The curing of thermosetting resins is an exothermic process. According to Hatakeyama and Quinn [151], the reaction is activated when a particle of the reactants attains sufficient energy to overcome the potential energy barrier impeding the reaction. The total heat or enthalpy  $\Delta H_R$ , released by the reaction of the resin components up to the point when curing is completed, is constant and characteristic for a given system. The heat released at any time throughout the cross-linking process is expressed as  $\Delta H_t$ . The released heat can be measured using a Differential Scanning Calorimeter (DSC).

The degree of cure  $\alpha$  is defined in Equation (2-20) as the fraction of heat released at a given time ( $\Delta H_t$ ), with respect to the heat released by a fully cured system ( $\Delta H_R$ ).

$$\alpha = \frac{\Delta H_t}{\Delta H_R} \quad (2-20)$$

When full cure is achieved, the degree of cure becomes unity ( $\alpha = 1$ ). The cure reaction rate can be calculated from the instantaneous enthalpy according to Equation (2-21).

$$\frac{d\alpha}{dt} = \frac{1}{\Delta H_R} \frac{dH_t}{dt} \quad (2-21)$$

Two approaches can be used to describe the evolution of cure in a cross-linking thermoset system, the mechanistic and phenomenological. Mechanistic models describe each reaction taking place during cure (microscopic). Phenomenological models treat the cure process as a whole, addressing the kinetics of the dominant reaction (macroscopic).

Mechanistic models provide significant insights of the cure process, though they require detailed knowledge of the reactions which take place between the various species. Sophisticated techniques are required to track the instantaneous concentration of all species in a heterogeneous resin system as a function of temperature and time (Fourier infrared spectroscopy, chromatography, nuclear magnetic resonance etc.).

Phenomenological models express the rate of resin reaction  $d\alpha/dt$ , as the product of a function of the evolution of reactant's concentration and a rate coefficient  $k(T)$ . In heterogeneous systems, the evolution of the reaction can be determined via monitoring the rate of heat consumed over time  $dH_t/dt$  with DSC. The expression of the rate of reaction in its general form is given in Equation (2-22) [151]:

$$\frac{d\alpha(t)}{dt} = k(T) \cdot f(\alpha(t), T) = k(T) \cdot f(\alpha(t)) \cdot h(\alpha, T) \quad (2-22)$$

Where  $k(T)$  a rate coefficient defined by an Arrhenius relationship,  $h(\alpha, T)$  is omitted [151], while  $f(\alpha(t))$  can take different forms, with the simplest being the  $n^{\text{th}}$  order model, with  $n$  being a constant which reflects the dominating reaction order [148, 151]. Details on models and fitting parameters used to describe reactions taking place in various resin systems are provided in the references [148, 151].

### Resin Viscosity

A fluid's viscosity is a measure of its resistance to deformation or flow [4]. The viscosity of a thermoset resin is a function of time, temperature and the degree of cure if the resin is Newtonian (no effect of shear rate on the viscosity). Out-of-Autoclave processing is generally a slow process, taking place under low pressures and therefore shear rate effects on the viscosity evolution are be considered negligible.

The two phenomena strongly depending on the molecular structure of an epoxy resin, which compete and govern its rheological behavior, are [148, 152–154]:



- The polymer mobility intensification due to temperature increase, which may lead to viscosity reduction.
- The growing size of the molecules due to increasing cross-linking as the cure progresses, which may lead to an increase of the resin viscosity.

The expression describing the viscosity evolution based on a reference temperature  $T_s$  and a temperature of interest  $T$  based on the free volume theory proposed by Williams-Landel-Ferry (WLF) is given in Equation (2-23) [155], where  $C_1$  and  $C_2$  are constants.

$$\ln \frac{n(T)}{n(T_s)} = - \frac{C_1(T - T_s)}{C_2 + (T - T_s)} \quad (2-23)$$

This model is successful in predicting the viscosity of a system for low degrees of cure. Karkanis et al. [156] enhanced the model by WLF to capture the viscosity evolution of an RTM epoxy system up to gelation.

Two approaches can be used to describe the evolution of viscosity without a detailed knowledge of the material chemistry. The direct correlation of the viscosity with the temperature and the degree of cure [148, 157–159], or the indirect correlation through temperature and time [148, 160–166].

Several empirical models express the viscosity evolution as a product of two functions, one correlating the effect of the temperature and the other one the degree of cure, according to the general form of Equation (2-24).

$$n = f(T) \cdot g(\alpha) \quad (2-24)$$

Stolin et al. [148, 160] correlated the viscosity evolution with the cure rate as a function of the temperature and degree of cure via Equation (2-25).

$$n(T, \alpha) = n_0 \exp\left(\frac{E_n}{RT} + c_k \alpha\right) \quad (2-25)$$

The initial viscosity of the resin is depicted by  $n_0$ , while  $E_n$  is the fluid activation energy and  $R$  the gas constant ( $8.3144 \text{ JK}^{-1}\text{mol}^{-1}$ ). The constant  $c_k$  accounts for the effect of chemical reaction on the viscosity and it is independent of the degree of cure [148].

The viscosity at zero-time and temperature  $T$  writes according to Roller et al. [162]:

$$n_0(T) = n_\infty \exp\left(\frac{E_n}{RT}\right) \quad (2-26)$$

The viscosity of a fully cured resin system is expressed as  $n_\infty$ ,  $E_n$  is the fluid activation energy and  $R$  is the gas constant. The expressions proposed for the prediction of isothermal and non-isothermal viscosity are given in Equation (2-27) and (2-28) respectively.



$$\ln n(t) = \ln n_{\infty} + \frac{E_n}{RT} + tk_{\infty} \exp\left(\frac{E_k}{RT}\right), \quad T = \text{constant} \quad (2-27)$$

$$\ln n(t) = \ln n_{\infty} + \frac{E_n}{RT} + \int_0^t k_{\infty} \exp\left(\frac{E_k}{RT}\right) dt, \quad T = f(t) \quad (2-28)$$

The coefficients  $k_{\infty}$  and  $E_k$  are the direct kinetic analogues of the viscosity  $n_{\infty}$  and the activation energy  $E_n$  in the temperature domain, for a single cure reaction.

Castro and Macosko [157] correlate the viscosity, with the instantaneous degree of cure  $\alpha$ , the degree of cure at the gel-point  $\alpha_g$  and temperature evolution via Equation (2-29):

$$n = n_i(T) \left[ \frac{\alpha_g}{\alpha_g - \alpha} \right]^{A+Ba} \quad (2-29)$$

This model is extended according to Equation (2-30) by Khoun et al. [158] in order to describe the viscosity evolution of an epoxy resin system used in RTM processing.

$$n = n_1(T) + n_2(T) \left[ \frac{\alpha_g}{\alpha_g - \alpha} \right]^{A+B\alpha+C\alpha^2} \quad (2-30)$$

While the individual viscosities  $n_i(T)$  are expressed by the Arrhenius Equation (2-31).

$$n_i(T) = A_{n,i} \exp\left(\frac{E_{n,i}}{RT}\right) \quad (2-31)$$

The parameters  $A, B, C, A_{n,i}, E_{n,i}$  are fitting constants [148, 158].

This approach can be used to model the viscosity evolution of the resin, once the cure kinetics model for the system of interest is available. The degree of cure  $\alpha$ , is predicted by Equation (2-20), while the degree of cure at gelation  $\alpha_g$ , is an average of the degrees of cure at all tested temperatures [159, 167].

The viscosity model of Equation (2-30) has been used to characterize three OoA pre-pregs, namely the MTM 45 and the Cycom 5320 [159] and the Hexcel M18-1 [168]. The model captures well the viscosity evolution up to gelling of the MTM 45 and 5320 systems, for temperatures up to 130°C. Best fit is achieved for dynamic cycles with temperature heating rates lower than 1°C/min [159]. Similarly, in the case of the M18-1 resin the model captures well the viscosity evolution at low temperatures (100-130°C). Fontana and Kiuna et al. [163, 164] developed an approach to model viscosity, solely through viscosity measurements, combining the principles of the WLF equation and Roller et al. [162]. The new model was developed according to Fontana et al. [163], to address the reduced applicability of existing models to capture the viscosity evolution of an epoxy resin at low temperatures, relevant for RTM processing. Fontana et al. [163]

used Equation (2-32) in combination with look-up tables to model the isothermal viscosity of a thermoset resin system.

$$n = \exp(\ln(n_s) + f(T_s - T)) \quad (2-32)$$

The variables  $n, n_s$  stand for the viscosities at temperatures  $T, T_s$  and  $f$ , a shifting function independent of temperature and cure state, normalizing the data to a reference temperature  $T_s$ .

Kiuna et al. [164] adapted Fontana's approach, proposing a model able to capture both isothermal and non-isothermal viscosity evolution without the need for look-up tables [164]. The non-isothermal viscosity is calculated via Equation (2-33).

$$\frac{dn}{dt} = n \cdot \left( \frac{k(T)}{g'(\ln(\frac{n}{n_0}))} + \frac{1}{n_0} \cdot \frac{dn_0}{dT} \cdot \frac{dT}{dt} \right) \quad (2-33)$$

The initial viscosity of the resin at temperature  $T_0$  is  $n_0$ ,  $k(T)$  is the kinetic factor (introduced by Roller) and  $g'$  is a function of the dimensionless viscosity  $\ln(n/n_0)$ .

Keller et al. [165] advanced this model to address the viscosity evolution of fast curing systems. This approach was applied by Kourkoutsaki et al. [12] to model the viscosity of the Cytec MTM44-1 OoA epoxy resin, achieving a good match with the experimental data for temperatures in the range of 100-140°C. More details on this approach are provided in Chapter 3, Section 3.4

Generally none of the phenomenological viscosity models is universally applicable. Their applicability shall be checked individually against experimental data generated at the temperature range considered, heating rates or degrees of cure of interest, for the resin system of interest. The most prominent method of measuring a resin's viscosity for characterization purposes is with a rheometer in oscillatory mode (for more details see Appendix d and Chapter 3.4.2). Nevertheless, when the measurement of a resin's viscosity during processing, or inside a prepreg/preform is concerned, the electrical conductivity (AC or DC) can be used as a direct analogue of the viscosity [161, 169, 170]. According to May et al. [161, 170], an excellent correlation between the complex viscosity and the voltage or phase angle (AC measurements) or the resistance is obtained (DC measurements), when the resin is at its fluid state. Dielectric measurements can also be used to detect resin aging even inside a prepreg [161, 170–172].

## Gelation

Gelation is responsible for the abrupt transformation of a resin system from a viscous liquid to an elastic gel, according to the definition given in the EN6043:1995 standard [173]. As the reaction proceeds, the molecular mass of the oligomers increases significantly, up to a point defined as the gel-point, at which all polymer chains are connected

and form a network of infinite molecular weight. The macroscopic consequence of gelation is typically a rapid approach towards infinite viscosity accompanied by a reduced ability to flow.

The gel point in a resin system can be determined with the use of several methods, such as: rheometer, dynamic scanning calorimetry (DSC), thermal mechanical analysis (TMA), Fisher Johns melting point apparatus [173, 174], dielectric measurements (DEA) using either AC or DC current [161, 169, 171, 175, 176], torsional braid analysis (TBA) and nuclear magnetic resonance (NMR) [174]. A comprehensive review of all established methods for viscosity determination and a comprehensive list of standards available in each case, are given in the review paper by Halley et al. [174]. The method most broadly applied to determine the gel point of the resin, is through oscillatory rheometry performed at constant frequency (see Appendix d for more details).

Capturing the viscoelastic properties of the resin, such as the storage  $G'$  and the loss modulus  $G''$ , the gel point can be identified as the point where the two curves intersect ( $G' = G''$ ), at which point by definition the loss factor equals to unity ( $\tan \delta = G''/G' = 1$ ) [152, 177] or more precisely it becomes independent of the test frequency [178, 179]. The evolution of the gel-point at different isothermal conditions is typically fitted to an exponential or extended Arrhenius fit [165]. A rule of thumb given in the EN6043:1995 Standard [173] suggests that gelling is reached when  $n_{gel} = 10^3 \cdot n_{min}$ . Nevertheless, this rule cannot be generalized and has to be used with caution after checking its validity against measurements performed according to one of the above-suggested methods.

## 2.3 Air Flow through a Porous Medium

### 2.3.1 Mechanisms of Gas Transport

The physics of gas transport through porous media are grouped by Mason and Malinauskas [180] as reviewed by Hou et al. [36, 180] in five independent mechanisms, the viscous and free molecular flow, continuum or ordinary diffusion of gas species, diffusion or surface flow and chemical interactions with neighboring fluids (absorption). Chemical interactions between neighboring fluids in a fibrous medium are considered to be negligible in the context of this work and will not be discussed further.

#### 2.3.1.1 Diffusion Processes – Mass Transport

The diffusion processes are concerned with the movement and redistribution of selected gas species. The movement of the gas species can either be relative to each other, or along a solid surface under the influence of concentration, temperature or force gradients. In composites manufacturing such phenomena take place when volatiles or water migrate, merge, nucleate or dissolve under specific processing conditions.

The first attempt to model the void formation physics in prepregs is performed by Kardos et al. [15, 16]. A similar approach which investigates the conditions of void formation is developed by Wood et al. [181]. These early modeling attempts are followed by models coupling the volatile generation with and the consolidation process, such as the work by Upadhyaya et al. [182] and bubble motion during flow through a porous medium, by Lundström et al. [183], amongst others. The effect of moisture diffusion on prepreg porosity formation during OoA manufacturing is investigated by Grunenfelder et al. [54], based on the approach proposed by Kardos et al. [16]. Grunenfelder et al. [54] demonstrated that intra-ply porosity due to diffusion of moisture is more prone to develop in laminates manufactured OoA, since the reduced pressure available in the laminate during processing cannot assist in the void dissolution. Helmus [184] developed a numerical model, which describes the influence of temperature, pressure and relative humidity on the bubble growth inside the resin [184].

### 2.3.1.2 Momentum Transport

The non-dimensional Knudsen number  $K_n$  defined in Equation (2-34) [36, 185] can be used to determine the gas flow regime in a porous medium.

$$K_n = \frac{\lambda}{l} \quad (2-34)$$

The mean free path  $\lambda$  expresses the average distance traversed by a molecule between successive collisions [186], while it depends on the pressure, temperature and molecular weight of the gas [186]. The symbol  $l$  is used for the characteristic length of the pores in the medium under investigation. The mean free path for gas molecules at standard temperature and pressure (at 25°C and 1atm) is approximately  $\lambda \sim 8 \cdot 10^{-8} \text{ m}$  [186]. The gas flow regimes are classified into the following three categories [36, 180]:

- Viscous flow ( $K_n \ll 1$ )

This mechanism is dominant when the characteristic length of the pores in the medium is much larger than the mean free path [36]. Hence the intramolecular collisions in the gas are more significant than the molecular collisions with the walls of the medium. In this case the gas flow in the porous medium is considered laminar, closely resembling the creeping flow of a liquid (though compressible) [180]. As this work is primarily concerned with the viscous flow of gas through a fibrous domain, the governing equation will be presented in more detail in 2.3.3.1.

- Free-molecular or Knudsen flow ( $K_n > 1$ )

When the number of collisions between the gas molecules is negligible compared to the number of collisions of the molecules with the walls, the flow is free-molecular [36]. The continuum fluid flow equations break down and alternative diffusion-based formulations shall be used to accurately predict the velocity and permeability [187]. Deviation from the viscous flow behavior is particularly observed at low pressures [108] and tight

porous media, with low permeability [108, 187, 188]. Inappropriate use of the viscous flow governing equations in such media can lead to significant underestimation of the permeability [36, 187].

- Sliding flow ( $K_n \sim 1$ )

If the Knudsen number is close to unity ( $K_n \sim 1$ ) [36, 187], both Knudsen and Viscous flows co-exist in the porous medium. The additional flux results in a faster gas flow compared to the pure viscous flow [108]. This pattern is known as sliding gas flow [36, 189]. The sliding flow is initially observed by Klinkenberg [189] who demonstrated the deviation of the effective rock permeability when measured using gas ( $K_a$ ), from their intrinsic permeability when measured using a liquid ( $K_r$ ) [189]. This effect can be explained by the slippage of the gas at the walls of the porous medium [36, 38, 187, 188]. Klinkenberg's permeability [189] is in practice the intrinsic permeability enhanced by sliding effects described by Equation (2-35), also known as the effective permeability.

$$K_a = K_r \left( 1 + \frac{b}{P_{gas}} \right) \quad (2-35)$$

The intrinsic or viscous permeability of a fluid when the Klinkenberg effect is negligible is written as  $K_r$ , while  $P_{gas}$  is the gas pressure in the porous medium. The Klinkenberg factor  $b$  depends on the mean free path of the gas molecules and the microstructure of the pores. Various relationships for the Klinkenberg's gas slippage factor and a range of porous media can be found in Ziarani and Aguilera's work [187]. The range of the Knudsen number which defines each flow regime varies in different publications [36, 187, 188], possibly due to characterization of processes essentially taking place at different pressure magnitudes.

### 2.3.2 Ideal Gas Law

An ideal gas consists of freely moving molecules. When the intramolecular collisions are short in duration and close to being elastic, the behavior of the gas can be described by the equation of state of an ideal gas, according to Equation (2-36). The ideal gas law describes the behavior of gases at low pressures (below  $10^5$  Pa) with a good accuracy, without considering their compressibility.

$$P_{gas}V_{gas} = n_{gas}RT \quad (2-36)$$

The ideal gas law in a closed system at isothermal conditions (Boyle's Law), correlates the absolute gas pressure and its volume according to Equation (2-37). In the context of this work this relationship correlates the air pressure ( $P_{gas}$ ), with the air volume inside the fiber tows ( $V_{gas}$ ).

$$P_{gas}V_{gas} = constant \quad (2-37)$$

At non-isothermal conditions, the air density ( $\rho_a$ ) is correlated with the absolute gas pressure ( $P_{gas}$ ) and the temperature ( $T$ ) according to Equation (2-38).

$$\rho_a = \frac{P_{gas}}{R_{sp}T} = \frac{P_{gas} M_n}{R T} \quad (2-38)$$

The  $R_{sp}$  stands for the specific gas constant, while  $M_n$  stands for the mean molar mass of dry air ( $28.97 \cdot 10^{-3}$  kg/mol).

### 2.3.3 Governing Equations

The conservation of mass in a non-consolidating porous medium (without sinks) and for small density variations writes for air:

$$\phi \frac{\partial \rho_a}{\partial t} + \nabla \cdot (\rho_a \langle \mathbf{v}_a \rangle) = 0 \quad (2-39)$$

The air density is depicted as  $\rho_a$ ,  $\phi$  is the porosity of the medium through which air flow takes place and  $\langle \mathbf{v}_a \rangle$  is the volume average air velocity. If air is considered an ideal gas, its density can be correlated with the gas pressure through Equation (2-38). The momentum conservation equations for the three air flow regimes are given below.

#### 2.3.3.1 Viscous Flow

Viscous air flow takes place in a porous medium with large pores. If air is considered to be a Newtonian fluid which flows under laminar conditions in the porous medium ( $R_e < 0.1$ ), Darcy's Law for air expressed by Equation (2-40) can be used. The permeability of the porous medium during viscous flow, measured either with a gas or a liquid are equivalent. The permeability of the porous medium, when the flow of the fluid is viscous [36], is known as the viscous or intrinsic permeability given in Equation (2-41) [38, 39].

$$\langle \mathbf{v}_a \rangle = -\frac{K_a}{\mu_a} \nabla \langle P \rangle^a = -\frac{K_a}{\mu_a} \nabla P_{gas} \quad (2-40)$$

$$K_a = K_r = K_\infty \quad (2-41)$$

Combining the conservation of mass (2-39) and momentum (2-40) with the ideal gas law (2-37), leads to the governing Equation (2-42) for viscous air flow at isothermal conditions [19, 26, 30, 33, 35, 36, 190–192].

$$\frac{\partial P_{gas}}{\partial t} - \frac{K_a}{\phi \mu_a} \nabla \cdot (P_{gas} \nabla P_{gas}) = 0 \quad (2-42)$$

A range of approaches [19, 30, 35, 190–192] is used to calculate the gas pressure from the non-linear, transient expression of Equation (2-42).

Arafath et al. [35] derived the approximate, empirical expression of Equation (2-43), which correlates the mass of air flowing out of an OoA prepreg ( $m_a$ ), as a function of a dimensionless time ( $\tau_a$ ). The function is derived from fitting the results of the mass of air measured with a flow meter during steady state air permeability tests, for the material system and experimental set-up described by Arafath et al. [35]. The dimensionless time is described as a function of the initial pressure  $P_{gas}(t = 0)$ , permeability  $K_{a,xx}$ , air viscosity  $\mu_a$  and the square of the length of the part  $L^2$ , according to Equation (2-44).

$$\frac{m_a}{m_{a0}} = e^{-0.9\tau_a^{0.6}} \quad (2-43)$$

$$\tau_a = \frac{K_{a,xx} P_{gas}(t = 0)}{\mu_a L^2} t \quad (2-44)$$

According to Arafath et al. [35], the purpose of this correlation is ‘to offer guidance in the design of the bagging and vacuum system’ [35]. Since the function of the expelled air mass of Equation (2-43) lumps together the contributions of the prepreg, the bagging set-up and the auxiliary materials, its applicability is limited to the particular set-up and prepreg. For that same reason it cannot be considered as a universally applicable relationship which can be readily transferred to other OoA prepreps. Therefore its validity has to be checked before use in the description of the air evacuation of a different material system, or bagging set-up than the one used for the development of this expression.

Kim et al. [190] derived the in-plane, dimensionless and linearized diffusion Equation (2-45) using as a basis Equation (2-42), for which an analytical solution is derived in Equation (2-47) using the initial and boundary conditions of Equation (2-46). For this simplification the gas pressure variation is considered small compared to the atmospheric pressure ( $P_{gas} \partial^2 P_{gas} / \partial x^2 \ll (\partial P_{gas} / \partial x)^2$  and  $P_{gas} / P_{gas}(t = 0) \cong 1$  [190]).

$$\frac{\partial P_{gas}^*}{\partial t^*} = \frac{\partial^2 P_{gas}^*}{\partial x^{*2}} \quad (2-45)$$

$$\text{IC} \quad P_{gas}^*(x^*, 0) = 1$$

$$P_{gas}^*(0, t^*) = 0 \quad (2-46)$$

$$\text{BCs} \quad \mathbf{u}_{af}(1, t) = 0 \rightarrow \frac{\partial P_{gas}^*(1, t^*)}{\partial x^*} = 0$$



$$P_{gas}^*(x^*, t^*) = 2 \sum_{n=1}^{\infty} \frac{1}{\lambda_n} \exp(-\lambda_n^2 t^*) \sin \lambda_n x^* \quad (2-47)$$

$$\text{where } \lambda_n = \frac{\pi(2n-1)}{2}$$

The author showed [19, 30, 192] that the simplified analytical approach proposed by Kim et al. [190] cannot accurately predict the gas distribution in an OoA fiber tow. To address the shortcomings of the available approaches, the author proposed a numerical scheme to solve the full non-linear, transient Equation (2-42) [19, 30, 192]. Details on the implementation scheme and the governing equations used, are given in Chapter 4, Section 4.1. Hou et al. [36] use Equation (2-42) to predict the transient 1D permeability of fibrous preforms. The author [12] also utilizes this method in order to measure the in-plane permeability of OoA prepregs to air. More details on the characterization method and the resulting permeabilities are given in Section 3.3.1.

Levy et al. adapted Equation (2-42) to describe the 2D air flow through a sandwich panel consisting of two OoA prepreg face-sheets and a honeycomb [191]. An equivalent permeability  $K_{a,eq}$  is defined according to Equation (2-48) [191], which lumps the permeability of the core and the face-sheets. A correction factor  $a_f$  is incorporated in the permeability definition, determined by mesoscopic flow model in a honeycomb RVE [191].

$$K_{a,eq} = (1 + a_f)K_a \quad (2-48)$$

The governing equation proposed by Levy et al. [191] for the flow of air through the sandwich panel modifies Equation (2-42) by the addition of a term which includes the contribution of the air volume in the prepreg and core given in Equation (2-49) [191].

$$\underbrace{\left(\phi + \frac{h_c}{2h_s}\right)}_{\text{Air Volume Term}} \frac{\partial P_{gas}}{\partial t} - \nabla \cdot \left( \frac{K_{a,eq}}{\mu_a} P_{gas} \nabla P_{gas} \right) = 0 \quad (2-49)$$

### 2.3.3.2 Sliding Flow

In a tight porous medium, the sliding effect of the gas can become significant. In such occasions, the conservation of momentum is reformulated either by utilizing the corrected Klinkenberg permeability, or effective permeability  $K_a$  in Darcy's law given by Equation (2-50) [26, 33, 38, 39], or by utilizing the dust gas model [36, 180].

$$K_a = K_{\infty} \left( 1 + \frac{b}{P_{gas}} \right) \quad (2-50)$$

Governing Equations (2-51) and (2-52) express the 1D flow of air through the porous medium, utilizing the Klinkenberg permeability and the dust gas model respectively.



$$\frac{\partial P_{gas}}{\partial t} - \frac{K_{\infty}}{\phi \mu_a} \frac{\partial}{\partial x} \left( (P_{gas} + b) \frac{\partial P_{gas}}{\partial x} \right) = 0 \quad (2-51)$$

$$\frac{\partial P_{gas}}{\partial t} - \frac{1}{\phi} \frac{\partial}{\partial x} \left( \left( K_m \bar{v}_a + \frac{K_{\infty} P_{gas}}{\mu_a} \right) \frac{\partial P_{gas}}{\partial x} \right) = 0 \quad (2-52)$$

The intrinsic, viscous permeability of the medium at conditions where the Klinkenberg effect is negligible is  $K_{\infty}$ ,  $b$  is the Klinkenberg factor,  $\phi$  is the porosity, while  $\mu_a$  is the air viscosity. The coefficient  $K_m$  is an additional parameter related to the pore geometry and the gas surface scattering law incorporated in the expression of Knudsen's air flow [36, 180], while  $\bar{v}_a$  is the mean velocity of the gas. Hou et al. [36] demonstrated the equivalence of Equations (2-51) and (2-52), in a medium where significant sliding is present [36].

Cender et al. [38, 39] extended the dimensionless form of Equation (2-51) into Equation (2-53) by incorporating a dimensionless 'pseudo' or 'slip' pressure ( $P_s^*$ ).

$$\frac{\partial P_{gas}^*}{\partial t^*} - \frac{\partial}{\partial x^*} \left( (P_{gas}^* + P_s^*) \frac{\partial P_{gas}^*}{\partial x^*} \right) = 0 \quad (2-53)$$

$$P_s^* = \frac{(P_{vac} + b)}{(P_{atm} - P_{vac})} \quad (2-54)$$

According to Cender et al. [38, 39] when  $P_s^* \gg 0$ , significant sliding takes place ( $b > 10^5$ ), or there is a small pressure drop across high pressures. In this case Equation (2-53) can be linearized into a diffusion equation according to Equation (2-55).

$$\frac{\partial (\partial P_{gas}^* + P_s^*)^2}{\partial t^*} - P_s^* \frac{\partial^2 (\partial P_{gas}^* + P_s^*)^2}{\partial x^{*2}} = 0 \quad (2-55)$$

The diffusion Equation (2-55) has an analytical solution for selected boundary and initial conditions.

Tavares et al. [33] used the linearized expression of Equation (2-55) as a basis for the development of a real-time through thickness permeability measurement of OoA pre-pregs during the cure cycle. Once the relevant initial and boundary conditions are applied, Klinkenberg's permeability  $K_a$  is calculated from Equation (2-56).

$$\ln \left[ \frac{(P_{atm} + P_{gas}(t))(P_{atm} - P_{gas_i})}{(P_{atm} - P_{gas}(t))(P_{atm} + P_{gas_i})} \right] = \frac{K_a A_c P_{atm}}{\mu_a V_t} t \quad (2-56)$$

Where  $A$  is the cross-sectional area of the preform through which flow takes place,  $V_t$  the gas volume of the tank used for the measurement,  $P_{atm}$  the atmospheric pressure and  $P_{gas_i}$  and  $P_{gas}(t)$  the measured and calculated pressure in the domain respectively.

On the other hand, when  $P_s^* \approx 0$ , Equation (2-53) is transformed into Equation (2-57), which recovers the viscous flow Equation (2-42) in a dimensionless form.

$$\frac{\partial P_{gas}^*}{\partial t^*} - \frac{\partial}{\partial x^*} \left( P_{gas}^* \frac{\partial P_{gas}^*}{\partial x^*} \right) = 0 \quad (2-57)$$

## 2.3.4 Constitutive Laws

### 2.3.4.1 Air Viscosity

The dynamic viscosity of dry air at various temperatures is independent of pressure (except at very low vacuum pressures) and is given by Sutherland's Equation (2-58) [36, 186, 193].

$$\mu_a = \mu_0 \left( \frac{T_0 + C_s}{T + C_s} \right) \left( \frac{T}{T_0} \right)^{3/2} \quad (2-58)$$

The absolute temperature  $T_0 = 273.15\text{K}$  is and the initial viscosity of air at this temperature is  $\mu_0 = 1.71 \cdot 10^{-5}$  (Pa·s), correlated by Sutherland's constant  $C_s=120$  [193]. Several approximations of Sutherland's constants and the absolute temperature and viscosity can be found in the literature [36, 186, 193]. The differences are caused by the variation in the consistency of air and temperature measurements and are negligible [36].

### 2.3.4.2 Air Permeability Measurements in OoA Prepregs

Characterization of the air permeability of OoA prepregs has attracted significant attention in the literature. As the only means of applying pressure to consolidate a laminate outside the Autoclave is via the distribution of vacuum through its fibrous domain, determining a prepreg's permeability to air is key to OoA processing. The experimental determination of air permeability in OoA prepregs is generally performed either with the use of a flow meter measuring the volumetric air flow rate out of the laminate [31, 35, 53, 56, 194, 195], or via pressure gauges, along the domain through which transient flow takes place [12, 33, 34, 36, 39, 120].

Hickey et al. [37] introduced a method which can be used to characterize the air permeability evolution of an OoA prepreg under compaction. In this approach, the radial permeability of the prepreg is determined via correlating the information from a mass flow meter and a pressure sensor [37, 120]. Tavares et al. proposed an experimental method based on a falling pressure measurement, in order to evaluate the evolution of the out of plane air permeability of prepregs and honeycomb sandwich structures [33, 34]. The

method proposed by Tavares et al. [29, 33] was applied by Kratz et al. to define the honeycomb panel evacuation time of three OoA preregs based on different textile architectures, used as face sheets [26]. Fernlund et al. characterized the in-plane and through thickness air permeability of several OoA preregs and lay-ups [35] based on work published by Seferis group in the 90s [31, 32, 194]. The same methodology [32, 194, 196] was used by Grunenfelder et al. [54] to examine the effects of fiber orientation, prepreg direction and distance from the vacuum source. Cender et al. performed experiments in order to characterize the air permeability of textile based OoA preregs after processing at various impregnation states [38, 39]. Kourkoutsaki et al. [12] measured the effective air permeability of the MTM 44-1 prepreg based on a 2x2 twill weave at various impregnation states and porosity contents, using a transient dropping pressure method (DPM) initially proposed by Hou et al. [36] to characterize textile reinforcements. The permeability measurement method used to characterize the MTM 44-1 prepreg will be presented in detail in Section 3.3.1.

## 2.4 Coupling Air and Resin Flow

This Section reviews methods used to couple air and resin flow in a fibrous medium. A short overview of the main principals used in the simulation of unsaturated resin flow in conventional and Out-of-Autoclave composite manufacturing processes is presented. Emphasis is placed on methods which enable porosity predictions, either via capturing characteristics of the air flow (Section 2.4.1) or enabling tracking of the resin front (Section 2.4.2).

### 2.4.1 State of the Art

The presence of air in preforms which are being impregnated with resin can be either treated with the use of single phase flow equations, with ad-hoc phenomenological functions (Section 2.4.1.1), or by a detailed multiphase flow approach (Section 2.4.1.2).

#### 2.4.1.1 Introducing Air Flow in Single Phase Flow Models

To address the difference in the saturation rates of tows in textiles with dual scale porosity with resin, during Liquid Composite Molding, a sink term is introduced in the mass balance equation (see Equation (2-7)) [67]. The sink term is defined as a step function, which becomes zero once all tows are fully saturated with resin. Its magnitude depends on the pressure surrounding the tow and the saturation index, defined as the fraction of the tow filled with resin [68]. Though the method is not derived from first principals, its use is wide-spread due to the ease of implementation and computation.

This approach can be used to address the partial saturation and air entrapment which can occur inside tows of an impregnating preform. Several methods are available in the literature to derive sink term functions (see overview in 2.2.1), a few of which address the mechanisms of air entrapment inside the tow. Gourichon et al. [70, 71] developed a

method to include effects of air entrapment using the Ideal Gas Law. Gourichon et al. [70, 71] evaluated the local pressure of an air bubble trapped inside a tow against the capillary pressure. If the bubble pressure is smaller than the capillary pressure, the air will stay entrapped, until the pressure becomes higher than the capillary pressure leading to its collapse [70].

Lawrence et al. [69] developed a model to describe the gradual air escape from tows in a dual scale porous medium. Using an air entrapment factor, Lawrence et al. [69] derived an expression which captures the quantity of air escaping the tow through a transition between complete air escape or entrapment with or without including the influence of capillary pressure [69].

To avoid the singularity occurring when the saturation index becomes unity in the original sink term definition [68], Simacek et al. [73] replaced it with an expression of the tow filling time as a function of the pressure evolution. The filling time can be calculated by applying Darcy's law in the tow geometry concerned [73]. Due to difficulties in the accurate determination of a single scale permeability for a dual scale medium, fitting the experimental results of the tow saturation evolution is suggested as a practical approach to develop an empirical sink term function [73]. This expression is expanded to include the effect of capillary pressure, volatile entrapment or transient transport with escape rates based on i.e. an Arrhenius relationship [73].

Arafath et al. [35] developed an expression which correlates the mass of air flowing out of an OoA prepreg as a function of time, lumping the contributions of air flow through the material system and the experimental set-up (Equation (2-43)). Helmus et al. [132] developed a model, which uses the model proposed by Arafath et al. [35], to couple the air flow out of the dry consolidating fiber bed of an OoA prepreg at room temperature. In the debulking phase of the OoA prepreg resin flow is considered insignificant and is not taken into account [132]. In a second model presented in the same work, Helmus et al. [132] translates Arafath's relationship [35] into a pressure boundary condition for the resin flow through a consolidating OoA tow. Local differences in the air evacuation and consolidation along the tow length and the impact of temperature variations on the air pressure and local resin viscosity evolution are not addressed in this framework.

The single phase models including phenomenological functions to describe the saturation evolution, are limited in their application to isothermal processes. A generalized approach, able to capture heat transfer and curing effects is developed through rigorous derivation by expressing the governing equations in each of the scales of the fibrous media using volume averaging [74–80].

### 2.4.1.2 Multiphase Flow Models

The flow of resin in a partially saturated fibrous medium can be described by a two phase flow model which considers the flow of two immiscible fluids, resin and air, through the fibrous domain. Each domain of the fibrous medium is considered to be fully saturated

with one of the two fluids. The methodology is widely used in the soil or earth sciences [108] with Michaud and Mortensen [66] unifying the framework for multiphase flow modeling in consolidating fibrous media for composites [66]. In multiphase flow, the domain of interest contains all three phases, air, resin and fibers. In this case Equation (2-3) can be used to correlate the volume fractions of all three phases. The key parameters introduced in the governing equations of single scale flow are the saturation and the relative permeability, discussed here in more detail [66, 103].

The saturation parameter expressing the percent of the fibrous medium occupied by the fluid of interest  $S_j$  is by Equation (2-59). It is a scalar, which varies between zero and one. The extreme values of the saturation parameter reflect the two extreme cases encountered when a fibrous medium is not saturated ( $S_j = 0$ ) or fully saturated with a fluid of interest ( $S_j = 1$ ).

$$S_j = \frac{\phi_j}{(1 - V_f)} \quad (2-59)$$

The mass conservation equation for the fluid in a non-consolidating porous medium writes according to Park et al. [197]:

$$\phi_j \frac{\partial S_j}{\partial t} = \nabla \cdot \langle \mathbf{v}_j(S_j) \rangle \quad (2-60)$$

The expression for the mass conservation of the fluid and the fibers in a consolidating porous medium is included in the work by Michaud and Mortensen [66].

For the conservation of momentum, Darcy's law is modified according to Equation (2-61) to include the saturation [103, 197–199].

$$\langle \mathbf{v}_j(S_j) \rangle = \mathbf{v}_{jD}(S_j) = -\frac{\mathbf{K}_j}{\mu_j} \nabla(P - P_c(S_j)) \quad (2-61)$$

Michaud and Mortensen [66] expressed the modified Darcy's law for multiphase flow and consolidating porous media. Nordlund et al. [98] used Richardson's equation as the law for momentum conservation, initially derived to capture the movement of water in unsaturated soils. Breard et al. [103] modified the approach, considering an additional term in the macroscopic balance, Equation (2-61), for the saturation phase. This term represents a dispersive flux relative to the transport of the phase aiming to unify the flow and air transport through the porous medium [103], later extended by Garcia, Gascon and collaborators [198–200]. Wolfrath et al. [102] considered multiphase flow in a compressible, two phase fibrous medium deriving expressions for the saturation. The permeability included in Equation (2-61) is defined as the product of the saturated or intrinsic permeability of the medium and the relative permeability [66, 103], according to

Equation (2-62). The relative permeability  $K_{rel}$  is a scalar which varies from zero to one, in the same range as the saturation of the fibrous domain [66, 103].

$$\mathbf{K}_j = K_{rel}(S_j)\mathbf{K}_r \quad (2-62)$$

It is evident that the transition from a single to a multiphase simulation, requires a priori the knowledge of the resin saturation as a function of the fluid pressure, as well as the relative permeability and the capillary pressure as a function of the saturation [197]. The saturation curves as a function of the fluid pressure, also known as drainage/imbibition curves, are derived via micro-scale flow modeling [102], as a solution of the saturation advection-diffusion equation [103, 199, 200] or via fitting of the experimental saturation measurements to semi-empirical models [66, 98]. For the definition of relative permeability functions, semi-empirical equations in the form of power laws are typically used combined with experimental data [66]. The capillary pressure as a function of the material saturation is difficult to determine and therefore mostly considered constant at the boundary when significant [197]. A newly developed approach by Larsson, Wysocki, Rouhi and collaborators [134–137] addresses consolidation and flow of partially impregnated fibrous media, describing the intra and inter-tow resin flow and compaction.

A new approach is developed in the context of this work, which addresses the intra-tow impregnation of partially impregnated prepregs, under the influence of transient air evacuation taking place during OoA processing [12, 19, 30, 192]. The macroscopic air flow through the dry fibrous domain of the OoA prepreg under non-isothermal conditions is explicitly modeled using the governing Equation (2-42). The difference between the atmospheric pressure and the predicted air pressure in the dry tow drives the resin impregnation [19, 30, 192]. The model considers the presence of two immiscible fluids, air and resin, in the same fibrous domain, coupled through a moving boundary [12]. More details on the model development are discussed in Chapter 4.

## 2.4.2 Resin Front Propagation

Several researchers have simulated the impregnation of textiles with resin under vacuum pressure, in processes such as VARI [201, 202] and RFI [203] amongst others. In such processes it is assumed that before initiating the resin impregnation, the pressure inside the fibrous medium has reached equilibrium. For this purpose a constant vacuum pressure is used as boundary condition [201–203]. Though this assumption is realistic for most traditional vacuum processing scenarios, this is not always the reality when OoA processing is concerned [9, 33]. Since the OoA prepregs are partially saturated with resin, they are less permeable to air compared to textiles. As the vacuum distribution takes place through the dry fibrous domain of the tow, it is a slower process which is significantly influenced by its dimensions and the boundary conditions of the flow [12]. For this purpose Out-of-Autoclave process models incorporate the influence of air evacuation on the tow filling time [19, 28, 30, 132, 192, 204].

The transient air flow along the dry tows of OoA prepregs can lead to inhomogeneous vacuum pressure distribution, particularly in long parts. This can in turn cause the development of an inhomogeneous pressure difference responsible for resin flow and a heterogeneous tow impregnation and intra-tow porosity formation. Since OoA processing takes place inside an oven, the transient heat flow exasperates the local tow impregnation differences further. Therefore, tracing the position of the resin front during the tow saturation, assists in predicting the potential for air entrapment and designing a strategy for minimizing residual intra-tow porosity. The local evolution of a textiles saturation is typically simulated using commercial finite element packages based on the following three approaches:

- Fixed mesh methods

Mainly based on a combined finite element and control volume method FE/CV [85, 205, 206], or implicit FE simulations [207]. The degree of impregnation can be tracked via updating local saturation/fill factors in an RVE. These methods guarantee a good mass conservation, are fast, but have reduced accuracy in exact localization of the flow-front.

- Moving mesh methods

With the use of moving mesh approaches, the location of the flow front can be accurately predicted for simple geometries, guaranteeing very good mass conservation. When very complex fronts or part geometries are involved, this method becomes less attractive due to the high meshing effort, computational cost and reduced repeatability. The approach primarily relies on Arbitrary Eulerian Lagrangian formulations (ALE) [129, 208]. This approach is used to simulate the tow impregnation of OoA prepregs under transient heating conditions by the author [12]. More details are given in Chapter 4.

- Stochastic flow front propagation

Variations in the initial degree of impregnation of partially saturated prepregs and their influence on resulting laminate content after OoA processing, can be captured with a stochastic framework proposed by Helmus et al. [28, 184].

## 2.5 Heat Transfer through a Porous Medium

The energy equation for porous media saturated with one fluid, derived as a sum of the energy balance equations for the fluid and the solid phase per unit volume when the fluid and fibers have the same local average temperature, writes according to the local equilibrium model [4, 81, 82, 209]:

$$\underbrace{\langle \rho C_p \rangle_j \frac{\partial \langle T \rangle}{\partial t}}_{\text{Transient}} + \underbrace{\langle \rho C_p \rangle_j \langle \mathbf{v}_j \rangle \cdot \nabla \langle T \rangle}_{\text{Convection}} = \underbrace{\nabla \cdot (\langle \mathbf{k} \rangle_j \nabla \langle T \rangle)}_{\text{Conduction}} + \underbrace{\langle Q \rangle_j}_{\substack{\text{Energy} \\ \text{Dissipation}}} \quad (2-63)$$



The subscript  $j$  denotes the fluid phase which saturates the porous medium,  $\langle T \rangle$  is the average temperature,  $\langle \rho C_p \rangle_j$  the effective volumetric heat capacity at constant pressure,  $\langle \mathbf{v} \rangle_j$  the volume averaged fluid velocity (Darcy's velocity – Equation (2-14)),  $\langle \mathbf{k} \rangle_j$  the effective thermal conductivity and finally  $\langle Q \rangle_j$  the energy dissipation rate per unit volume. The dissipation rate per unit volume  $\langle Q \rangle_r$ , is the sum of two independent contributions given in Equation (2-64) [210]: the energy generation due to curing  $\langle \dot{R} \rangle$  (Equation (2-65)) and the viscous dissipation  $\langle \Phi_v \rangle$  given by Equation (2-66) [4, 81, 82].

$$\langle Q \rangle_r = \langle \dot{R} \rangle + \langle \Phi_v \rangle \quad (2-64)$$

$$\langle \dot{R} \rangle = (\phi_r \rho_r) \Delta H_R \frac{d\alpha}{dt} \quad (2-65)$$

$$\langle \Phi_v \rangle = n \langle \mathbf{v} \rangle_r \cdot \mathbf{K}_r^{-1} \cdot \langle \mathbf{v} \rangle_r \quad (2-66)$$

The volume of the porous medium saturated with resin is depicted as  $\phi_r$ ,  $n$  is the viscosity of the resin and  $\rho_r$  its density,  $\Delta H_R$  the total heat released by the reaction and  $d\alpha/dt$  the cure reaction rate,  $\mathbf{K}_r^{-1}$  is the inverse of the permeability tensor, while  $\langle \mathbf{v} \rangle_r$  expresses the volume average Darcy velocity. When the exothermic curing reaction of the resin is limited, the energy generation term can be neglected [4]. In most mold filling applications, the ratio of viscous heat generation to external heating is small (small Brinkman number) and therefore the viscous dissipation can also be neglected [81].

The effective volumetric heat capacity of the material at constant pressure  $\langle \rho C_p \rangle_j$ , is calculated according to Equation (2-67).

$$\langle \rho C_p \rangle_j = \phi_j (\rho_j C_{p_j}) + V_{f,j} (\rho_f C_{p_f}) \quad (2-67)$$

A wide range of models can be used to determine the effective thermal conductivity of porous media  $\langle k \rangle_j$ , saturated with a fluid expressed by the subscript  $j$  [211–213]. The most commonly utilized models for determining the conductivity of a homogeneous porous medium are the series model of Equation (2-68), the parallel model of Equation (2-69) and the geometric mean model of Equation (2-70) [211, 212]. The series model provides an upper bound, while the parallel or reciprocal average model provides a lower bound for the calculation of the effective thermal conductivity. According to Nield [212], the geometric mean is intermediate between the parallel and series model.

$$\langle k \rangle_j = \phi_j k_j + V_{f,j} k_f \quad (2-68)$$

$$\langle k \rangle_j = \frac{\phi_j}{k_j} + \frac{V_{f,j}}{k_f} \quad (2-69)$$

$$\langle k \rangle_j = k_j^{\phi_j} k_f^{V_{f,j}} \quad (2-70)$$



These equations formed the basis for the development of more elaborate expressions often linked to the microstructure of the porous medium, such as those reviewed by Bories and Prat [213]. The conductivity tensor is described by an  $n \times n$  matrix, in an  $n$ -dimensional problem [214]. Particularly in continuous fiber composites the conductivity of the medium is inhomogeneous and has a directionality according to the direction of the fibers. The series model is often used to calculate the composite material conductivity along the fiber direction [4, 211, 215]. The transverse conductivity of a continuous fibrous composite made of carbon fibers is generally lower than the in-plane conductivity, due to the reduced through thickness conductivity of the carbon fiber [4, 211, 215]. Due to the strong dependence of the through thickness conductivity on the fiber size, shape, spatial distribution and the wetting fluid type, a wide range of empirical equations are derived for different materials [211, 213, 214].

## 2.6 Summary and Discussion

Simulation of prepreg processing in the Autoclave typically addresses aspects related to the prediction of the part thickness and fiber volume fraction development due to resin bleeding [4, 6] void transport or growth primarily between plies or inside the resin [15, 16] and part warpage [6]. Nevertheless, the partial saturation of OoA prepregs involves additional challenges, such as the intra-tow porosity formation due to insufficient tow wetting [18]. Therefore phenomena such as the resin flow in fibrous media, air distribution and entrapment in the dry domain, traditionally investigated in LCM processing, transient heat application and heat transfer have to be additionally addressed in the context of OoA processing and simulation. Since the focus of this work is placed on modeling the intra-tow saturation of OoA prepregs, the literature review covered primarily state of the art methods used to model resin (Section 2.2) and air flow in fibrous media (Section 2.3) and their coupling (Section 2.4). The most significant literature of rheokinetics and air permeability characterization of OoA prepregs has also been covered (Sections 2.2.4 and 2.3.4).

A summary of relevant state-of-the-art models developed for Out-of-Autoclave processing is also included. Traditional flow and consolidation models are enhanced to include effects such as: transient air flow inside the dry channels of OoA prepregs [12, 19, 27, 30, 35, 57, 132, 184, 192], the non-isothermal temperature distribution considering all three phases present in the material (air, resin, fibers) [12] and the transient laminate consolidation of a partially impregnated material [28, 132, 136]. As the field of OoA process simulation is relatively new, enhancing the accuracy of the simulations will provide a better understanding of the process capabilities and limitations.



## 3 Characterization of the MTM 44-1 Prepreg

This Chapter presents key material characteristics of the Cytec MTM 44-1 prepreg, used as a basis for modeling the flow of resin and air through the tows, performed in Chapters 4 and 5. Focus is placed on characterizing the main properties influencing the flow of air and resin through the porous medium, such as the rheokinetics (viscosity and cure kinetics) and the prepreg's in-plane permeability to air. The tow morphology and the volume fraction of the prepreg's constituents and its impregnation scheme are determined using a range of methods presented in Section 3.1. All characterization methods discussed in this Chapter are based on established methodologies, adapted to capture the influence of the evolving prepreg microstructure during Out-of-Autoclave processing, to the properties of interest.

### 3.1 Morphological Characterization

As discussed in Section 1.4, the design of the initial impregnation pattern of an Out-of-Autoclave prepreg plays a decisive role in the production of parts with low porosity. The microscopic characterization of a prepreg enables the identification of a representative volume, which is the basis for describing the air and resin flow and therefore the intra-tow porosity formation physics.

Several methods can be used to define the volume fractions of all constituents and to quantify the initial state of impregnation. A detailed overview of methods applicable for this purpose are evaluated in the context of the Diploma thesis of S. Özer [S1]. The most promising techniques identified by Özer [S1], i.e. microscopy, CT and mercury porosimetry were pursued further in order to measure the thicknesses, initial porosity and fiber volume fraction of the MTM 44-1 prepreg. The initial degree of impregnation of the MTM 44-1 prepreg is compared against the degree of impregnation of three other Out-of-Autoclave prepreps based on a variety of reinforcements, characterized in the context of S. Özer's thesis [S1] (PW/5HS -Proprietary Prepreps, UD-Cycom 5320, 2x2 TW-MTM 44-1). Testing showed that no single method is capable for characterizing all properties of interest [S1]. The difficulty arises primarily by the fact that the prepreg shall be characterized at its uncured, flexible state. Therefore the resin and air can be locally distorted due to sample handling prior or during testing (embedding, clamping) as well as resin debris deteriorating the image quality and increasing the variability when standard image analysis techniques are utilized.

Optical microscopy provides insights on local features at a cross section (i.e. ply thickness, dimensions of tows, local porosity) and a good estimate of fiber volume fractions.

CT provides a global view of the volume of a prepreg stack. The air content of the prepreg can be determined via  $\mu$ CT due to sufficient contrast between the air and the rest of the composite. A high contrast allowing discrimination between carbon fibers and resin is not yet within the capabilities of industrial X-ray CT. The best-suited method to extract specific information from the material combined with information available in material data-sheets is used to determine the macroscopic volume content of all constituents. SEM is used to examine details of the impregnation pattern, while mercury porosimetry is used to provide an evaluation of the connected porous network available in the prepreg. These methods are reviewed in more detail in the following paragraphs.

### 3.1.1 Microscopy and Computed Tomography

The MTM44-1/CF5804A prepreg, is based on a  $285\text{g/m}^2$  2x2 twill weave carbon fabric which consists of 6k HTA5131 tows. The prepreg is partially impregnated with the MTM44-1 epoxy resin film, with a specified 40% resin weight content.

SEM is used to image the upper and lower planar surfaces of the prepreg, to derive information about the prepreg impregnation pattern and morphology of the tows. Fig. 3-1 reveals a single sided impregnation of the prepreg via a resin film application process. A continuous resin film has been applied only on one side of the fabric, with no ‘open channels’ nor dry locations which could enable air evacuation outside of the ply visible (Fig. 3-1(b)). The other side of the prepreg is mostly dry, with some resin concentrated in the gaps between warp and weft tows (Fig. 3-1(c)), while the air fills up all locations inside the fibers which are not impregnated by resin.

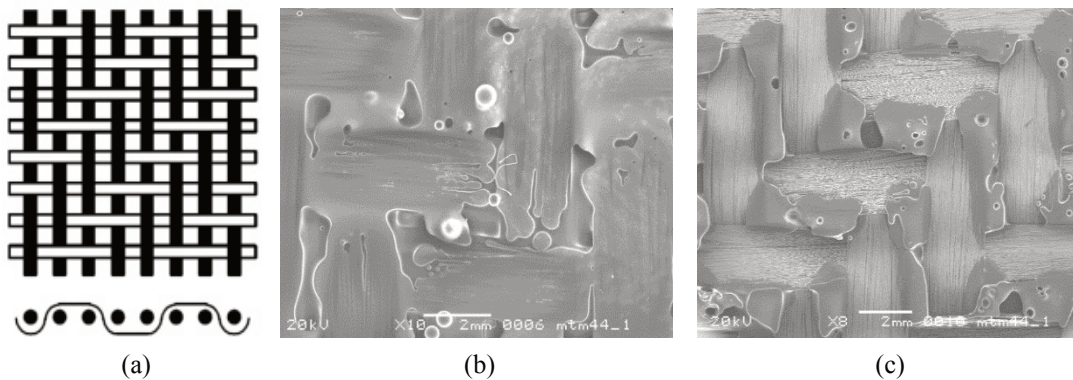


**Fig. 3-1: Planar views of (a) a 2x2 twill weave textile, consisting the basis of the MTM44-1 prepreg [216] (b) top side and (c) bottom side of the MTM44-1 prepreg**

A cross-sectional view of the prepreg using both optical microscopy and  $\mu$ CT was used to derive more information on the through thickness impregnation levels of the MTM 44-1 tows. Selected images of the tows are depicted in Fig. 3-2, where it can be seen that the resin is deposited as a layer on top of the fabric, impregnating the tow cross-section only minimally at the initial state of the material before vacuum is applied. Lo-

cations where a warp and a weft tow overlap are thicker and the tows are less impregnated as shown in the pictures with red and green circles, while locations where only one tow is present due to the weaving pattern, a higher percentage of resin is present (Fig. 3-2, cyan).

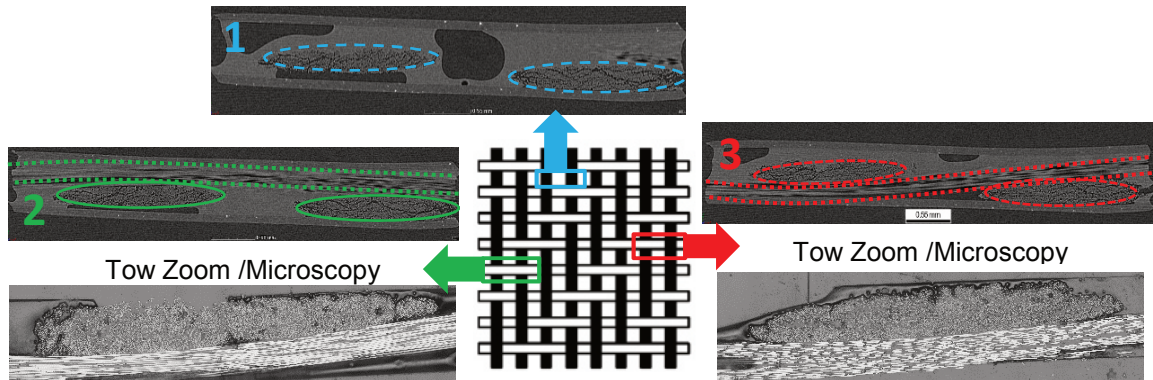


**Fig. 3-2: Cross-sectional views of the MTM44-1 prepreg at different locations and magnifications**

The images with the black background shown in Fig. 3-2 are generated at GE Global Research (by A. Singhal), on square 15x15mm samples using a Phoenix Nanotom  $\mu$ CT scanner at 60kV tube voltage, 130 $\mu$ A filament current and 4.3 $\mu$ m voxel size. The black color represents the air while the various shades of grey represent the resin and fibers. The edges of warp tows are more easily identifiable and are marked in Fig. 3-2 with ellipses. The weft tows crossing over and under the warp tows are more difficult to discern. The prepreg is imaged with the backing-paper (grey lines of constant thickness at the top and bottom of the material on 1-3). The images of single tows with the grey background were taken by the author and S. Özer [S1] using an Olympus BX41M optical microscope with a 20x times magnification and exposure time of approximately 15ms. Since the depth of field of the optical microscope is limited, embedding and polishing is required to acquire images with good resolution. The prepreg was kept at room temperature for a minimum of three weeks before embedding in a fluorescent epoxy resin (EpoFix), in order to achieve stiffening of the sample before polishing and reduce debris. In the images generated by microscopy the resin layer deposited on top of the prepreg is black and can be clearly identified from the embedding resin due to the difference in the reflectivity of light. The warp fibers appear as white dots, while the weft fibers are polished at an angle and are therefore larger and brighter. In the microscopy images it is generally easier to detect individual tows and the border between impregnated and non-impregnated tow, as well as acquire information on fiber volume fractions. The difference in color shades originating from the imaging of warp/weft fiber tows at various angles and the debris from polishing only partially cured resin make it difficult to use image thresholding techniques to automatically quantify intra-ply and intra-tow porosity from microscopy images. This becomes more challenging particularly when the material is imaged at 0 or 90° to the fibers.



### 3.1.2 Geometry Definition

As shown in Section 3.1.1 a textile based OoA prepreg is strongly heterogeneous and consists of three phases: the fibrous domain, resin and air. The heterogeneity of an OoA material goes beyond that of a conventional prepreg or even textile, due to the co-existence of all three phases. Each prepreg ply consists of the fiber-bed, which contains air at its initial state, the resin film layer deposited on top of the textile, while locations with pure resin can be identified between the tows. The first level of inhomogeneity is inherited by the structure of the textile, which influences the local resin deposition pattern of each single prepreg ply (Fig. 3-1 and Fig. 3-2). A second level of inhomogeneity is present when prepreg plies are stacked on top of each other as shown in Fig. 3-3 (b), since nesting of the plies and individual tows may occur.

The ‘tow equivalent’ consisted of two overlapping tows shown in Fig. 3-3 (a) is selected as a basis for OoA model development. The tow is simplified into a rectangular domain with clearly separated regions, one fibrous region saturated with resin and one with air and a pure resin layer on top, as shown in Fig. 3-3 (c). The ply stack imaged with microscopy in Fig. 3-3 (b) confirms the clear separation of the dry tows from the resin.

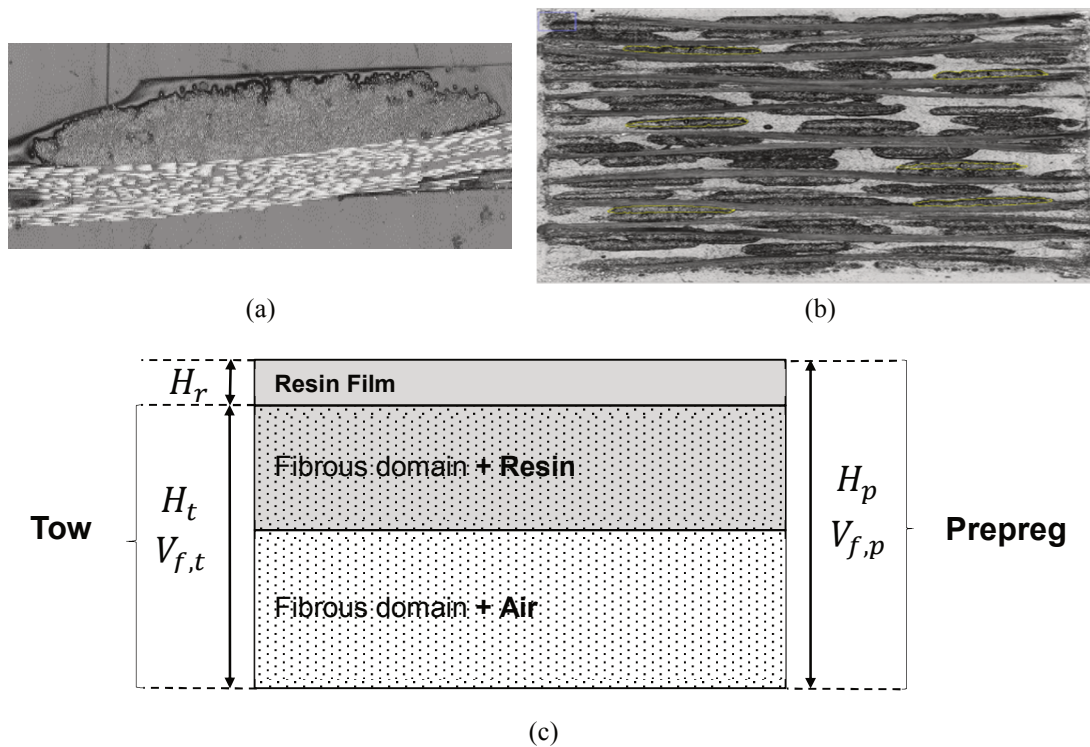


**Fig. 3-3: (a) Zoom of the ‘tow equivalent’ domain of the MTM 44-1 prepreg [S1] (b) cross-section of an MTM44-1 prepreg stack [S2] (c) simplified domain used as a basis for modeling**

Since the mass and weight content of all prepreg constituents is known at its initial state, the idealized ‘equivalent tow’ geometry shown in Fig. 3-3 and the ply, tow and resin thickness measurements allow the quantification of the volume fraction of all constituents, which is performed in detail in the following Section (Section 3.2).

## 3.2 Quantification of the Volume Fraction of all Prepreg Constituents at the Initial State

In this Section, a combination of measurements and information from material data-sheets are used to determine the macroscopic and the local volume content of all prepreg constituents. Mercury porosimetry is presented in more detail since it provides quantitative information on the size and distribution of the porous network and an estimate of the initial prepreg porosity. Finally, a characterization of local features is performed as a first step towards a mesoscopic model development.

### 3.2.1 Determination of Global Volume Fractions

Several techniques were investigated in order to determine the global volume fractions of the constituents of an MTM 44-1 prepreg ply at its initial state, prior to vacuum application. These techniques either provide local information on material thickness, or the volume fraction of its constituents, in a selected cross-section or volume. The following methods are selected for this purpose, presented in this Chapter:

1. Measurement of the thickness of a prepreg ply and theoretical calculations of its constituent's volume content, in combination with data sheet information.
2. Direct determination of air volume content via analysis of  $\mu$ CT images.
3. Direct determination of air volume content via mercury porosimetry.

To take into account the variability caused by handling of the uncured prepreg, an average value of the determined volume fraction of the constituents is calculated.

#### 3.2.1.1 Theoretical and Experimental Determination of the Volume Content of Constituents at the Ply Level

Equation (3-1) can be used to determine the fiber volume fraction  $V_{f,p}$  of a single prepreg ply once the ply thickness  $H_p$  at the initial state of the prepreg, the areal weight of the fiber bed  $aw_f$  and the fiber density  $\rho_f$  are known (considering  $N = 1$ ).

$$V_{f,p} = \frac{aw_f}{(\rho_f N H_p)} \quad (3-1)$$

While the fiber density (material data-sheet) and the areal weight are provided in material data sheets, the ply thickness of the prepreg  $H_p$  was determined with a caliper, microscopy and  $\mu$ CT. A summary of the average ply thickness, the standard deviation and error of each measurement is given in Tab. 3-1.

**Tab. 3-1: MTM 44-1 ply thickness and measurement error (using a range of methods)**

Measurement Method	# Plies	$\overline{H_{p0}}$ (mm)	$d_{H_{p0}}$ (mm)	# Samples	$e_{H_{p0}}$ (mm)
Optical Microscope	1	0.43	0.02	4	0.01
Stereoscope	1	0.46	-	1	-
$\mu$ CT	1	0.45	0.02	9	0.01
Caliper	5	0.47	0.02	25	<0.01
Caliper	18	0.43	0.01	21	<0.01
Average	-	0.45	0.02	60	0.01

The standard deviation and the measurement error are determined via Equations (3-2) and (3-3), where  $N$  is the amount of measurement points considered.

$$d_x = \sqrt{\frac{\sum_{i=1}^N (x_i - \bar{x})^2}{N}} \quad (3-2)$$

$$e_x = \frac{d_x}{\sqrt{N}} \quad (3-3)$$

Since the areal weight of the prepreg ( $aw_p$ ) and its resin content by weight ( $W_r$ ) is known, the resin areal weight can be calculated via Equation (3-4). Subsequently Equation (3-5) can be used to calculate the resin volume fraction  $V_{r,p}$  of a single MTM 44-1 ply, similarly to the fiber volume content.

$$aw_{r0} = W_r \cdot aw_p \quad (3-4)$$

$$V_{r,p} = \frac{aw_r}{\rho_r H_p} \quad (3-5)$$

Finally the air content or porosity of the prepreg ply is calculated via Equation (3-6), applying conservation of mass in the prepreg domain.

$$\phi_p = 1 - (V_{f,p} + V_{r,p}) \quad (3-6)$$

The material properties are calculated as an average of three MTM 44-1 prepreg batches. The variability in the determination of the weight and weight content of all raw materials is captured by means of standard deviation within one batch (reported as individual) and the standard error of multiple batches is also reported (average). The definition of upper and lower boundaries can be used as a basis for evaluating the volume contents resulting from the other two measurement methods. For comparison purposes all material properties and their standard error are listed in Tab. 3-2. The last decimal of the density is considered to vary. The error of the resin areal weight ( $e_{aw_r}$ ) is not provided in the data



sheet and was calculated using the error propagation methodology according to Equation (3-7), assuming the areal weight of the prepreg ( $aw_p$ ) and its resin content by weight ( $W_r$ ) are independent properties.

$$e_{aw_r} = aw_r \cdot \sqrt{\left(\frac{e_{W_r}}{W_r}\right)^2 + \left(\frac{e_{aw_p}}{aw_p}\right)^2} \quad (3-7)$$

**Tab. 3-2: Summarized properties of three MTM 44-1 prepreg batches**

	$aw_p$ (g·m <sup>-2</sup> )	$\rho_f$ (g·cm <sup>-3</sup> )	$aw_f$ (g·m <sup>-2</sup> )	$\rho_r$ (g·cm <sup>-3</sup> )	$W_r$ (%)	$aw_r$ (g/m <sup>2</sup> )
Mean	478	1.76	284	1.18	41	196
$e_x$	30	0.01	10	0.01	2	16
$e_x$ (%)	6	0.59	4	0.85	5	8

Once all inputs are determined, the constituent volume fractions of the prepreg are calculated from Equations (3-1), (3-5) and (3-6). The results are summarized in Tab. 3-3.

**Tab. 3-3: Theoretical volume content of the MTM 44-1 prepreg constituents (via Method 1)**

	$V_{f,p}$	$V_{r,p}$	$\phi_p$
Mean (%)	36.0	36.7	27.4
$e_x$ (%)	5.5	2.0	5.8

The error propagation method is used to calculate the error of the mean. Equations (3-8) and (3-9) are used for the calculation of the error in the resin and fiber volume fractions.

$$e_{V_{f,p}} = V_{f,p} \cdot \sqrt{\left(\frac{e_{aw_f}}{aw_f}\right)^2 + \left(\frac{e_{\rho_f}}{\rho_f}\right)^2 + \left(\frac{e_{H_p}}{H_p}\right)^2} \quad (3-8)$$

$$e_{V_{r,p}} = V_{r,p} \cdot \sqrt{\left(\frac{e_{aw_r}}{aw_r}\right)^2 + \left(\frac{e_{\rho_f}}{\rho_f}\right)^2 + \left(\frac{e_{H_p}}{H_p}\right)^2} \quad (3-9)$$

Since the air volume content of the prepreg at its initial state is determined through the calculation of the fiber and resin volume contents, variability in these properties directly affects the porosity. The error of the mean of the initial prepreg porosity is determined according to Equation (3-10).

$$e_{\phi_p} = \sqrt{\left(\frac{e_{V_{f,p}}}{V_{f,p}}\right)^2 + \left(\frac{e_{V_{r,p}}}{V_{r,p}}\right)^2} \quad (3-10)$$

### 3.2.1.2 Porosity Determination via Image Analysis

The  $\mu$ CT images of the MTM 44-1 prepreg cross-section used for thickness determination are also used here to determine the air volume fraction included in the material via image segmentation. The microscopy images were not used for this purpose as their quality was insufficient for reliable segmentation of the prepreg domain.

The simplest method of image segmentation, thresholding, essentially each pixel of the image is represented by a binary 1 or 0. These two levels are defined below and above a threshold value, through a histogram which shows the amount of pixels at each intensity level of the image. The Image J (Fiji) software was used for this analysis. All pictures were transformed into 8-bit grey scale, while a median filter was applied in order to reduce the influence of a speckle pattern visible in all images (de-speckle). Since the contrast between the intensity of fibers and resin was not sufficient for separate thresholding of the two phases, the de-speckling filter was used to smoothen the intensity differences and enable segmentation of both as one material (prepreg skeleton). Images were acquired without removing the backing paper of the prepreg, the resin deposited on top of the tows instead of complying with the shape of the fibers sticks to it, making the identification of the prepreg edges difficult. Due to this limitation, eight out of the nine cross-sections are considered. For the remaining sample, the prepreg edges are carefully selected (manually) and the area outside the prepreg domain is deleted. The variability in the background intensity is reduced and a clear peak, which represents the intensity of the prepreg domain can be discerned and segmented.

Image J offers a variety of thresholding techniques for automatic thresholding, while the operator can also adjust the thresholding levels manually. In this case all thresholding methods have been tested, with the Default (variation of the IsoData algorithm) and Otsu methods delivering results very close to each other reliably [217]. Both procedures rely on performing segmentation operations through a comparison of the intensity variance of the segmented phase, against the average intensity of the image. Otsu's algorithm searches for the threshold that minimizes the intra-class variance, defined as a weighted sum of variances of the two classes [218]. The IsoData procedure divides the image into object and background by taking an initial threshold and computes the averages of the pixels above and at or below the threshold. Once the averages of the values are computed, the threshold is incremented and the process is repeated until the threshold is larger than the average [219]. Finally, the percentage of the segmented area is calculated against the selected area of the prepreg.

An example of an image segmented with the Otsu algorithm is given in Fig. 3-4.

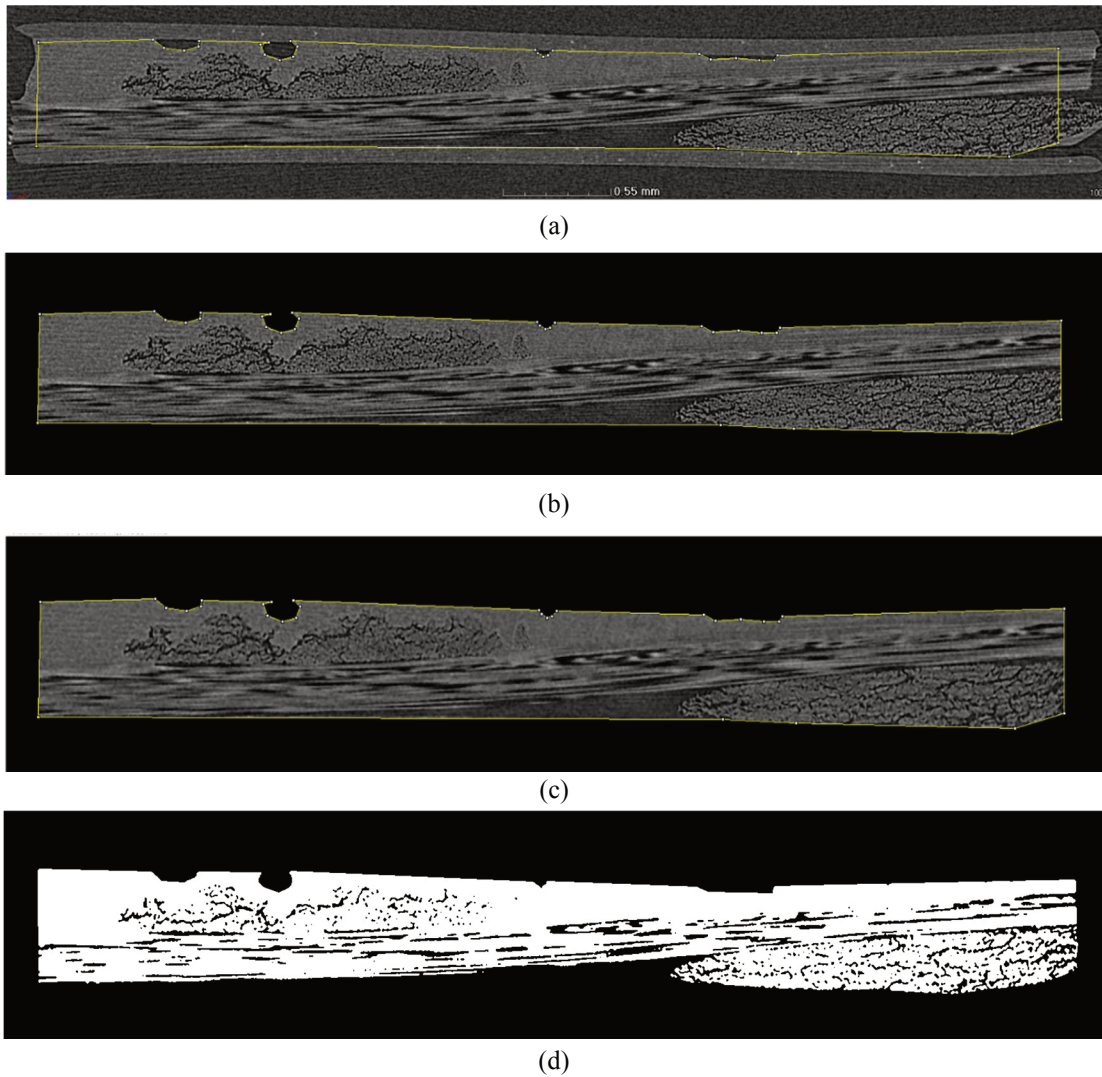


**Fig. 3-4: Image analysis process used for global porosity determination**

(a) Prepreg domain selection (b) deletion of part of the image outside of the domain of interest (c) image after de-speckling (d) image after segmentation.

The average porosity determined from the analysis of eight sections, was found to be 0.335 (or 33.5%), with a standard deviation of 0.036 (or 3.6%), as summarized in Tab. 3-4. A variety of segmented images and corresponding porosities calculated, are summarized in Appendix b.

**Tab. 3-4: MTM 44-1 ply porosity determined via segmentation of the  $\mu$ CT images**

$\phi_p$ (%)	$d_{\phi_p}$ (%)	$e_{\phi_p}$ (%)	Sample #
33.5	3.6	1.3	8

### 3.2.1.3 Porosity Determination via Mercury Porosimetry

Mercury porosimetry is a technique broadly used to characterize the dimensions of the network of porous and granular materials. Despite the broad use of this technique in other fields, it has not found its place in the field of composites.

The most prominent publication in the field of composite materials, discussing the potential of this method in characterizing the porosity in prepregs can be traced back in the 80s [220]. Thorfinnson and Biermann have used mercury porosimetry to characterize the porosity and degree of impregnation of prepregs and to highlight the benefits of partial impregnation [220]. Since mercury is a non-wetting liquid, it can be forced into a porous structure under controlled pressures. From the pressure versus the intrusion volume data (calculated directly by the instrument), the pore volume and the pore size can be determined using the Washburn Equation (3-11), if a cylindrical pore geometry is assumed [221].

$$\Delta P = \gamma \left( \frac{1}{r_1} + \frac{1}{r_2} \right) = \frac{2\gamma \cos\vartheta}{r_{pore}} \quad (3-11)$$

The pressure difference across the curved mercury interface  $\Delta P$ , is characterized by the positions  $r_1$  and  $r_2$ , which describe the curvature of mercury's interface to the pore with radius  $r_{pore}$ . The surface tension of mercury  $\gamma$  and the contact angle between the material measured and mercury  $\vartheta$ , have to be taken into account as well. A surface tension of  $0.485 \text{ N}\cdot\text{m}^{-1}$  and a contact angle of  $120\text{-}140^\circ$  between the material and mercury, are typically used for most materials tested at room temperature [221]. The pressure is inversely proportional to the size of the pores. Therefore the greater the applied pressures, the smaller the intruded and measured pores. The main benefit from utilizing porosimetry is its applicability for a wide range of pore sizes in the range of  $3\text{nm} - 400\mu\text{m}$ , able to be measured within a few hours in a single test [222, 223].

Dr. Robin Beddoe tested several OoA prepregs with different textile architectures (Cycocom 5320 -UD, Proprietary 5HS, PW, MTM 44-1 based on a 2x2 Twill weave) using an Auto Pore porosimeter by Micrometrics at the Center of Building Materials and Material Testing of the Technical University of Munich.. Primary aim of the activity is the characterization of the dimensions of the porous network, available to transport gas at the initial state of the prepregs. The volume of air contained in the prepreg, is determined in combination with a pycnometer and a precision balance.

A prepreg sample cut into 30cm long stripes with a maximum width of 1.5cm and rolled in order to fit into the dimensions of the intrusion chamber (dilatometer) is used to perform the test. A schematic of the intrusion chamber is given in Fig. 3-5 (a), while a typical intrusion curve generated by the porosimeter is given in Fig. 3-5 (b). The samples used weigh between 0.7-2.5g, within 1mg accuracy.

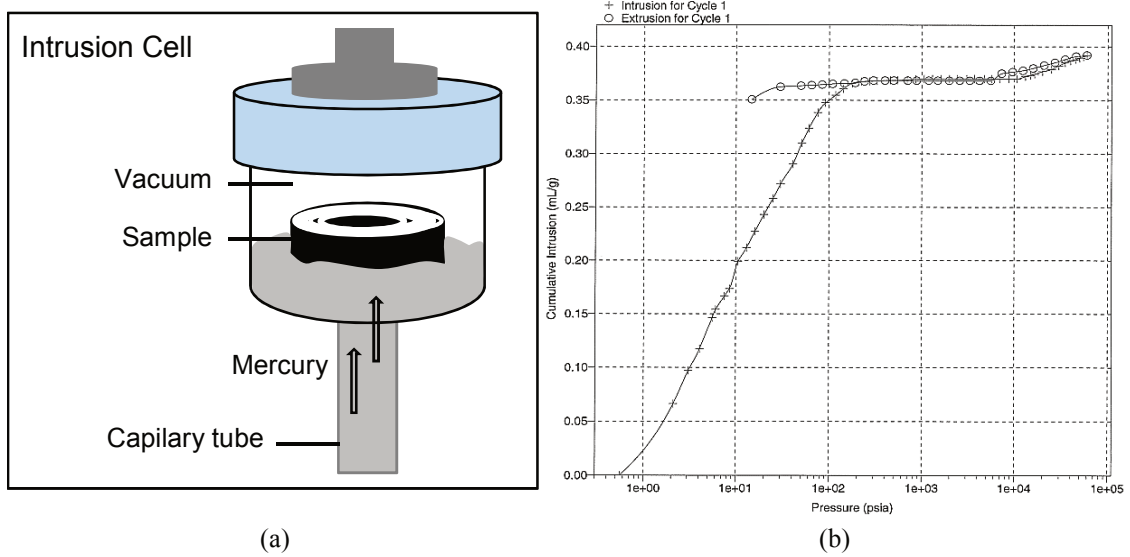


**Fig. 3-5: (a) sketch of a mercury penetrometer and (b) typical curve acquired during prepreg porosity measurements using mercury porosimetry**

The measurement procedure is summarized in the following steps:

- The sample ( $m_B$ ) and intrusion cell weights ( $m_{c0}$ ) are measured before the test.
- The sample is placed in the penetrometer, while mercury is allowed to enter the cell until it fills up, with low pressure applied on the sample. The sum of the weights of the cell, the sample and the mercury used to fill up the cell is therefore known ( $m_{tot}$ ). The bulk mercury weight is determined via Equation (3-12).

$$m_{Hg} = m_{tot} - (m_{c0} + m_B) \quad (3-12)$$

Its volume can easily be determined from its density, which is known. This volume reflects the bulk volume of the prepreg material  $v_B$ , which consists of fibers  $v_{f,p}$ , resin  $v_{r,p}$  and air  $v_{a,p}$ , given in Equation (3-13).

$$v_B = v_{f,p} + v_{r,p} + v_{a,p} \quad (3-13)$$

The bulk density of the prepreg can be determined via Equation (3-14).

$$\rho_B = \frac{m_B}{v_B} \quad (3-14)$$

- In a following step, more mercury is pressed in the cell in order to intrude the open pore network of the material within a wide pressure range ( $10^4$  Pa up to  $\sim 10^8$  Pa). The volume of mercury required in order to fill all accessible pores ( $v_I$ ) can be determined from a Pressure vs Cumulative Intrusion Volume plot at  $P_{max}$ . An example of such curve is shown in Fig. 3-5(b). The bulk volume of the prepreg sample, minus the volume of mercury intruded into the pores ( $v_I$ ) provide

the skeletal volume. The skeletal volume reflects the volume of the prepreg occupied by resin and fibers. If the prepreg contains pores with no access for mercury to intrude ('closed'), the volume of those pores is also included in the skeletal volume. The skeletal density of the prepreg ( $\rho_S$ ) is calculated from Equation (3-15) (in a similar fashion as in Equation (3-14)).

$$v_S = v_B - v_I = v_{f,p} + v_{r,p} \quad (3-15)$$

- The difference between the bulk and the skeletal volume of the prepreg is given by Equation (3-16) and can be used to calculate the volume of open pores.

$$v_{a,p} = v_B - v_S = v_I \text{ at } P = P_{\max} \quad (3-16)$$

- Finally, the percentage of open pores intruded by mercury over the bulk volume is the porosity of the material, according to Equation (3-17).

$$\phi_p = \frac{v_{a,p}}{v_B} = \frac{v_I}{v_B} \quad (3-17)$$

A comparison of the porosity and pore distribution of four OoA prepregs with different textile architectures and impregnation patterns is performed in Fig. 3-6. Preliminary porosimetry results for all but the MTM 44-1 prepreg are included in [S1].

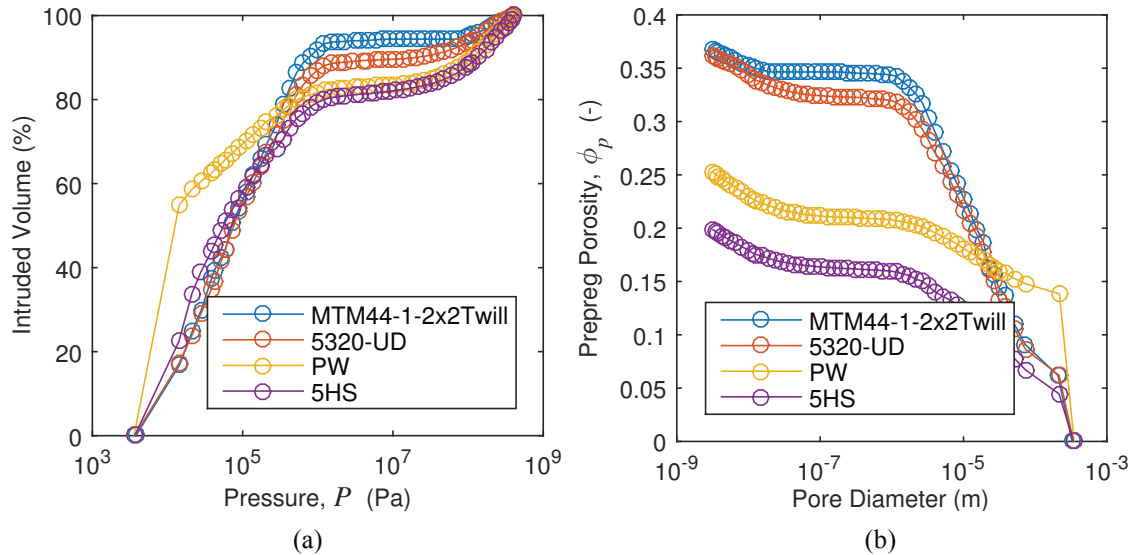


**Fig. 3-6: Mercury porosimetry curves for all OoA prepregs**

- (a) Percentage of cumulative intruded mercury volume plotted against the applied pressure.  
 (b) Prepreg porosity correlated with measured pore diameters.

The pressure required to force mercury inside the open pores is plotted against the percent of intrusion achieved in Fig. 3-6(a). The pore diameter is plotted against the measured porosity of all prepregs in Fig. 3-6(b), for pores with sizes of mm down to nm. The larger pores reflect the air between tows or the gaps in the weaving pattern (mm), while



the smaller porosities reflect the air entrapped between the individual fibers within a tow ( $\mu\text{m}$ - $\text{nm}$ ). The slope of the yellow curve in Fig. 3-6(a) shows that a high percentage of mercury intrusion is achieved at relatively low pressures, at large pore diameters (Fig. 3-6(b)). This observation was confirmed after imaging the material using SEM, pictures depicted in Fig. 3-7, where the PW prepreg tows of the proprietary material depicted, have a high level of impregnation, though gaps can be identified in the relatively ‘loose’ textile pattern. Its porosity content was measured to be 0.252 or 25.2%.

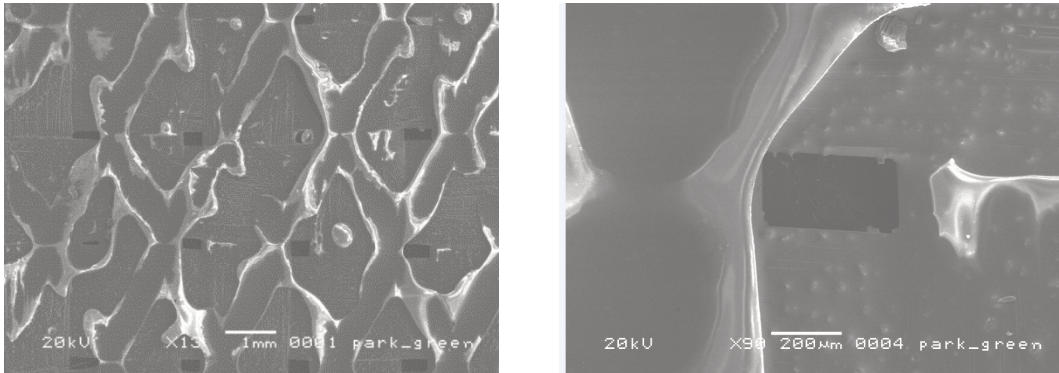


**Fig. 3-7:** SEM pictures of the proprietary PW OoA prepreg

The proprietary prepreg based on a 5-HS textile contains 0.199 or 19.9% porosity at its initial state, though its porosity is smaller. Approximately 0.367 or 36.7% and 0.361 or 36.1% of the MTM 44-1/2x2 TW and Cycom 5320/UD prepreg volumes respectively are pores. All prepregs, apart from the one based on the PW textile, have a similar distribution of pore dimensions. The porosity of the MTM 44-1 prepreg determined via porosimetry is higher than the theoretically calculated porosity and the porosity determined via image segmentation. A potential reason for the deviation may be explained by the volumetric expansion of the prepreg during mercury intrusion, due to the lack of resin backing-layers from both sides of the prepreg. In the literature, the compressibility of a material is a common source of error in the measurement [221]. Nevertheless, mercury porosimetry is a promising technique, as it can offer quantitative information of a prepreg’s impregnation state and porosity distribution, particularly when materials with a two-sided impregnation are concerned. Due to limited availability of the mercury porosimeter, it has not been possible to perform a series of tests to establish an understanding of the measurement repeatability and the associated uncertainty in the porosity determination, nor to establish the inherent variability of each material.

### 3.2.1.4 Summary

The amount of pores included in the MTM 44-1 prepreg at its initial state was determined using three methods: theoretical calculations based on material data-sheet properties and ply thickness measurements, direct segmentation of images acquired via  $\mu\text{CT}$  and mercury porosimetry.

The summary of all prepreg porosity results are presented in Fig. 3-8 with the measurement error included where available. The red lines represent the mean, minimum and maximum of the theoretically determined prepreg porosity.

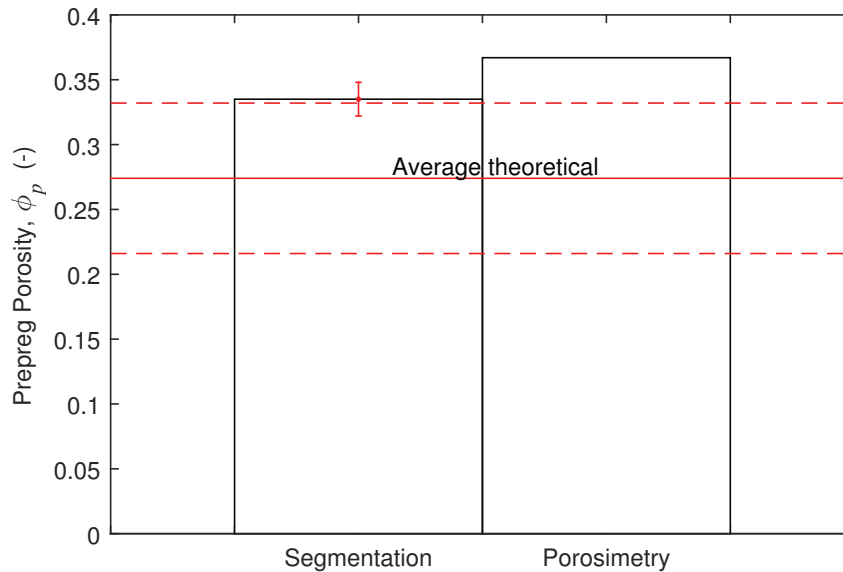


**Fig. 3-8: Porosity of an MTM 44-1 ply determined via image segmentation and porosimetry**

The results are compared against the theoretically calculated porosity volume content, with the continuous red line depicting the average theoretical porosity  $\phi_p$ , while the dotted lines the minimum and maximum prepreg porosity determined.

In this Chapter the significant amount of variation inherent to the uncertainty in the determination of the initial volume fractions of the material is highlighted. The variations originate from the variability of the measurement techniques (image segmentation) or handling differences, leading to sample deformation before and during the measurement influencing the results. Taking this into account the porosity determined via image segmentation agrees well with the theoretical porosity, while the porosity determined via porosimetry is higher. It can be concluded that the MTM 44-1 prepreg has a high initial porosity content, with  $\phi_p$  ranging between 0.274 (or 27.4%) and 0.367 (or 36.7%).

### 3.2.2 Determination of Local Volume Fractions

This Chapter presents the process used for the determination of the tow dimensions of the MTM 44-1 prepreg, initially only saturated with air. Image segmentation techniques are used to determine the local fiber and air volume content of the tows.

The images generated via  $\mu$ CT were analyzed using thresholding and particularly the IsoData algorithm. The microscopy images were analyzed using several segmentation techniques in the context of the Term Project of T. Glockner [S2]. The most repeatable method for defining fiber volume content from microscopy images was found to be the application of a Gaussian Blur filter, in combination with a noise reduction filter. Subsequently an algorithm able to identify high intensity pixels within a specified tolerance



range was used (Find Maxima) [S2]. The Find Maxima algorithm creates a binary image of the same size as the original by marking one segmented particle per maximum identified with a cross [217]. In our case these particles are the single fibers inside each tow. Using Image J, the amount of points where a maximum is detected can be identified and counted. The number of fibers measured with image analysis and the theoretical number of filaments present in a 6K tow assist in the reduction of outliers in the measurement. The geometrical information of a tow are usually not available in material data-sheets. Therefore after testing various shape options [S2], an ellipse with major axis  $l_e$ , minor axis  $h_e$  and the cross-sectional area  $A_t$  fitted to each tow shown in Fig. 3-9(a), for eight tows imaged with microscopy and ten tows imaged with  $\mu$ CT. The results are summarized in Tab. 3-5.

**Tab. 3-5: Area and dimensions of MTM44-1 tows fitted to an ellipse**

Properties		Microscopy				$\mu$ CT			
Symbol	Unit	Mean	$d_x$	# Tows	$e_x$	Mean	$d_x$	# Tows	$e_x$
$A_t$	mm <sup>2</sup>	0.45	0.02	8	0.01	0.43	0.04	10	0.01
$l_e$	mm	2.32	0.08	8	0.03	2.17	0.06	10	0.02
$h_e$	mm	0.25	0.02	8	0.01	0.25	0.02	10	0.01

Once the area of the tow is defined and the fibers counted, the local fiber volume fraction can be determined directly from Equation (3-18).

$$V_{f,t} = \frac{N \cdot (\pi R^2)}{A_t} \quad (3-18)$$

The  $N$  reflects the number of single fibers in the tow (in this case 6K or 6000 filaments [224, 225]),  $R$  the fiber radius (3.5 $\mu$ m for the Tenax HTA 40 E13/ Tenax HTA 5131 fibers [224]) and  $A_t$  the cross-sectional area of the tow.

Since tows consist solely of air and fibers, they can be represented as a two phase porous domain, with the local porosity volume content calculated from Equation (3-19).

$$\phi_t = 1 - V_{f,t} \quad (3-19)$$

Examples of all image analysis steps used in the tows are shown in Fig. 3-9. The results of the theoretical and experimentally determined fiber volume fractions are summarized in Tab. 3-6. The average fiber volume fraction of the tows is approximately 50%, when all tows and calculation methods are considered. It can be concluded that the difference between the fiber volume fraction assuming  $N$  fibers are included in the tow ellipse and the fiber volume fraction determined via image analysis is small, if the standard deviation of the measurement is taken into account.

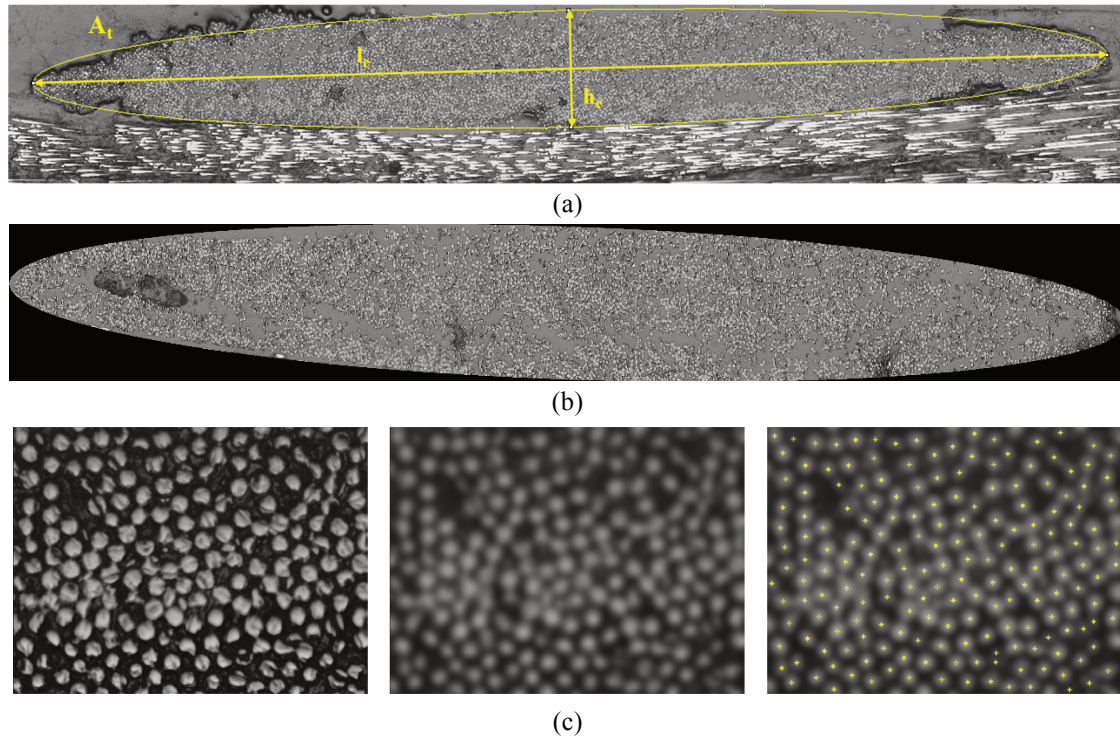


**Fig. 3-9: Microscopy images of the MTM 44-1 prepreg and image analysis**  
 (a) Selection of tow using an ellipse (b) erasing background to analyze the tow domain (c) zoom on the fibers to demonstrate the impact of Gaussian blur and Find Maxima [S2].

The fiber volume fraction determined via image analysis is in both cases lower than the one calculated. This difference originates from the difficulty of accurately detecting the tows edges. The idealization of the tow as ellipse occasionally leaves fibers outside the ellipse uncounted and the local presence of resin and impurities inside the tow domains masks the presence of some fibers as well.

**Tab. 3-6: Local fiber volume fraction of the MTM 44-1 tows**

Properties			Microscopy				$\mu$ CT			
Method	Symbol	Unit	Mean	$d_x$	Tows	$e_x$	Mean	$d_x$	Tows	$e_x$
Image	$V_{f,t}$	%	49	2	8	0.7	46	3	10	0.9
	$\phi_t$	%	51	2	8	0.7	54	3	10	0.9
Theory	$V_{f,t}$	%	52	3	8	1.1	54	2	10	0.6
	$\phi_t$	%	48	3	8	1.1	46	2	10	0.6

## 3.3 Prepreg Characterization

The method used to determine the MTM 44-1 prepreg permeability to air is presented in this Section. The air permeability is characterized at different prepreg impregnation levels, while regression is used to determine the equation which better fits the permeability as a function of the prepreg porosity. The intrinsic permeability of the tow is determined via the equations proposed by Gebart [140], assuming the initial volume fraction of the prepreg remains constant throughout the process. Both properties play a decisive role in the distribution of the pressure inside the laminate during OoA processing.

### 3.3.1 Permeability to Air

The in-plane air permeability of the MTM 44-1 prepreg  $K_{a,xx}$  is characterized in order to quantify its capacity to transport air. The air permeability of the prepreg is measured using a transient dropping pressure method (DPM) initially proposed by Hou et al. [36] for the characterization of textile reinforcements. In this approach the error between the calculated and measured pressure is minimized and used for the calculation of the effective permeability of the prepreg [36]. This work was performed in the context of a scientific exchange at Ecole Centrale de Nantes in collaboration with Marie Devisse, Julie Hemmer and Hermine Tertrais [SN1]. All measurements are performed at room temperature, after conditioning a 5-ply prepreg stack at various temperatures under vacuum. The in-plane air permeability of the MTM 44-1 prepreg,  $K_{a,xx}$  is calculated for a range of porosities  $\phi_p$ , which are obtained via conditioning the material at a range of temperatures. The equation resulting from fitting the in-plane air permeability as a function of the prepreg porosity is used as an input in the OoA process simulation developed in the context of this work, which is presented in detail in Section 4.2.

#### 3.3.1.1 Measurement Set-up

The test set-up developed by Hou et al. [36] was replicated at the Research Institute in Civil Engineering and Mechanics (GEM) of Ecole Centrale de Nantes. A picture of the test-bench and the test cavity set-up used for the measurement of the in plane air permeability of the MTM 44-1 prepreg is given in Fig. 3-10. The set-up consists of a metal base plate and a transparent Plexiglas lid. The base plate includes fitting for the installation of pressure sensors and vacuum inlets/outlets are drilled at several locations. Two of which are used in the context of this work, one close to the vacuum inlet before the stack and one after. The holes not in operation for each experiment are sealed with a custom plug fitting. The prepreg stack is placed in the area between the two pressure sensors, while the other two edges of the prepreg are sealed with tacky tape. O-rings are placed at the front and back side of the cavity, which assists with the sealing of the preform and the definition of a reduced area for air flow and a constant cavity thickness. The prepreg is placed in the cavity as shown in Fig. 3-10(b), with the backing paper of the top and bottom ply in place, in order to avoid contamination of the mold surfaces

with resin. Steel shims are used to define the cavity thickness of thicker stacks. To avoid unwanted cavity deformations during the test, four steel bars are evenly distributed and fixed on top of the Plexiglas and sealed with the rest of the set-up.

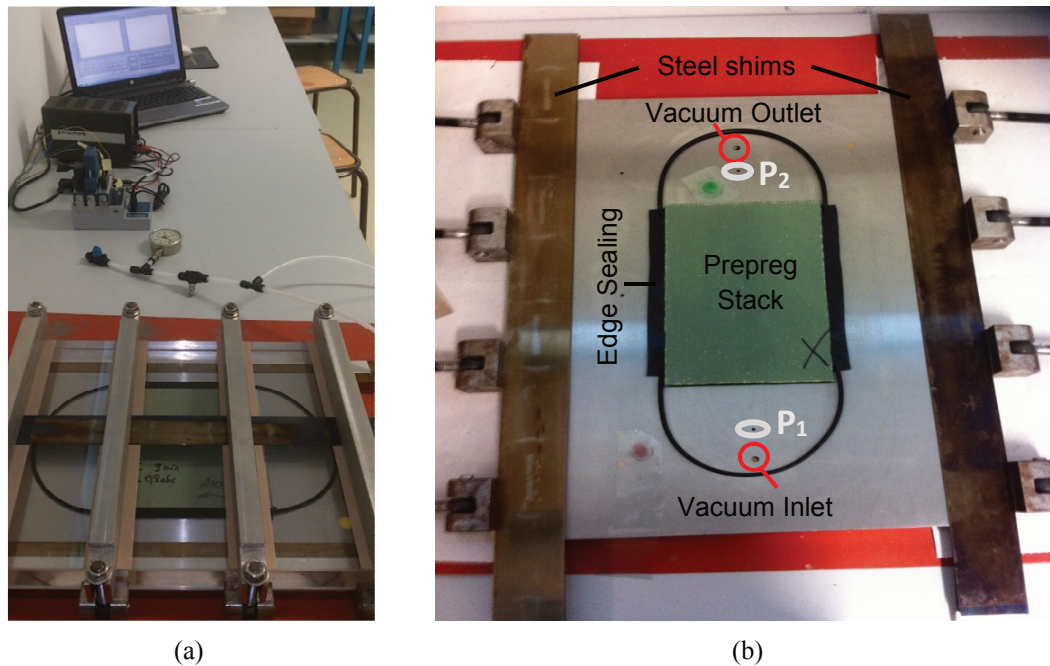


**Fig. 3-10: Experimental test-bench used for the determination of the in-plane air permeability**  
 (a) General view of the set-up during a measurement (b) placement of the prepreg sample inside the test-cavity and test-cavity lay-out [SN1].

The sensors used for pressure acquisition (Kistler) can measure absolute pressure in the range of 0-2 bar ( $0-2 \cdot 10^5$  Pa). They are powered by a DC supply delivering 20 mA and 22V, with a current output of 4 and 20 mA. The pressure and temperature signals are registered via a cDQ-9174 data acquisition system from National Instruments. A Lab-View program acquires the signals and converts them through a calibration routine to pressure read-outs, each registered in a separate ASCII file. All measurements are performed at room temperature, while the exact temperature is measured and used to calculate and adjust the air viscosity as necessary.

### 3.3.1.2 Theoretical Approach and Sample Preparation

To calculate the 1D in-plane permeability of the prepreg to air using a transient measurement concept based on the approach of Hou et al. [36], it is considered that the flow of air through the prepreg is laminar, it is in the viscous regime and gravity is neglected. Equation (2-42) can be used for the permeability determination, combining the conservation of mass for air from Equation (2-39) with Darcy's law (Equation (2-40)) and the ideal gas law at isothermal conditions and constant volume (Equation (2-37)). The set-up can be either to perform both dropping (DPM) and raising pressure experiments (RPM). In this study, the dropping pressure method is selected, as it better reflects the condition of pressure distribution in the prepreg during OoA processing.



The initial and boundary conditions for the dropping pressure measurement expressed for pressure ( $P_{gas}$ ) are given in Equations (3-20) and (3-21) respectively [36]. Since the inlet pressure ( $x=0$ ) is logged during the experiment by a data acquisition software ( $P_1$  - Fig. 3-11), it can be used as a boundary condition in COMSOL Multiphysics (Equation (3-21) at  $x=0$ ). A schematic presentation of the principal is given in Fig. 3-11.

$$IC \quad P_{gas}(x, t = 0) = P_{atm} \quad (3-20)$$

$$at \ x = 0 \rightarrow P_{gas}(t) = P_1(t)$$

$$BC \quad at \ x = L \rightarrow \frac{K_{a,xx}}{\mu_a} (P_{gas} \nabla P_{gas}) + \frac{V_m}{A_m} \frac{\partial P_{gas}}{\partial t} = 0 \quad (3-21)$$

Where  $P_{gas}$  the air pressure,  $P_{atm}$  the atmospheric pressure (approximately  $10^5$  Pa),  $\mu_a$  the viscosity of air,  $A_m$  the area of the cavity excluding the prepreg (initially empty and fills with air only during the test) and  $V_m$  the volume of air trapped in the initially empty cavity,  $L$  the length of the prepreg sample measured and finally  $K_{a,xx}$  the effective in-plane permeability of the prepreg to air determined using this method.

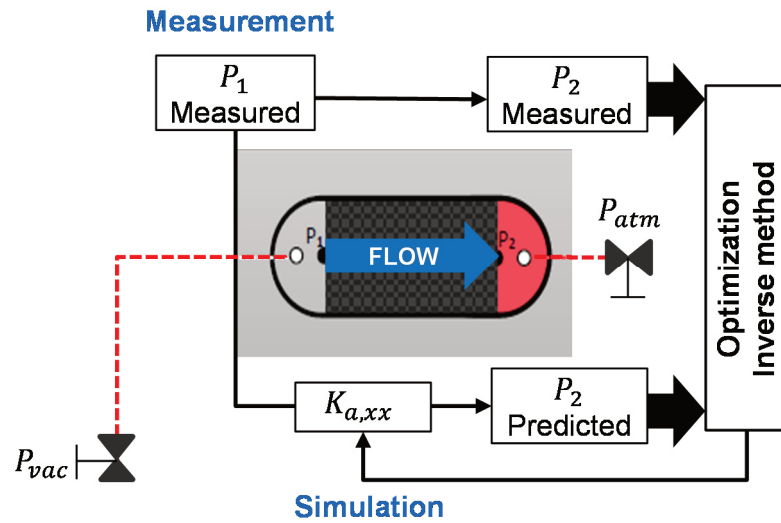


Fig. 3-11: Schematic of the approach used to determine the MTM 44-1 air permeability

The governing equation, initial and boundary conditions and the input parameters:  $A_m, V_m, L, V_{f,p}, \mu_a$  are implemented in COMSOL Multiphysics, where the transient isothermal air flow through the prepreg is considered in order to calculate the pressure at the end of the sample ( $x=L$ ). To perform this calculation, an initial guess of the expected permeability of the medium shall be made. Consecutively, an algorithm implemented in Matlab calculates the permeability of the prepreg via minimizing of the error between the theoretical and simulated pressures according to Equation (3-22) [36].

$$e_{P_{gas}} = \frac{1}{P_{atm}} \sqrt{\frac{1}{M} \sum_i^M (P_{gas_{exp}}^i - P_{gas_{sim}}^i)^2} \quad (3-22)$$

Where  $i$  stands for the number of points interpolated out of a total number of points  $N$ , while  $P_{gas_{exp}}^i, P_{gas_{sim}}^i$  are respectively the experimental and simulated pressures.

The samples consisted of five plies with a size of 210mm x 200mm. Air flow took place along the long side of the sample, which coincided with the warp axis of the textile. Prior to testing, each sample was kept under vacuum, at room temperature, for 10min. Consecutively the sample was transferred to a convection oven where it was heated for another 10min at temperatures between 40-100°C under vacuum, as shown in Fig. 3-12. After temperature conditioning, vacuum was released and the samples were kept at room temperature. Once the prepreg has cooled-down, a sample was placed inside the cavity at a selected thickness, smaller than the initial prepreg thickness and vacuum was applied. The fixed cavity thickness of the test-bench defines the prepreg thickness under test. To ensure the influence of race-tracking is minimized, the stack is compressed to a slightly smaller thickness than the one measured at room temperature. Testing the material only once it is cold serves in maintaining the prepreg microstructure attained after conditioning, through inhibiting significant resin flow during the measurement. Since heating reduces the viscosity of the resin, applying pressure to a hot prepreg stack can lead to a change of the impregnation state. The sample preparation before testing may last 1-2 hrs, while the testing can take from several minutes up to few hours depending on the amount of porosity enclosed in the sample.

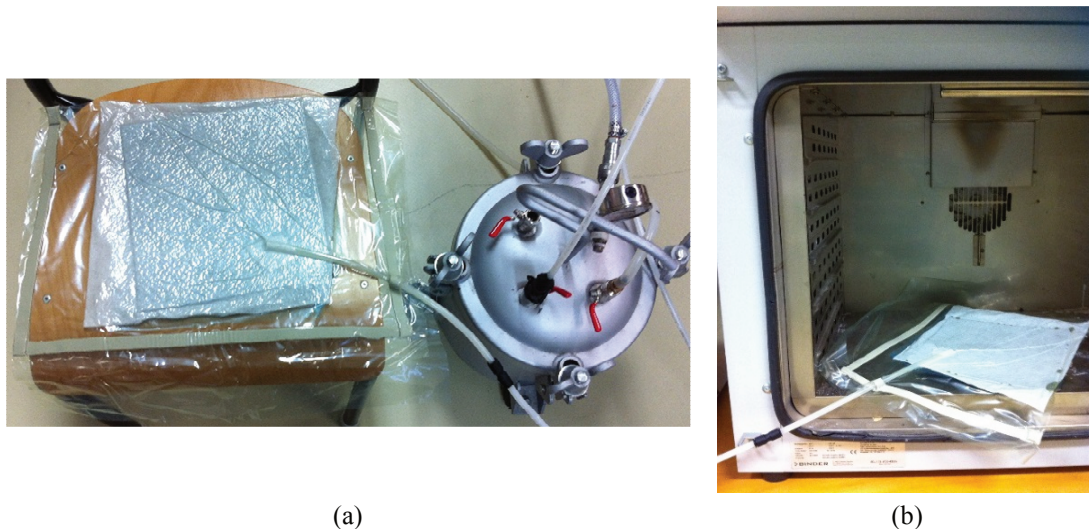


**Fig. 3-12: Conditioning of the prepreg stack before testing its air permeability [SN1]**  
 (a) Room temperature debulking of the stack (b) sample conditioning inside the oven.

### 3.3.1.3 Air Permeability as a Function of Prepeg Porosity

The fiber and resin volume fractions  $V_{f,p}$  and  $V_{r,p}$  are determined according to Equations (3-1) and (3-5) respectively after determining the thickness of the sample at the end of each measurement. Once the fiber and resin volume fractions are known, the global prepreg porosity  $\phi_p$  can be determined from Equation (3-6). Conditioning the prepreg at different temperatures produced samples with porosity in the range of 0-0.3 (or 0 – 30%) and resulting in-plane air permeability  $K_{a,xx}$  which is summarized in Fig. 3-13.

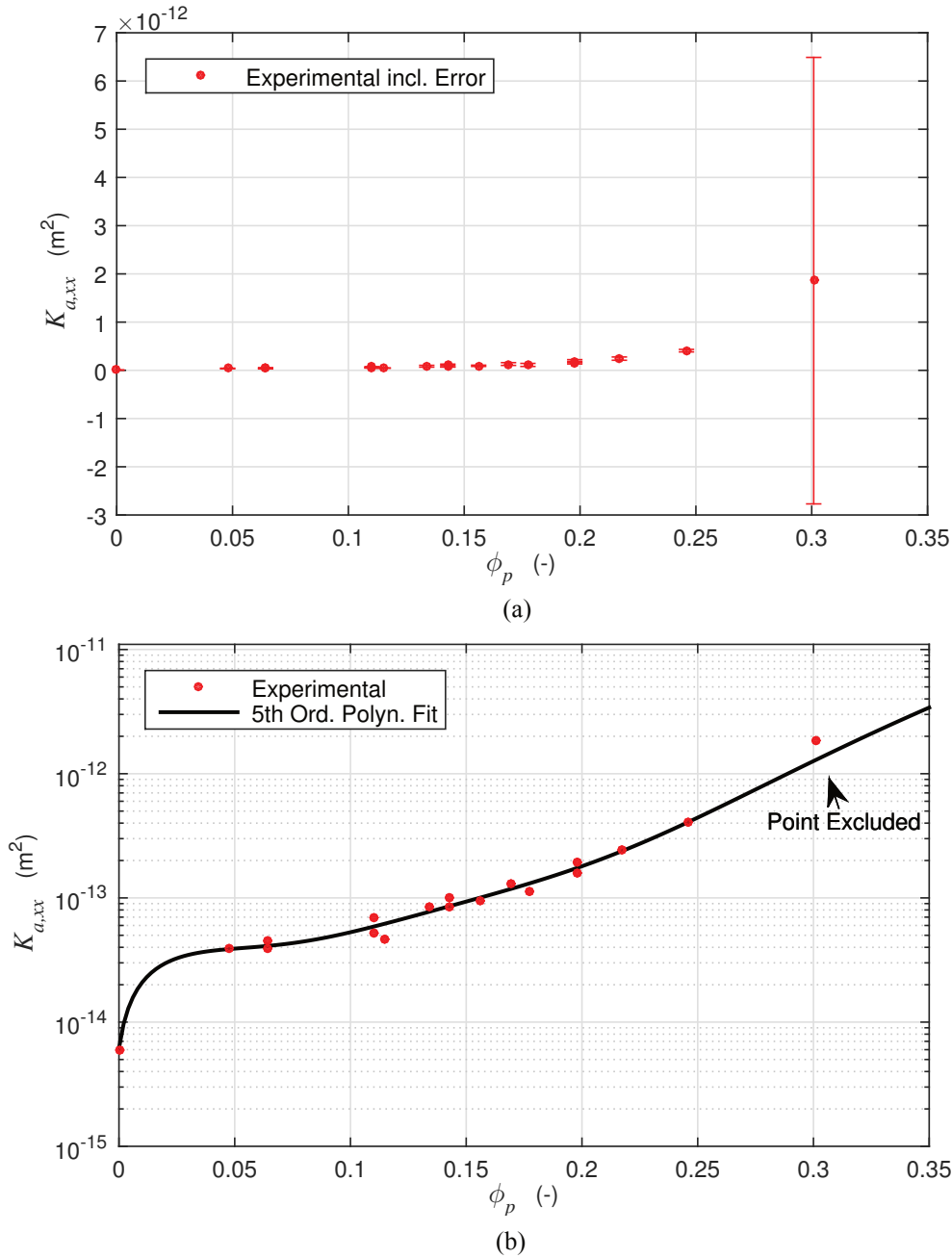


**Fig. 3-13: Air permeability of the MTM 44-1 prepreg for a range of porosities**  
 (a) Experimental points and measurement error – linear scale  
 (b) Experimental points and 5<sup>th</sup> order polynomial fit – logarithmic scale.

The first permeability data point was measured after consolidating the prepreg at room temperature solely under vacuum, for approximately ten minutes. The stack after the measurement had a porosity  $\phi_p$  of 0.30 or 30%, fiber volume fraction  $V_{f,p}$  of 0.36 or 36% and resin volume fraction  $V_{r,p}$  of 0.34 or 34%. Its air permeability at 0.3 or 30% porosity was the highest permeability determined for the MTM44-1 prepreg,  $1.86 \cdot 10^{-12} \text{ m}^2$ .

In some occasions, the test cavity was closed with uneven or insufficient torque, which resulted in a higher cavity thickness than the initial sample thickness. During these tests race-tracking can result in an over-estimation of the measured permeability. This effect was observed at the initial state of the prepreg, for a porosity content of 0.3 or 30%, therefore the first data-point is excluded from the analysis as shown in Fig. 3-13(a). Nevertheless, this data point is still included in Fig. 3-13(b) for comparison purposes due to unavailability of other test results at this porosity level.

The air permeability was initially fitted to an exponential function, typically used to describe the permeability of textiles. Nevertheless, the best fit was attained by a fifth order polynomial as a function of the prepreg's porosity given in Equation (3-23).

$$K_{a,xx}(\phi_p) = p1 \cdot \phi_p^5 + p2 \cdot \phi_p^4 + p3 \cdot \phi_p^3 + p4 \cdot \phi_p^2 + p5 \cdot \phi_p + p6 \quad (3-23)$$

The Bisquares weight method, minimizing the effect of outliers within a 95% confidence interval (95% CI), was used to determine the coefficients of Equation (3-23) in Matlab R2014b. The coefficients  $p1 - p6$  are summarized in Tab. 3-7 including an upper and lower band for 95% CI. The parameters describing the regression quality are included in the same table.

**Tab. 3-7: Fitting coefficients of the MTM 44-1 in-plane air permeability as a function of the prepreg's porosity and regression quality attained (see Equation (3 23))**

Parameters	Units	Coefficients	Lower Band	Upper Band
$p1$	$\text{m}^2$	$3.68 \cdot 10^{-9}$	$-3.61 \cdot 10^{-9}$	$1.10 \cdot 10^{-8}$
$p2$	$\text{m}^2$	$-2.01 \cdot 10^{-9}$	$-6.62 \cdot 10^{-9}$	$2.59 \cdot 10^{-9}$
$p3$	$\text{m}^2$	$4.35 \cdot 10^{-10}$	$-5.97 \cdot 10^{-10}$	$1.47 \cdot 10^{-9}$
$p4$	$\text{m}^2$	$-4.08 \cdot 10^{-11}$	$-1.37 \cdot 10^{-11}$	$5.59 \cdot 10^{-11}$
$p5$	$\text{m}^2$	$1.84 \cdot 10^{-12}$	$-1.42 \cdot 10^{-12}$	$5.10 \cdot 10^{-12}$
$p6$	$\text{m}^2$	$6.14 \cdot 10^{-15}$	$-2.24 \cdot 10^{-14}$	$3.47 \cdot 10^{-14}$
Quality of fit				
$R^2$		0.988		
$R_{\text{adj}}^2$		0.982		

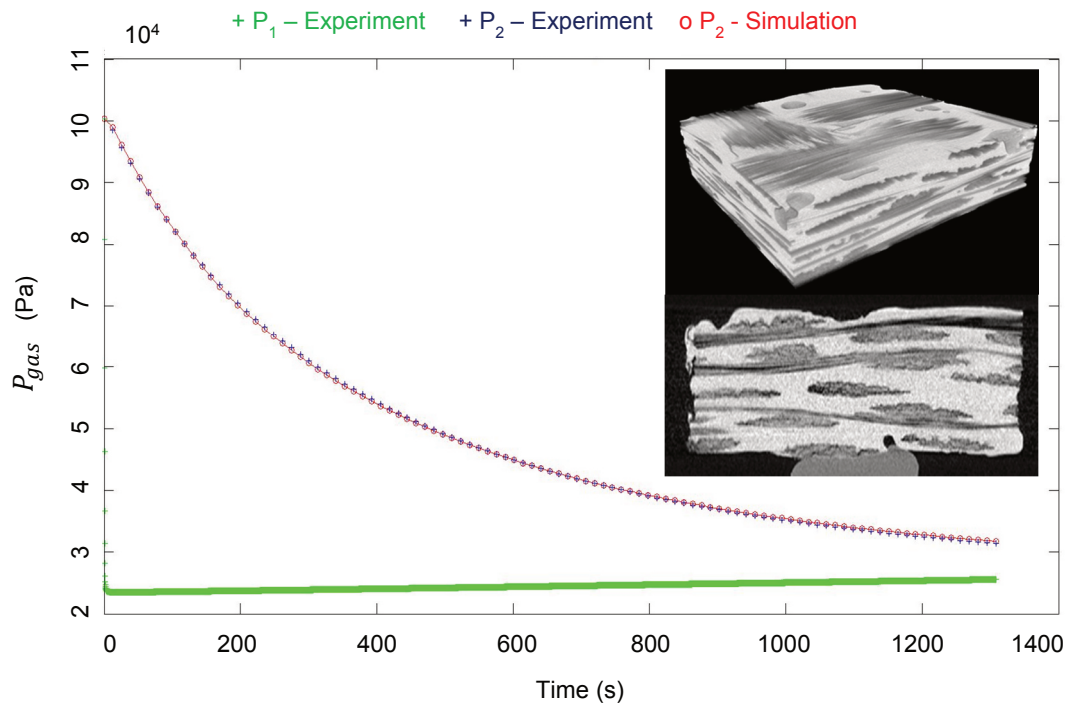


Since only two samples were measured in the 0-0.5 (or 0-5%) porosity range, the confidence of the model in this region is low. A poor fit between the measured and simulated pressure was obtained and therefore these points are excluded from the regression for determining the air permeability. The permeability equation can nevertheless qualitatively capture the drop of permeability in this porosity region.

Potential reasons for this discrepancy between experimental and simulated pressure may be attributed to:

- Mold leakage, which has a higher influence on the measurement's accuracy in samples with lower porosity content and therefore lower permeability.
- Modification of the prepreg's microstructure at different porosity levels, directly affects the physics of air flow. The increase of the prepreg impregnation causes a reduction of the characteristic length for air flow. When this effect becomes significant, the dominating mechanism of air flow through a highly saturated prepreg most likely switches from viscous to sliding flow. Furthermore, the application of vacuum for a significant amount of time during the measurement may contribute towards a more significant reduction of the characteristic length of the porous network, further impregnation and 'locking' of the air channels.

Inspection of the sample's microstructure with  $\mu$ CT after performing air permeability measurements (images included in Fig. 3-14) shows evidence of the significant change occurring in the microstructure between the sample conditioned at 80°C and 100°C.



(a)

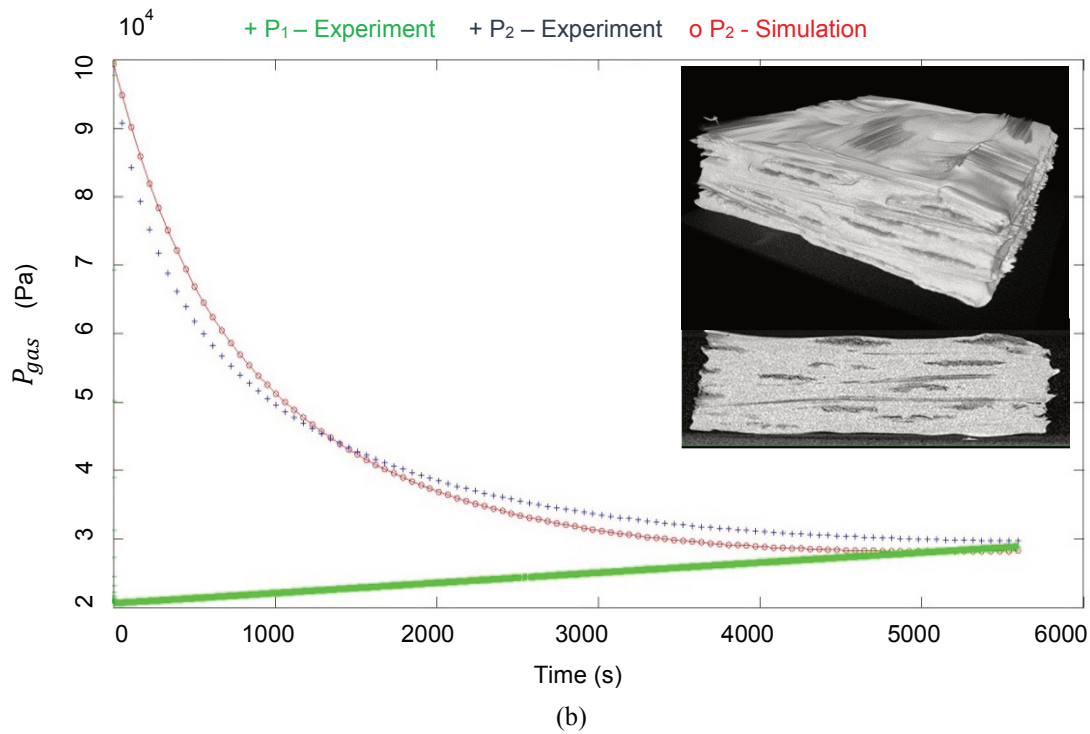


Fig. 3-14: Experimental versus simulated pressures and resulting microstructures imaged with  $\mu$ CT after conditioning the MTM 44-1 prepreg for 10min at (a) 80°C (b) 100°C

### 3.3.1.4 Effects of Temperature on the Prepreg Microstructure and the Air Permeability

The sensitivity of the prepreg permeability to the conditioning temperature and duration of its application was investigated and the results plotted in Fig. 3-15.

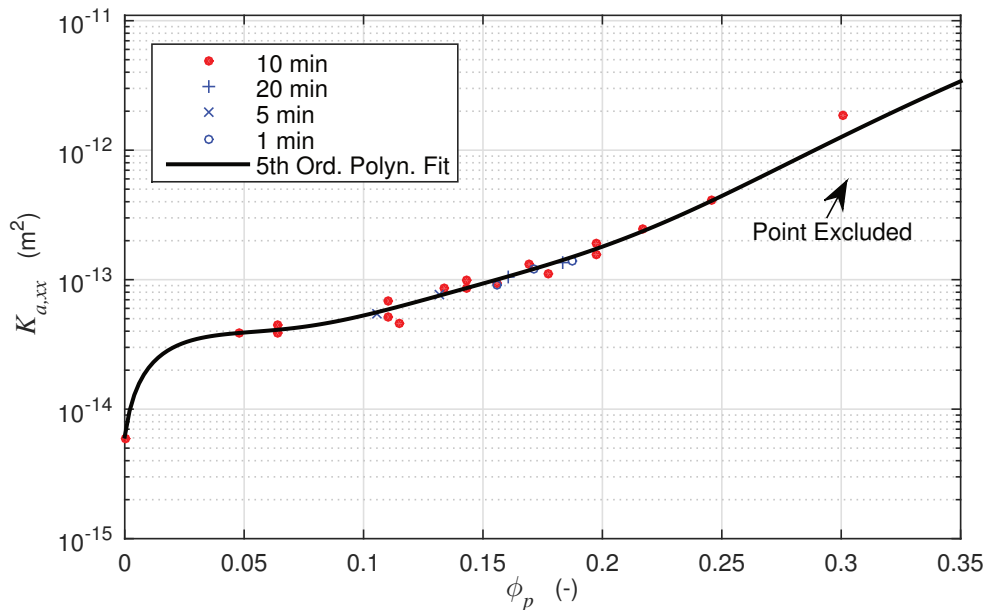


Fig. 3-15: MTM 44-1 permeability vs. porosity of samples conditioned at various temperatures and times

Three temperatures (40°C, 60°C and 80°C) and three durations of conditioning (1, 5, 20 min) were selected for this purpose. The red points, are points used to derive the fitting equation  $K_{a,xx}(\phi_p)$ , reflecting samples conditioned for 10min, while the blue points represent all other samples conditioned for 1min and 20min, before the permeability of the material was measured. As shown in Fig. 3-15, the influence of temperature and temperature conditioning duration does not have an effect on the shape of the permeability vs. porosity curve. A shift along the porosity axis due to longer conditioning times at elevated temperatures, contributes towards measuring a lower air permeability in the sample. It can be concluded that the air permeability is independent of the conditioning temperature of the prepreg and therefore the 5<sup>th</sup> order polynomial fit can be used as a generalized expression to describe the permeability of the MTM44-1 prepreg solely as a function of its porosity. This function is implemented in COMSOL Multiphysics and can depict the influence of the porosity reduction of the prepreg on the air permeability, which may take place either during debulking, or during the cure cycle (see Section 4.2 for implementation details).

### 3.3.1.5 Conclusions and Perspectives

In this Section the application of a transient air permeability measurement method, initially developed for the characterization of textiles by Hou et al. [36], is used to measure the permeability of the MTM44-1 OoA prepreg. Measurements were performed at a range of saturation levels, representing the evolution of the material's permeability with evolving impregnation during OoA processing. While no information about the in-plane air permeability of the MTM44-1 prepreg is available in the literature, the permeability determined in this work agrees well with the permeability range reported by Hickey et al. [37], Cender et al. [39], Arafath et al. [35] for other OoA prepreg systems. The initial permeability of textile based OoA prepreg stacks (8 plies) is reported to be in the range of  $5.49 \cdot 10^{-13}$  and  $5.69 \cdot 10^{-14}$  m<sup>2</sup>, without reference on the porosity or fiber volume fraction of the sample measured [35]. Cender et al. [39] presented the evolution of the air permeability of two OoA prepregs based on a TW fabric (Gurit ST94), at different saturation levels. The permeability measured by Cender et al. [39] reduced with increasing resin saturation, causing a simultaneous decrease in the in-plane air permeability of the prepreg from approximately  $5 \cdot 10^{-12}$  up to  $3 \cdot 10^{-14}$  m<sup>2</sup> from 0 to 0.6 or 0 to 60% saturation of the prepreg with resin [39]. Correlating a prepreg's permeability with its porosity using a 5<sup>th</sup> order polynomial equation provide the means to mathematically describe the permeability evolution taking place during OoA processing. This direct correlation of the air permeability evolution with its macroscopic porosity as the impregnation progresses, enables an accurate and convenient implementation of the air flow physics in the virtual processing toolkit, developed in the context of this work. The approach of correlating the air permeability with the porosity instead of the fiber volume fraction of the prepreg, enables decoupling the air flow from the compaction, if the resin content is assumed to remain constant.

Future work shall enable a more detailed study of the MTM44-1 prepreg at high (0.3 or 30%, or higher) and low porosity contents (0-0.06 or 0-6%), to enable an increased confidence in the validity of the developed model in these regions. Furthermore the implementation of the Klinkenberg sliding effect for measurements performed at low porosity levels will be improve the prediction accuracy. A detailed study of the microstructure shall be performed in order to quantify the dimensions of the mean free path of the gas molecules in the prepreg (Klinkenberg factor). To determine if resin flow takes place during the test at low porosity levels, it would be interesting to image the vacuum application process in a small scale, real time, using a  $\mu$ CT. Finally, a comparative study of the resulting pressures during the permeability measurement could be performed using a prepreg with a higher viscosity or an aged prepreg sample.

### 3.3.2 Tow Permeability to Resin

The analytical equations developed by Gebart [140] describe the permeability of unidirectional fibrous materials with idealized fiber distributions (Section 2.2.4). These equations are used to calculate the through thickness tow permeability of the MTM 44-1 prepreg defined as the ‘tow equivalent’ in Fig. 3-3. The simplified rectangular tow of Fig. 3-3(c) is considered to saturate exclusively through its thickness, while the through thickness permeability of the warp and weft tow is equal. The through thickness permeability of the MTM 44-1 prepreg  $K_{r,zz}$ , for a range of fiber volume fractions  $V_{f,p}$  and for a quadratic, a hexagonal fiber distribution and their average is presented in Fig. 3-16.

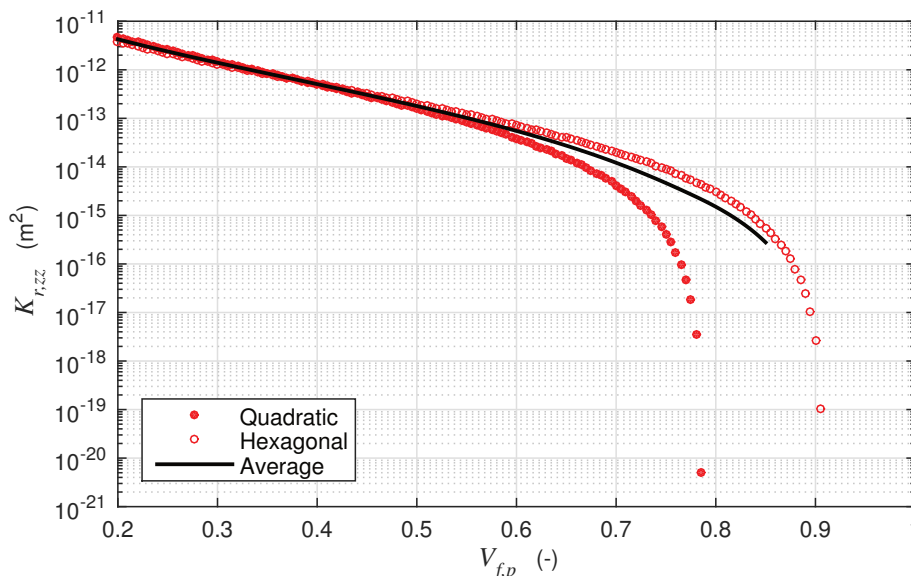


**Fig. 3-16:** Through thickness permeability of the MTM 44-1 tow for a quadratic and a hexagonal distribution of fibers in the tow and their average

The fiber radius of the MTM 44-1 prepreg is  $3.5\mu\text{m}$  [224, 225], while their distribution is rather erratic (Fig. 3-9 (a)). Since it does not resemble any idealized distributions, the average permeability is calculated instead as an input for the OoA simulation presented

in Chapter 4. The through thickness permeability of the ‘tow equivalent’ for the average prepreg volume fraction ( $V_{f,p} = 0.36$  or 36% - Tab. 3-3) is  $K_{r,zz} = 7.58 \cdot 10^{-13} \text{ m}^2$ . If the average tow volume fraction is considered instead (approximately  $V_{f,t} = 0.5$  or 50% - Tab. 3-6), the tow permeability reduces to  $K_{r,zz} = 1.79 \cdot 10^{-13} \text{ m}^2$ .

## 3.4 Resin Film Characterization

The MTM 44-1 prepreg is partially impregnated by an epoxy resin film based on a TGMDA/TGGDM epoxy (N,N,N',N'Tetraglycidyl 4,4' Diaminodiphenylsulphone), while it also contains two tertiary amines (4,4' Methylenebis[2,6 Diethylaniline] and 4,4' Methylenebis[2-Isopropyl-6-Methylaniline]) [226]. The resin also contains toughening agents [225], nevertheless the chemistry of the toughening agents has not been reported.

### 3.4.1 Cure Kinetics

In this Section the curing process of the MTM44-1 resin is investigated via isothermal and non-isothermal (ramp) Differential Scanning Calorimetry measurements (DSC). The characterization results are summarized in Section 3.4.1.2 and are used as an input for the development of a cure kinetics model presented in Section 3.4.1.3.

#### 3.4.1.1 Differential Scanning Calorimetry (DSC)

DSC can be used to quantify the energy released from an initially uncured polymer, during its cure at controlled isothermal or non-isothermal conditions. Furthermore, the cured and uncured glass transition temperature of a polymer can be characterized at a range of heating rates using DSC. A TA Q2000 Heat Flux DSC is used to measure the temperature difference between a reference pan and a pan containing an MTM 44-1 sample. The DSC System has a temperature range of  $-90^\circ\text{C}$  and  $725^\circ\text{C}$ . The sample pans are placed inside the same furnace, while their temperature difference during heating is used to calculate the heat flow [151]. Apart from the sensors used to measure the temperatures of the sample ( $T_{sp}$ ) and reference pan ( $T_{rp}$ ), another temperature sensor is included between the two pans ( $T_{op}$ ). The introduction of a sensor in the furnace ( $T_{zero}^{\text{TM}}$  Sensor), enables the measurement of the furnace's thermal resistance, reducing the error caused by the resistance modification during the measurement [227]. The acquired heat-flow signal is therefore stable within the temperature range of interest. The differential heat flow rate measured in a pan is given by Equation (3-24)[228].

$$\frac{dH_t}{dt} = C_{p_s} \frac{dT_{sp}}{dt} + \frac{dQ}{dt} \quad (3-24)$$

Where  $C_{p_s}$  is the heat capacity of the pan containing the sample,  $T_{sp}$  is the sample temperature and  $dQ/dt$  is the heat flow produced or absorbed by a kinetic response in the

material, according to Dykeman [229]. The heat flow rate introduced to, or emitted by the sample can be calculated from Equation (3-25).

$$\frac{dQ}{dt} = \frac{T_{0p} - T_{sp}}{R_s} \quad (3-25)$$

Where  $T_{sp}$  stands for the sample temperature,  $T_{0p}$  is the furnace temperature, and  $R_s$  the thermal resistance between the heat source and the pan. The heat flow rate of the reference pan can be calculated similarly, by replacing the sample temperature, resistance and heat capacity of the sample with that of the reference pan. Substituting Equation (3-25) into (3-24) and subtracting the heat flow equations of the reference from the sample (Equations (3-27) and (3-28)) leads to the differential equation (3-26)[227].

$$\frac{dH_t}{dt} = -\frac{\Delta T_p}{R_r} + \Delta T_{0p} \cdot \left(\frac{1}{R_s} - \frac{1}{R_r}\right) + (C_{p_r} - C_{p_s}) \cdot \frac{dT_s}{dt} - C_{p_r} \cdot \frac{d(\Delta T_p)}{dt} \quad (3-26)$$

$$\Delta T_p = T_{sp} - T_{rp} \quad (3-27)$$

$$\Delta T_{0p} = T_{sp} - T_{0p} \quad (3-28)$$

This is a four-term heat flow equation, with the first term expressing the principle heat flow, while all other terms account for any imbalances within the measuring system and sample pans [227, 228]. Recording two differential measurements has played an important role in achieving a flat baseline for the measurements.

Modulated DSC is better suited when materials with overlapping transitions, or transitions difficult to discern are to be characterized. In MDSC two heating rates, one linear and one sinusoidal (modulated) are applied simultaneously on the sample. To perform an MDSC measurement the average heating rate, the temperature modulation period ( $t_p$ ) and amplitude ( $T_A$ ) have to be specified. The MDSC can measure the Total Heat Flow, but also two individual components, the Reversing and Non-Reversing Flow presented in Equations (3-29) and (3-30) respectively.

$$\frac{dH_{Rev}}{dt} = C_{p_{Rev}} \frac{dT}{dt} \quad (3-29)$$

$$\frac{dH_{Non-Rev}}{dt} = \frac{dH_t}{dt} - \frac{dH_{Rev}}{dt} \quad (3-30)$$

The Reversing Heat Flow signal  $H_{Rev}$  is calculated from the Reversing Heat Capacity signal  $C_{p_{Rev}}$ . The Total Heat Flow signal  $H_t$  is calculated from the average value of the measured Modulated Heat Flow signal, with the use of Fourier Transform (FT) on the sinusoidal wave signal. The difference between the Total Heat Flow and the Reversing Heat Flow gives the Non-Reversing Heat Flow  $H_{Non-Rev}$ . Generally material phase



transitions (i.e.  $T_g$ ) which are reflected in the heat capacity can be measured in the Reversing signal, while kinetic events such as chemical reactions and crystallization or evaporation processes are investigated using the Non-Reversing signal.

### 3.4.1.2 Sample Preparation and Measurement

#### Sample Preparation

The MTM 44-1 resin supplied in the form of a resin film was cut in small samples (mass ~15-17mg) and transferred to an aluminum pan (type  $T_{zero}$  - Al Hermetic). A large sample mass is selected (at the limit of the capacity of the pan) to increase the measurement sensitivity. The mass of the sample, pan and lid were in the range between 52-69mg. The mass of each sample and the pan/lid weight was determined before the DSC measurement, with the use of a high accuracy Mettler Toledo XS205 balance (0.01mg). Accurate determination of the sample mass is critical to the accuracy of the results, while a limited mass variability reduces the variability in the calculated energy of reaction. Care was taken to not significantly extend the resin film during the cutting process, as this could cause alterations in the physical behavior of the polymer and to ensure good contact with the bottom of the pan [151]. The pan was finally sealed and the lid was perforated and loaded in the furnace at room temperature.

#### Baseline and Temperature Calibration

Before testing the actual material an evaluation run of the heat flow signal was performed within the temperature range of interest. For this purpose two empty pans sealed with a lid are placed in the furnace (of the same type as the ones later used in the actual measurement). A  $T_{zero}$  calibration, entailing two empty furnace runs was performed to determine the resistance of the cell, while two runs with sapphire samples (one per pan side) were used to determine its heat capacitance. To improve the sensitivity of the measurement, a calibration run was performed using a metal with a transition in the temperature range where phase transitions are expected to take place. Since the glass transition temperature of the MTM 44-1 resin is expected at 170-190 °C, a calibration using Indium (In) with a melting point at 156.6 °C and Tin (Sn) with a melting point at 231.9 °C was performed at each heating rate used in the characterization.

#### Non-Isothermal Characterization and Data Extraction

The total enthalpy and the glass transition temperature before and after cure (namely  $T_{g0}$  or  $T_{g\infty}$ ) can be determined via dynamic DSC measurements on the MTM 44-1 resin. Since the MTM 44-1 resin is a mix of at least three main components, the glass transition temperature is not clearly discernable with simple DSC measurements. Therefore MDSC was chosen to perform non-isothermal MTM 44-1 resin characterization. The linear heating rate  $dT_{dyn}/dt$  is selected according to the heating rates suggested for processing of the MTM 44-1 prepreg from the material manufacturer [225].

The temperature modulation period  $t_p$  and amplitude  $T_A$  were selected according to the TA guidelines, for materials with glass transition temperatures hard to detect [230]. The temperature measurement range  $T_{dyn}$  spans 30°C below the expected  $T_{g0}$  and stops below 280°C, where most epoxies start decomposing during the first run [148]. Before initiating the temperature scan and after its completion, the measurement is left to equilibrate at temperature for 10-20min. Cooling the sample to 20°C takes place fast. The settings used for the MTM 44-1 characterization are summarized in Tab. 3-8.

**Tab. 3-8: Non-isothermal MDSC settings used for the measurement of the MTM44-1 resin**

1 <sup>st</sup> – Run		2 <sup>nd</sup> – Run		MDSC Settings	
$\frac{dT_{dyn}}{dt}$ (°C·min <sup>-1</sup> )	$T_{dyn}$ (°C)	$\frac{dT_{dyn}}{dt}$ (°C·min <sup>-1</sup> )	$T_{dyn}$ (°C)	$T_A$ (°C)	$t_p$ (s)
1		1		0.636	60
2	-60 up to 280	2	20 up to 280	1.272	60
3		3		1.908	60

Fig. 3-17 depicts signals of the Reversing (blue) and Non-Reversing Heat flow (green) during an indicative non-isothermal scan of the MTM 44-1 resin at 1°C/min.

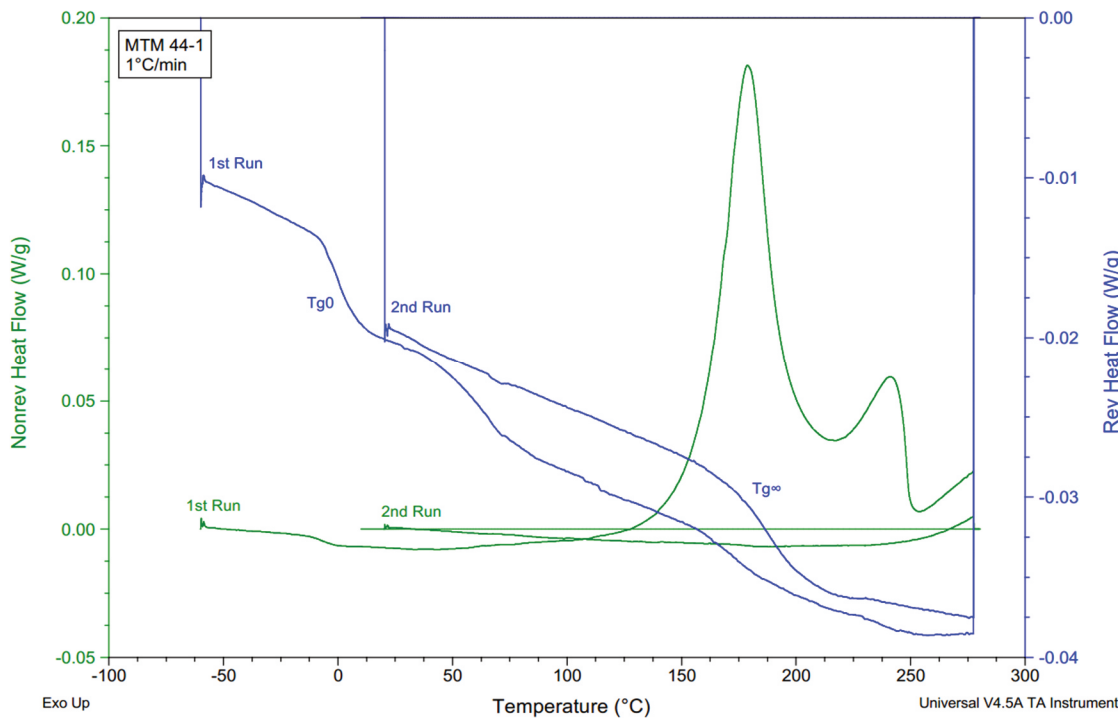


**Fig. 3-17: MDSC thermogram of the MTM 44-1 resin depicting two consecutive scans performed at 1°C/min on the same sample**

The Reversing signal shows a complex response with more than one glass transition temperature present in the uncured material (-30 °C up to 30 °C, 30 °C up to 80 °C &



120 °C up to 220°C). The total enthalpy of the MTM44-1 resin was determined by calculating the area under the curve of the Non-Reversing heat flow rate at the time where an exothermic curing reaction takes place (first MDSC run), divided by the sample mass. The trapezoidal rule is used to integrate the Non Reversing Heat Flow signal (in mW) over time above a selected baseline in Matlab R2014b. A local weighted linear least squares regression with a 2<sup>nd</sup> degree polynomial was used to smoothen the data before the integration (loess). An example of a typical curve of the MTM 44-1 Non Reversing Heat Flow rate and the baseline used to perform the integration and determine the total enthalpy, is shown in Fig. 3-18 (a). The total enthalpy released by the reaction of the MTM 44-1 resin at three heating rates is summarized in Fig. 3-18 (b).

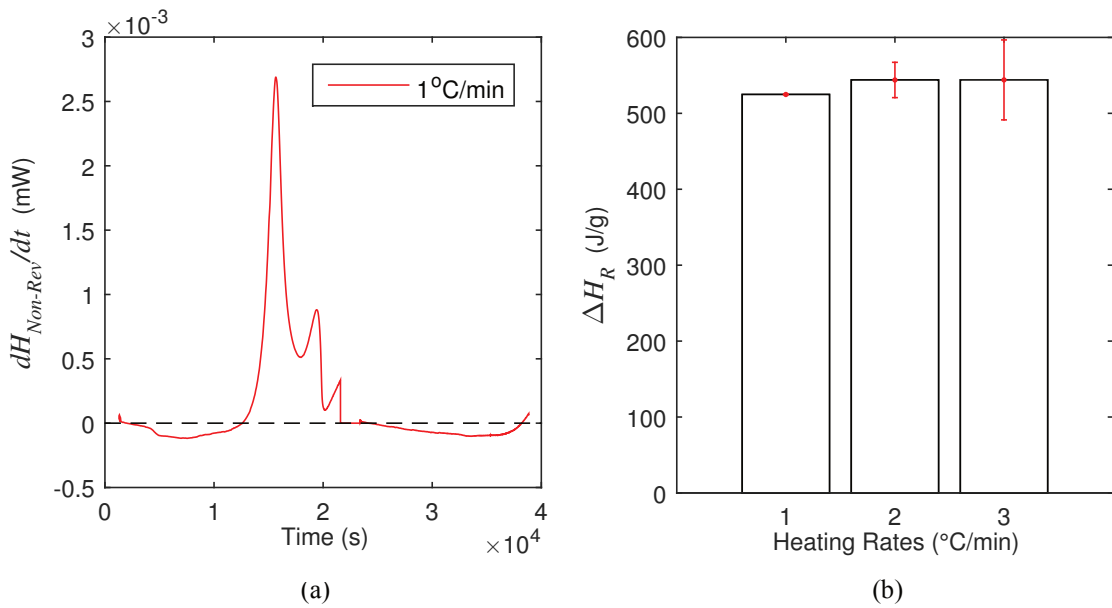
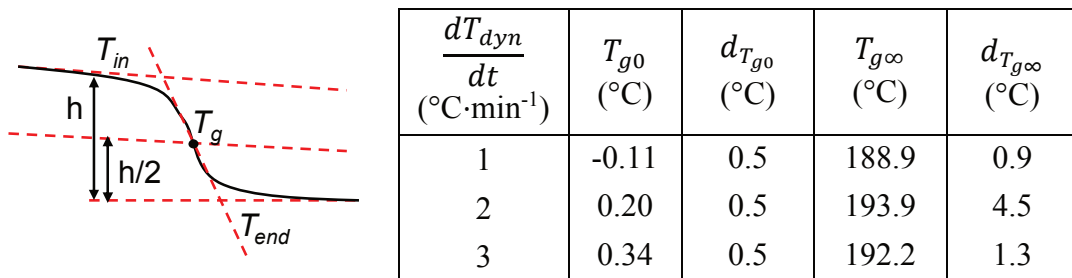


**Fig. 3-18: Total enthalpy of the MTM 44-1 resin determined via non-isothermal measurements**

The glass transition temperature of the uncured material ( $T_{g0}$ ) was measured during the first temperature scan while the glass transition temperature of the cured material ( $T_{g\infty}$ ) was measured on the second, in both cases on the Reversing Signal (Fig. 3-17 – blue).

**Tab. 3-9: Glass transition temperatures of the MTM 44-1 resin and method of calculation**



The glass transition temperature was determined from the mid-point of the step transition as shown in Tab. 3-9 along with the MTM 44-1 glass transition temperatures.

### Isothermal Characterization and Data Extraction

The determination of the total enthalpy of reaction by isothermal DSC measurements for a resin system of choice is generally favored over the non-isothermal determination [229]. Since the total enthalpy is a characteristic of the material, the reaction enthalpy measured with any measurement method should match closely. A reduced enthalpy determined from an isothermal test can be compensated by performing a consecutive dynamic measurement on the same sample, enabling the material to release any residual enthalpy ( $H_{res}$ ). The total heat of reaction is determined by the sum of the isothermal and the residual enthalpy of the material according to Equation (3-31).

$$\Delta H_R = H_{iso} + H_{res} \quad (3-31)$$

The isothermal heat of reaction was measured in the DSC, while the residual enthalpy was determined using MDSC and a dynamic temperature scan of the sample. The settings of both measurements (isothermal and residual) used for the characterization of the MTM 44-1 resin are summarized in Tab. 3-10.

**Tab. 3-10: Settings used for isothermal DSC measurements on the MTM44-1 resin, followed with an MDSC scan for the quantification of the total enthalpy of the material**

Isothermal - DSC		Dynamic - MDSC			
$\frac{dT_{iso}}{dt}$ (°C·min <sup>-1</sup> )	$T_{iso}$ (°C)	$\frac{dT_{res}}{dt}$ (°C·min <sup>-1</sup> )	$T_{res}$ (°C)	$T_A$ (°C)	$t_p$ (s)
40	100, 120, 130, 140, 160, 180, 200	2	20-280	1.272	60

One or two samples were tested at each temperature  $T_{iso}$ . The heating ramp  $dT_{iso}/dt$  from room temperature up to the temperature of interest, should be as fast as possible in order to minimize the influence of the transient heating to the curing state of the material though avoiding significant temperature overshoot. The isothermal enthalpy was determined by calculating the area under the curve of the Total Heat flow signal during the time of the exothermic reaction, divided by the sample mass. Each test extends intentionally beyond the end of the reaction, in order to capture the signal up to the point where negligible change was observed.

The isothermal and residual heat flow data are transposed along the y-axis in order to define a baseline heat flow rate at zero mW, as shown in Fig. 3-19 (a). The trapezoidal rule was used to integrate the Total Heat Flow signal (in mW) above the baseline over time, after smoothing the curves to reduce measurement noise (loess – Matlab R2014b). The residual enthalpy was calculated from the Non Reversing Heat flow signal in a similar fashion as in the case of the Non-Isothermal measurements. The curves presented in Fig. 3-19 (b) are shifted to reflect a baseline –where at zero heat flowrate, no cure takes place.

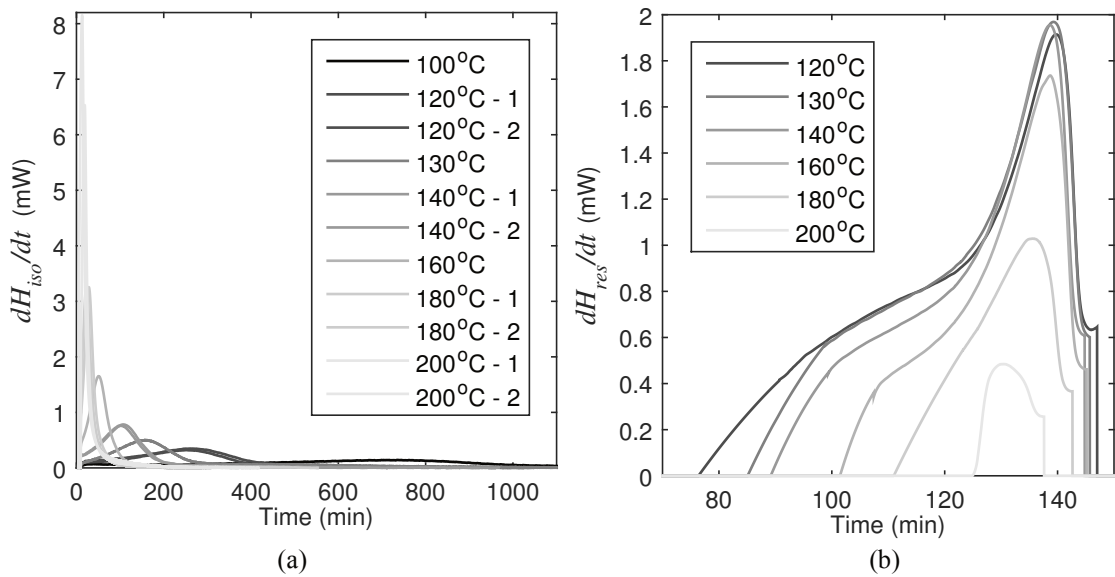


**Fig. 3-19: (a) Isothermal heat flow of the MTM 44-1 resin measured between 100 °C-200 °C and (b) residual heat flow determined via a subsequent dynamic scan**

The results of the total enthalpy determined from the sum of the isothermal and residual enthalpies are summarized in Fig. 3-20. The enthalpy cannot be accurately determined at 100 °C, since a significant part of the heat flow emitted during the isothermal test lies within the measurement error of the system.

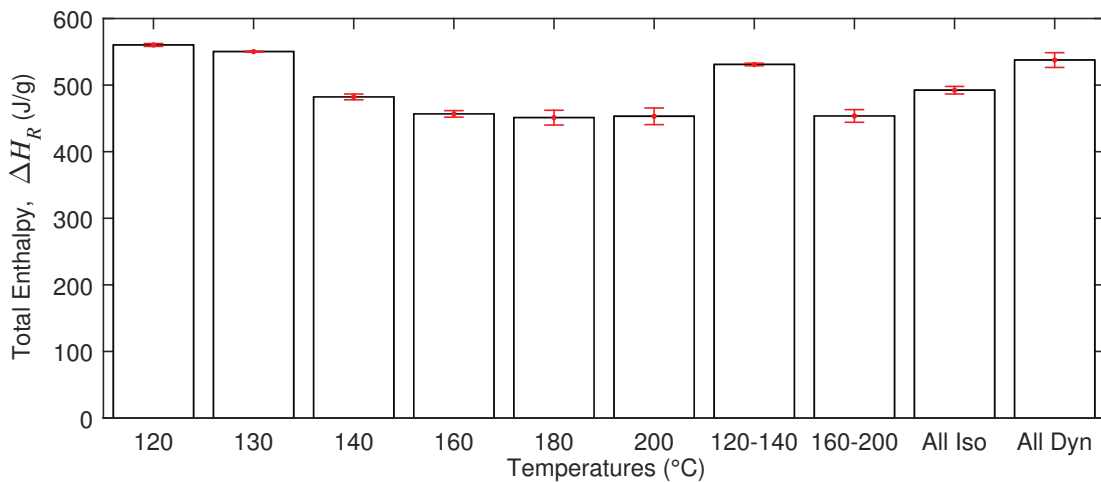


**Fig. 3-20: Total enthalpy of the MTM 44-1 resin determined at isothermal temperatures**

Depicted average temperatures at low range (120-140°C) and high range (160-200°C), average of all isothermal temperatures (All Iso) and all heating rates tested (All Dyn).

The total enthalpy calculated as an average of the enthalpy of all isothermal measurements (All Iso - Fig. 3-20) is lower than the average enthalpy of all dynamic measurements (All Dyn - Fig. 3-20). This behavior is commonly encountered in the literature and discussed in detail by Calado et al. [148] and Dykeman [229] amongst others. It can be further observed that the total enthalpy measured at the low temperature range (120-

140°C) is higher than the one measured at the high temperature range (160-200 °C). This behavior could be explained by two potential reasons:

- The advancement of the cure during the transient heating phase is more significant at higher temperatures leading to only part of the total energy being captured with the selected method of integration of the curve.
- The material demonstrates a complex kinetic behavior, with more than one reaction mechanism involved, which dominate at different temperature ranges. The MTM 44-1 resin is a mixture of the primary epoxy and two amines, which could justify the presence of two kinetic mechanisms at two temperature ranges.

Several step responses were observed at different temperature ranges on the Reversing Heat Flow signal of the uncured material on the MDSC thermograms (Fig. 3-17). This could be an indication of the different phases formed at different testing/processing temperatures. The presence of different kinetics at different temperatures can also be seen in the evolution of the MTM 44-1 viscosity up to the gelling point. Discussion on the results of the viscosity measurements is included in Section 3.4.3.2. In the following Section, the isothermal measurements are used as a basis for the development of a cure kinetics model for the MTM 44-1 resin system.

### 3.4.1.3 Cure Kinetics Modeling

A cure kinetics model based on a phenomenological modeling approach able to capture the development of the degree of cure of the MTM 44-1 resin as a function of its cure rate is presented. The isothermal DSC measurement results were fitted to a range of models available in the literature by Wilson Tan [S4], while the model which better described the experimental behavior of the MTM 44-1 resin is discussed in detail here.

As presented in Section 2.2.4.2, the degree of cure and cure reaction rate of the material can be directly calculated from the heat flow rate measured by DSC or MDSC, according to Equations (2-20) and (2-21). The principal of phenomenological modeling relies on identifying the best correlation between cure rate  $d\alpha/dt$  and the temperature and degree of cure  $\alpha$ . Specifically  $\alpha$  is a function which closely fits the shape of the heat flow curve generated by DSC. The most commonly applied model for  $\alpha$  when reaction kinetics of an amine-based epoxy system is concerned is the autocatalytic model, given in Equation (3-32)[148, 231].

$$\frac{d\alpha}{dt} = (k_1 + k_2\alpha^m)(1 - \alpha)^n \quad (3-32)$$

Cole extended the autocatalytic expression into Equation (3-33) in order to capture the switch from a kinetics to a diffusion controlled reaction, which usually takes place at high degrees of cure ( $\alpha > 0.1$ ) [232, 233].

$$\frac{d\alpha}{dt} = \frac{k\alpha^m(1-\alpha)^n}{1 + e^{[D(\alpha - (\alpha_{c0} + \alpha_{cT}))]}} \quad (3-33)$$

Nevertheless none of the two models could describe the cure behavior of the MTM 44-1 resin accurately enough [S4].

For this purpose the model proposed by Kratz et al. [159] and Shahkarami et al. [167], combines the principals of the above models in a single expression given in Equation (3-34). Since the model is used to characterize the cure kinetics of the MTM 45-1 OoA epoxy resin, a better match of the experimental data is expected.

$$\frac{d\alpha}{dt} = k_1\alpha^{m_1}(1-\alpha)^{n_1} + \frac{k_2\alpha^{m_2}(1-\alpha)^{n_2}}{1 + e^{[D(\alpha - (\alpha_{c0} + \alpha_{cT}))]}} \quad (3-34)$$

Where:

- $n_1, m_1, n_2, m_2$ : Reaction orders
- $D$ : Diffusion coefficient
- $\alpha_{c0}, \alpha_{cT}$ : Critical degree of cure at  $t=0$  and during the temperature evolution  $T$

The coefficients  $k_1, k_2$  are described by an Arrhenius Equation (3-35).

$$k_i(T) = A_{k,i} \exp\left(\frac{-E_k}{RT}\right) - \text{where } i = 1,2 \quad (3-35)$$

The activation energy  $E_k$  was calculated from the slope of the line of  $\ln(k_i(T))$  versus  $1/T$  via linear regression, using a 1<sup>st</sup> order polynomial to fit the whole temperature range and for each temperature range (low and high) separately (multiplied by the gas constant  $R$ ). It was also determined for the complete range of degrees of cure ( $0 < \alpha < 1$ ), as well as for low ( $\alpha < 0.1$ ) and high degrees of cure ( $\alpha > 0.1$ ) separately. The resulting activation energies are summarized in Tab. 3-11. A good fitting was achieved in most cases, with  $R^2$  and  $R_{adj}^2 \geq 0.8$ . A reduced quality was only obtained at the low temperature range and at low degrees of cure ( $R^2 = R_{adj} = 0.67$ ).

**Tab. 3-11: Activation energy of the MTM 44-1 for a range of temperatures and degrees of cure**

Range	$E_k$ (J/mol)		
	All Temperatures	120-140 °C	160-200 °C
$0 < \alpha < 1$	60784	62530	56768
$\alpha < 0.1$	65090	63910	72689
$\alpha > 0.1$	60484	60800	56818

A higher activation energy was measured at low degrees of cure, while the highest energy was attained at the high temperature range and at low degrees of cure. In a second step Equation (3-35) is inserted into Equation (3-34), leading to Equation (3-36).

$$\frac{d\alpha}{dt} = A_{k,1} \exp\left(\frac{-E_k}{RT}\right) \alpha^{m_1} (1-\alpha)^{n_1} + \frac{A_{k,2} \exp\left(\frac{-E_k}{RT}\right) \alpha^{m_2} (1-\alpha)^{n_2}}{1 + e^{[D(\alpha - (\alpha_{c0} + \alpha_{cT}T))]}} \quad (3-36)$$

Non-linear regression and particularly the trust-region reflective algorithm was used to determine the nine coefficients  $A_{k,1}$ ,  $A_{k,2}$ ,  $m_1$ ,  $m_2$ ,  $n_1$ ,  $n_2$ ,  $D$ ,  $\alpha_{c0}$ ,  $\alpha_{cT}$ . The cure behavior of the resin at the low and high temperature ranges as well as the whole temperature range was fitted with the coefficients summarized in Tab. 3-12.

**Tab. 3-12: Fitting coefficients of the cure rate versus degree of cure model proposed by Kratz and Shahkarami et al. [159, 167] (Equation (3-34)) adapted for the MTM 44-1 resin**

Parameters	Fitting Coefficients		
	All Temperatures	120-140 °C	160-200 °C
$A_{k,1}$ (s <sup>-1</sup> )	$5.80 \cdot 10^5$	$1.46 \cdot 10^5$	$5.74 \cdot 10^5$
$m_1$ (-)	1.00	0.94	0.51
$n_1$ (-)	2.32	1.81	2.31
$A_{k,2}$ (s <sup>-1</sup> )	$1.00 \cdot 10^6$	$6.00 \cdot 10^5$	$4.89 \cdot 10^5$
$m_2$ (-)	0.65	0.50	0.73
$n_2$ (-)	1.83	0.72	1.94
$D$ (-)	9.83	17.26	8.66
$\alpha_{c0}$ (-)	-1.50	-1.48	-1.50
$\alpha_{cT}$ (K <sup>-1</sup> )	$5.00 \cdot 10^{-3}$	$5.00 \cdot 10^{-3}$	$5.00 \cdot 10^{-3}$

The fitting error  $e_{\frac{d\alpha}{dt}}$  was quantified by Equation (3-37), where  $\widehat{d\alpha}/dt_i$  the predicted and  $da/dt_i$  the experimental cure rate, while  $\overline{d\alpha}/dt$  the average experimental cure rate, for a total of  $N$  measurement points.

$$e_{\frac{d\alpha}{dt}} (\%) = \frac{1}{\overline{\frac{d\alpha}{dt}}} \sqrt{\frac{\sum_{i=1}^N \left(\frac{d\alpha}{dt_i} - \widehat{\frac{d\alpha}{dt_i}}\right)^2}{N}} \quad (3-37)$$

A comparison between the experimental and modeled curves is shown in Fig. 3-21, where it can be seen that defining two sets of fitting coefficients to describe the cure behavior of the MTM 44-1 resin at low and high temperatures is beneficial. This behavior confirms the assumption of a complex kinetic behavior of the system, with more than one reaction activated at different temperature ranges (the low and high investigated).

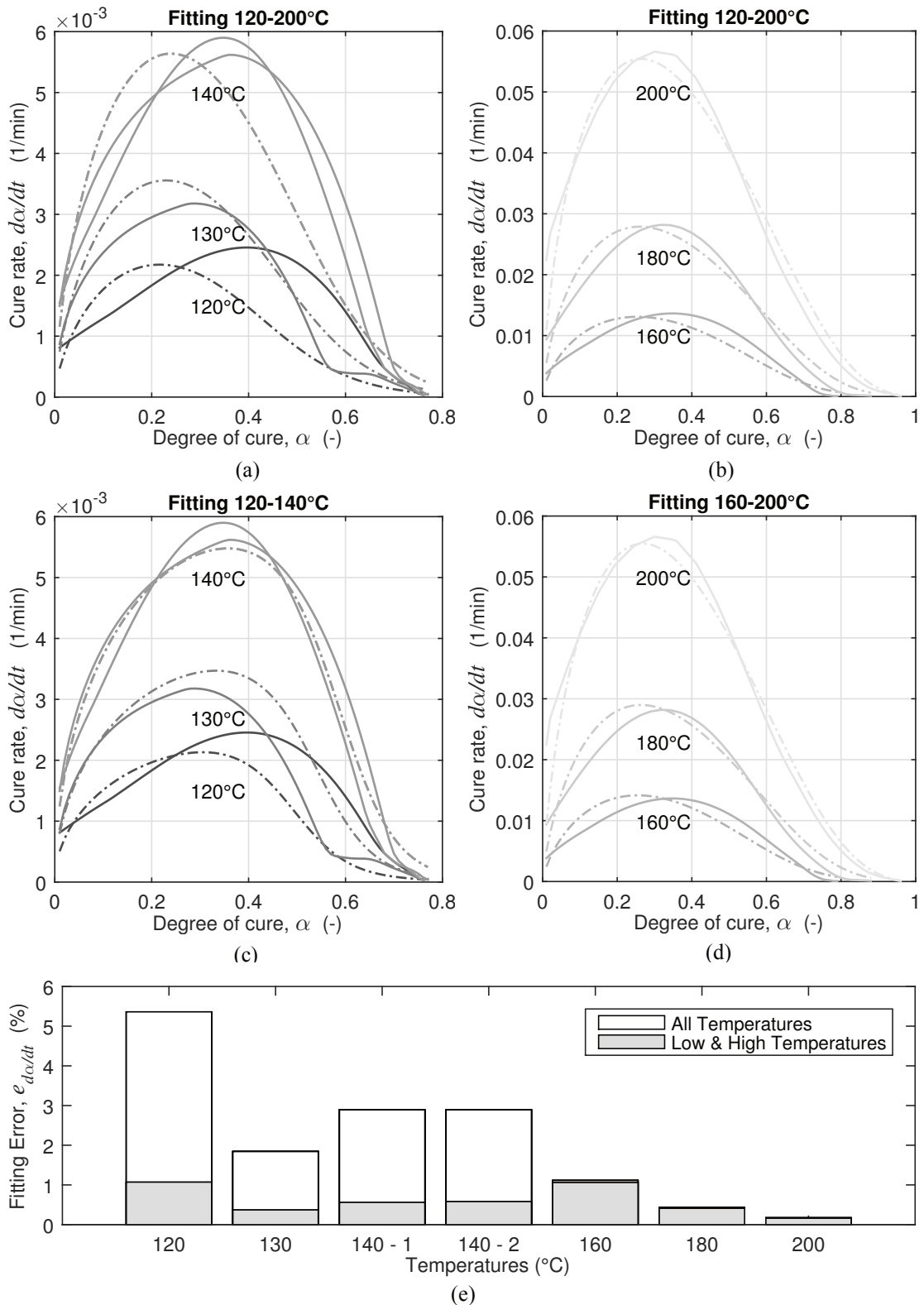


**Fig. 3-21: MTM 44-1 cure rate vs. degree of cure and global fitting error**

(a) & (b) Modeled (dotted line) and experimental data (solid line) using one set of coefficients to model the whole temperature range (c) & (d) modeled (dotted line) and experimental data (solid line) using two sets of coefficients, one per temperature range (e) Fitting error for whole (white) or part of the temperature range (grey).

## 3.4.2 Rheometry

Rheological characterization of the MTM 44-1 resin is performed with the aim to determine the material's viscosity and the time available until gelation for a range of temperatures relevant to OoA processing. The measurements are used as a basis for the development of a model which will predict the resin viscosity evolution for a wider range of temperatures and heating rates. This model is used in OoA process simulation to predict the impregnation time of the MTM 44-1 prepreg tows and plies. Details of the characterization method, data analysis and viscosity fitting are presented in this Section.

### 3.4.2.1 Material Preparation

The MTM44-1 resin is supplied from the manufacturer as a film with a nominal areal weight of 182gsm and a thickness of 0.2mm, deposited between two backing papers. Eight or nine plies of the film are stacked on top of each other at room temperature, in order to form a sample thick enough to be tested with the Rheometer. A 300mm x 300mm plate of resin with a thickness of 1.6-1.8mm is constructed for this purpose. As conventional degassing of the resin led to adverse effects (i.e. foaming), to reduce the air entrapped between the resin films due to stacking samples in the size of the plate diameter (25mm) were cut out of the resin plate and compacted in the Rheometer. During the compaction a temperature of approximately 40 °C was used, with a parallel application of 0.9 bar of pressure ( $9 \cdot 10^4$  Pa and a maximum force of 45 N), until a thickness between 0.9-1.1mm was attained. At this stage the sample is wider and thinner, while most of the air initially enclosed in the samples (i.e. due to ply stacking) shall be pushed out. Once the required thickness was obtained, the force was released and the material was removed from the rheometer and left at room temperature to cool down. Once the sample was sufficiently cold, it was cut to the size of the plate used for testing in order to perform the actual measurement.

### 3.4.2.2 Method

The viscosity of the MTM44-1 epoxy resin film was measured using an Anton Paar MCR 302 Rheometer in an oscillatory mode. A plate-plate configuration was selected (see Appendix d), while the tests were performed inside a Peltier Chamber assisted by a water cooling/heating system (Viscotherm VT2). Disposable aluminum plates of 25mm diameter were used for the measurements. Several parameters, such as the storage ( $G'$ ) and loss modulus ( $G''$ ) and the loss factor ( $\tan \delta$ ) could be measured simultaneously in the rheometer apart from the viscosity, which were used to determine the gel-time of the resin when the loss factor is unity (see Section 2.2.4.2 for more details). Isothermal viscosity measurements were performed in the temperature range 100-200 °C, while heating rates of 1, 2 and 3 °C/min were selected for the dynamic measurements. The selection of the temperature range used for testing was driven by the two-step cure cycle proposed by the prepreg manufacturer [41, 225]. Amplitude and frequency sweeps were



performed in advance of the characterization tests, in order to establish that the resin viscosity was measured in the Linear Viscoelastic Domain (see Appendix d and e). Based on these preliminary tests, a constant frequency of 1Hz and constant strain amplitude of 0.1% was selected for the resin's gel-point determination. The settings selected for the rheological characterization of the MTM 44-1 resin closely match those utilized by Kratz et al. for the MTM 45 resin characterization [159].

Before initiating oscillatory testing, a small normal force was applied to the material ( $F_N \simeq 0.06 N$ ) to ensure a good contact of the plate with the sample. To avoid significant squeeze-out of the resin, the minimum distance allowed between the plates was restricted to a minimum of 0.75mm. Shortly before the oscillatory test starts, force control is activated, though no force was actually applied on the material throughout the test ( $F_N = 0 N$ ). By enabling force control, an electromagnetic sensor positioned under the bottom plate of the rheometer was activated throughout the measurement, ensuring the plate distance was respected. This aspect was crucial to accurate viscosity characterization of a curing resin at high temperatures, since a deformation of the set-up may lead to a false determination of the distance between the plates of the rheometer and modify the material's stress state. The exact sampling time is not pre-defined by the user. The first point is selected automatically once the noise of the measurement is reduced and a constant value of viscosity can be measured. During isothermal measurements, the sampling rate was universally defined to extend further than the gel-time of the resin (5000 points). To avoid potential damage of the shaft caused by an increased torque due to eventual resin gelling and curing, the tests are interrupted manually at an earlier time. A constant logging frequency of one measurement point per second is selected during the rheological tests performed at non-isothermal temperature.

### 3.4.2.3 Results and Analysis

Isothermal measurements of the MTM 44-1 resin viscosity were used as a basis for the development of a model, which can predict the viscosity evolution at isothermal as well as non-isothermal conditions in the composite laminate. Non-isothermal measurements were used to validate the developed model. Furthermore, the storage and loss moduli were used to develop a model for the gelation time of the material. A summary of the temperature conditions used during isothermal and non-isothermal viscosity tests are given in Tab. 3-13 and Tab. 3-14 respectively. Four samples were tested at each temperature and heating rate, nonetheless fewer samples were eventually used in model fitting, due to unwanted influences on the experimental results such as the presence of large air bubbles in the sample, or sample handling effects.

#### **Isothermal Characterization**

The evolution of the average viscosity, storage, loss modulus and loss factors of the MTM 44-1 resin were determined for temperatures between 110-180 °C and presented

in Fig. 3-22. Viscosity measurements above 180 °C were not possible, due to the advanced curing state of the material before the beginning of the measurement.

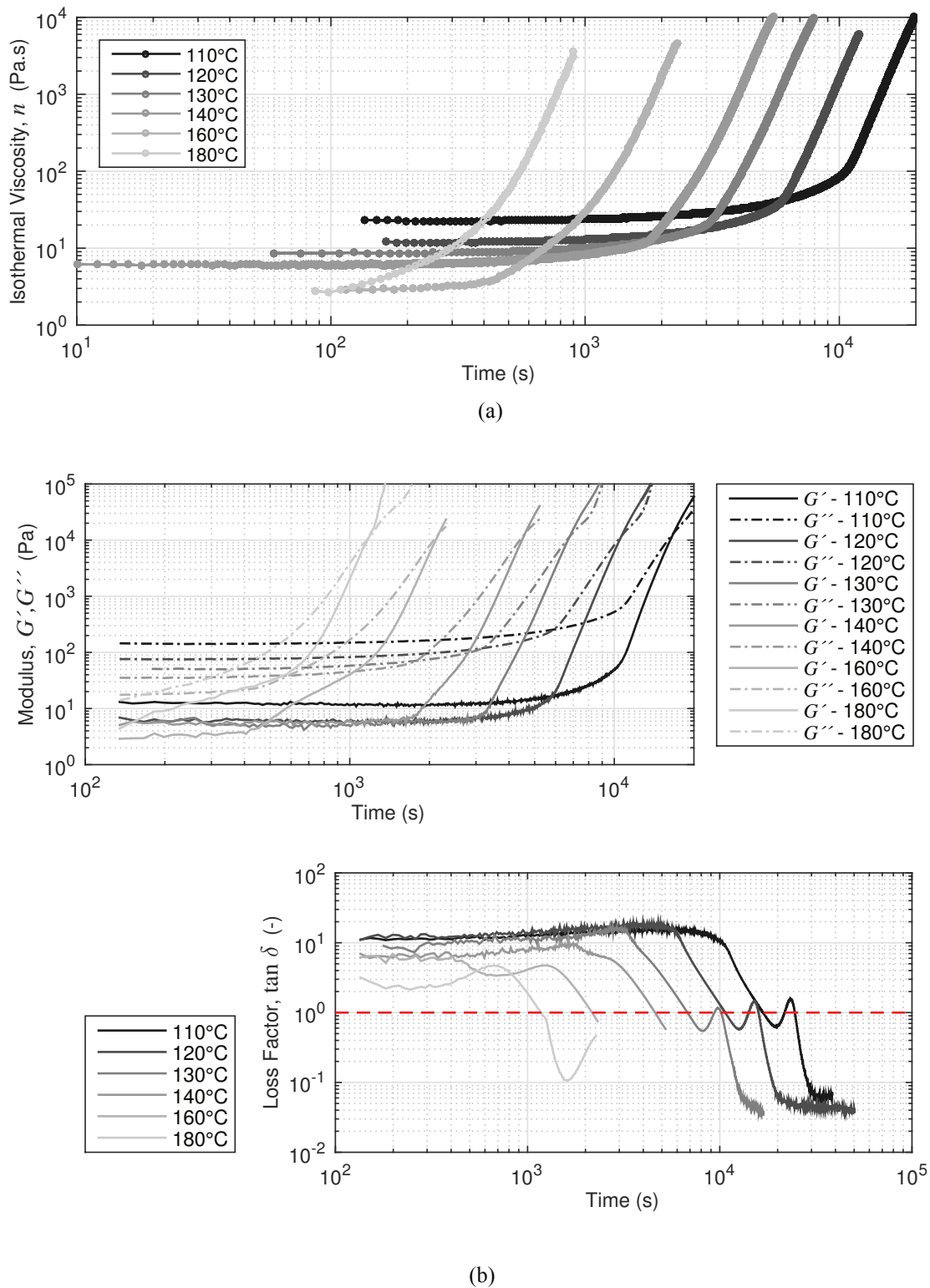


**Fig. 3-22: Rheological properties of the MTM 44-1 resin generated between 110-180°C using isothermal oscillatory parallel plate rheometry (see Appendix d)**

(a) Viscosity ( $n^* = n$ ) and (b) storage ( $G'$ ), loss modulus ( $G''$ ) and loss factor ( $\tan \delta$ ).

The initial resin viscosity  $n_0$  was higher at lower temperatures. The time delay between sample insertion in the heated plate and measurement initiation varied between 20-100s, depending on sample quality, handling and contact quality between the plates and sample. This time delay was included in the elapsed time, captured in the  $x$ -axis of Fig. 3-22. Particularly at high temperatures (160-180 °C), this delay had a significant effect on the initial viscosity measured. The time and viscosity of the MTM 44-1 resin at the gel-point is summarized in Tab. 3-13, for all temperatures evaluated. The gel time was identified as the time when  $\tan \delta = 1$  (see discussion in 2.2.4.2).

**Tab. 3-13: Minimum viscosity  $n_0$ , gel time  $t_{gel}$  and viscosity at the gel point  $n_{gel}$ , measured at a range of temperatures during isothermal characterization of the MTM 44-1 resin**

$T$ (°C)	$n_0$ (Pa·s)	$t_{gel}$ (s)	$n_{gel}$ (Pa·s)	Sample #
110	23.2	16800	$3.00 \cdot 10^3$	1
120	12.0	10700	$2.68 \cdot 10^3$	3
130	8.6	6780	$2.58 \cdot 10^3$	3
140	6.0	4600	$3.25 \cdot 10^3$	4
160	2.9	2150	$2.73 \cdot 10^3$	4
180	2.4	1200	$2.82 \cdot 10^3$	4

Increasing temperatures lead to a decrease in the resin's gel-time ( $n_{gel}$ ). This shift in lower gelation times ( $t_{gel}$ ) observed at higher measurement temperatures has limited effect in the magnitude of the viscosity at gel. The MTM 44-1 viscosity at the gel point remains constant between  $2.6 \cdot 10^3 - 3.3 \cdot 10^3$  Pa·s. This is an important observation which can assist in developing a process monitoring scheme to detect the resin gel point using the average viscosity as a detection criterion, independent of processing temperatures.

### Non-Isothermal Characterization

Non-isothermal viscosity measurements were performed according to the processing cycles proposed by the material supplier (1, 2, 3 °C/min – see Fig. 3-23 (a) and (c)) and served as validation to the model developed and presented in Section 3.4.3.3. The measurement of the loss, storage modulus and the loss factor (see Fig. 3-23 (b), (d)), provide information on the time and temperature at which gelling occurs during each cure cycle. Since gelling implies the transition of the polymer from its liquid to its gelled state (gel-point), at this stage the macroscopic flow velocity of the resin and the compaction of the laminate slow down significantly. This marks the end of the process, which can be modeled using flow and compaction physics, since at higher states of cure other effects are dominant (i.e. diffusion). Knowledge of the resin gel-time and the pressure state in the material will assist in selecting the processing cycle, which enables maximum wetting of the prepreg before gelation takes place (see Chapter 4 for details on the OoA simulation framework developed).

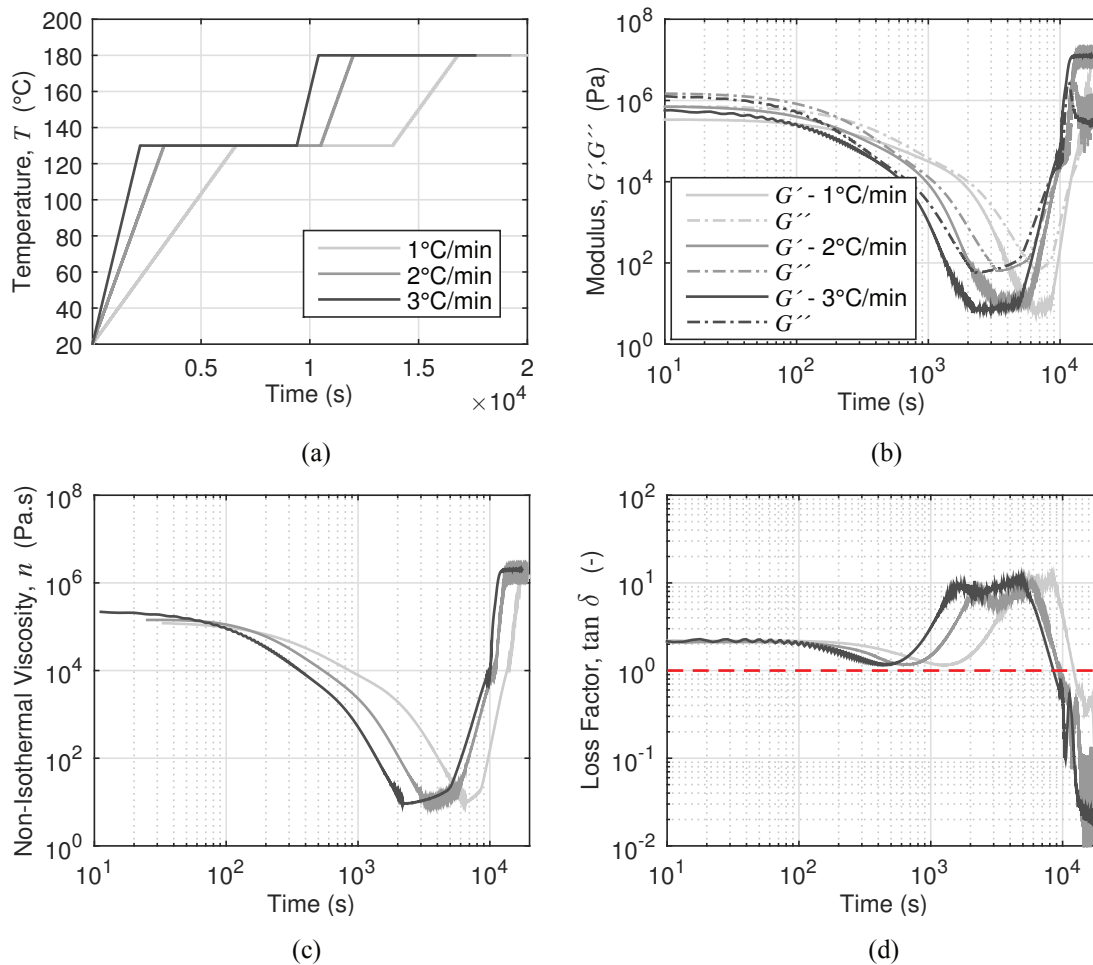


**Fig. 3-23: Non-isothermal oscillatory measurements of MTM 44-1 resin at three heating rates generated using a parallel plate rheometer (see Appendix d)**  
 (a) Applied temperature cycles (b) storage and loss modulus ( $G'$ ,  $G''$ ) (c) viscosity ( $n^* = n$ ) and (d) loss factor ( $\tan \delta$ ).

Although the time to minimum viscosity  $t_{min}$  is longer at slower heating cycles, the minimum viscosity  $n_{min}$  can be considered constant (10 Pa.s). A non-linear time delay between curves generated at different heating rates is observed. This may imply a difference in the molecular interaction between resin constituents at different heating rates. Gelling takes place during the first temperature hold (130 °C), at  $3 \cdot 10^3$  Pa.s.

**Tab. 3-14: Minimum viscosity  $n_{min}$ , time at minimum viscosity  $t_{min}$ , gel time  $t_{gel}$  and viscosity  $n_{gel}$  of the MTM 44-1 resin, for three cure cycles with heating rates between 1-3 °C/min**

$\frac{dT}{dt}$ (°C·min <sup>-1</sup> )	$t_{min}$ (s)	$n_{min}$ (Pa·s)	$t_{gel}$ (s)	$n_{gel}$ (Pa·s)	Sample #
1	6597.9	9.9	12122	$3.28 \cdot 10^3$	2
2	3344.3	9.6	9400.2	$3.13 \cdot 10^3$	5
3	2320.2	9.2	8515.2	$3.19 \cdot 10^3$	2

### 3.4.3 Rheological Modeling

The MTM 44-1 resin viscosity was modeled based on data generated using a rheometer according to the methods described in Section 3.4.2. The approach proposed by Kiuna et al. [164] and Keller et al. [165] is modified and used as a basis for simulating the resin viscosity evolution during the OoA process. Furthermore, a model able to predict the resin gelation time at isothermal conditions was developed to offer insights within the processing window of the prepreg OoA.

#### 3.4.3.1 Isothermal Gel-time

The results of the rheological measurements presented in Section 3.4.2 are used to define the resin gel time at temperatures between 110-180 °C. To enable prediction of the gel time at temperatures beyond those characterized, the results of gel-time versus temperature were fitted to Equation (3-38).

$$t_{gel} = G_1 \exp(G_2 T) \quad (3-38)$$

The fitting of the experimental results are presented in Fig. 3-24 (the temperature  $T$  is given in °C). The least-square fit method is used to determine the coefficients  $G_1$ ,  $G_2$  in Matlab R2014b. The fitting coefficients and parameters characterizing the quality of the fit are summarized in the table of the Fig. 3-24.

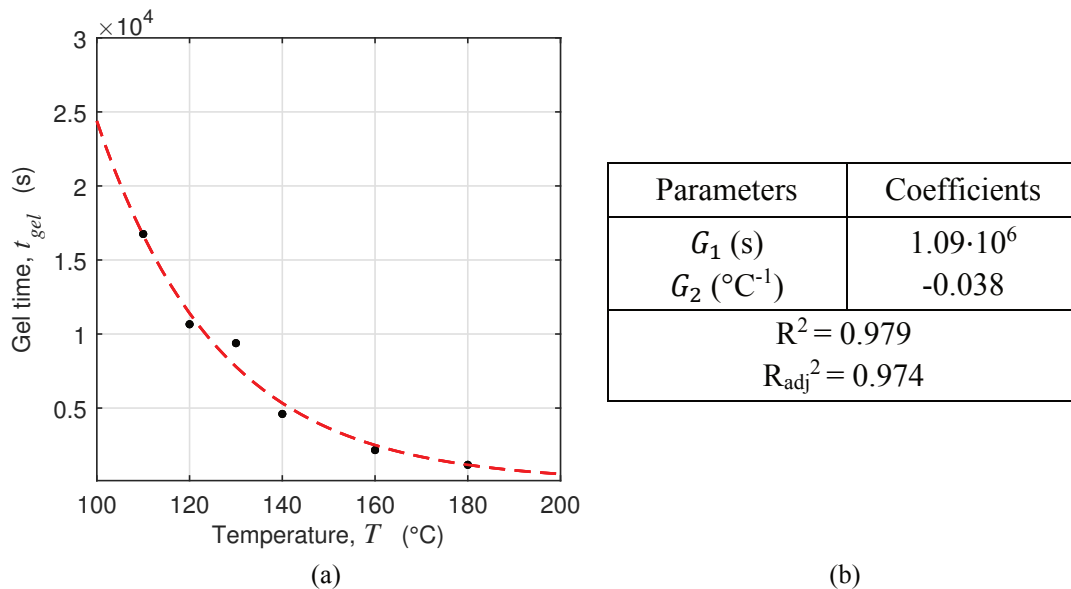


**Fig. 3-24: Predicted gel time of the MTM 44-1 resin at isothermal temperatures (100-200 °C)**

(a) Plot of the MTM 44-1 gel times, measured at various isothermal temperatures and  
 (b) Table incl. fitting coefficients and regression quality achieved (Equation (3-31)).

### 3.4.3.2 Isothermal Viscosity Model

Kiuna et al. [164] introduced two non-dimensional terms in order to capture the viscosity evolution of a resin system with evolving temperature. The first term  $a$  expresses the viscosity evolution as a function of cure according to Equation (3-39), while  $\tau$  expresses the elapsed cure time according to Equation (3-40), both being dimensionless quantities.

$$a = \ln\left(\frac{n}{n_0}\right) \quad (3-39)$$

$$\tau = k(T) t \quad (3-40)$$

The uncured resin viscosity at different isothermal temperatures is expressed as  $n_0(T)$ , while  $k(T)$  reflects the cure rate advancement at temperature  $T$ .

The viscosity evolution during an isothermal heating cycle is calculated from Equation (3-41), after substituting Equations (3-39) and (3-40). Knowledge of the functions  $n_0(T)$ ,  $k(T)$ ,  $g(a)$  at the temperatures of interest is required, in order to implement a model, which explicitly reflects the rheochemical behavior of the MTM 44-1 resin.

$$a = f(\tau) \quad (3-41)$$

The relationship of Equation (3-41) is defined by the shape of the curve which best fits the normalized viscosity  $a$ , against the dimensionless time  $\tau$ , for all temperatures of interest. Kiuna et al. [164], developed a simple linear relationship to describe the behavior of a two part epoxy/amine resin (LY5052/HY5052). Keller et al. [165] used Equation (3-42) to describe the behavior of the normalized viscosity against the normalized time, for a toughened DGEBA epoxy resin (XB3585, Huntsman Advanced Materials).

$$a = y_0\tau + A_{n,3} \exp\left(\frac{\tau}{E_{n,3}}\right) \quad (3-42)$$

The evolution of  $a$  versus  $\tau$  for the MTM 44-1 resin system for all isothermal temperatures is shown in Fig. 3-25. A significant difference in the slope of the curves is observed between the curves at low (110 - 140 °C) and high temperature ranges (160 - 200 °C). This difference could imply a difference in the reaction kinetics of the resin at the two temperature ranges concerned, possibly explained by the presence of two hardeners activated at different temperatures. This assumption is also confirmed by the DSC investigations, as discussed in Section 3.4.1.2. Fitting the isothermal curves with one set of coefficients throughout the temperature range is therefore not feasible.

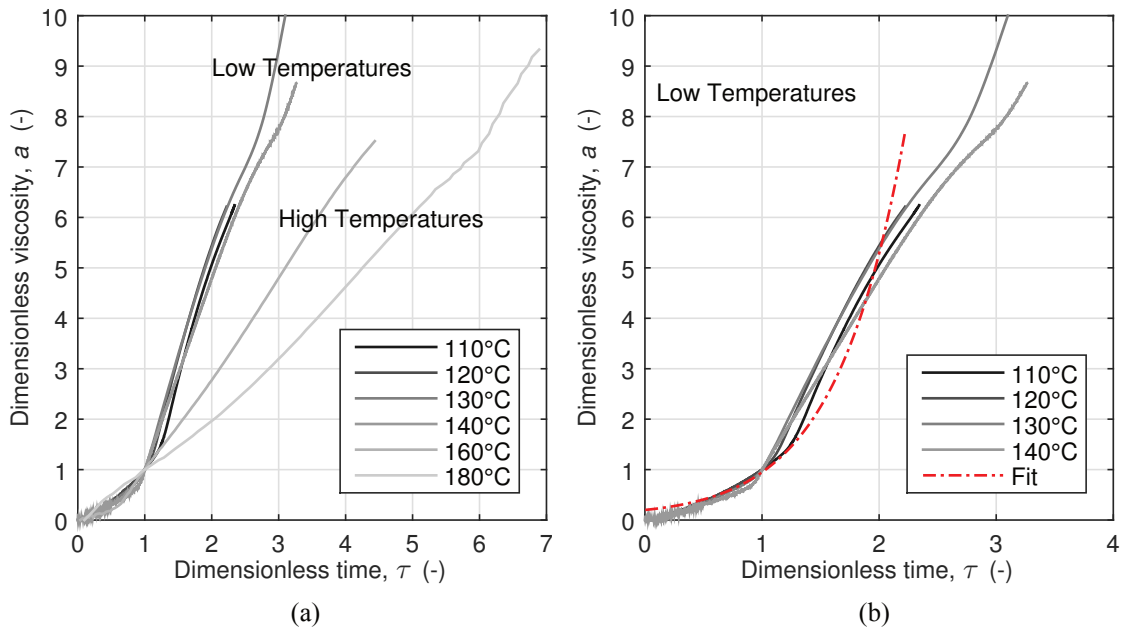


**Fig. 3-25: Dimensionless MTM 44-1 resin viscosity (a) vs dimensionless time ( $\tau$ )**  
 (a) All temperatures tested (b) Selection of the low temperature range used for fitting.

A non-linear fit utilizing the trust-region reflective algorithm and the Bisquares weight method was used in Matlab to determine the coefficients of Equation (3-42). The determined constants and regression quality are summarized in Tab. 3-15. As shown in Fig. 3-25 (b), Equation (3-42) fits well the isothermal viscosity curves of the MTM 44-1 resin for viscosities up to approximately the gel-point.

**Tab. 3-15: Coefficients of Equation (3-42), determined through the best fit of the normalized viscosity vs normalized time for the MTM 44-1 resin (95% Confidence Interval)**

Parameters	Coefficients	Lower Bound	Upper Bound
$y_0$ (-)	-0.1	fixed	fixed
$A_{n,3}$ (-)	0.2	fixed	fixed
$E_{n,3}$ (-)	0.604	0.6037	0.6042
Quality of fit			
$R^2$	0.962		
$R_{adj}^2$	0.962		
SSE	1315		

The terms  $n_0$  and  $k$  have an Arrhenius dependency with temperature.

$$n_0(T) = A_{n,1} \exp\left(\frac{E_{n,1}}{RT}\right) \quad (3-43)$$

$$k(T) = A_{n,2} \exp\left(\frac{E_{n,2}}{RT}\right) \quad (3-44)$$

The y-intercept and slope of the line of  $\ln n_0$  and  $\ln k$  versus  $1/T$  depicted in Fig. 3-26 (a) and (b) were used to calculate the coefficients  $E_{n,1}$  and  $A_{n,1}$  as well as  $E_{n,2}$  and  $A_{n,2}$  respectively in the low temperature range (110-140°C), utilizing Equations (3-43) and (3-44).

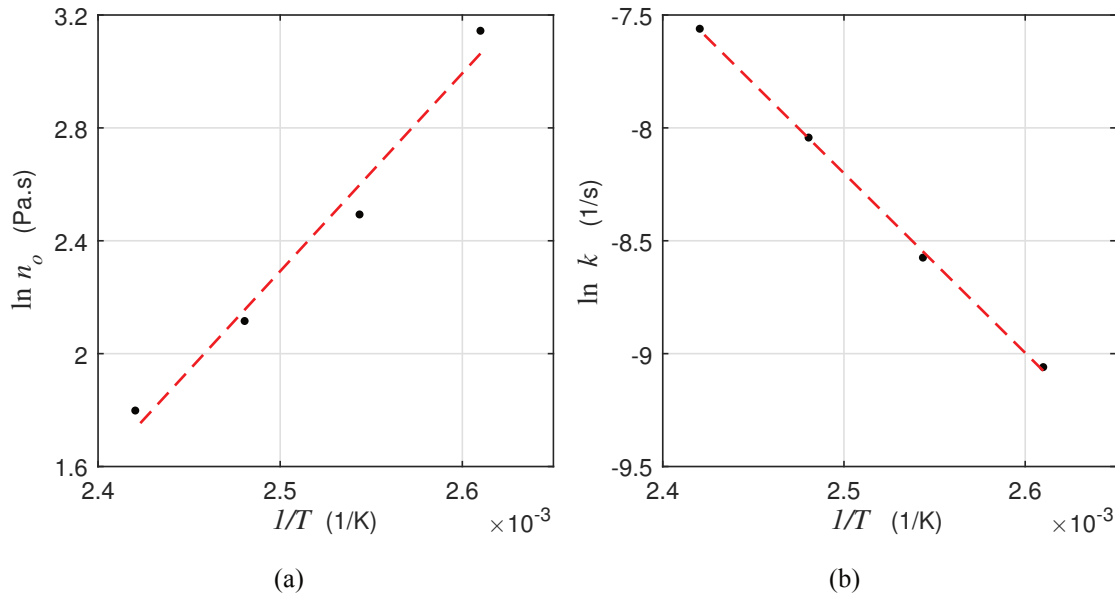


**Fig. 3-26: Determination of viscosity coefficients  $A_{n,1}$ ,  $A_{n,2}$ ,  $E_{n,1}$ ,  $E_{n,2}$  using linear regression**  
 (a) Initial viscosity and (b) cure rate advancement functions for the MTM 44-1 resin.

The linear least-square method is used to determine the two sets of coefficients, as shown in Fig. 3-26(a) and (b) respectively. The fitting coefficients, the constants  $A_{n,1}$ ,  $E_{n,1}$  as well as  $A_{n,2}$ ,  $E_{n,2}$  and the regression quality parameters are summarized in Tab. 3-16.

**Tab. 3-16: Coefficients determined via linear regression of the viscosity  $n_0(T)$  and cure rate advancement  $k(T)$  functions of the MTM 44-1 resin**

Properties	Coefficients	Parameters	Coefficients
Slope - $\ln(n_0)$ vs $1/T$	-7956	$A_{n,1}$ (Pa·s)	$2.41 \cdot 10^{-7}$
y - Intercept	11.69	$E_{n,1}$ (J·mol <sup>-1</sup> )	58301.9
Quality of fit			
$R^2 = 0.977$			
$R_{adj}^2 = 0.9654$			
Slope - $\ln(k)$ vs $1/T$	7013	$A_{n,2}$ (s <sup>-1</sup> )	$1.19 \cdot 10^5$
y - Intercept	-15.24	$E_{n,2}$ (J·mol <sup>-1</sup> )	-66150
Quality of fit			
$R^2 = 0.999$			
$R_{adj}^2 = 0.999$			



An empirical term,  $S_f$ , is implemented by Keller et al. [165] to adjust the shift in gel time of the viscosity at different temperatures. This coefficient is a linear function of the temperature for the MTM 44-1 resin, described by Equation (3-45).

$$S_f(T) = A_{n,4} T + E_{n,4} \quad (3-45)$$

The shifting factor of the highest temperature modeled was set to one  $S_f(200\text{ }^\circ\text{C}) = 1$ , while it becomes zero at a temperature where no gelling is considered to take place, which in this case is  $S_f(100\text{ }^\circ\text{C}) = 0$ . The coefficients  $A_{n,4}, E_{n,4}$  are summarized in Fig. 3-27(b), determined via a linear least-square fitting via Equation (3-45).

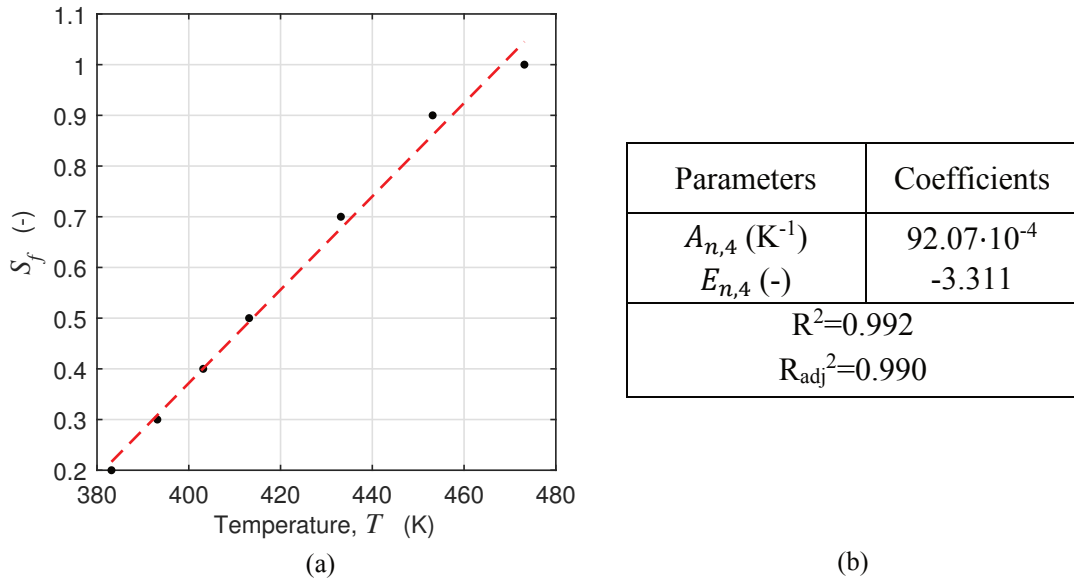


**Fig. 3-27: Determination of the shifting factor  $S_f$  using linear regression**

- (a) Plot of the MTM 44-1 gel times, for a range of isothermal temperatures and  
 (b) Table incl. fitting coefficients and regression quality achieved (Equation (3-45)).

The isothermal MTM44-1 viscosity at a given temperature was calculated by the analytical expression of Equation (3-46), developed by Keller et al. [165].

$$n(t) = A_{n,1} \exp\left(\frac{E_{n,1}}{RT}\right) \cdot \exp\left(\frac{\frac{A_{n,2} \exp\left(\frac{E_{n,2}}{RT}\right)}{E_{n,3}} \cdot S_f t}{\left(y_0 + A_{n,3} \exp\left(A_{n,2} \exp\left(\frac{E_{n,2}}{RT}\right) \cdot \frac{t}{E_{n,3}}\right)\right)}\right) \quad (3-46)$$

A comparison of the modeled and experimental viscosity of the MTM 44-1 resin is presented in Fig. 3-28. The model coincides well with the experimental data, particularly in the range between 110-130  $^\circ\text{C}$ . This temperature range is suggested for the first temperature dwell during OoA processing [225]. At 180  $^\circ\text{C}$ , curing of the resin has already

initiated prior to the measurement, which led to a loss of a significant amount of the initial viscosity evolution data.

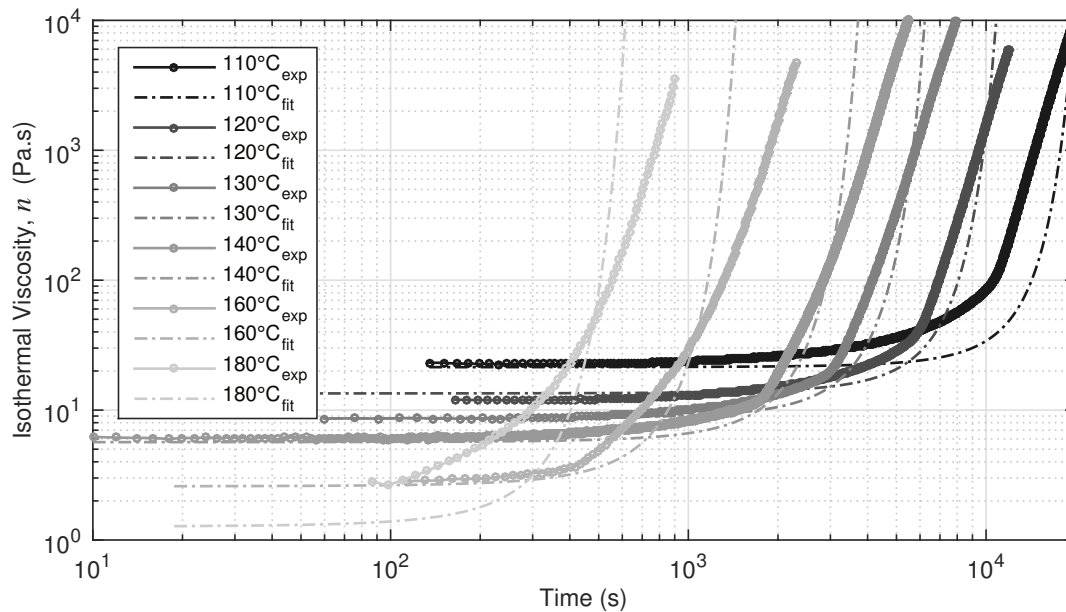


**Fig. 3-28: Comparison between the experimental and modeled isothermal resin viscosity**

The fitting quality of the rheological model is evaluated at each temperature using the global error  $e_{n_{iso}}$  expressed in percent according to Equation (3-47).

$$e_{n_{iso}} (\%) = \frac{1}{\bar{n}} \sqrt{\frac{\sum_{i=1}^N (n_i - \hat{n}_i)^2}{N}} \quad (3-47)$$

The average experimental viscosity is expressed as  $\bar{n}$ ,  $n_i$  is the experimental viscosity and  $\hat{n}_i$  the viscosity calculated by the rheological model, for a total of  $N$  measurements. Since the viscosity spans within a range of several orders of magnitude, the error calculations are limited to the time where the modeled and experimental viscosity curves cross each other, as shown in Fig. 3-28. The gel-time results and the fitting quality attained in the selected time-frame are summarized in Tab. 3-17.

**Tab. 3-17: Simulated MTM 44-1 resin gel time and time interval used for determining the fitting quality (Equation (3-46))**

$T$ (°C)	$t_{gel}$ (s)	Fitting time (s)	$R^2$	$R_{adj}^2$	$e_{n_{iso}}$ (s)
110	16800	135 up to 18700	0.639	0.640	1.11
120	10700	165 up to 10400	0.732	0.735	0.93
130	9380	63 up to 5600	0.842	0.824	0.69
140	4600	10 up to 3200	0.824	0.825	0.55
160	2160	113 up to 1200	0.615	0.632	0.69

### 3.4.3.3 Non-Isothermal Viscosity Model

Knowledge of the MTM44-1 resin viscosity is of great significance to the prediction of the resin flow velocity under non-isothermal conditions. Therefore, the development of a model which accurately predicts the evolution of the MTM44-1 viscosity at non-isothermal conditions is critical to OoA processing. The approach presented in Section 3.4.3.2, is adapted here to enable non-isothermal viscosity prediction.

In this case the differential form of Equation (3-46) proposed by Kiuna et al. [164] given by Equation (3-49) is used with the aim to implement it directly in COMSOL Multiphysics.

$$d\tau = g'(a) da \rightarrow \frac{da}{dt} = \frac{k(T)}{g'(a)} \quad (3-48)$$

$$\frac{dn}{dt} = n \cdot \left( \underbrace{\frac{k(T)}{g'(a)}}_I + \underbrace{\frac{1}{n_0} \frac{dn_0}{dT} \frac{dT}{dt}}_II \right) \quad (3-49)$$

The first term of Equation (3-49) captures the cure advancement, while the second captures the viscosity evolution due to the effect of temperature. The term  $g'(a)$  given in Equation (3-50) represents the first derivative of Equation (3-42) and correlates the dimensionless viscosity  $a$ , versus the dimensionless time  $\tau$ .

$$g'(a) = \left( y_0 + \frac{A_{n,3} k(T)}{E_{n,3}} \right) \cdot \exp \left( \frac{k(T)}{E_{n,3}} \cdot t \right) \quad (3-50)$$

Equation (3-49) is fully determined when Equations (3-43), (3-44) and (3-50) are substituted and the initial viscosity  $n_0$  and the temperature evolution over time is known. Matlab R2014b and the trust region reflective non-linear least squares method is used to determine the coefficients  $A_{n,1}, E_{n,1}, A_{n,2}, E_{n,2}, A_{n,3}, E_{n,3}, S_f$  and  $y_0$  from the best fit of Equation (3-51) to the experimental data.

$$n(t, T) = A_{n,1} \exp \left( \frac{E_{n,1}}{RT} \right) \cdot \exp \left( \frac{\frac{\sum_i^N A_{n,2} \exp \left( \frac{E_{n,2}}{RT} \right) \cdot S_f \cdot t_i}{E_3}}{\left( y_0 + A_{n,3} \exp \left( \frac{\sum_i^N A_{n,2} \exp \left( \frac{E_{n,2}}{RT} \right) \cdot \frac{t_i}{E_{n,3}} \right) \right)} \right) \quad (3-51)$$

The coefficients of Equation (3-51) are determined and utilized in the implementation of the MTM 44-1 viscosity model in COMSOL Multiphysics in the form of the partial differential equation of Equation (3-49). The shifting factor included in Equation (3-51) is omitted in Equation (3-49), since the temperature evolution is explicitly included in

the second term of the partial differential equation. The global fitting error between the measured and simulated viscosity (in COMSOL Multiphysics) up to the gel-point  $e_{n_{dyn}}$  is calculated via Equation (3-52).

$$e_{n_{dyn}} (\%) = \frac{1}{n_o} \sqrt{\frac{\sum_{i=1}^N (n_i - \hat{n}_i)^2}{N}} \quad (3-52)$$

The viscosity of the MTM 44-1 resin predicted by the analytical equation (3-51) and the partial differential Equation (3-49) which was implemented in COMSOL Multiphysics are compared in Fig. 3-29 against the experimental viscosity, for a heating rate of 2 °C/min. The coefficients determined from the best fit of the models to the experimental viscosity measured at 2 °C/min are summarized in the Table of Fig. 3-29 (b).

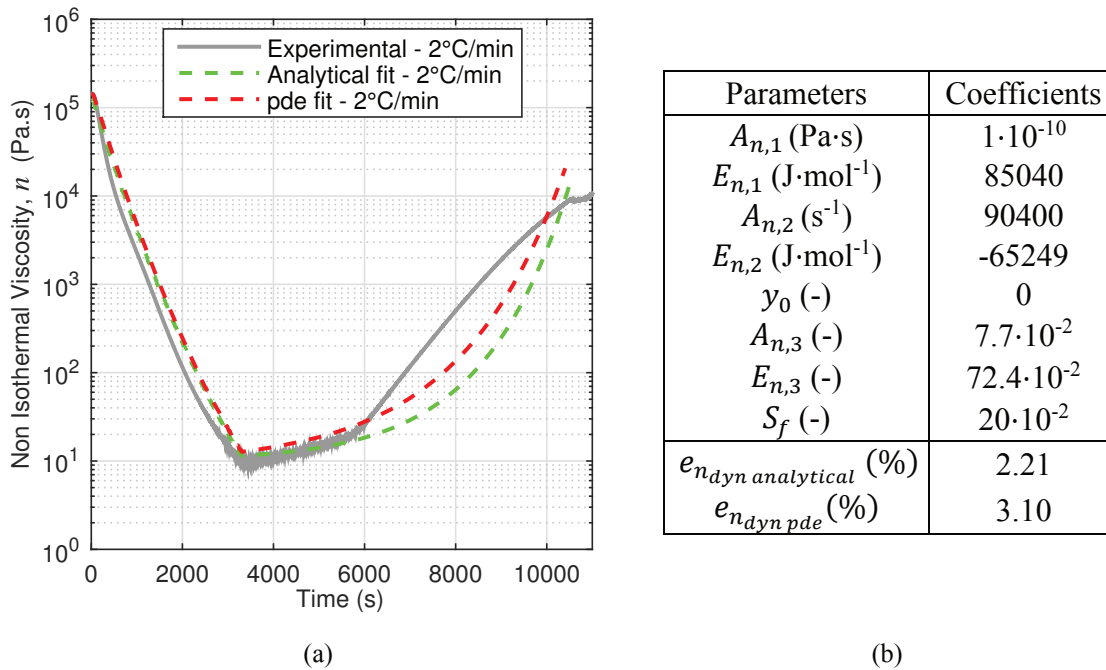


**Fig. 3-29: Comparison of the experimental and modeled MTM 44-1 resin viscosity resulting from the analytical (3-51) and pde (3-49) expressions at a heating rate of 2°C/min**

- (a) Graph showing the modeled viscosity, compared against the experimental data.  
 (b) Fitting coefficients and quality of fit quantified in each case by the global error.

Within the first 6000s of the heating cycle, a good fit is attained between measured and simulated viscosity. Beyond this time the experimental MTM44-1 viscosity increases almost linearly up to the gel point, while the model predicts a slower exponential increase. Nevertheless, the global error quantified up to 10000s is below 5%. Equations (3-49) and (3-51) are equivalent and both predict the MTM44-1 viscosity development as a function of temperature and time. The non-isothermal viscosity evolution of Equation (3-49) is incorporated in the OoA process simulation platform based on COMSOL Multiphysics, developed in the context of this work (see Section 4.2 for implementation

details). As shown in Fig. 3-29, the fit attained using both approaches is satisfactory. The difference in the predicted viscosity between the two approaches is due to:

- A higher initial viscosity, closer to the experimental one, is set as an initial condition for the pde implemented in COMSOL Multiphysics.
- A delayed resin heating rate is present in COMSOL compared to the experimental temperature utilized as an input in the analytical viscosity calculation.

During OoA processing, the laminate typically experiences a range of heating rates between 1-2 °C/min. Therefore, the coefficients of Equation (3-51) are determined in the specified range of heating rates using the trust region reflective, non-linear least squares method. The fitting coefficients determined are utilized to implement Equation (3-49) in COMSOL Multiphysics, while the quality of fit attained up to 6000s is shown in Fig. 3-30.

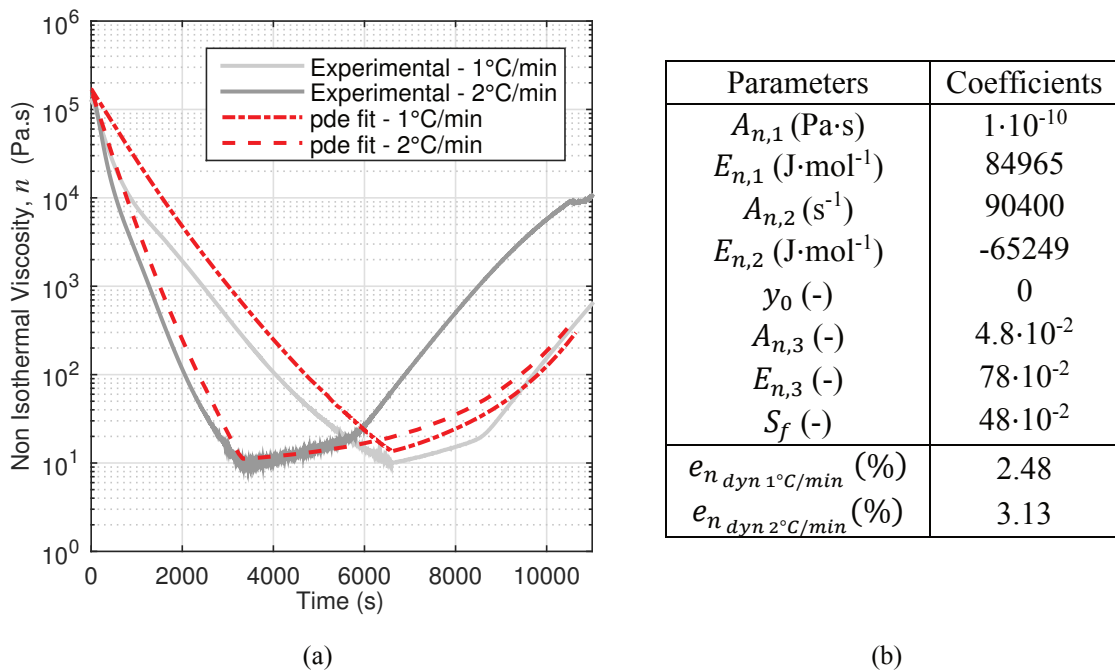


**Fig. 3-30: Comparison of the experimentally measured and modeled MTM 44-1 viscosity of Equation (3-49) implemented in COMSOL Multiphysics at 1 and 2 °C/min**

- (a) Graph showing the modeled viscosity, compared against the experimental data.  
 (b) Fitting coefficients and quality of fit quantified in each case by the global error.

The difference in the heating rate has an effect on the viscosity reduction rate in the early stages as well as the kinetics of network formation towards gelling. As shown in Fig. 3-30, the viscosity model can capture well the aspect of viscosity reduction and the minimum viscosity attained for both cycles up to approximately 6000s. A non-linear effect of the measured viscosity at 1 °C/min within the first 1000s may be caused by the increased air-content in the resin during the experiments and has a negative effect on the fitting quality of the experimental viscosity in this area. The viscosity increase towards

gelling for both heating rates cannot be captured accurately with only one set of fitting parameters. The simulated viscosity increase better matches the gelling characteristics of the viscosity measured at 1 °C/min.

#### **3.4.3.4 Conclusions and Perspectives**

The rheo-kinetics of the MTM44-1 resin system were investigated using Differential Scanning Calorimetry and a Rheometer. Particular emphasis was given in the development of models, which describe the resin viscosity evolution under isothermal or non-isothermal conditions, based on the experimental data generated in the context of this work. A model of the MTM 44-1 resin viscosity evolution as a function of time and temperature is implemented in COMSOL Multiphysics in the form of a partial differential equation (Equation (3-49)). The coefficients of the model were optimized for cycles with heating rates between 1-2°C/min, up to the resin gel-point and are utilized to perform sensitivity studies in Section 4.2 and for model validation in Chapter 5.

Since most air evacuation takes place within the first minutes of the OoA cure cycle, an accurate prediction of the initial resin viscosity enables accurate depiction of the interaction between the flow of resin and air through the dry tow, particularly at low temperatures where vacuum is being established. The quality of fit achieved between experimental and modeled data is very good during the time of transient heat evolution (6000s) and for heating rates in the range of 1-2 °C/min. The development of a model with broader applicability in terms of heating rates based on a thorough investigation of the chemical interactions, which lead to the untypical, non-exponential, heating rate dependent behavior of the MTM44-1 resin towards the gelling point shall be aimed. This will provide insights for further modification of the relationship proposed or the development of a mechanistic model, with the aim to improve the fitting quality of the experimental viscosities and an increase in applicability in terms of heating rates.

### **3.5 Summary and Discussion**

This Chapter provides an overview of all material characterization aspects of the MTM 44-1 resin and prepreg, which are utilized as input for the Out-of-Autoclave Process simulation developed in the context of this thesis and presented in Chapter 4. The material characterization effort focused on the characterization of the viscosity and cure kinetics (rheokinetics) of the resin film and the air permeability of the prepreg, at various processing stages.

The microscopic characterization of the model material was imperative for the development of a geometrically representative modeling scheme. The rest of material inputs required for the simulation are acquired from literature data. The single-sided, partial prepreg impregnation with resin and the quantification of the initial volume fractions of constituents assisted in the development of a suitable flow modeling strategy and the

definition of appropriate initial and boundary conditions for modeling the OoA impregnation process. Apart from the microstructure, the transient in-plane permeability of the MTM 44-1 prepreg to air was characterized for a range of porosities. The measurement results were fitted to an equation describing the evolution of the prepreg's permeability in relation to its residual porosity.

Finally the rheo-kinetic characterization of the MTM 44-1 resin was performed with the primary goal to develop a model able to predict the resin viscosity evolution during OoA processing (isothermal and non-isothermal). Both the permeability and viscosity models presented in this Chapter were integrated in the OoA processing simulation developed in COMSOL Multiphysics (see Section 4.2). Well-established techniques were adapted as necessary to reflect the specific needs of the materials under study, since there is limited literature available specifically for the characterization of OoA prepregs. The mesoscopic structure of the prepreg and the local volume fractions and tow shapes have been extensively characterized using optical (i.e. microscopy or CT) and physical techniques (i.e. mercury porosimetry). This information can be used in future work to expand the simulation, in order to further include a detailed mesoscopic representation of the material and therefore a more detailed representation of the textile architecture of the fabric utilized as a basis for the MTM 44-1 prepreg.





## 4 The Impact of Air Evacuation on the Impregnation of OoA Prepregs

Aim of the simulation framework developed in the context of this work is the optimization of large monolithic parts manufactured outside the Autoclave and specifically the reduction of the resulting intra-tow porosity. A toolkit of models is developed to address the air evacuation through the initially dry tows of OoA prepregs, with emphasis on capturing the local air pressure evolution and its influence on the simultaneous impregnation of the tows with resin. Strategies for intra-tow porosity reduction can be developed through virtual testing and down-selection of the temperature and pressure cycles, which is the focus of this work.

In Section 4.1, a toolkit of models implemented in Matlab is developed and can be used to calculate the impregnation time of a prepreg tow with resin at isothermal conditions, under the influence of three in-plane air evacuation scenarios, which can be encountered during vacuum processing outside the Autoclave. To capture all potential air evacuation states encountered during OoA processing, the ‘delayed air evacuation model’ is developed and presented in Section 4.1.2.2. By explicitly modeling the transient air flow through the dry fibrous domain of the tow and coupling the local air pressure to the resin front progression via boundary conditions, the local tow impregnation state can be predicted. This methodology comes as an improvement of the state-of-the-art expression developed by Arafath et al. [35], which provides information on the lumped mass of air evacuated out of the laminate and is thus not able to capture the local evolution of vacuum pressure in the tows. Sensitivity studies using the ‘delayed air evacuation model’ demonstrate the robustness of the proposed scheme for a wide range of time scales at isothermal conditions.

A 2D Finite Element simulation based on a moving mesh formulation (Deformed Geometry) is implemented in COMSOL Multiphysics (v.5.2), presented in Section 4.2. This is an extension of the coupling approach presented in Section 4.1 to include transient heating effects at a prepreg/ply level. Sensitivity studies demonstrate the effect of various material properties in the vacuum quality attained during debulking (Section 4.2.4.2) and provide guidelines for cure cycle optimization (Section 4.2.4.3). Finally the influence of temperature gradients on the impregnation quality and the porosity developed inside the prepreg, are discussed based on two case studies presented in Section 4.2.4.4. A summary of the findings and comparison with literature is performed in Section 4.3. It shall be noted that the consolidation of the laminate during OoA processing has not been taken into account.

## 4.1 Isothermal Tow Impregnation

The equations used for modelling resin flow under the influence of three air evacuation scenarios are presented in this Section. In 4.1.1 the domain and assumptions used as the basis for the development of the model presented in 4.1.2 are defined. Sensitivity studies show the capabilities of the delayed air evacuation model in 4.1.3.

Parts of this Section, including text and figures, are based on the article [19] and conference proceedings [30, 192] published in the context of this dissertation. The content is reused here, in agreement with the co-authors.

### 4.1.1 Domain and Assumptions

Imaging of the MTM 44-1 prepreg plies, revealed a single sided impregnation via a resin film application process (images and detailed discussion included in Section 3.1). The ‘tow equivalent’ domain comprises of two overlapping tows (warp and weft), simplified to an equivalent rectangular tow shown in Fig. 4-1.

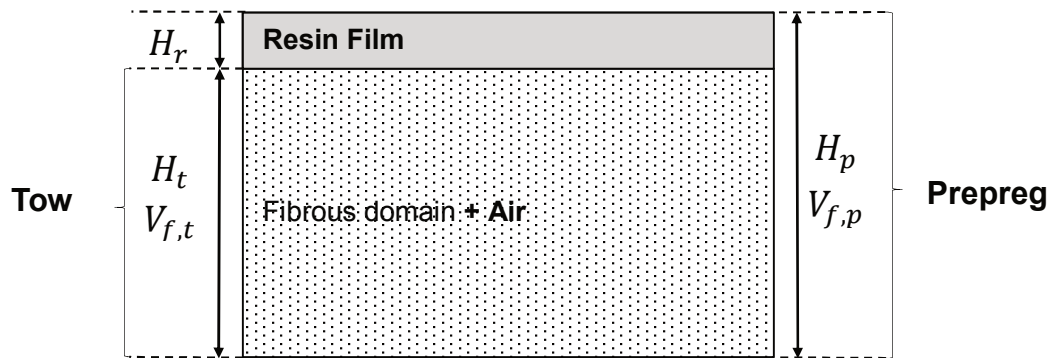


**Fig. 4-1:** ‘tow equivalent’ used as a basis for the development of isothermal tow impregnation models in Matlab

The impregnation time of the dry tow depicted in Fig. 4-1 is calculated for all air evacuation scenarios presented in detail in 4.1.2. The resin is assumed to impregnate the fibrous domain solely through its thickness  $H_t$ , due to the pressure difference between the atmospheric and vacuum pressure  $\Delta P_f$  developed in the resin impregnated fibrous domain. The vacuum pressure is initially established along the dry tows of the prepreg consisting a connected porous network, which enables air transport along the length of the part ( $x - axis$ ). When the prepreg plies are stacked on top of each other, the ‘dry core’ of the tows will be enclosed between two impermeable resin films. Hence, no interconnected pore network and can enable significant air evacuation through the thickness of the part. The significant reduction of the through thickness air permeability, when prepreg plies are stacked on top of each other is also discussed in the review paper by Centea et al. [18], therefore the through thickness air evacuation has been neglected.

Fig. 4-2 shows the boundary conditions applied for modelling the tow impregnation with resin.

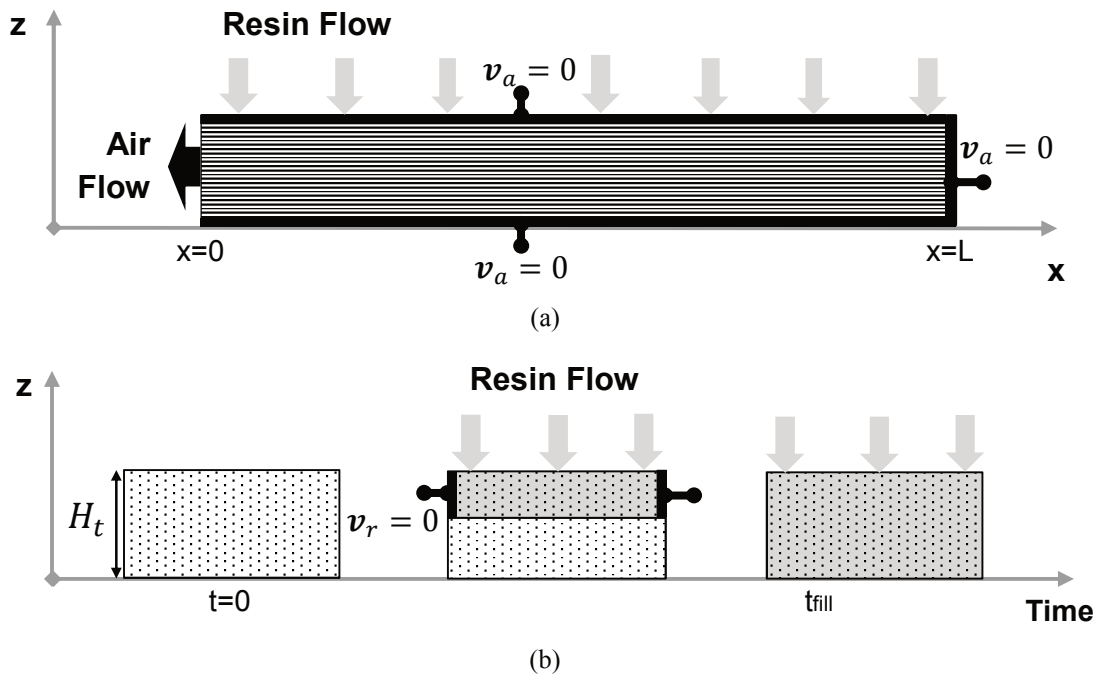


**Fig. 4-2: Boundary conditions used in isothermal tow impregnation model development**  
 (a) In-plane air flow ( $x$  - axis) and (b) through thickness resin flow ( $z$  - axis).

### 4.1.2 Modeling Approach

Three models are developed for the prediction of the dry prepreg tow impregnation during OoA processing: the instantaneous air evacuation, compromised vacuum connection and delayed air evacuation model.

In the two first cases the tow impregnation time is calculated analytically. The delayed air evacuation model, couples numerically the flow of both fluids (air and resin) in the fibrous domain. The coupling is performed iteratively through updating the pressure boundary conditions for air flow, during the time scale of the resin flow. The delayed air evacuation model captures the transient behavior of the air flow through the tow during isothermal processing. In reality the delayed air evacuation model reflects the state of vacuum inside the tow in the majority of cases, since the gas distribution through the dry tows of a partially impregnated material is rarely instantaneous. In the following Sections the calculation of the tow impregnation time as well as the development of the gas pressure inside the tow is presented for all three scenarios. The analytically predicted impregnation time of the tow via the instantaneous air evacuation and compromised vacuum connection models consist the lower and upper boundary of the impregnation time respectively, in the case of a very permeable tow and an obstructed vacuum distribution.

### 4.1.2.1 Resin Flow

As shown in Fig. 4-2 the resin impregnates the fibrous domain solely through its thickness  $H_t$  ( $z - axis$ ), while the air flows exclusively in-plane ( $x - axis$ ). The following assumptions are used for modeling the resin flow through the tow:

- The porous medium is not consolidating ( $H_t, V_{f,t}, \phi_t = constant$ ).
- The through thickness permeability of the warp and weft tow is equal and constant ( $K_{r,zz}$ ).
- Resin flow takes place exclusively through the thickness of the tow ( $z - axis$ ).
- The resin is incompressible ( $\rho_r = constant$ ).
- The pressure drop within the pure resin is negligible.
- The domains wetted by resin are fully saturated.
- Resin is viscous and the flow is slow ( $Re < 1$ ).
- Resin flow modelled at a quasi-steady state ( $\frac{\partial \rho_r}{\partial t} = 0$ ).
- Infinite resin supply, while flow stops when the domain is filled with resin.

These assumptions enabled the use of the simplified mass conservation of Equation (2-8) and Darcy's law (Equation (2-14)), which combined provide Equation (4-1) used to determine the resin pressure developed along the  $z - axis$ . It shall be noted that the resin is in a fluid state throughout the impregnation and therefore its pressure is expressed here as  $P_f$  ( $P_r = P_f$ ).

$$\frac{\partial^2 P_f}{\partial z^2} = 0 \rightarrow P_f(z) = Az + B \quad (4-1)$$

The fluid pressure in the saturated fibrous domain is calculated via the application of the boundary conditions of Equation (4-2) at the entry  $H_t$ , and flow front  $z_f$ .

$$\begin{aligned} P_f(H_t) &= P_{atm} \\ P_f(z_f) &= P_{gas} \end{aligned} \quad (4-2)$$

Equation (4-3) is used to calculate the flow front velocity, where  $\Delta P_f$  the pressure difference developed in the impregnated domain,  $\phi_t$  the tow porosity,  $K_{r,zz}$  its through thickness permeability and  $n$  the viscosity of the resin.

$$u_{rf,zz} = -\frac{K_{r,zz}}{n\phi_t} \frac{\partial P_f}{\partial z_f} = -\frac{K_{r,zz}}{n\phi_t} \frac{\Delta P_f}{(H_t - z_f)} \rightarrow u_{rf,zz} = \frac{\partial z_f}{\partial t} \quad (4-3)$$

The impregnation time of the tow  $t_{fill}$  is calculated via integrating the flow front velocity  $u_{rf,zz}$  given in Equation (4-3). The boundary conditions for the air pressure and the respective tow impregnation time calculated, are presented in Section 4.1.2.2.

### 4.1.2.2 Air Flow and Evacuation

#### Instantaneous Air Evacuation

When the air evacuation takes place instantaneously, a constant vacuum pressure is present at the resin front, which for this study is considered to be  $P_{gas} = P_{vac} = 2 \cdot 10^3$  Pa.

This results to the establishment of a constant pressure difference  $\Delta P_f$ , which drives the impregnation of the tow with resin.

$$\Delta P_f = P_{atm} - P_{vac} \quad (4-4)$$

The impregnation time of a tow with resin, is calculated in this case via Equation (4-5).

$$t_{fill} = \frac{n\phi_t}{K_{r,zz}} \frac{H_t^2}{2\Delta P_f} \quad (4-5)$$

The resin and gas pressure at various flow front positions  $z_f$  and with evolving time  $t$  are presented in Fig. 4-3.

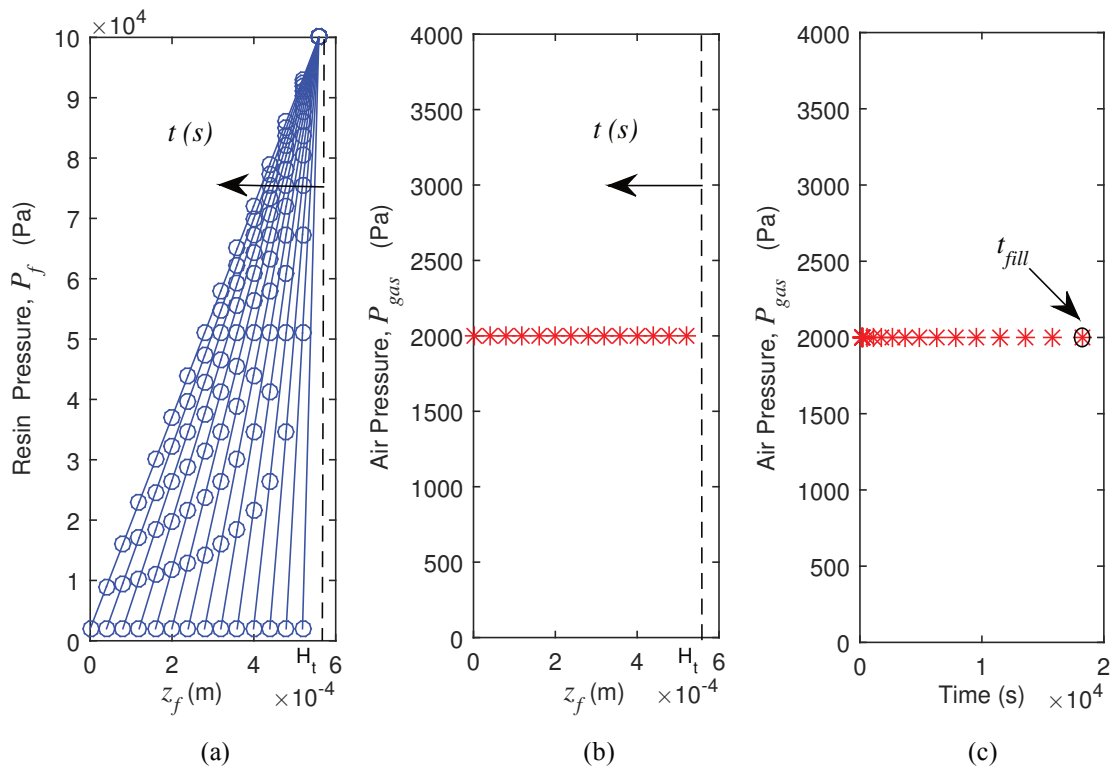


**Fig. 4-3: Resin and gas pressure evolution – Instantaneous air evacuation**

(a) Resin pressure in the impregnated domain, versus flow front position (b) gas pressure versus the flow front position (c) gas pressure versus tow impregnation time.

The calculations are based on the inputs summarized in Appendix f, Tab. A- 5.

### Compromised Vacuum Connection

During vacuum processing, the connection to the vacuum source may fail unexpectedly either due to a leak in the vacuum bag, or due to a microscopic obstruction of the air paths in the prepreg. The gas pressure driving the tow impregnation increases, provided the mass of air inside the tow remains constant. The gas pressure at the flow front  $z_f$ , is calculated according to Equation (4-6):

$$P_{atm} H_{min} = P_{gas} z_f \rightarrow P_{gas} = P_{atm} \frac{H_{min}}{z_f}, \forall z_f < H_{min} \quad (4-6)$$

It should be noted that the gas will equilibrate with the atmospheric pressure at a position  $z_f = H_{min}$ , preventing the complete tow impregnation. If we assume the minimum attainable pressure is  $P_{vac} = 3 \cdot 10^3$  Pa while the atmospheric pressure is  $P_{atm} = 10^5$  Pa, the percentage of thickness which does not impregnate for a tow with thickness  $H_t$  is  $H_{min} = 3\%$ . The pressure is calculated from Equation (4-1), applying the boundary condition of Equation (4-6) at the flow front. At  $z_f = H_{min}$  the resin velocity is zero, implying an infinite amount of time required to impregnate 97% of the tow. For comparison purposes, the impregnation time of 96.9% of the tow thickness defined as  $t_{fill_{96.9\%}}$  at the position  $z_{min} = 3.1\% \cdot H_t$  is given by Equation (4-7).

$$t_{fill_{96.9\%}} = 0.6405 \frac{n\phi_t H_t^2}{K_{r,zz} P_{atm}} \quad (4-7)$$

The resin and gas pressure based on the inputs of Tab. A- 5 are shown in Fig. 4-4.

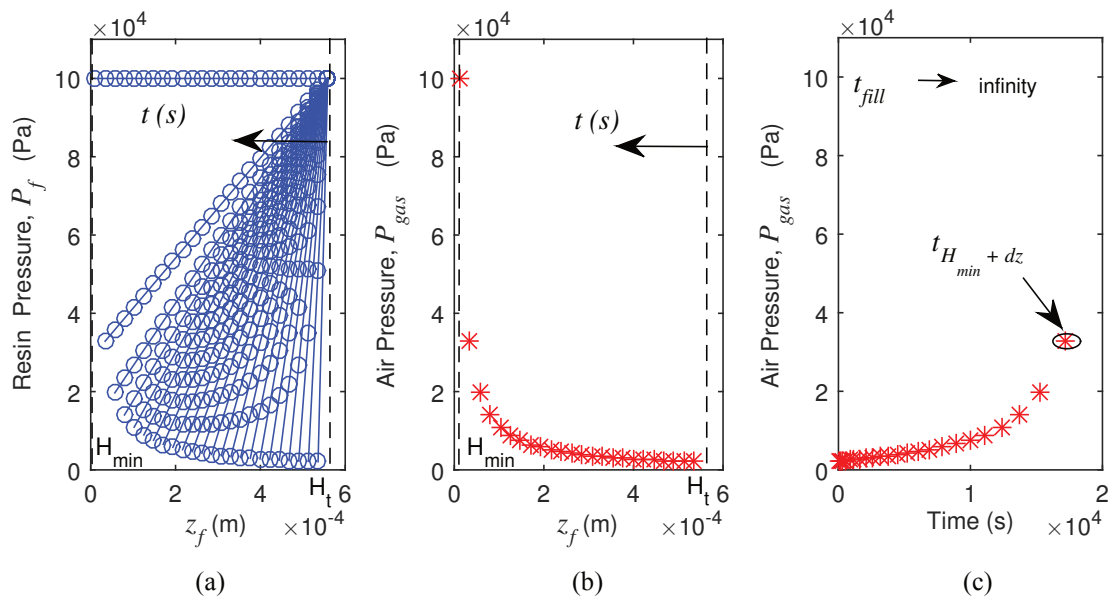


**Fig. 4-4: Resin and gas pressure evolution – Compromised vacuum connection**

(a) Resin pressure in the impregnated domain, versus flow front position (b) gas pressure versus flow front position (c) gas pressure versus tow impregnation time.



## Delayed Air Evacuation

Instantaneous air evacuation is in practice only rarely encountered, mostly when processing short parts directly connected to a vacuum pump. The delayed air evacuation model captures the influence of the local air pressure variations on the tow impregnation time along the length of long tows, when processing is performed solely under vacuum pressure. Resin flows perpendicularly through the tow thickness and it is coupled in a time iterative fashion to the local gas pressure developed at the flow front.

Basis for this development is the constitutive Equation (2-42) depicting the flow of air through the porous medium at isothermal conditions, originating from the combination of the conservation of mass, momentum and ideal gas law, for viscous air flow. Equation (2-42) has no known analytical solution. Kim et al. [190] linearized and solved analytically Equation (2-44) in order to predict the air evacuation in preforms for quality control purposes, assuming the variation of the gas pressure is small, compared to the atmospheric pressure [190]. Nevertheless, in [19] we show that the simplified equation proposed by Kim et al. [190] underestimates the gas pressure within the complete range of the air evacuation process, therefore making the linearized equations inappropriate for use in the scope of this work. Therefore Equation (2-42) is solved numerically using the pdepe function available in Matlab R2013a considering the initial (IC) and boundary conditions (BC) given in Equation (4-8).

$$\begin{aligned}
 \text{IC} \quad & P_{gas}(x, 0) = P_{atm} \\
 & P_{gas}(0, t) = P_{vac} \\
 \text{BCs} \quad & \mathbf{v}_a(L, t) = 0 \rightarrow \frac{\partial P_{gas}(L, t)}{\partial x} = 0
 \end{aligned} \tag{4-8}$$

To ensure the stability of the coupling concept, the following conditions have to be simultaneously fulfilled:

- Discretization of the tow thickness  $H_t$  along the,  $z - axis$  should guarantee resin flow initiation, after the initialization of the air flow.
- Initialization of the air flow solver at  $dt_0 < t_c$ . This will ensure that the transient phase of the air evacuation process will be included in the calculations.

The variable  $t_c$  is the characteristic time for air flow defined according to Equation (4-9).

$$t_c = \frac{\mu_a \phi_t L^2}{K_{a,xx} (P_{atm} - P_{vac})} \tag{4-9}$$

The characteristic time for air flow is used to develop the dimensionless form of Equation (2-42), given in Equation (4-10). The characteristic time for air flow expresses the time it takes for 63-64% of the total mass of air to be evacuated out of the tow, for the range of material properties considered in the sensitivity study, when the pde of Equation

(2-42), with boundary conditions of Equation (4-10) is considered. The percentage of the mass of air evacuated up to  $t = t_c$  is calculated by integrating the pressure profile along the length of the tow at  $t = 0$  ( $m_0$ ) and  $t = t_c$  ( $m_{t_c}$ ).

$$\frac{\partial P_{gas}^*}{\partial t^*} = \left( \frac{K_{a,xx} t_c (P_{atm} - P_{vac})}{\phi_t \mu_a L^2} \right) \nabla \cdot (P_{gas}^* \nabla P_{gas}^*) \quad (4-10)$$

$$x^* = \frac{x}{L}, \quad 0 \leq x^* \leq 1$$

$$t^* = \frac{t}{t_c}, \quad 0 \leq t^* \leq \infty \quad (4-11)$$

$$P_{gas}^* = \frac{P_{gas} - P_{vac}}{P_{atm} - P_{vac}}, \quad 0 \leq P_{gas}^* \leq 1$$

A  $\Delta P_{gas} \sim 2.4\%$  ensures that  $dt_0 < t_c$  in the complete range of time scales investigated. Therefore it is selected as the minimum pressure required to initiate resin flow in the model. Resin flow is iteratively coupled to the air flow at every location inside the tow according to the scheme of Fig. 4-5.

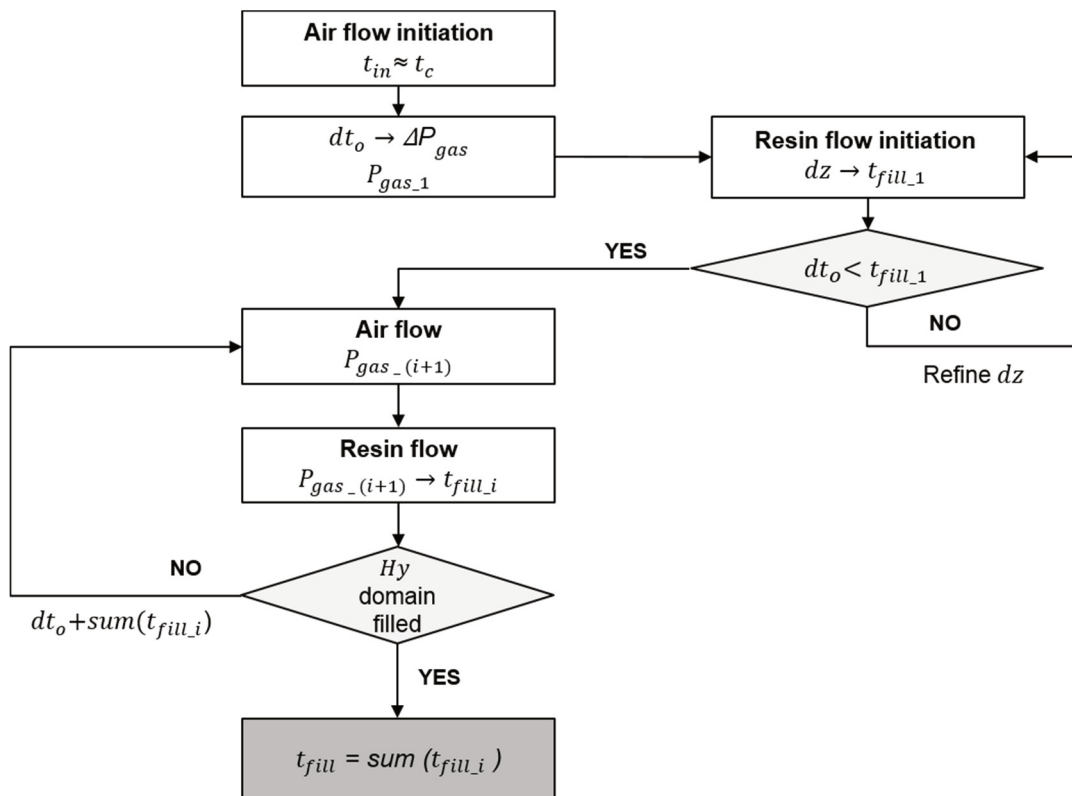


Fig. 4-5: Modeling scheme of the delayed air evacuation out of the Out-of-Autoclave tows

The impregnation time  $t_{fill}$  of a tow domain  $dz$  (Equation (4-12)) under the influence of gas pressure is calculated from Equation (4-13).

$$dz = \frac{H_t}{(N_z - 1)} \quad (4-12)$$

The impregnation time for an incompressible porous medium with constant viscosity is:

$$t_{fill_i} = - \frac{idz^2 \phi_t \mu_a}{K_{a,xx}(P_{atm} - P_{gas_i})} \quad (4-13)$$

The total impregnation time of the tow with resin  $t_{fill}$  is calculated by the sum of the filling time instances  $t_{fill_i}$  during the resin flow timeframe (see Equation (4-14)).

$$t_{fill} = \sum_{i=1}^{N_z} t_{fill_i} \quad (4-14)$$

The total impregnation time is set as the time span within which the pdepe solver is used to calculate the air pressure. A typical example of resin and air pressure development in an OoA tow is presented in Fig. 4-6. Calculations are based on inputs summarized in Tab. A- 5.

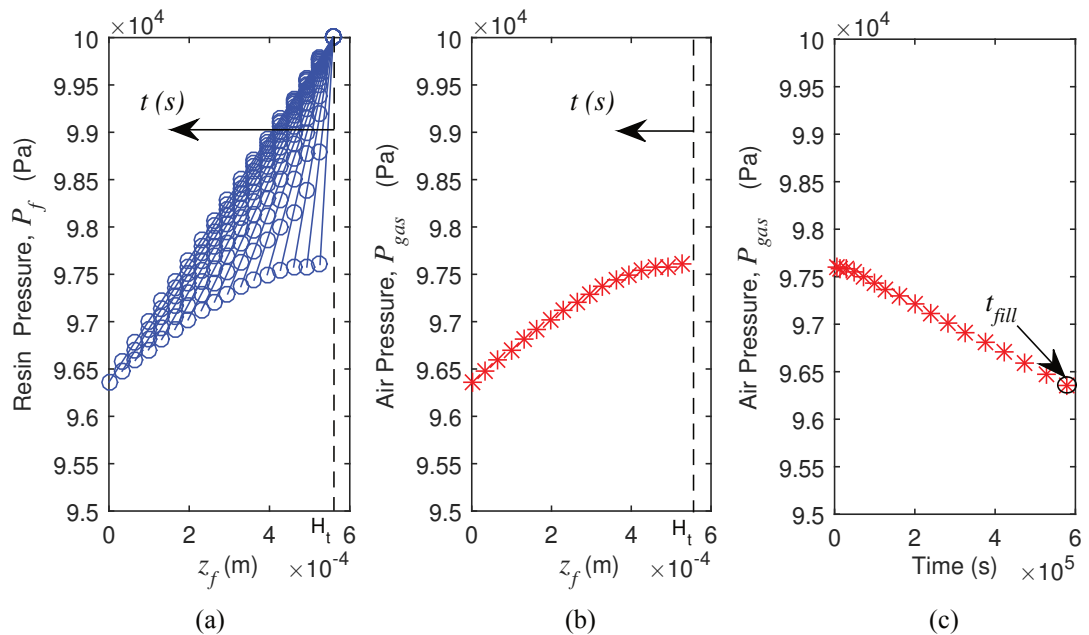


**Fig. 4-6: Resin and gas pressure evolution – Delayed air evacuation**

(a) Resin pressure in the impregnated domain, versus flow front position (b) gas pressure versus flow front position (c) gas pressure versus time of impregnation.

Convergence studies showed that the global error in the prediction of the filling time using the delayed air evacuation model reduces with a denser discretization of the tow thickness [19]. Discretizing the tow thickness with more than 300 points is sufficient to provide an error smaller than 1% of the calculated tow impregnation time [19].

### 4.1.3 Sensitivity Studies

The delayed air evacuation model is used to investigate the impact of the tow properties and processing conditions on the tow impregnation time of an OoA prepreg. The tow has a constant thickness, porosity and permeability, while the flow takes place under isothermal conditions, considering a resin with constant viscosity. The impregnation time is predicted in the mid-span of the tow ( $x = L/2$ ), while the impact of the following parameters on the impregnation time is investigated:

- Air and resin viscosity at various temperatures (Fig. 4-7 and Fig. 4-8)
- Part length and material type (Fig. 4-9 and Fig. 4-10)

The resulting tow impregnation time is compared against the analytical steady state solution, derived by the equations of instantaneous air evacuation (Equation (4-5)) and compromised vacuum connection (Equation (4-7)).

The flow of resin through three tows with the same thickness, but different porosity and through thickness permeability is considered (referred to as Materials 1-3). The tows considered consist of unidirectional fibers with  $7\mu\text{m}$  diameter, which have fibers distributed either hexagonally or quadratically. The out-of-plane permeability is calculated via Gebart's equations [140]. The range of in-plane permeability is based on literature data extrapolated towards higher permeability values (Materials 1-3, Tab. A-6, Appendix f). As the tow is filling with resin, its in-plane air permeability decreases significantly, up to the point that no air can flow through the fibrous domain.

The tow can be classified in one of the following categories, based on the magnitude of the ratio of the through thickness resin permeability, versus its air permeability:

- Anisotropic porous medium, with a higher in-plane permeability ( $K_{r,zz}/K_{a,xx} < 1$ ) or a higher out of plane permeability ( $K_{r,zz}/K_{a,xx} > 1$ )
- Nearly isotropic porous medium ( $K_{r,zz}/K_{a,xx} = 1$ )

The flow of both fluids through the tows takes place either at  $30^\circ\text{C}$  (elevated room temperature) or  $130^\circ\text{C}$  (1st dwell temperature in the MTM 44-1 cycle Ref MTM MDS). Tow lengths of  $0.5 - 20\text{m}$  are considered. The air viscosity is calculated from Sutherland's equation [186], while the minimum air pressure is  $P_{vac} = 2.00 \cdot 10^3 \text{ Pa}$ . All inputs used in the calculations are summarized in Appendix f, Tab. A-6.

A new metric expressing the air resistance to filling  $AR_f$  given by Equation (4-15) is proposed in order to classify the relative impact of the air evacuation on the tow impregnation time. The ratio of air resistance to filling  $AR_f$  correlates the tow impregnation time-scale with resin,  $t_{fill}$  (given by Equation (4-14) in  $z - axis$ ), with the characteristic time for air flow through the same tow,  $t_c$  (given by Equation (4-9) in  $x - axis$ ).

$$AR_f = \frac{t_{fill}}{t_c} \quad (4-15)$$

Though  $t_c$  does not express the time it takes to evacuate the complete mass of air out of the tow, it correlates the physical parameters involved in the air evacuation process given the lack of an analytical solution. Therefore, the ratio of air resistance to filling for the minimum gas pressure achievable at the location of interest during the tow impregnation process  $P_{gas\_min}$  is simplified into Equation (4-16).

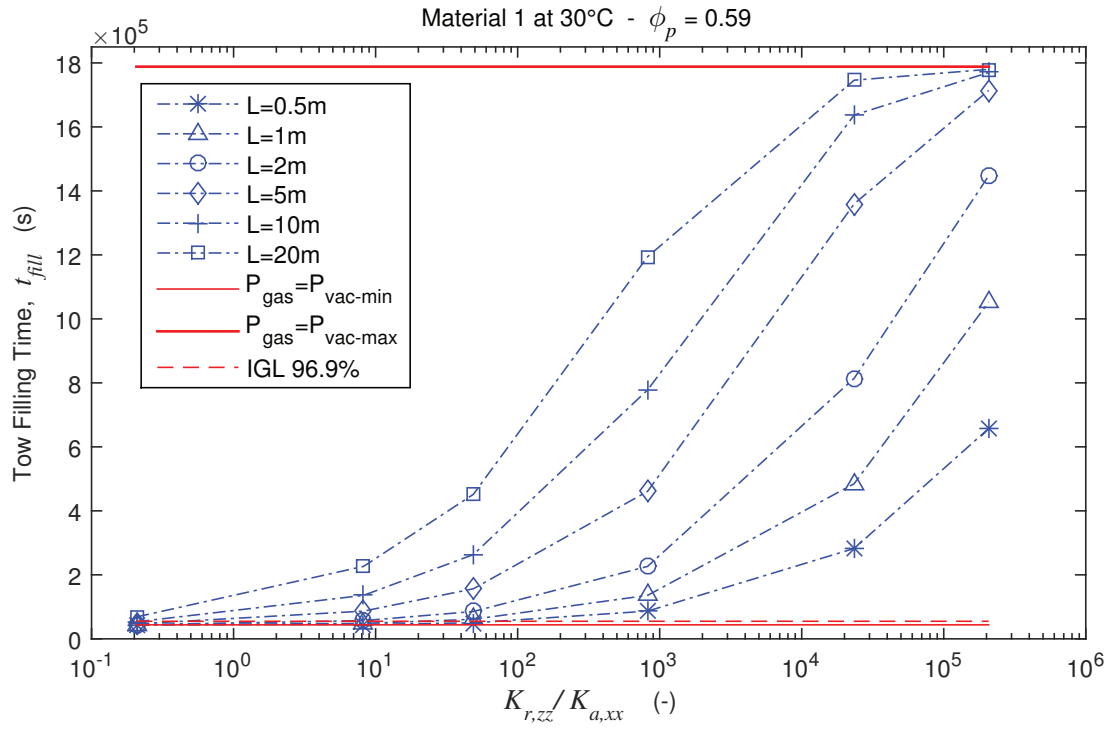
$$AR_f \approx \frac{K_{a,xx} n H_t^2 (P_{atm} - P_{vac})}{2K_{r,zz} \mu_a L^2 (P_{atm} - P_{gas\_min})} \quad (4-16)$$

As the timescale for flow of the two fluids (air and resin) varies significantly, classifying their relative magnitude assists in defining the most effective strategy for the calculation of the tow impregnation time. In particular:

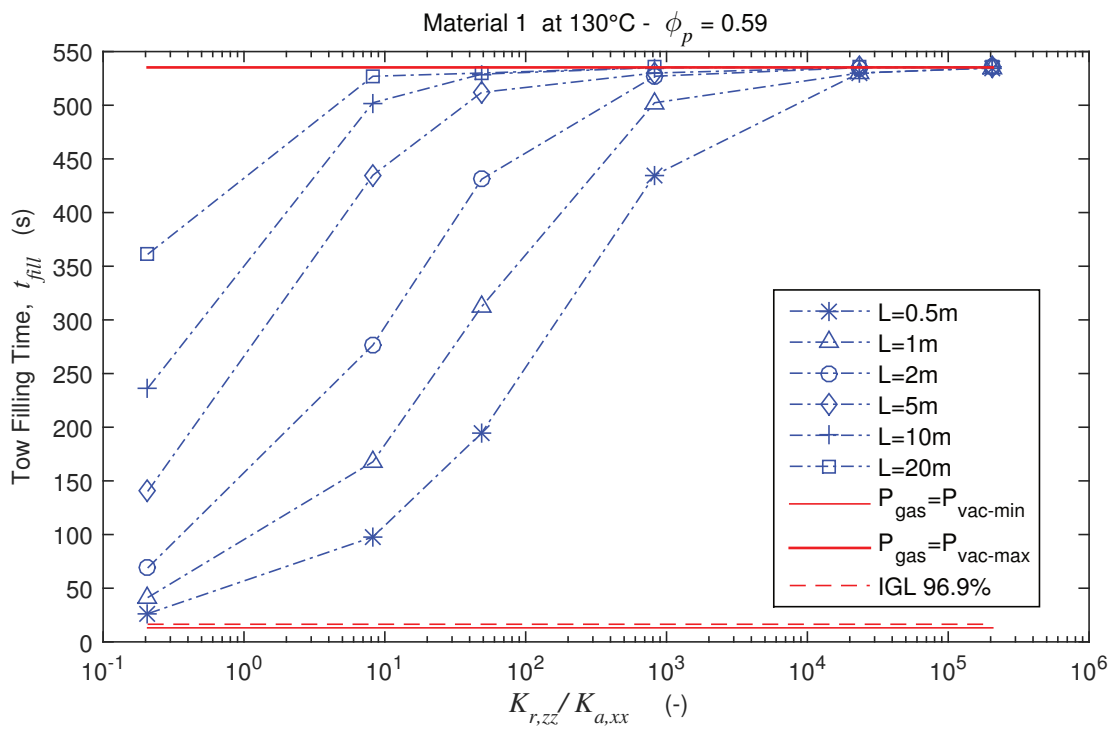
- To achieve an accurate prediction of the tow filling time when the characteristic times of resin  $t_{fill}$  and air flow  $t_c$  are of similar magnitude,  $AR_f \approx 1$  the transient air flow shall be captured via the delayed air evacuation model.
- When the filling time of the tow with resin is much slower than the characteristic time of air flow,  $t_{fill} \gg t_c$  the ratio of air resistance to filling is significantly larger than unity,  $AR_f \gg 1$ . The air evacuation takes place during the very early stages of the resin flow establishing a steady state along the part length and it is therefore sufficient to describe the air flow as instantaneous.
- If the ratio of air resistance to filling, is several orders of magnitude smaller than unity  $AR_f \ll 1$  the air is evacuated much slower than the tow impregnation with resin  $t_{fill} \ll t_c$ . In this case the tow impregnation time can be either calculated via the delayed air evacuation model or via the instantaneous air evacuation model, considering a reduced gas pressure attained during the time of resin flow in the tow ( $P_{gas\_min}$ ).

Two studies demonstrate the influence of the resin viscosity and the porosity on the interaction between air and resin flow through the tow.

Initially the impregnation time of the tows from Material 1 (Tab. A- 6) is captured at 30°C in Fig. 4-7 and at 130°C in Fig. 4-8, for a variety of permeability ratios and lengths. The difference between the impregnation time predicted by the instantaneous and the delayed air evacuation model is defined as  $dt_{fill}$  (%) and is plotted against the ratio of air resistance to filling  $AR_f$  in Fig. 4-8. The tow impregnation time predicted by the delayed evacuation model is bound between the analytical solutions derived by the instantaneous air evacuation model (Equation (4-5)), considering a minimum  $P_{vac\_min} = 2.00 \cdot 10^3 Pa$  and a maximum constant vacuum pressure  $P_{vac\_max} = 9.76 \cdot 10^4 Pa$ . When the air evacuation takes place significantly faster than the impregnation of the tow with resin, its impregnation time is independent of the tow length and approaches the time predicted by the instantaneous air evacuation model.



(a)



(b)

**Fig. 4-7: Impregnation time of a Material 1 tow, for a range of lengths and permeability ratios**  
 (a) Impregnation taking place at 30°C and (b) impregnation taking place at 130°C.

The filling time at elevated room temperature, (30°C) was shown in Fig. 4-7 (a) to be independent of the tow length if the in-plane permeability is higher than the through thickness permeability  $K_{r,zz}/K_{a,xx} < 1$ . The increase in processing temperature leads to a reduction of the tow impregnation time, caused by the reduction of the resin viscosity. When  $K_{r,zz}/K_{a,xx} < 1$ , the ratio of air resistance to filling is larger than unity  $AR_f \gg 1$ . If  $K_{r,zz}/K_{a,xx} > 1$  and  $AR_f \leq 1$ , the length of the tow has a significant influence on the tow filling time. Therefore an accurate description of the air flow through the tow using the delayed air evacuation model is preferred.

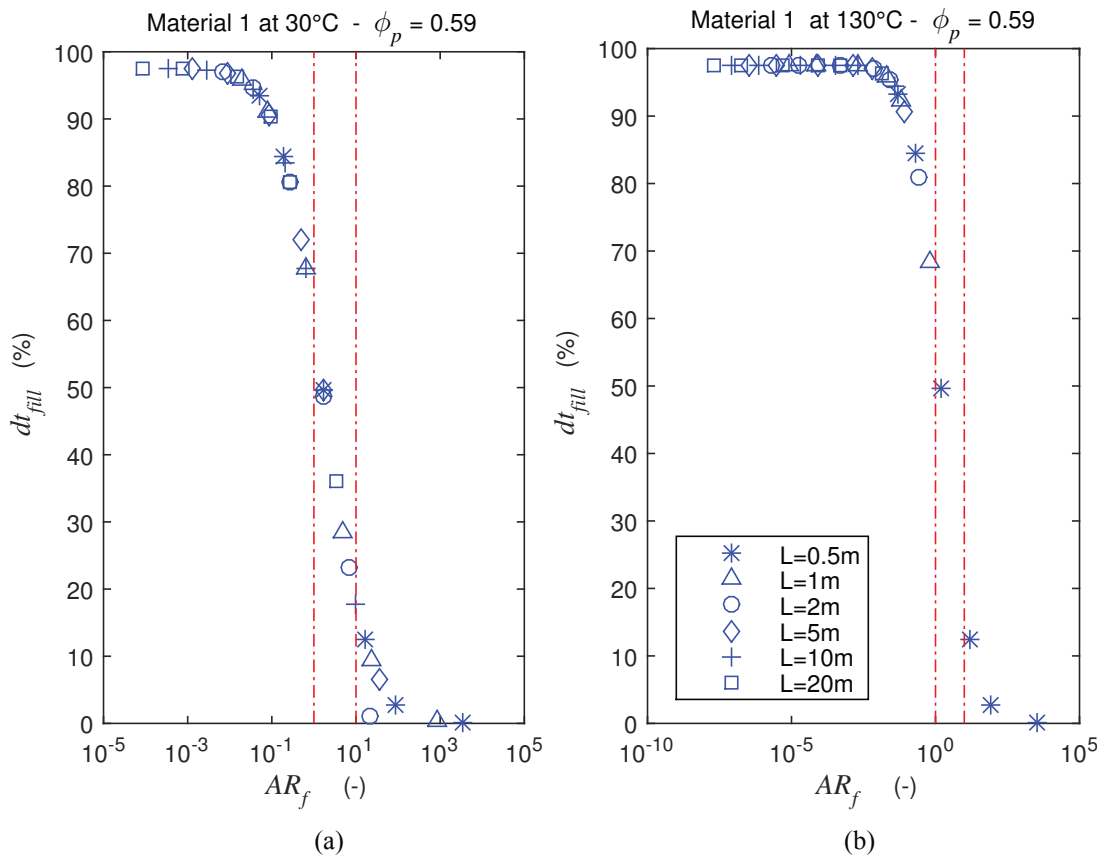


**Fig. 4-8:** The impact of the air resistance to flow  $AR_f$  on the tow impregnation time difference  $dt_{fill}$  between the instantaneous and delayed air evacuation models  
 (a) Material 1 at 30°C and (b) Material 1 at 130°C, for the lengths and permeability ratios investigated in Fig. 4-7.

The reduction of the resin viscosity at elevated temperature (130°C) and the subsequent reduction of the tow impregnation time, leads to a reduced resistance to filling. It can be deduced that the resin impregnation inhibits the air evacuation, which is progressing much slower. This leads to the development of a small pressure gradient, which assists the tow impregnation, for all lengths investigated with the exception of those with 0.5m length. The tow filling time was approximated with the use of the instantaneous air evacuation model, considering a reduced vacuum pressure as a boundary condition at the

flow-front  $P_{vac} = P_{gas\_min}$ . Equation (2-42) shall be used to calculate the  $P_{gas\_min}$ , unless it is known from experiments. Therefore, the suggested and most accurate method to calculate local tow filling times is via the use of the delayed air evacuation model. Concerning the predictions of the tow impregnation at elevated room temperature (30°C), it is shown that the impregnation would have progressed significantly in a days' time for most cases investigated. This is in agreement with Ridgard's comment [9] on the adverse effects caused by the cold flow of resin, induced during long vacuum cycles performed at room temperature. In a second study, the impregnation time of three tows with the same thickness  $H_t$ , various lengths  $L$  and with different porosity contents  $\phi_t$  is investigated (Appendix f, Tab. A- 6, Materials 1-3). The influence of the porosity on the impregnation time of the tow and the ratio of air resistance to filling is summarized graphically in Fig. 4-9 and Fig. 4-10.

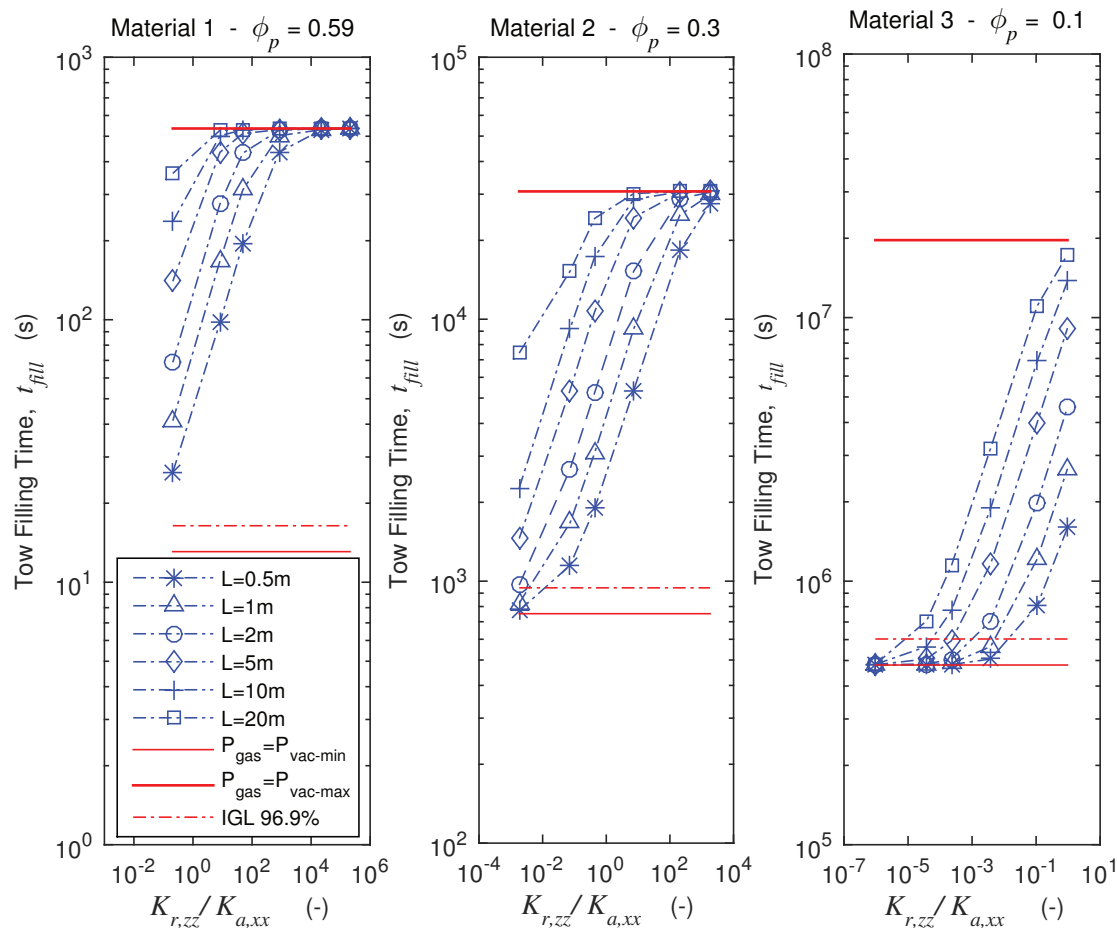


**Fig. 4-9: Impregnation time of three tows (Materials 1-3) at 130°C for a range of lengths and permeability ratios**

It is evident that the lower the porosity of the tow, the slower its impregnation with resin. A more interesting observation from Fig. 4-9 is that the tows with high porosity levels impregnate faster, nevertheless their filling times vary significantly with the part length.



This is also depicted in Fig. 4-10, where the time difference  $dt_{fill}$  increases from right to left, while  $AR_f$  becomes much smaller than unity for all tow lengths considered.

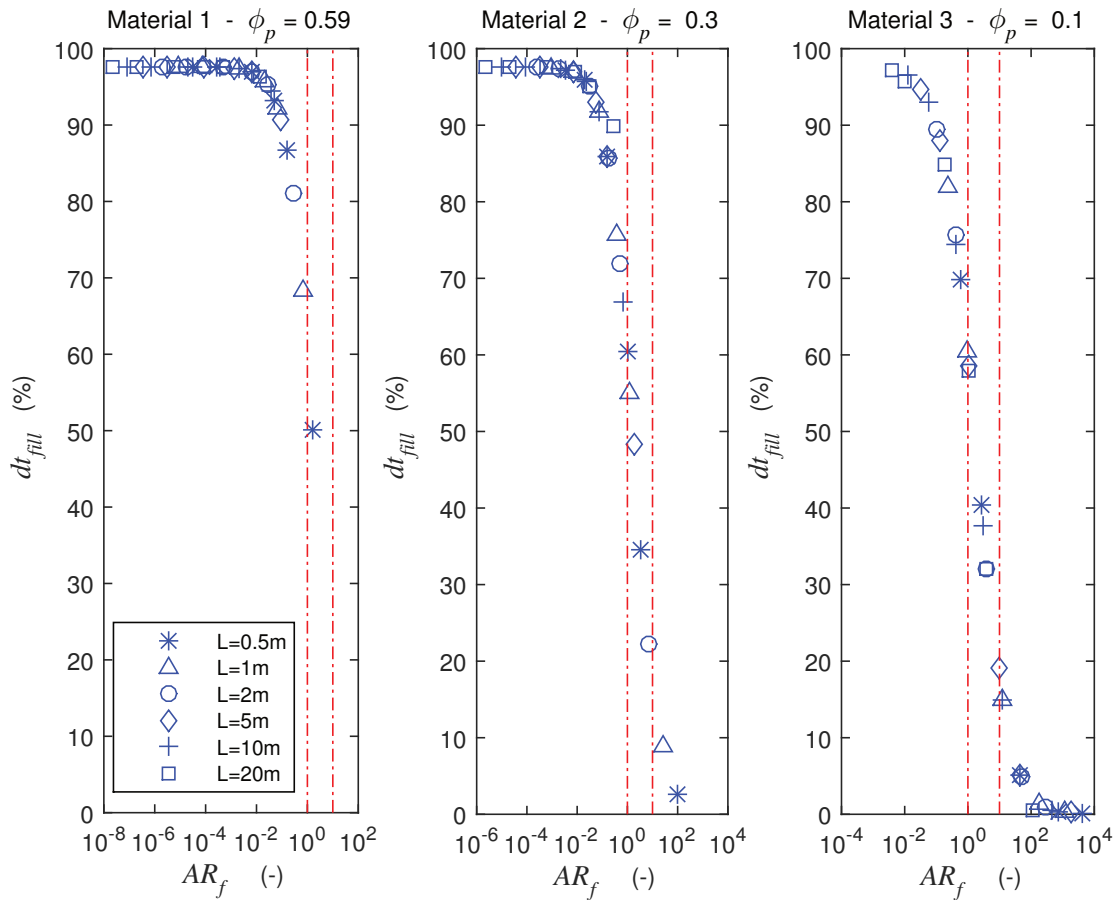


**Fig. 4-10:** The impact of the air resistance to flow  $AR_f$  on the impregnation time difference between the instantaneous and delayed air evacuation models  $dt_{fill}$  at 130°C

The tow impregnation time calculated by the delayed air evacuation model is validated against the analytical instantaneous air evacuation model and provides a good agreement when highly permeable tows are concerned. The permeability ratio and the air resistance to filling, assist in the categorization of the relative impact of the time for flow of the two fluids through the porous medium. The assumption of instantaneous air evacuation mostly underestimates the local impregnation time of the tow away from the vacuum source, on the contrary to the delayed air evacuation model. When vacuum is applied on one side of the tow, the location close to the vacuum source will impregnate first. At this point the tow will be cut-off from the vacuum and no pressure will be available to enable further tow saturation, leading to air entrapment. The longer the tow and its distance to the vacuum source, the more pronounced the impregnation time difference along the tow length and hence the chance for air entrapment. If the resin gels before the tow is fully impregnated, the lack of saturation will become residual porosity. Therefore, an accurate knowledge of the impregnation state everywhere inside the tow is needed to accurately quantify the residual intra tow porosity.

## 4.2 Non-Isothermal Prepreg Impregnation

The simulation of the Out-of-Autoclave process at non-isothermal conditions is implemented in COMSOL Multiphysics (v.5.2). The model describes the impregnation of an OoA prepreg ply with resin under the influence of transient air flow through the fibrous tows of the prepreg, at non-isothermal conditions during the cure cycle. Local pressure and temperature inhomogeneity can lead to formation of local air pockets inside the impregnating tows, essentially by cutting them off from the vacuum supply. Once the access of the tows to vacuum is disrupted, no external pressure is available to enable further saturation. Thus residual intra-tow porosity may develop, an undesirable defect reducing the quality of the produced composite part as discussed in more detail in Section 1.6. The modeling toolkit developed in the context of this work can be used for virtual testing of temperature and pressure cycles with the aim to enable an optimized process design, which will lead to the reduction of undesired intra-tow porosity on the finished part produced outside the Autoclave.

The simplified prepreg ply shown in Fig. 4-11 is used here as the basis for model development of the non-isothermal OoA simulation. Its thickness and the volume fractions of all constituents reflect the initial state of the MTM44-1 prepreg determined in Section 3.2.1, since the fiber bed compaction is not taken into account.

Implemented physics in the OoA simulation include the flow of air through the porous/fibrous media and the ideal gas law for air (Section 4.2.2.1), the flow of resin in porous media (Section 4.2.2.1) combined with a moving resin impregnation front (Section 4.2.3) and heat transfer from the tool or oven to the part (Section 4.2.2.2). The evolution of the MTM 44-1 resin film viscosity is depicted as a function of time and temperature described according to the semi-empirical model of Equation (3-49), derived in Section 3.4.3.3. Furthermore, the permeability of the prepreg to air is implemented as a function of the prepreg porosity according to Equation (3-23), derived from the characterization of the MTM 44-1 prepreg. The air flow is described according to the delayed air evacuation model developed in Section 4.1.2.2. The resin and air flow are coupled via pressure boundary conditions, according to the principal presented in Section 4.1.2. The approach is extended to include a two-way coupling between the air and resin flow in 2D (length and thickness of the prepreg). The numerical approach and coupling scheme used, are discussed in Section 4.2.3.

A number of sensitivity studies are presented in Section 4.2.4 in order to provide debulking and process optimization guidelines using as a basis the MTM 44-1 prepreg. The Chapter concludes with a summary and discussion of the most interesting findings, correlating them to findings discussed literature.

The theoretical development presented in this Section as well as selected graphs and figures are based on the conference proceedings [12] published by the author in the context of this dissertation. The content is reused here, in agreement with the co-authors.

### 4.2.1 Domain and Assumptions

The development of the non-isothermal model is based on the domain of Fig. 4-11. The prepreg consists of two clearly separated fibrous sub-domains, one saturated with resin (with thickness  $H_{t,r}$ ) and one with air (with thickness  $H_{t,a}$ ). The thickness of the resin film is much smaller than the prepreg's thickness and is therefore omitted for simplicity. The tow and prepreg sub-domains are therefore equivalent and have the same thickness ( $H_p = H_t$ ) as well as the same fiber volume fraction ( $V_{f,p} = V_{f,t}$ ). The fiber volume fraction of the domain is constant throughout the process as the compaction of the fibrous medium is not taken into account. The initial thickness of the resin impregnated domain is  $H_{t,r}(0) = 57.3\% \cdot H_p$ .

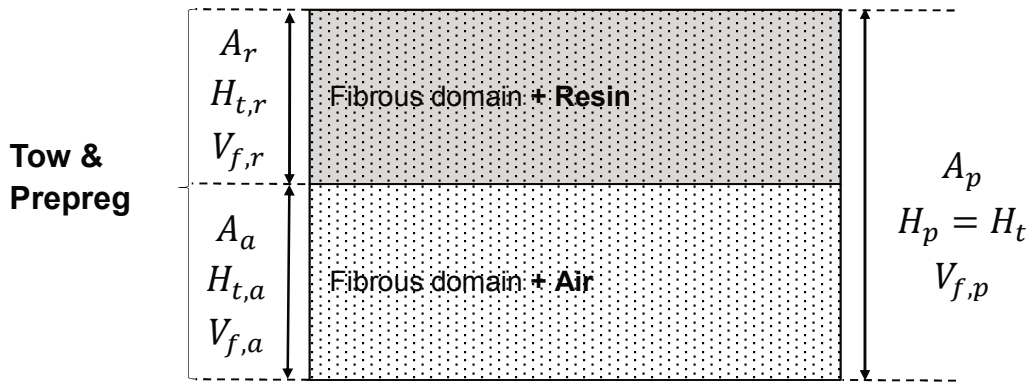


Fig. 4-11: Prepreg domain used as a basis for non-isothermal impregnation modeling using COMSOL Multiphysics

The degree of impregnation of the prepreg with resin,  $I_r$  and air,  $I_a$  are calculated via Equations (4-17) and (4-18) respectively, while the domain width remains constant.

$$I_r(t) = \frac{A_r(t)}{A_p} = \frac{H_{t,r}(t)}{H_p} \quad (4-17)$$

$$I_a(t) = \frac{A_a(t)}{A_p} = \frac{H_{t,a}(t)}{H_p} \quad (4-18)$$

The cross-sectional areas of the tow occupied respectively with resin and air are depicted as  $A_r$  and  $A_a$ , while  $A_p$  is the cross-sectional area of the prepreg. The ply area remains constant throughout the process ( $A_p = A_a + A_r$ ) since the prepreg consolidation is not yet implemented. Several researchers [57, 66, 132, 184, 196, 204, 220] have defined similar functions to describe the degree of impregnation presented in Equations (4-17) and (4-18), such as the initial degree of impregnation of a prepreg, IDoI [57, 132, 204, 220], the resin distribution function,  $f^*$  [196], or the degree of saturation,  $S$  [66].

The initial global porosity of the MTM44-1 prepreg  $\phi_p$  is calculated from the conservation of mass of Equation (3-6), once the fiber volume fraction  $V_{f,p}$  and resin volume

fractions  $V_{f,r}$  are known. The initial volume fractions of the prepreg constituents  $V_{f,p}(0)$ ,  $V_{r,p}(0)$ ,  $\phi_p(0)$  are determined theoretically according to the method discussed in Section 3.2.1 and are summarized in Tab. 3-3. The local fiber volume fraction of the prepreg sub-domains  $V_{f,j}$  and fluid volume fraction  $\phi_t = \phi_j$  are considered to remain constant in each subdomain. They are calculated from Equation (4-19), where the subscript  $j = a$  stands for the air and  $r$  for the resin saturated sub-domains of the prepreg. The fiber volume fraction of the sub-domains is equal to the volume fraction of the prepreg  $V_{f,a} = V_{f,r} = V_{f,p}$ .

$$V_{f,j} + \phi_j = 1 \quad (4-19)$$

As the degree of impregnation of the prepreg with resin  $I_r(t)$  increases, so does its global resin content  $V_{r,p}(t)$ . The degree of impregnation of the prepreg with air reduces and so does its global porosity  $\phi_p(t)$ . The instantaneous resin and air content of the prepreg are calculated from the local properties of the sub-domains ( $\phi_r, \phi_a$ ) and the fluid saturation via Equations (4-20) and (4-21).

$$V_{r,p}(t) = \phi_r \cdot I_r(t) \quad (4-20)$$

$$\phi_p(t) = \phi_a \cdot I_a(t) \quad (4-21)$$

The initial degree of impregnation of the MTM 44-1 prepreg with resin  $I_r(0) = 57.3\%$  is calculated from Equation (4-20), since the initial tow porosity in the resin impregnated domain  $\phi_r$  and prepreg resin content  $V_{r,p}$  are known. The thickness of the domain impregnated with resin  $H_{t,r}$  can be subsequently calculated from Equation (4-17).

## 4.2.2 Modeling Approach

The theoretical background used as a basis for the development of the non-isothermal OoA simulation is presented in this Section including utilized governing equations, constitutive laws and initial and boundary conditions.

### 4.2.2.1 Flow through a Porous Medium

At the beginning of the process, the prepreg is at atmospheric temperature and pressure ( $10^5$  Pa). At its initial state 57.3 % of the tow is saturated with resin, while the remaining domain is saturated with air. The air flows along the dry fibrous network once vacuum pressure is applied. Vacuum is pulled from one end of the tow ( $x = L$ ), causing the resin to impregnate the tow through its thickness  $H_p$ , with a flow front velocity  $u_{rf,zz}$ . The prepreg impregnation is driven by the difference between the atmospheric  $P_{atm}$  and the local air pressure  $P_{gas}$  developed at the interface of its two sub-domains saturated with air and resin. A linear discretization of the air and resin pressure is used in both domains. The boundary conditions for flow of both fluids (air and resin) are shown in Fig. 4-12.

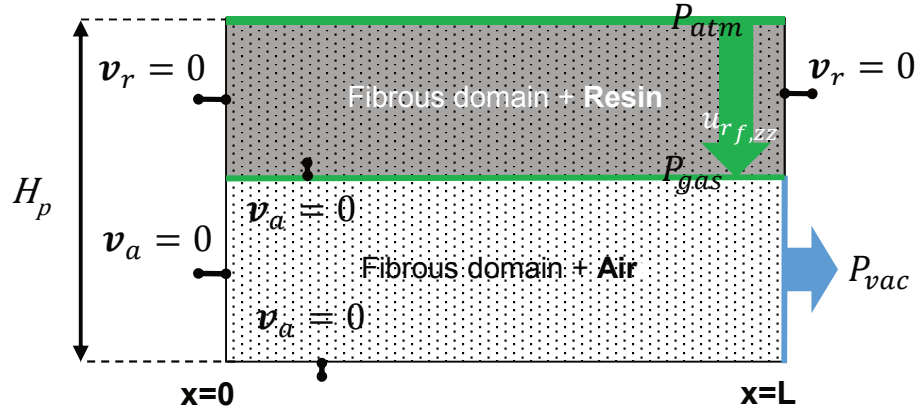


Fig. 4-12: Boundary conditions for air and resin flow

Equation (4-22) expresses the conservation of mass for each fluid saturating the fibrous medium, considering their flow through the prepreg is Darcian. The subscript  $j$  reflects either properties of the air ( $a$ ) or resin saturated phase ( $r$ ). The volume averaged velocity of the resin  $\mathbf{v}_{rD}$  is calculated via Equation (4-23), while that of air  $\mathbf{v}_{aD}$  by Equation (4-24). Equation (4-25) is used to calculate the flow front velocity of the fluids.

$$\frac{\partial(\rho_j \phi_j)}{\partial t} + \nabla \cdot (\rho_j \mathbf{v}_{jD}) = 0 \quad (4-22)$$

The resin is considered to be in a fluid state throughout the process and its pressure is expressed as  $P_f = P_r$ . The air pressure is expressed as  $P_{gas} = P_a$ .

$$\mathbf{v}_{rD} = -\frac{\mathbf{K}_r}{n} \nabla P_f \quad (4-23)$$

$$\mathbf{v}_{aD} = -\frac{\mathbf{K}_a}{\mu_a} \nabla P_{gas} \quad (4-24)$$

$$\mathbf{u}_{jf} = \frac{\mathbf{v}_{jD}}{\phi_j} \quad (4-25)$$

The resin permeability  $\mathbf{K}_r$  is the permeability of the MTM 44-1 prepreg tows (Equation (4-28)), while  $\mathbf{K}_a$  is the air permeability of the prepreg (Equation (4-29)). The viscosity of the resin  $n$  evolves during the process according to Equation (3-49), determined experimentally in Section 3.4. The air viscosity  $\mu_a$  is calculated by Equation (4-30). Equations (4-26) and (4-27) are used to quantify the pressure drop between the initial pressure  $P_{atm}$  and the pressure at time  $t$  in the prepreg domains, respectively.

$$\Delta P_f(t) = -(P_{atm} - P_f(t)) \quad (4-26)$$

$$\Delta P_{gas}(t) = -(P_{atm} - P_{gas}(t)) \quad (4-27)$$

## Resin Flow

The permeability of the prepreg's sub-domain saturated with resin  $\mathbf{K}_r$  (in  $m^2$ ), is described by a diagonal 2x2 tensor with components in the principal directions  $xx$  and  $zz$ , given by Equation (4-28).

$$\mathbf{K}_r = \begin{bmatrix} K_{r,xx} & 0 \\ 0 & K_{r,zz} \end{bmatrix} \quad (4-28)$$

Since only a limited amount of resin flows outside the part during OoA processing, the in-plane permeability  $K_{r,xx}$  is set to a low value in all simulations ( $K_{r,xx} = 10^{-20} m^2$ ) in order to inhibit in-plane resin flow from taking place. The out-of-plane permeability  $K_{r,zz}$  is the intrinsic permeability of the MTM 44-1 prepreg as depicted in Fig. 4-12. Its permeability  $K_{r,zz} = 7.58 \cdot 10^{-13} m^2$  is determined as the mean value of the quadratic and hexagonal permeability given by Equations (2-18) and (2-19) for the prepreg's fiber volume fraction  $V_{f,p} = 36 \%$ , which remains constant throughout the process as compaction of the fibrous medium is not taken into account (see Section 3.3.2). The semi-empirical viscosity model of the MTM 44-1 resin film is developed experimentally in the context of this work (see Section 3.4.3.3) and is implemented as a partial differential equation in COMSOL Multiphysics.

## Air Flow

The Ideal Gas Law is used to capture the thermodynamic behavior of air within the range of pressures and temperatures developed during OoA processing. The ratio of specific heat for dry air is set to  $\gamma = 1.4 = \text{constant}$  for the temperature range considered [234]. The heat capacity of air is considered to be constant (listed in Tab. 4-1). The density of air  $\rho_a$  at constant temperature is calculated from Equation (2-38). The permeability of air  $\mathbf{K}_a$  (in  $m^2$ ), is determined by the diagonal 2x2 tensor of Equation (4-29).

$$\mathbf{K}_a = \begin{bmatrix} K_{a,xx}(\phi_p) & 0 \\ 0 & K_{a,zz} \end{bmatrix} \quad (4-29)$$

As both sub-domains are considered to have the same fiber volume fraction, they have the same out-of-plane permeability  $K_{r,zz} = K_{a,zz} = 7.58 \cdot 10^{-13} m^2$ .

The effective in-plane air permeability of the MTM44-1 prepreg  $K_{a,xx}$ , is a function of its porosity  $\phi_p(t)$ . A fifth order polynomial correlates the in-plane permeability with the porosity according to Equation (3-23). A fourth order polynomial is used to approximate the dependency of the air viscosity  $\mu_a$  (in Pa·s) with temperature  $T$  (in K) [234]:

$$\begin{aligned} \mu_a(T) = & -8.38 \cdot 10^{-7} + (8.36 \cdot 10^{-8} T) - (7.69 \cdot 10^{-11} T^2) \\ & + (4.64 \cdot 10^{-14} T^3) - (1.07 \cdot 10^{-17} T^4) \end{aligned} \quad (4-30)$$

### 4.2.2.2 Heat Transfer in a Porous Medium

Out-of-Autoclave processing takes place in an oven or a heated tool. The part is heated either directly through its bottom side (heated tool), or through forced convection (oven). The temperature boundary conditions vary in the following Chapters, they will therefore be presented in each Section as necessary.

The conservation of energy expressed separately for each prepreg sub-domain, which is saturated either with air or resin ( $j = a, r$ ) is expressed by Equation (4-31).

$$\langle \rho C_p \rangle_j \frac{\partial T}{\partial t} = \nabla \cdot (\langle \mathbf{k} \rangle_j \nabla T) \quad (4-31)$$

Since the MTM 44-1 resin has limited exothermic capacity at the concerned temperatures as observed during the course of validation experiments (Chapter 5), the viscous dissipation is insignificant and therefore the term  $\langle Q \rangle_j$  included in the general expression of Equation (2-63) is omitted. The convection term, which incorporates the contribution of the volume averaged fluid velocities  $\mathbf{v}_{jD}$  has also been omitted due to the small magnitude of the flow velocities and therefore the negligible contribution of the term.

The effective volumetric heat capacity of each sub-domain  $\langle \rho C_p \rangle_j$ , is calculated at constant pressure according to Equation (2-66), while the density of air  $\rho_a$  is calculated by Equation (2-38). The resin  $\rho_r$  and fiber density  $\rho_f$  are considered to be independent of the processing temperatures. The heat capacity of the MTM 44-1 resin  $C_{p_r}$ , is characterized by Dimopoulos et al. [235]. Since curing does not take place during the simulated process, the  $C_{p_r}$  of the uncured resin (from Dimopoulos et al. [235]) is used in this work.

The heat transfer in porous media interface available in COMSOL Multiphysics is based on the theory of soils. The skeleton of soils, in contrast to the fibrous media utilized in composites manufacturing have homogeneous heat transfer properties [108, 234] and hence a single model is sufficient to describe their in and out-of-plane thermal conductivity. Composite parts on the other hand are often manufactured using long fibers. In particular carbon fibers investigated in this work have a significantly higher in-plane conductivity ( $k_{f,xx} > k_{f,zz}$ ). Therefore the effective in-plane conductivity of the prepreg and therefore the conductivity of the produced part is much higher than its out-of-plane conductivity. To capture this directionality, the thermal conductivity of the fibrous medium is expressed by the diagonal tensor of Equation (4-32) with contributions in the two primary axes ( $xx$  and  $zz$ ).

$$\mathbf{k}_f = \begin{bmatrix} k_{f,xx} & 0 \\ 0 & k_{f,zz} \end{bmatrix} \quad (4-32)$$

The thermal conductivity of air  $k_a$  (in  $\text{WK}^{-1}\text{m}^{-1}$ ) is expressed as a function of the temperature  $T$  (in K) as a fourth order polynomial, according to Equation (4-33) [236].



$$k_a(T) = -2.28 \cdot 10^{-3} + (1.15 \cdot 10^{-4} T) - (7.90 \cdot 10^{-8} T^2) + (4.12 \cdot 10^{-11} T^3) - (7.44 \cdot 10^{-17} T^4) \quad (4-33)$$

To include the insulating effect caused by the presence of air inside the tows, the effective thermal conductivity of the air saturated domain  $\langle \mathbf{k} \rangle_a$  is calculated from the reciprocal average of the conductivities of air and fibers, according to Equation (2-69). The effective thermal conductivity of the resin saturated domain  $\langle \mathbf{k} \rangle_r$  is calculated by the volume average of the fiber and resin conductivities, according to Equation (2-68). All coefficients utilized as inputs in the heat transfer model are summarized in Tab. 4-1.

**Tab. 4-1: Material properties used to model heat transfer in COMSOL Multiphysics**

Property	Value	Unit	Property	Value	Unit
$V_{f,a} = V_{f,r} = V_{f,p}$	36	%	$k_{f,xx}^*$	10	$W \cdot m^{-1} \cdot K^{-1}$
$\phi_a = \phi_r = 1 - V_{f,p}$	64	%	$k_{f,zz}^{***}$	3.89	$W \cdot m^{-1} \cdot K^{-1}$
$\rho_f^*$	1760	$kg \cdot m^{-3}$	$k_r^{****}$	0.24	$W \cdot m^{-1} \cdot K^{-1}$
$\rho_r^{**}$	1180	$kg \cdot m^{-3}$	$C_{p_f}^*$	710	$J \cdot kg^{-1} \cdot K^{-1}$
*Tenax HTA 40 Product Data Sheet [224]			$C_{p_r}^{****}$	2700	$J \cdot kg^{-1} \cdot K^{-1}$
**Cytac MTM 44-1 Product Data Sheet [225]			$C_{p_a}$	1.00	$J \cdot kg^{-1} \cdot K^{-1}$
*** Zimmerman et al. [237]					
**** Dimopoulos [235]					

### 4.2.3 Coupling Scheme

Constructing a part with thickness  $H$ , requires stacking of a number of prepreg plies of thickness  $H_p$  on top of each other. Each ply consists of two sub-domains, the bottom, saturated with air and the top, saturated with resin. Relevant material properties and boundary conditions are assigned to each prepreg domain.

The finite element method is used to discretize the coupled resin, air flow and heat transfer equations inside the fibrous domain. The time variable problem is integrated by implicit Backward Differentiation Formulas (BDF) in COMSOL Multiphysics v. 5.2 [234]. The non-linear equations are solved according to the Newton method, producing several linear systems, solved by a Direct Gauss solver (MUMPS) [234]. The temperature, air and resin pressure fields and their respective velocities, the local or global porosity evolution and the degree of impregnation during the cure cycle are calculated. Accurate resin front localization enables capturing local impregnation differences, which may occur because of local air pressure, or temperature differences present in the prepreg. The heat transfer affects the air and resin viscosity, the air density of the material. The air density and pressure are directly correlated through the ideal gas law, contributing significantly to the final air pressure development inside the prepreg.



The boundary between the resin and air saturated fibrous domains deforms as a function of the normal component of the resin velocity developed at the flow front  $u_{rf,zz}$ , utilizing an Arbitrary Eulerian Lagrangian scheme, implemented via a Deformed Geometry interface (DG). In this case, the deformation of the domain can be regarded as addition (resin) or removal (air) of material [234]. The new position of the resin front becomes the new boundary between the two domains, each saturated with a different fluid (air and resin). The gas pressure developed at the common boundary acts as a bidirectional, symmetric constraint for the properties of both prepreg sub-domains. Flux conditions introduced this way appear as reaction terms in the system of equations of the acting physics affecting all dependent properties involved [234]. The degree of the prepreg's impregnation with resin increases while its porosity reduces, leading to a subsequent reduction of its air permeability. The coupling scheme utilized is graphically presented in Fig. 4-13. As a result, the 2D, two-way interaction between the physics and the utilization of a moving flow-front enables the local variations of the pressure, density and porosity to affect not only the air evacuation but also the local progression of the resin front, closely mimicking the actual physics of the OoA process.

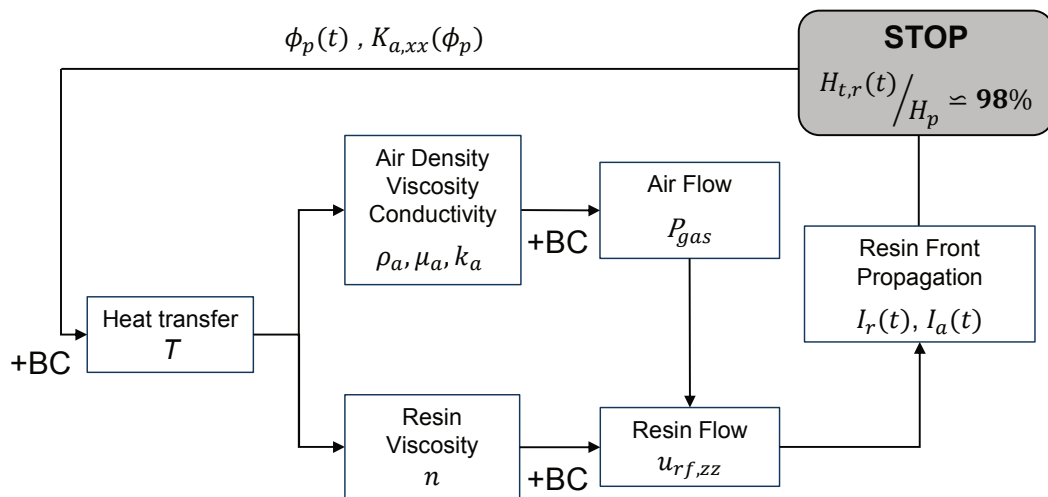


**Fig. 4-13: Coupling scheme utilized in modeling the non-isothermal impregnation of the OoA prepreg in COMSOL Multiphysics**

A structured mesh consisting of linear elements (1<sup>st</sup> order) which are denser close to the vacuum inlet where most of the boundary deformation takes place due to the presence of high pressure gradients. The mesh is less dense far from the vacuum source. The remaining domain is sparsely meshed in order to circumvent the calculation resource limitation occurring when a dense mesh is used in the whole geometry. The mesh density is defined by the interaction between the physics resolved in each sub-domain and test-case, examples of the utilized meshes are presented individually in each Section. Generally six elements are included as a minimum through the thickness of each ply, while at least three elements are included in each sub-domain of the prepreg (air or resin saturated). A variable element size is selected along the tow length, in order to limit the

calculation time, while avoiding compromising the quality of the results where a dense mesh is necessary. The mesh deformation is attained via the use of a Winslow smoothing equation [234]. To avoid its significant degradation, automatic re-meshing takes place at a predefined distortion ( $I_{isoMax} > 1.2$  or  $1.3$ ), reflecting the maximum of the first invariant of the isochoric mesh strain tensor [234]. When the resin impregnation front reaches approximately 98% of the ply thickness ( $z_f = 98\% H_p$ ), the local warpage of elements may lead to instability and physical inconsistencies since the air saturated domain cannot be fully replaced by the resin saturated domain. For this purpose, a step function which drives the local velocity field of the resin to zero between 97.5% and 98.5%  $H_p$  is implemented. Hence, the maximum amount of tow impregnation  $I_r$ , is limited to 98.5% of the tow area  $A_p$ . This leads to a maximum of 0.75% porosity, which will remain in the tow as residual porosity, considering 50% of the area consists of fibers. The competition between air and resin flow through the same tow is largely influenced by the pressure developed on the boundary between the two sub-domains. This pressure directly affects the flow front velocity, as shown in the coupling scheme depicted in Fig. 4-13. Fast progression of the flow front close to the vacuum, inhibits the vacuum distribution along the length of the tow and leads to air entrapment. On the other hand, slow impregnation enables homogeneous vacuum distribution and reduces chances of air entrapment in the tow, as long as the impregnation completes before gelling. Therefore the modeling framework proposed, can address the impregnation of a range of materials (as long as they can be described according to Section 4.2.1) and time scales of flow, while no adaptation of the coupling scheme or the underlying physics required, contrary to most state-of-the-art approaches [28, 68, 73, 76].

#### 4.2.4 Sensitivity Studies

The influence of selected material properties, such as the resin viscosity and prepreg permeability, as well as process conditions, such as the heating rate during the cure cycle, on the gas pressure and the residual part porosity is investigated in this Section. The following studies are used to draw conclusions on the influence of material characteristics and processing parameters, on the impregnation quality of a part manufactured outside the Autoclave and develop strategies, which will lead to the manufacturing of a part with reduced residual porosity.

The gas pressure development inside the prepreg without the influence of temperature is presented in Section 4.2.4.1. In this Section the gas pressure is not influenced by the impregnation of the prepreg with resin, since the resin flow is considered insignificant and is therefore ignored. Sections 4.2.4.2 and 4.2.4.3 are concerned with the coupled air and resin flow physics, with the former focusing on the influence of the material properties on the air evacuation during debulking at room temperature and the latter on the influence of the heating rate during the cure cycle. Finally, in Section 4.2.4.4, two studies demonstrate the influence of a temperature gradient developed along the length and the thickness of two parts manufactured OoA on an insulated heated tool. In the first case

the temperature gradient is introduced on the tool (consisted of three heating zones), while on the second case a thicker part is heated from the bottom to the top. The geometry of Fig. 4-14 depicts two MTM 44-1 prepreg plies stacked on top of each other, constructing a part of thickness  $H$  and length  $L$ . This part is used as a basis for the studies of Sections 4.2.4.1 up to 4.2.4.3.

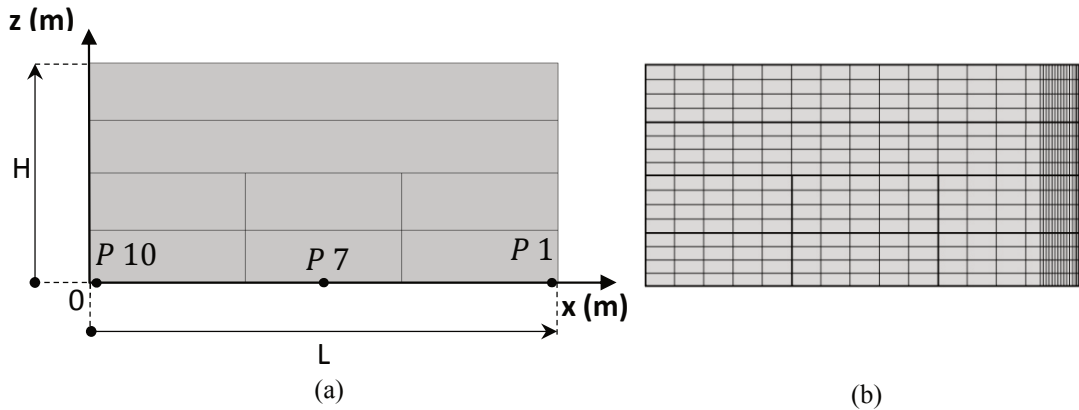


Fig. 4-14: (a) Domain geometry and (b) meshing concept used to perform sensitivity studies

Three probes are positioned at the bottom ply of the part depicted in Fig. 4-14(a), at three locations along the part length, at position  $P 1$  close to the vacuum source,  $P 7$  in the mid-span of the part and  $P 10$  far from the vacuum source (see Tab. 4-2).

Tab. 4-2: Part dimensions, probe coordinates and miscellaneous inputs for sensitivity studies

Category	Symbol	Unit	Value
Simulation Inputs	$P_{vac}$	$Pa$	400
	$\rho_\alpha$	$kg \cdot m^{-2}$	1.1886
	$H_p$	$m$	$0.45 \cdot 10^{-3}$
	$H$	$m$	$0.9 \cdot 10^{-4}$
	$L$	$m$	0.59
	$I_r$	%	53
	$V_{f,p}$	%	36
	$V_{r,p}$	%	34
Probes	$\phi_p$	%	30
	$P 1$	$m$	$(0.58997, 0)$
	$P 7$	$m$	$(0.3, 0)$
	$P 10$	$m$	$(1.719 \cdot 10^{-4}, 0)$

The domain as shown in Fig. 4-14(b) is discretized with 640 elements, 4 of which are equally spaced through its thickness. The computation time following the methodology presented in Fig. 4-14 is 10-20 min in a computer with 16 GB Ram and 8 Cores.

#### 4.2.4.1 Air Flow and Evacuation

##### Influence of Fiber Bed Characteristics on the Vacuum Distribution

Focus of this study is to demonstrate the effect of the in ( $K_{a,xx}$ ) and out-of-plane permeability ( $K_{a,zz}$ ) of the prepreg to air, on gas pressure development inside the material without the influence of the temperature and the interaction with resin flow. The air is considered to flow within the dry tow of each prepreg ply at 291.9K ( $\sim 19^\circ\text{C}$ ), under the influence of the boundary conditions shown in Fig. 4-15. The initial pressure within the domain is atmospheric ( $P_{atm} = 10^5 \text{ Pa}$ ). To avoid numerical instabilities from occurring within the first time steps, due to the large initial pressure drop between atmospheric and the vacuum pressure imposed at position  $x=L$ , the vacuum is applied through a step function in  $t_s = 1.5\text{s}$ , according to the profile shown in Fig. 4-15(b).

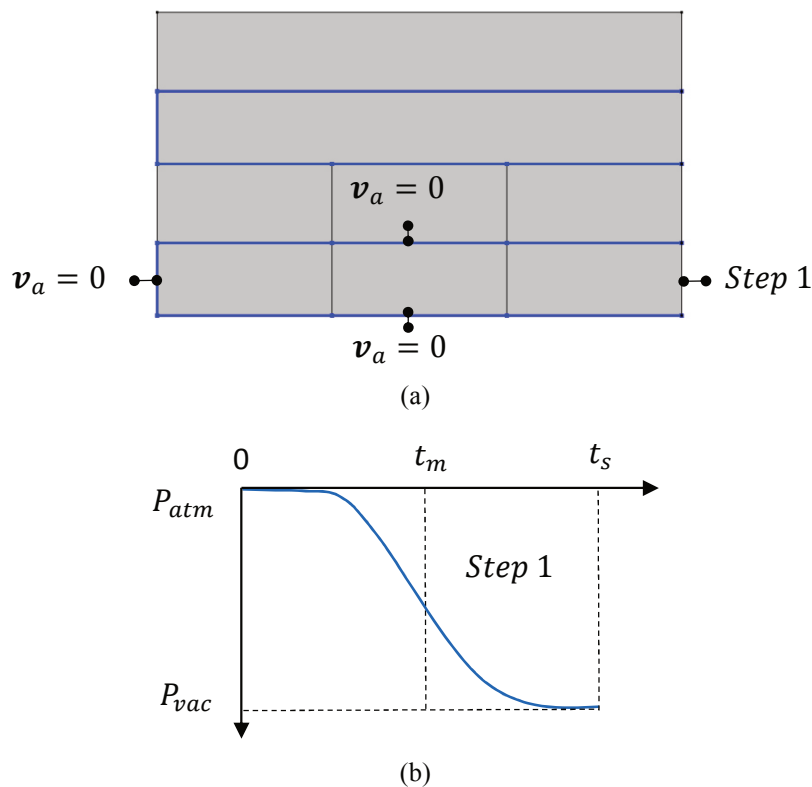


Fig. 4-15: (a) Boundary conditions for air flow and (b) vacuum application via a step function

The influence of five permeability ratios ( $K_{a,zz} / K_{a,xx}$ ) on the gas pressure development along the part length is investigated. Materials with the in and out-of-plane air permeabilities of Cases 1-5 presented in Tab. 4-3 are utilized for this purpose. The in-plane permeability in Cases 1-4 (see Tab. 4-3) reflects the permeability of the MTM 44-1 prepreg, at its initial porosity  $\phi_p(0)$ , which is considered to remain constant. The applied vacuum pressure  $P_{vac}$ , the ply thickness  $H_p$ , the volume fractions of all constituents and the air density  $\rho_\alpha$  are summarized in Tab. 4-2.

**Tab. 4-3: Permeability characteristics of the air saturated prepreg domain**

Case	$K_{a,xx} (m^2)$	$K_{a,zz} (m^2)$	$K_{a,zz} / K_{a,xx}$
1	$1.55 \cdot 10^{-12}$	$7.58 \cdot 10^{-13}$	$4.88 \cdot 10^{-1}$
2	$1.55 \cdot 10^{-12}$	$4.14 \cdot 10^{-15}$	$2.66 \cdot 10^{-3}$
3	$1.55 \cdot 10^{-12}$	$2.16 \cdot 10^{-18}$	$1.39 \cdot 10^{-6}$
4	$1.55 \cdot 10^{-12}$	$2.16 \cdot 10^{-20}$	$1.39 \cdot 10^{-8}$
5	$1.00 \cdot 10^{-15}$	$7.58 \cdot 10^{-13}$	$7.58 \cdot 10^2$

The simulated pressure at the three positions along the length of the part ( $P_1, P_7, P_{10}$ ) for prepregs having the same in-plane air permeability and reducing through thickness permeability (materials with the characteristics of Cases 1-4), is depicted in Fig. 4-16.

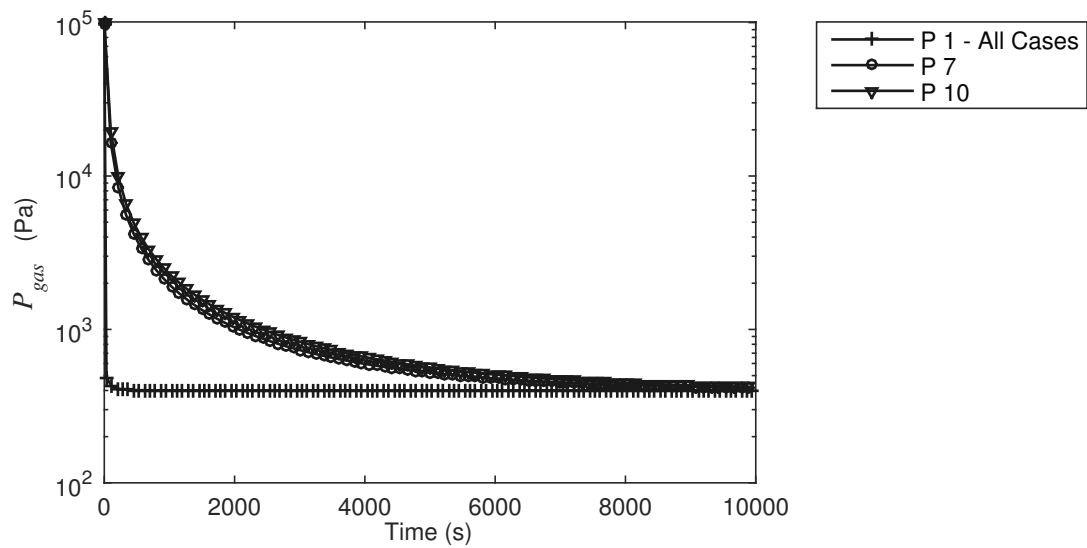


**Fig. 4-16: Gas pressure evolution over time at three locations along the part length, for the materials with permeabilities of Cases 1-4 (Fig. 4-3)**

In Fig. 4-16 it is shown that a reduction of the through thickness permeability occurring when replacing the material properties of Case 1 with Cases 2-4, has no effect on the gas pressure distribution along the part length. It is evident that in all cases considered, the air flow takes place predominantly in-plane.

A significant difference between the magnitudes of the in ( $v_{aD,xx}$ ) and out-of-plane velocities of air ( $v_{aD,zz}$ ) for the prepregs with characteristic properties of Cases 1-4 is observed in Fig. 4-17. The ratio of the two velocities is plotted as a function of time in Fig. 4-17, for the same four materials (Cases 1-4).

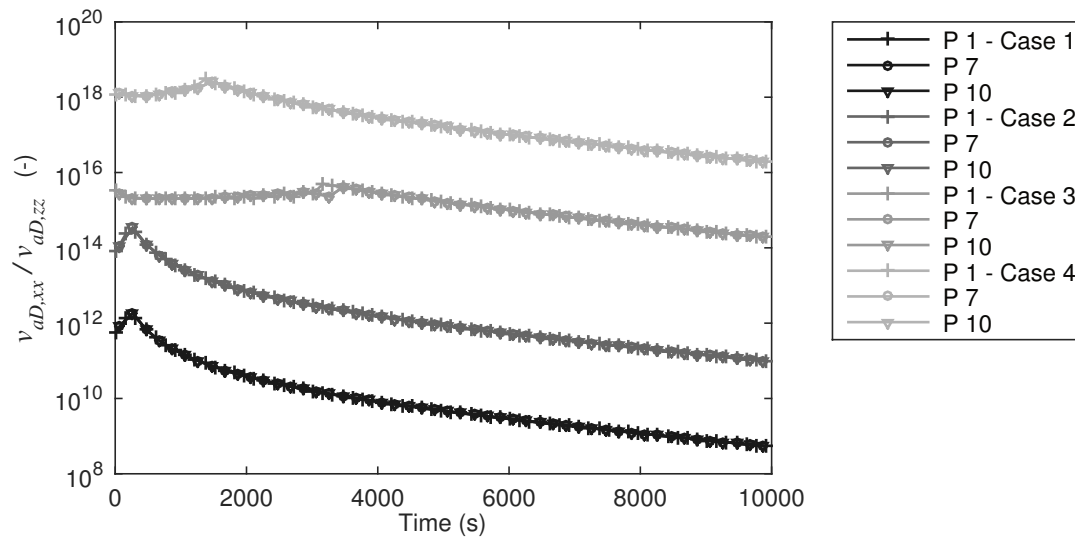


**Fig. 4-17:** Influence of the through thickness air permeability reduction  $K_{a,zz}$  (Cases 1-4) on the in-plane versus out-of-plane air velocity ratio  $v_{aD,xx}/v_{aD,zz}$

The Fig. 4-17 shows that the in-plane air evacuation is dominant in all materials investigated ( $v_{aD,xx}/v_{aD,zz} \gg 1$ ), even in Case 1 where the two permeabilities are of similar magnitude ( $K_{a,zz} \cong 0.5 K_{a,xx}$ ). This is a consequence of the boundary conditions applied in the domain (see Fig. 4-15), as well as the dimensions of the domain at the two principal flow directions, which contribute primarily to the development of a large pressure gradient along the  $x$  – axis.

The influence of the in-plane air permeability reduction on the gas pressure developed at positions  $P 1$ ,  $P 7$ ,  $P 10$  between the material of Case 1 and 5 (see Tab. 4-3), is shown in Fig. 4-18.

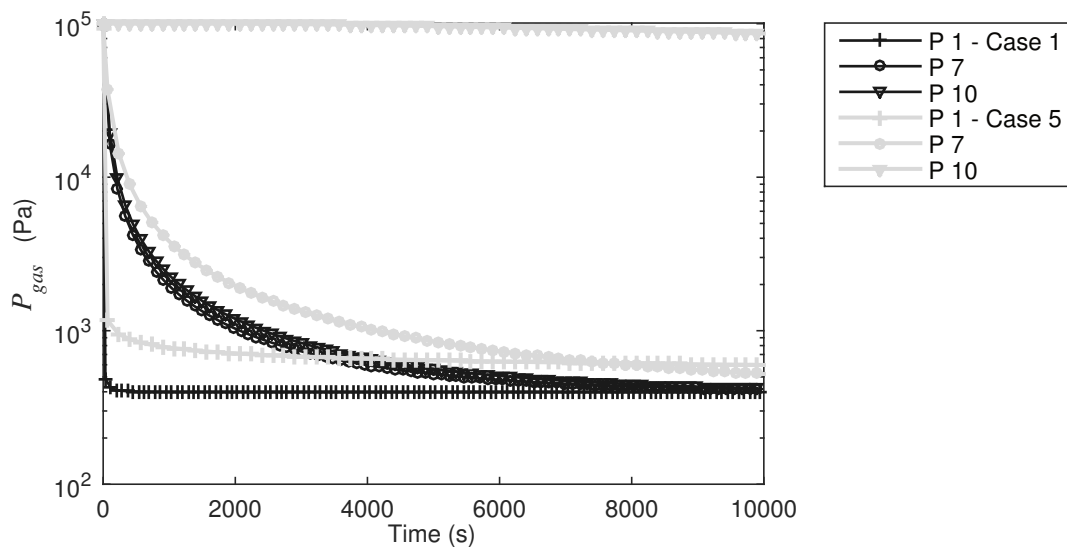


**Fig. 4-18:** The influence of the in-plane air permeability reduction from Cases 1 to Case 5, on the gas pressure evolution at three locations along the part length

The in-plane air permeability of the prepreg in Case 5 reduces by approximately three orders of magnitude compared to that of Case 1, while its through-thickness permeability remains the same in both cases. This causes a significant delay in the gas pressure distribution inside the prepreg. The gas pressure developed inside the dry tows of the prepreg is shown in Fig. 4-19.

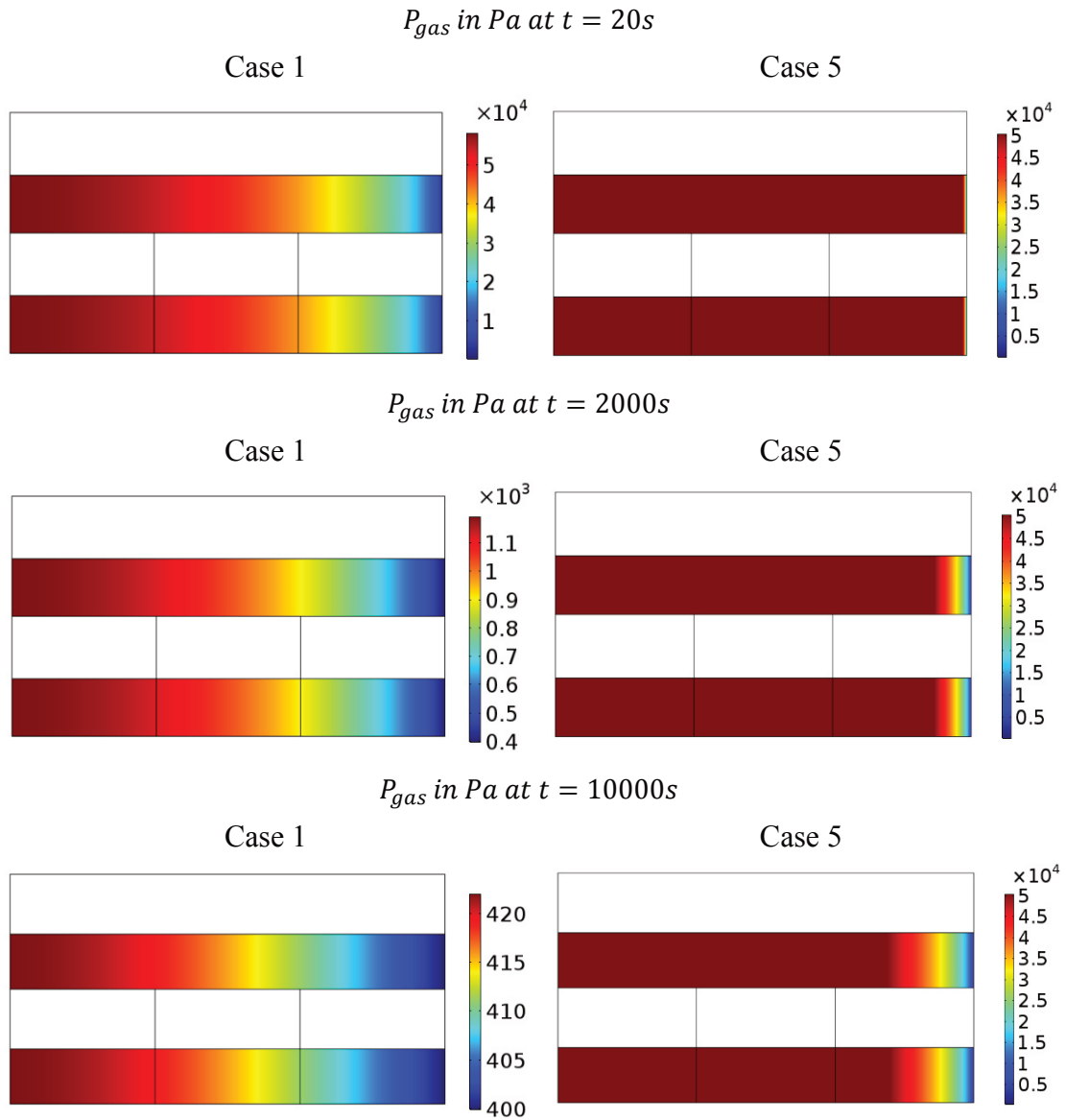


**Fig. 4-19: Gas pressure distribution in the air saturated prepreg sub-domain**

A homogeneous pressure distribution is attained in both parts through the thickness of the air saturated prepreg domain, while a large gas pressure gradient is developed in-plane, for prepregs with characteristic permeabilities of Case 1 and 5. Particularly in Case 1 a steady state of pressure is reached within the first 10000s of the study, while in Case 5, the distribution of the gas pressure is significantly slower.

### Influence of Temperature and Heating Rate on the Vacuum Quality

The influence of temperature and heating rate on the gas pressure distribution inside the prepreg with characteristics of Case 1 is investigated here for Fig. 4-14. Heat is introduced from the bottom of a single-sided tool as a temperature profile  $T(t)$ , reflecting the temperature development on the tool-part interface during the cure cycle. The top and the two sides of the part are insulated. The influence of two temperature profiles on the gas pressure is directly compared against the scenario of vacuum application on the same prepreg, at room temperature. The temperature profiles are depicted in Fig. 4-20.

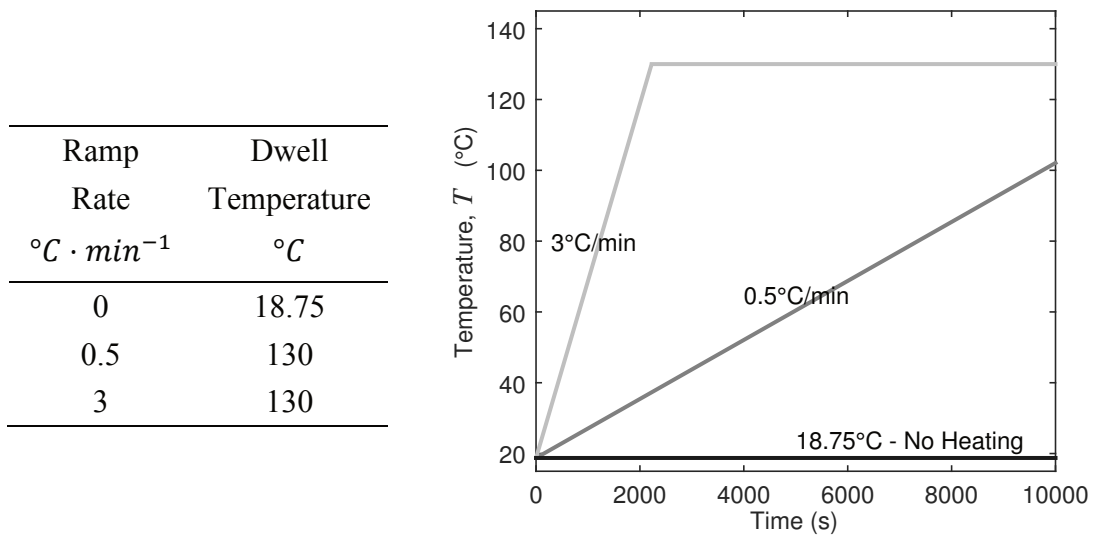


Fig. 4-20: Temperature development on the tool surface during three OoA cure cycles

The gas pressure and density are correlated via the Ideal Gas Law (Equation (2-40)) during the temperature cycles of Fig. 4-20, presented in Fig. 4-21 and Fig. 4-22.

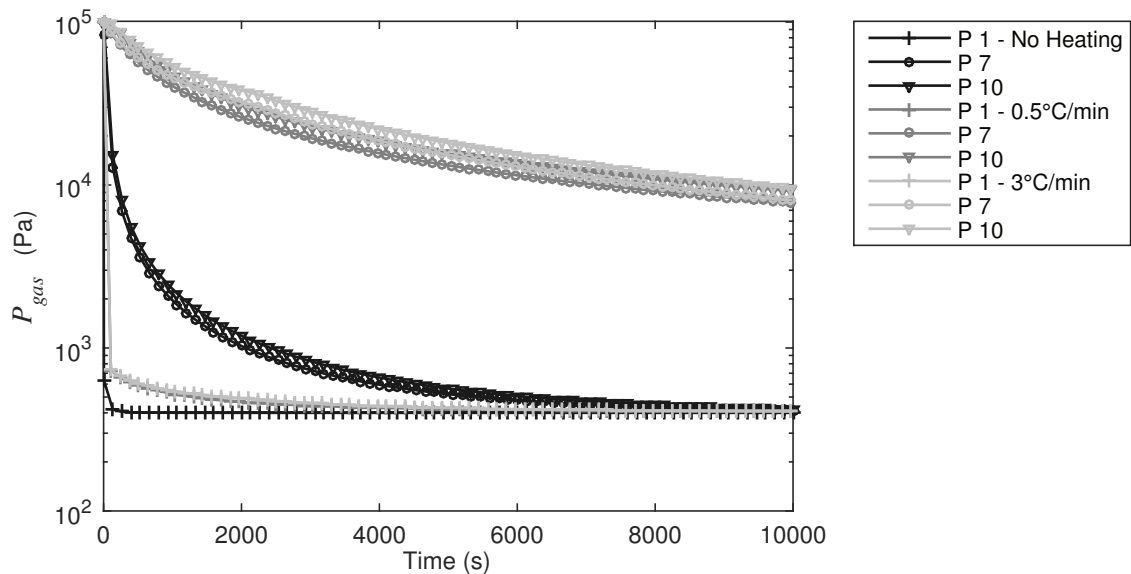


Fig. 4-21: Gas pressure evolution along the length of the air-saturated prepreg domain in the material of Case 1 and for cure cycles shown in Fig. 4-20



As shown in Fig. 4-21, heating the part before the vacuum or gas pressure reaches a steady state inside the tow has a negative influence on the pressure distribution along its length. The more pronounced effect is observed far from the vacuum source, at locations  $P 7$ ,  $P 10$ , where the vacuum pressure is established slower even when no heating takes place. The application of heat delays the gas pressure distribution far from the vacuum source as shown in Fig. 4-21, which consecutively leads to a slower air density reduction, presented in Fig. 4-22.

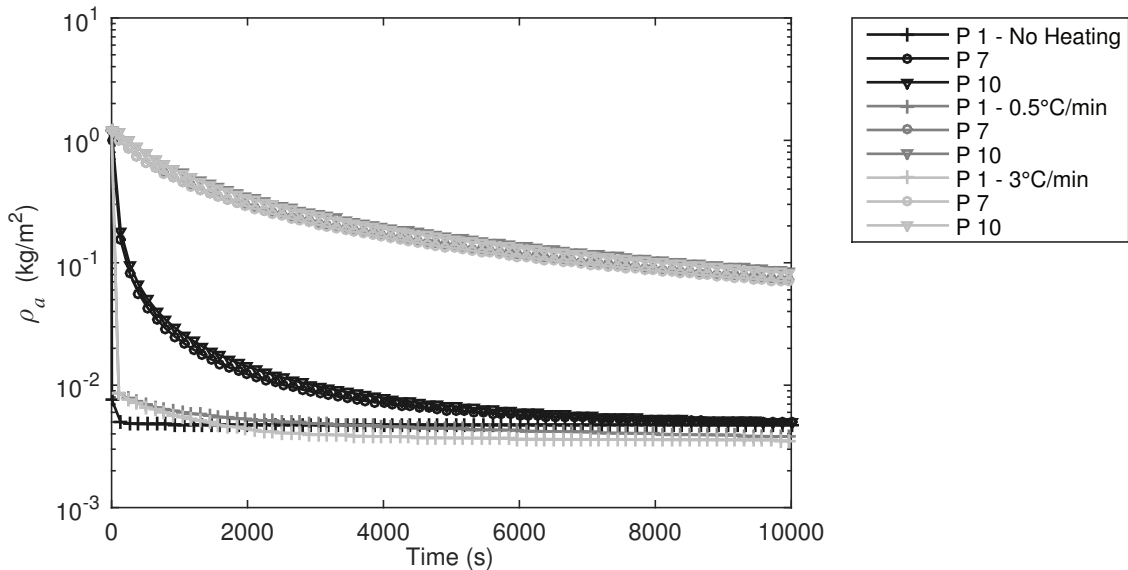


Fig. 4-22: Air density evolution along the length of the air-saturated prepreg of Case 1 and for cure cycles shown in Fig. 4-20

Generally, the higher the heating rate of the prepreg, the slower the vacuum distribution inside the tow and the larger the influence on the gas pressure, at the different locations along the length of the part. Once a steady state of pressure is attained inside the prepreg, the density is only influenced by the temperature development inside the part.

#### 4.2.4.2 Coupled Air and Resin Flow in OoA prepreps during Room Temperature Debulking

In this Section the coupled air and resin flow through the prepreg depicted in Fig. 4-1 is investigated at 291.9K ( $\sim 19^\circ\text{C}$ ). The investigation performed in Section 4.2.4.1 takes into account solely the air flow through the prepreg considering the resin does not flow at room temperature. This approach is extended here to consider also the influence of the resin flow at room temperature on the gas pressure distribution. The competition between the two flows in the same fibrous domain during debulking at room temperature and the influence it has on the gas pressure development and the prepreg saturation is investigated for a range of permeabilities and two resin viscosities.

### Influence of Fiber Bed Characteristics on the Vacuum Quality

The influence of three combinations of out-of-plane permeabilities for the two prepreg sub-domains ( $K_{a,zz}$ ,  $K_{r,zz}$ ) on the gas pressure distribution inside the prepreg is investigated. In both Case 1 and Case 3, the through-thickness permeability of the two sub-domains is equal ( $K_{a,zz} = K_{r,zz}$ ). The material of Case 6 has the same through-thickness permeability of the resin saturated sub-domain of Case 1 and a significantly reduced through-thickness permeability of the air saturated sub-domain ( $K_{a,zz} \ll K_{r,zz}$ ). The reduction of the through-thickness permeability to air creates a resistance to the resin flow through the thickness of the prepreg ply. Such a scenario may be realistic if the air evacuation leads to a dense packing of the fibers in the air saturated domain, causing a reduction of its through thickness permeability (resin saturated domain incompressible). The in-plane air permeability of the MTM 44-1 prepreg is implemented as a function of the global part porosity  $K_{a,xx}(\phi_p)$  according to the Equation (3-23). The in and out-of-plane permeability of the prepreg to resin  $K_{r,xx}$ ,  $K_{r,zz}$  and its out-of-plane permeability to air  $K_{a,zz}$  are summarized in Tab. 4-4. The initial resin viscosity is considered constant throughout the debulking process ( $n_o = 6.5 \cdot 10^5 \text{ Pa} \cdot \text{s}$ ).

**Tab. 4-4: Permeability characteristics of the materials from Case 1, 3, 6 under investigation**

Case	$K_{a,zz} \text{ (m}^2\text{)}$	$K_{r,xx} \text{ (m}^2\text{)}$	$K_{r,zz} \text{ (m}^2\text{)}$
1	$7.58 \cdot 10^{-13}$	$3.26 \cdot 10^{-20}$	$7.58 \cdot 10^{-13}$
3	$2.16 \cdot 10^{-18}$	$3.26 \cdot 10^{-20}$	$2.16 \cdot 10^{-18}$
6	$1.00 \cdot 10^{-20}$	$3.26 \cdot 10^{-20}$	$7.58 \cdot 10^{-13}$

The global porosity and in-plane air permeability evolution of the simulated part (see Fig. 4-14) for Cases 1, 3 and 6 are shown in Fig. 4-23.

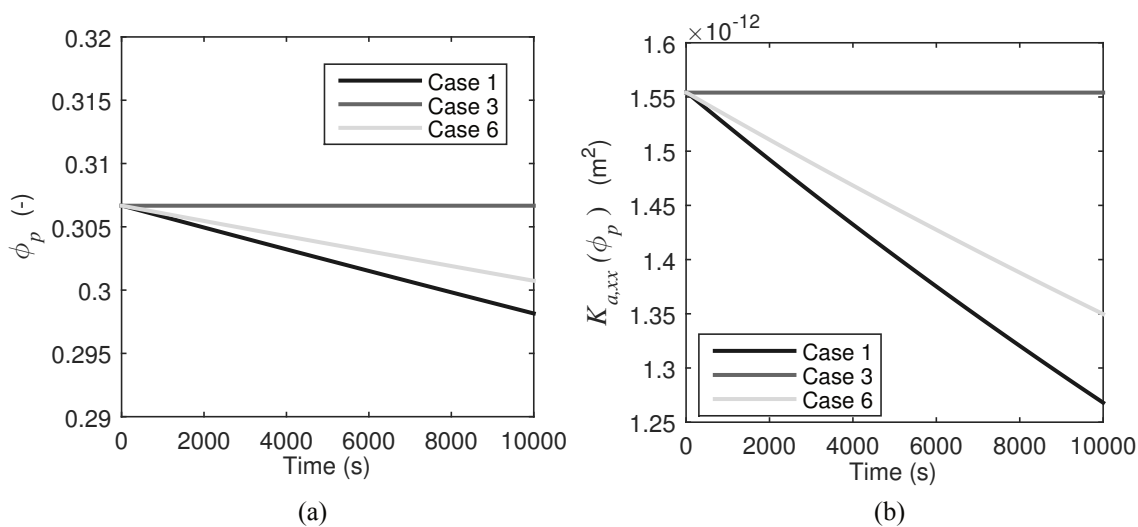


**Fig. 4-23: (a) Prepreg porosity evolution over time and (b) resulting in-plane air permeability evolution over time for Cases 1, 3 and 6 (see Tab. 4-4)**

From Fig. 4-23(a) it can be observed that the fastest porosity reduction is achieved when using the prepreg of Case 1, while the prepreg of Case 6 follows. Since the prepreg compaction is omitted, a faster reduction of the porosity reflects a faster impregnation of the prepreg with resin. The in-plane air evacuation reduces faster as a consequence (Fig. 4-23(b)). The competition between the air and resin flow inside the prepreg at 291.9K (~19°C) has an influence on the establishment of the gas pressure in the material, even when small porosity differences like those depicted in Fig. 4-23(a) are concerned. The gas pressure development at selected positions such as at position  $P$  1 close to the vacuum source, at position  $P$  7 in the middle of the part and at position  $P$  10 far from the vacuum source is depicted in Fig. 4-24 for all three Cases considered.

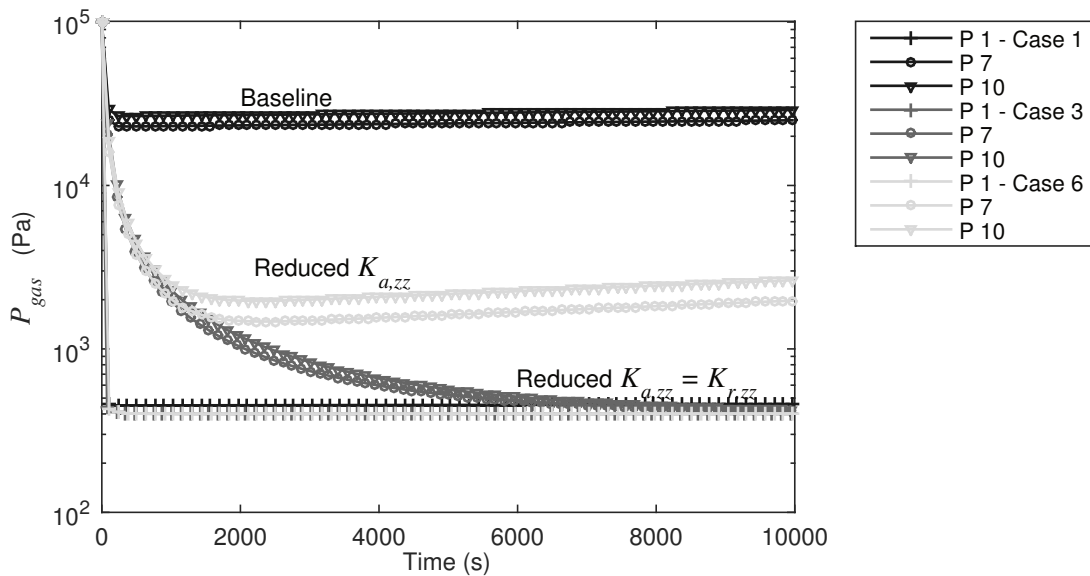


**Fig. 4-24:** Gas pressure evolution along the length of the air-saturated prepreg domain for prepreps with the properties of Cases 1, 3 and 6 (see Tab. 4-4) at 291.9K (~19°C)

The prepreps of Case 1 and 6 have the highest out-of-plane permeability to resin ( $K_{r,zz}$ ). Nevertheless the reduction of the through thickness air permeability ( $K_{a,zz}$ ) from Case 1 to Case 6, leads to an intensification of the in-plane air flow along the length of the part, which is beneficial for the vacuum distribution along its length while it simultaneously imposes a resistance to the resin flow through its thickness. The gas pressure developed in Case 6 in the middle ( $P$  7) and at the end of the part ( $P$  10) increases after approximately 2500s due to the significant porosity reduction, driven by the high initial vacuum (low gas pressure) established in the prepreg compared to Case 1 and the resulting air permeability reduction. A small increase of the gas pressure after approximately 2000s is also observed in Case 1, though at a much slower rate compared to Case 6, due to the presence of a limited pressure difference (higher gas pressure) responsible for the air flow inside the material as shown in in Fig. 4-25. The prepreg of Case 3 has a significantly reduced through thickness permeability in both of sub-domains compared to the prepreg of Case 1. A homogeneous and fast in-plane air evacuation is achieved in

Case 3, where the pressure developed in all three positions closely matches the gas pressure attained when no resin flow is considered (see Fig. 4-18), though at a cost of a slower prepreg impregnation rate with resin. This indicates a limited interaction between air and resin flow in this material.

The pressure difference between atmospheric and gas pressure attained after 20s and 10000s from the vacuum application ( $\Delta P_f$  &  $\Delta P_{gas}$ ) is depicted in Fig. 4-25. The dark red color stands for zero pressure-drop, while the dark blue reflects the maximum attainable pressure-drop.

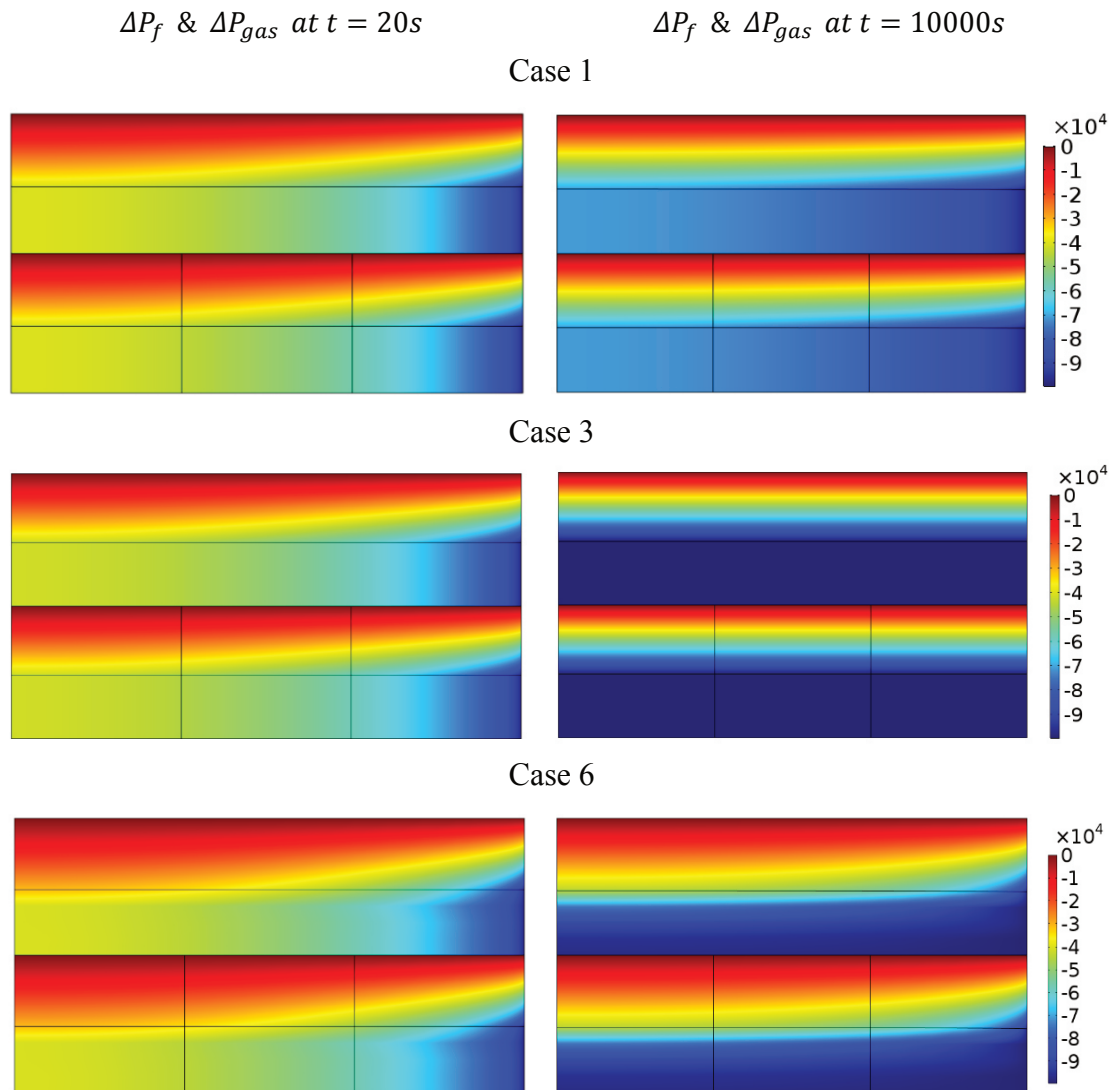


**Fig. 4-25:** 2D plots depicting the pressure difference developed along the length and thickness of the part at 20s and 10000s, for the prepregs of Cases 1, 3 and 6 (see Tab. 4-4)

A delay in the gas pressure distribution along the part length can be observed inside the air saturated domains of the prepreg, particularly for the prepregs of Case 1 and 6. Primary reason for this delay is the faster resin impregnation speed of these prepregs (Cases 1 and 6), reflected on the porosity reduction speed captured in Fig. 4-23(a). Particularly

in the prepreg of Case 6, a pressure gradient is present through the thickness of its air saturated domain. While the gas pressure close to the tool surface and along the complete part length approaches vacuum, it reduces close to the boundary between the two fluids.

### Influence of Initial Resin Viscosity on the Vacuum Quality

Focus of this Section is the identification of means to enhance the vacuum distribution along the part length, particularly for the prepregs with the permeabilities of Cases 1 and 6 where a homogeneous in-plane air evacuation is not possible. Since the impregnation speed of the prepreg with resin inhibits the vacuum distribution along its length, the reduction of the impregnation speed at room temperature shall be beneficial to attaining homogeneous vacuum distribution during debulking. Therefore the influence of a resin viscosity increase by two orders of magnitude is investigated (from  $6.5 \cdot 10^5 \text{ Pa} \cdot \text{s}$  to  $6.5 \cdot 10^7 \text{ Pa} \cdot \text{s}$ ). The influence of the viscosity increase on the gas pressure distribution along the part length for the prepregs of Case 1 and 6, is captured in Fig. 4-26.

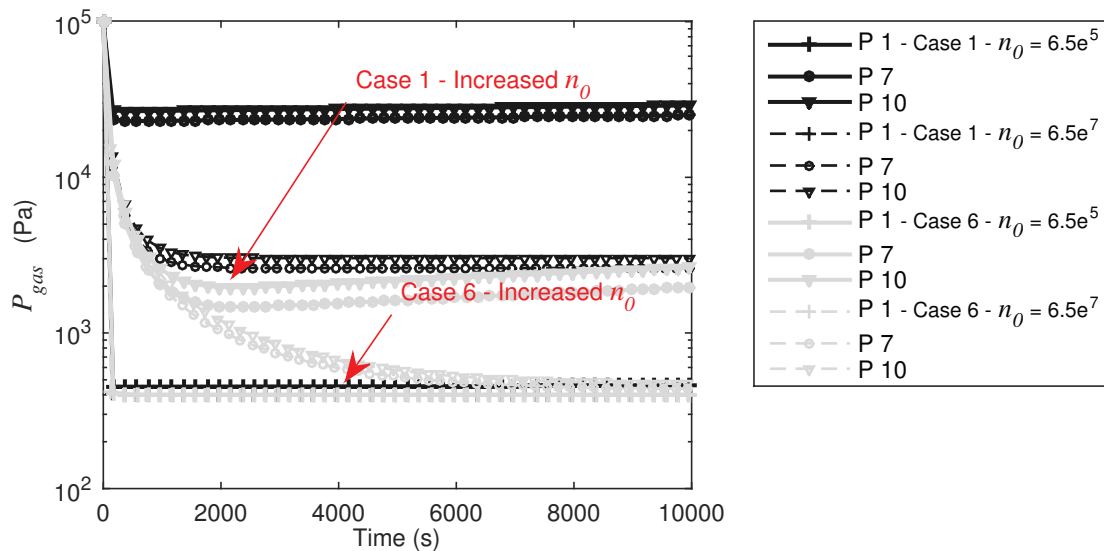
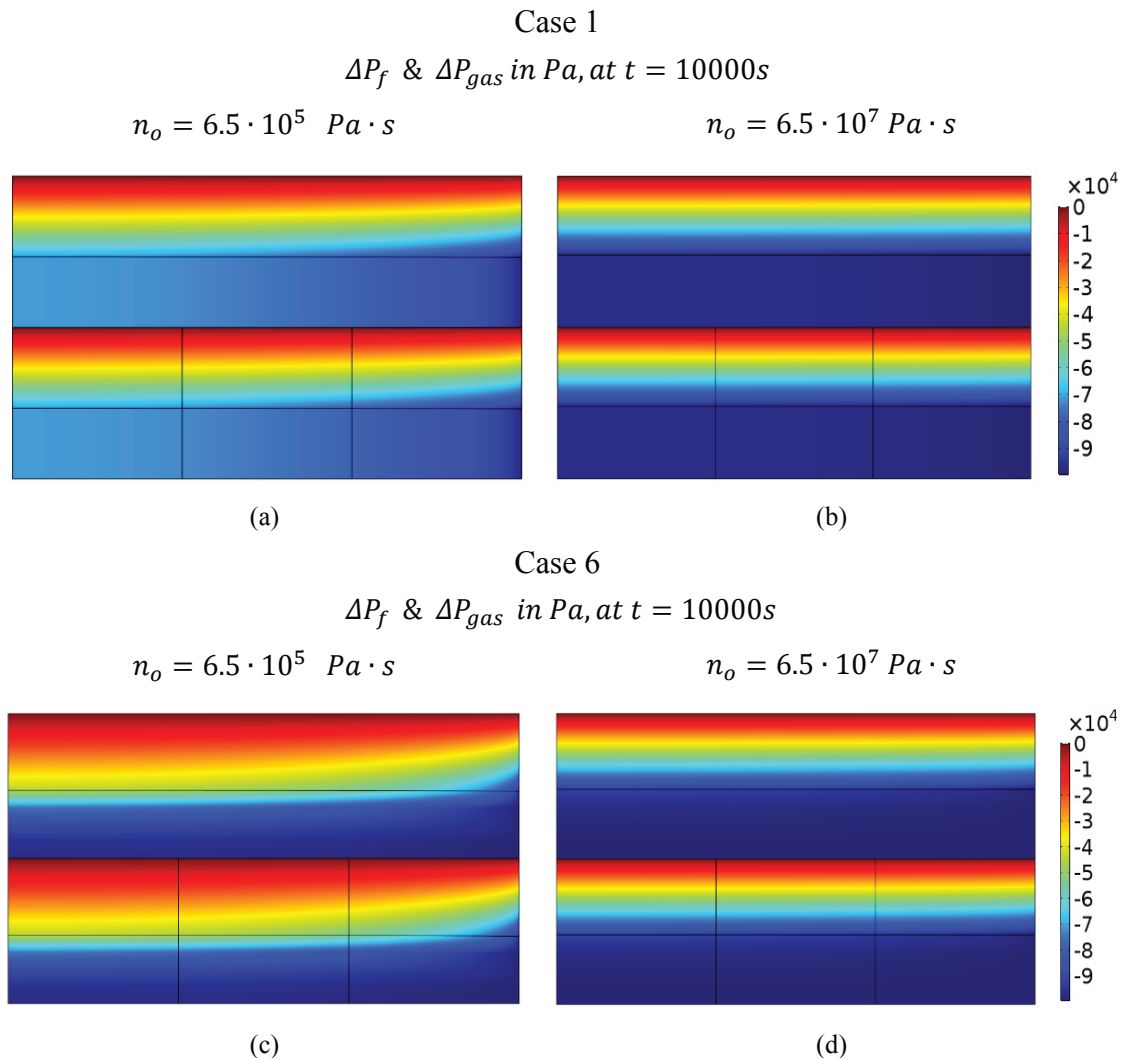


Fig. 4-26: Gas pressure evolution over time along the length of the air-saturated prepreg domain, for the prepregs of Cases 1 and 6 (see Tab. 4-4) at 291.9K ( $\sim 19^\circ\text{C}$ )

As shown in Fig. 4-26, a significant improvement in the homogeneity of the vacuum distribution is obtained along the length of the part in both materials investigated, when increasing the prepreg viscosity by two orders of magnitude. The gas pressure in Case 6 reaches steady state within the time frame of the test, demonstrating a very similar behavior to that shown in Fig. 4-18 where air evacuation takes place along the  $x$  - axis without the influence of resin flow. The gas distribution along the length of the part is significantly improved, also in Case 1.

The pressure difference established in the part after 10000s if the initial viscosity of the MTM44-1 resin is considered ( $n_0 = 6.5 \cdot 10^5 \text{ Pa} \cdot \text{s}$ ) is depicted in Fig. 4-27(a) and (c), while the pressure difference established in both prepregs if an increased viscosity is considered ( $n_0 = 6.5 \cdot 10^7 \text{ Pa} \cdot \text{s}$ ) is shown in Fig. 4-27(b) and (d). A larger pressure

difference ( $\Delta P_{gas}$ ) is available inside the air saturated domains of both prepregs when an increased resin viscosity is considered. This is shown by the shift of the colors inside the air saturated prepreg sub-domains of Fig. 4-27 towards a darker blue color, reflecting an air pressure closer to the vacuum applied at the inlet of the part.



**Fig. 4-27: Development of pressure difference after 10000s in the prepreg of Case 1 and 6**

(a), (c) Pressure development when the initial viscosity of the MTM 44-1 resin is considered in Case 1 and 6 respectively and (b), (d) for an increased initial resin viscosity.

The interaction between the resin and air flow through the same fibrous sub-domain at time-scales which depend on material characteristics such as the prepreg permeability and the viscosity of the resin were investigated. An effective air evacuation strategy can be ensured when the difference between the time-scale for flow of the two fluids increases. In particular, slowing down the resin flow assists in maintaining an efficient air evacuation out of the prepreg. This effect is depicted in both Fig. 4-27 and Fig. 4-28, where it is shown that in the cases where the initial viscosity of resin is increased by two orders of magnitude it leads to a significantly reduced porosity reduction rate (Fig.

4-28(a)). As a result, this assists in maintaining a high in-plane air permeability in the material for longer, within the time-scale of flows investigated (Fig. 4-28(b)).

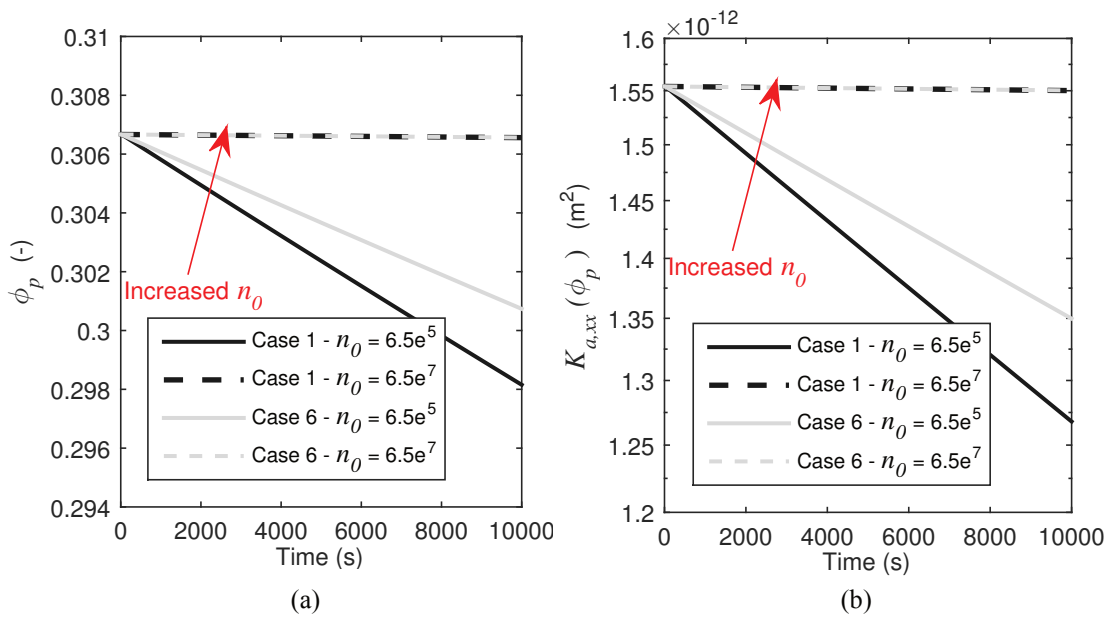


**Fig. 4-28: Influence of the increased initial resin viscosity on the prepreg porosity and the resulting in-plane air permeability evolution over time for Cases 1 and 6**

### Material Design for Optimized Debulking

Introducing a debulking cycle prior to processing an Out-of-Autoclave prepreg is said to enable the establishment of a high vacuum level inside the material, which will eventually assist in evacuating unwanted gas and volatiles out of the part and drive a homogeneous prepreg impregnation. To achieve this, material manufacturers kept part of the OoA prepregs intentionally dry. As discussed in Chapter 1, for this strategy to be effective it shall be ensured that vacuum application does not inhibit the gas pressure distribution by causing ‘cold flow’ of the resin inside the air saturated domains. To reduce the competition between the flows of the two fluids through the same domain, the material shall be designed to ensure a limited resin flow at room temperature.

The key material properties enabling efficient in-plane air evacuation and homogeneous gas pressure distribution during the prepreg debulking process are discussed using as a basis the geometry and properties of the MTM 44-1 prepreg. These properties are the permeability of the prepreg sub-domains (either saturated with air or resin) as reported also by Cender et al. [38, 39], as well as the resin viscosity at room temperature (initial viscosity), the influence of which is also discussed by Ridgard et al. [9].

As shown earlier a reduction of the out-of-plane permeability of the air saturated sub-domain leads to an intensification of the in-plane air evacuation and therefore an improvement of the gas pressure distribution along the part length close to the tool surface (Fig. 4-25). Reducing the out-of-plane permeability in both prepreg sub-domains (saturated with air and resin) can be more efficient since it leads to a simultaneous reduction



of the resin impregnation rate, which can be very beneficial if it simultaneously guarantees a complete impregnation of the tow before resin gelation. An extreme out-of-plane permeability reduction was considered in this work to demonstrate the effects of homogeneous air evacuation, considering the flow boundary conditions of Fig. 4-12. A significant increase in the resin viscosity of the prepreg at room temperature contributes towards an improved vacuum distribution and may be simpler to realize in practice compared to fiber-bed modifications (Fig. 4-27). This effect has also been highlighted in the review paper by Centea et al. [18], who points out the beneficial aspects of increased prepreg tack and viscosity at room temperature, ‘as long as it does not shift the resin viscosity too far from the designed range’ [18].

Key concern for increasing the resin viscosity at room temperature is the influence it may have on the minimum viscosity attainable during the cure cycle. A significant increase of the minimum viscosity might lead to micro-porosity development later in the process [2, 9]. This could impose limitations on what is practically achievable with the initial resin viscosity modification and a combined approach of adjusting both the resin and fiber properties might be required. Several researchers investigated the air evacuation of OoA prepregs at room temperature by decoupling the air from the resin flow, considering the amount of resin flow at room temperature insignificant [33, 38, 54, 57, 132]. In 4.2.4.2 we show through simulation that this is a very strong assumption when pure in-plane gas evacuation takes place in monolithic laminates. This behavior is experimentally verified in a debulking experiment utilizing the MTM 44-1 prepreg, which is summarized in Section 5.3. On the contrary, there is a strong interaction between the air and resin flow and the fibrous domain properties in both directions, unless the prepreg becomes practically impermeable through thickness, or the resin viscosity increases significantly beyond the standard viscosities of hot-melt epoxy systems at room temperature. Two-way coupling of the gas in 2D enables capturing potential deviations from the anticipated dominant in-plane air evacuation behavior seen in Cases 1 and 3, as in Case 6. These effects cannot be predicted with the 1.5D model presented in Section 4.1, nor with other models available in the literature to date. It shall be stretched that compressibility characteristics of the prepreg have not been taken into account, which may lead to an overestimation of the prepreg impregnation rate, since its thickness, the porosity and its fiber volume fraction remains constant. The comparison between simulated and experimentally measured gas pressures for a part manufactured using the MTM 44-1 prepreg follows in Chapter 5.

#### **4.2.4.3 Coupled Air and Resin Flow in OoA Prepregs and the Influence of the Heating Rate during the Cure Cycle**

This Section discusses the impact of temperature evolution during the manufacturing of a part OoA on the vacuum distribution and the gas pressure development in the material. The part of Fig. 4-14 and the prepreg with permeabilities of Case 1 (Fig. 4-4) is used as a basis for this study. The air and resin flow through the prepreg are coupled, while



heat is introduced in the form of a temperature profile  $T(t)$ . The effect of two heating rates (0.5 and 3 °C/min depicted in Fig. 4-20) on the prepreg impregnation and gas pressure development are investigated here. The part is heated from the bottom, while the top and sides of the part are insulated. The temperature influences amongst others the viscosity of the resin  $n$ , the porosity  $\phi_p$  and the in-plane air permeability of the prepreg  $K_{a,xx}$ , therefore it has a significant influence on the impregnation rate of the prepreg with resin  $I_r$  shown in Fig. 4-29.

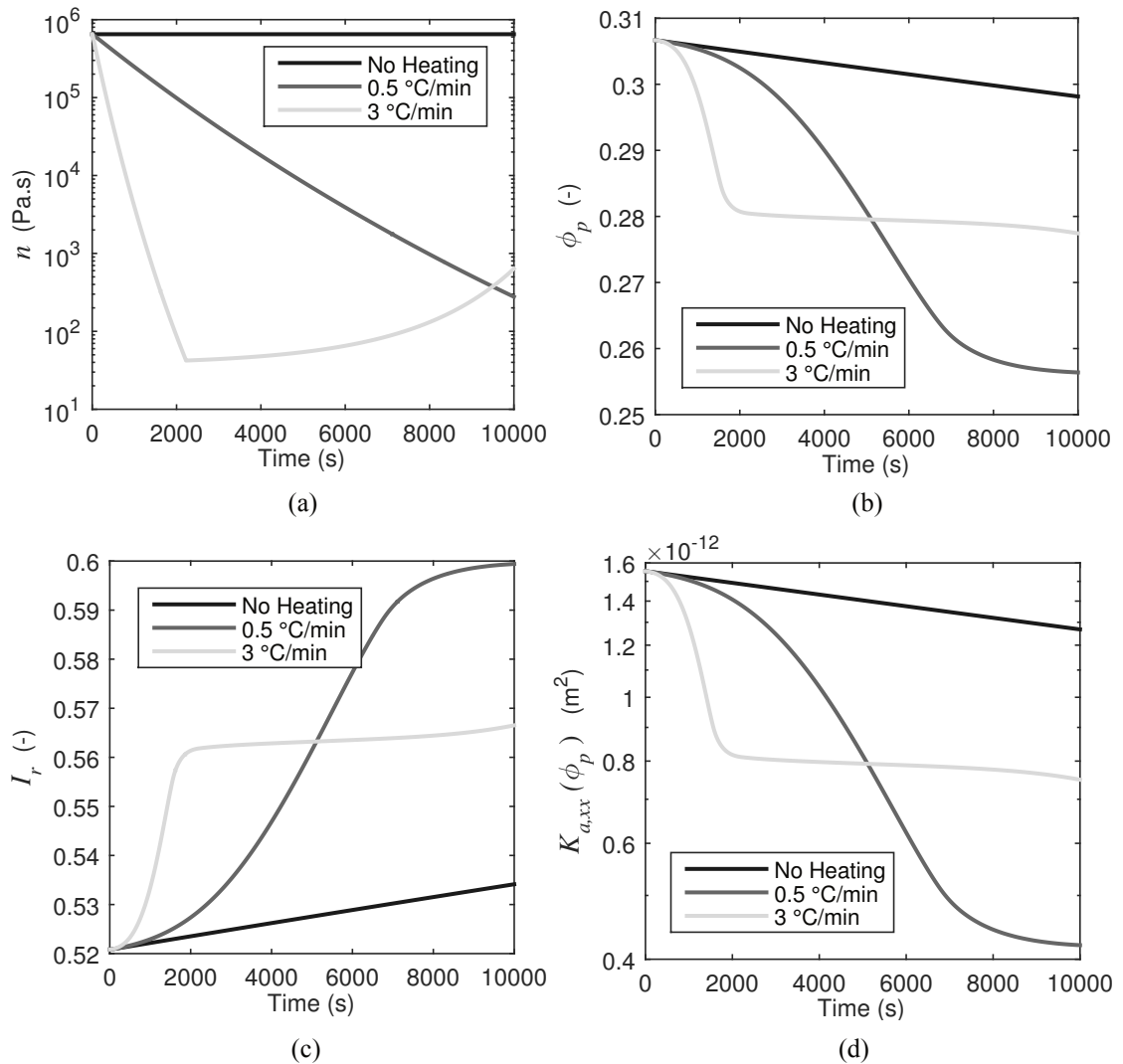


**Fig. 4-29: (a) Resin viscosity (b) prepreg porosity (c) impregnation state (d) in-plane air permeability as a function of porosity for three temperature profiles depicted in Fig. 4-20**

In Fig. 4-29(c) it can be seen that the use of a slower heating rate enables the impregnation of a larger area of the prepreg with resin, though at a slower rate, if the resin does not gel within the processing time considered. The same trend is observed with the porosity and the in-plane air permeability shown in Fig. 4-29(b) and (d). The viscosity reduces faster at higher heating rates. Slower heating leads to slower porosity reduction, which allows the prepreg to remain permeable to vacuum and thus maintain a lower gas

pressure for a longer time and producing a part with lower porosity after 10000s. While the resin viscosity evolves as a function of temperature and time (Equation (3-49)), the porosity, in-plane air permeability and the resin impregnation rate ultimately result from the interaction of the air, resin flow and heat transfer which take place during processing. Though air, resin flow and heat transfer take place simultaneously during Out-of-Autoclave processing, different physics dominate the gas pressure development at different times. Using a graphical representation of the gas pressure development during a typical temperature cycle in Fig. 4-30, five discrete phases are identified.

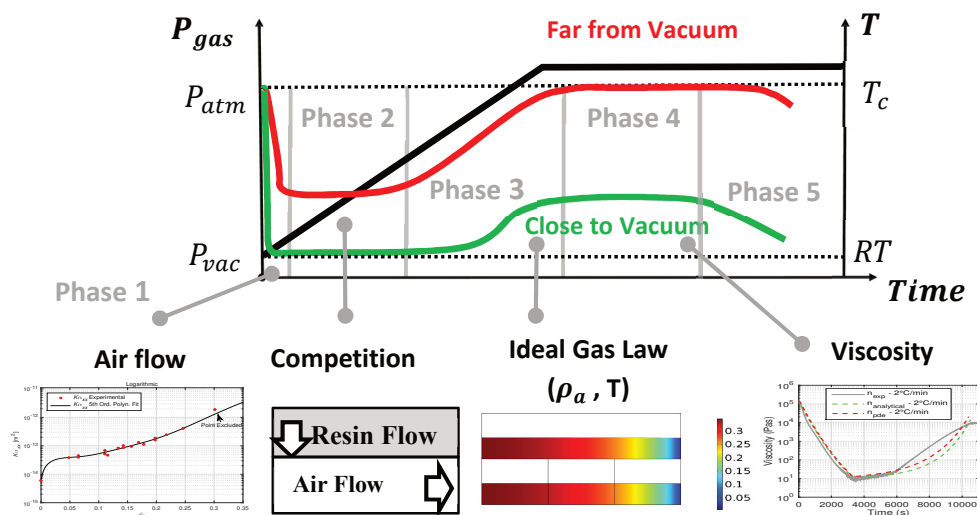


**Fig. 4-30:** The influence of various physical phenomena on the gas pressure development inside the air saturated prepreg domain

The gas pressure, established in the prepreg within the first seconds is primarily a result of the initial porosity and permeability development inside the dry prepreg sub-domain and the boundary conditions for vacuum application (Phase 1). The gas pressure distribution in the prepreg there-off strongly depends on the temperature development and the competition between air evacuation and resin impregnation (Phase 2). As the resin viscosity reduces, the prepreg impregnation speed increases, which in combination with the high pressure difference available close to the vacuum source and the increasing temperature, inhibits the air evacuation causing the gas pressure to increase (Phase 3). The pressure loss in the material is further intensified far from the vacuum source, since an increased gas pressure (reduced pressure difference) is initially available in this location. Once a steady state of temperature is attained in the prepreg accompanied by an insignificant viscosity evolution, the pressure remains constant (Phase 4). When the vacuum access is not fully blocked and a large viscosity gradient develops, the gas pressure decreases until gelation takes place in the resin (Phase 5). At this point, the prepreg does not impregnate further and the gas pressure in the part remains constant.

The gas pressure development at positions  $P 1$  close to the vacuum source,  $P 7$  in the mid-span of the part and  $P 10$  far from the vacuum source when processing at 0.5 and 3 °C/min is presented in Fig. 4-31(a).

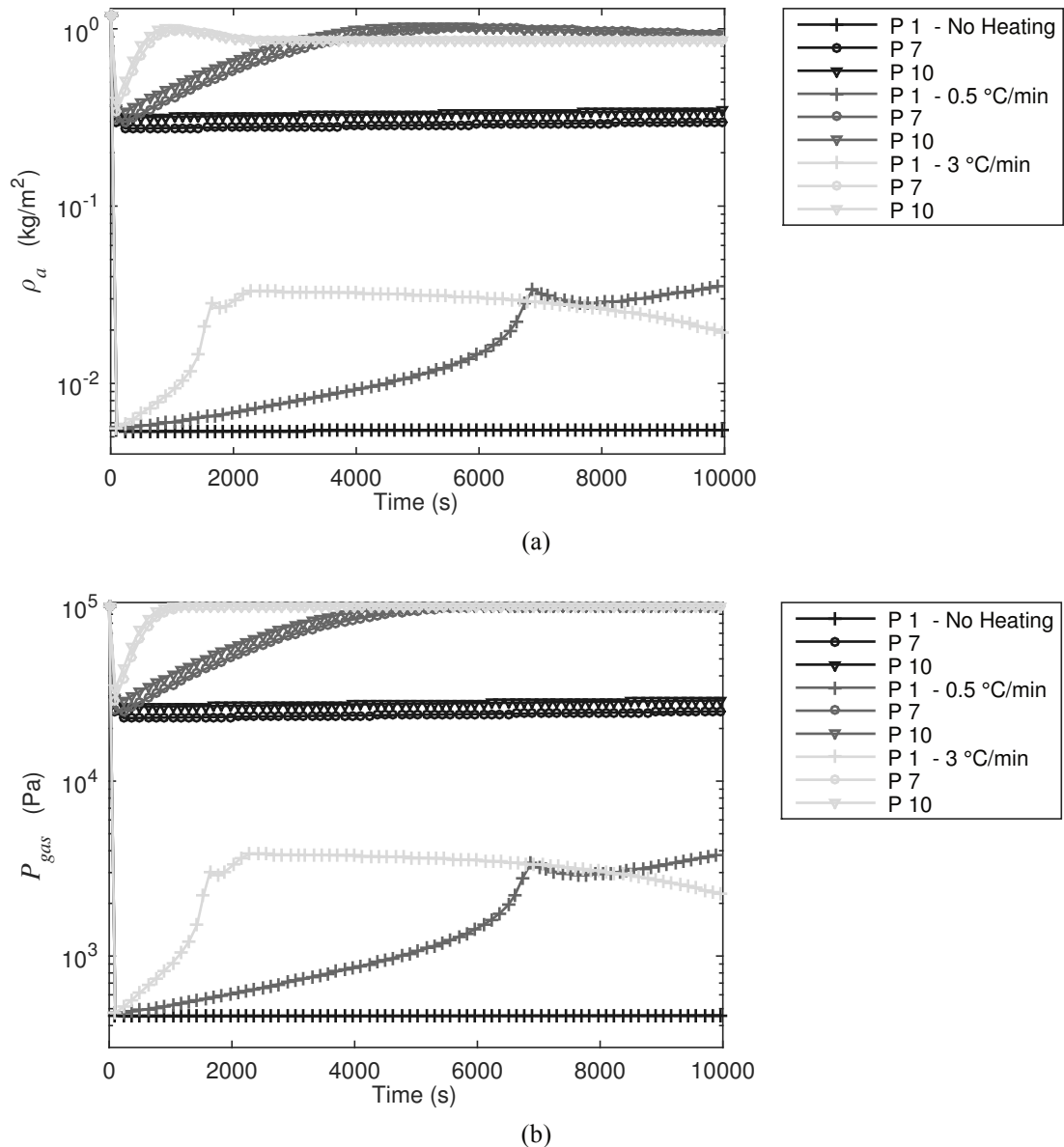


**Fig. 4-31: (a) Gas pressure (b) air density along the length of the air-saturated prepreg domain for the prepreg of Case 1 (Tab. 4-4) and three temperature profiles (Fig. 4-20)**

The gas pressure distribution at room temperature is included in Fig. 4-31 for comparison purposes. The air pressure is directly proportional to its density (Fig. 4-31(b)) and indirectly proportional to the applied temperature at non-isothermal conditions (Ideal Gas Law, Equation (2-38)). As shown in Fig. 4-31(a), the vacuum distribution along the length of the tow is poor even at room temperature. A large pressure differential is available in the resin domain close to the vacuum source  $\Delta P_f$ , which subsequently leads to a faster impregnation of the prepreg at this location. This essentially blocks the access

of vacuum inside the prepreg and reduces its air evacuation rate. This effect in combination with the global porosity and in-plane air permeability reduction (Fig. 4-29(b) and (d)) leads to a gradual increase of the gas pressure inside the prepreg until it reaches atmospheric pressure (Fig. 4-31(a) and Fig. 4-32). The time where the gas pressure becomes atmospheric is defined here as the ‘prepreg locking time’ since from this point onwards there is limited chance for further impregnation of the prepreg while the entrapped air will transition to residual porosity. As shown in Fig. 4-32 faster heating leads to faster impregnation and as a consequence faster equalization of the gas pressure with the atmospheric pressure inside the air saturated sub-domain of the prepreg. Heating at higher rates leads to earlier locking of the prepreg tows.

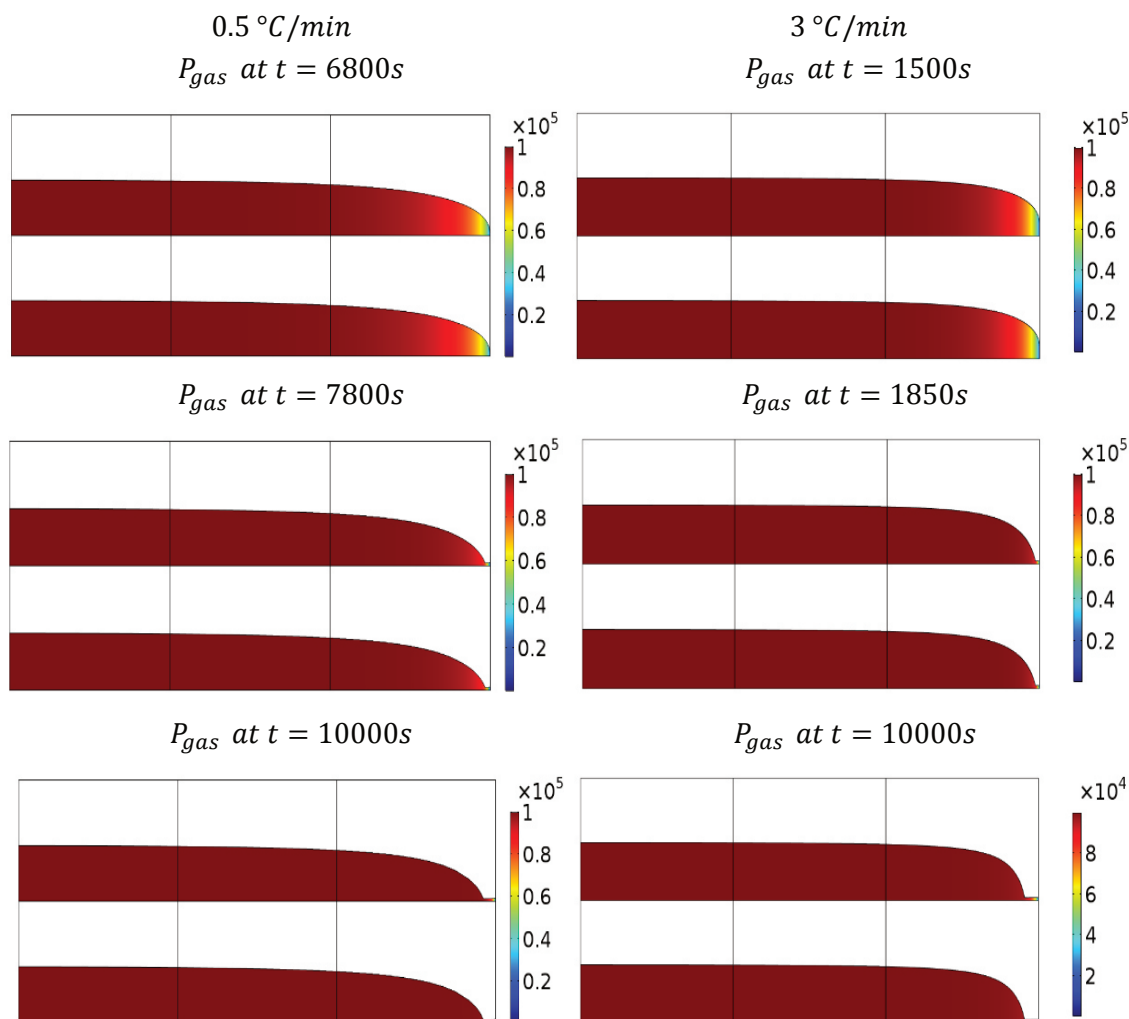


**Fig. 4-32:** Gas pressure evolution inside the dry prepreg sub-domain of Case 1 at selected times during two cure cycles with a heating rate of 0.5 and 3 °C/min

The access of the prepreg to vacuum at the furthest position from the vacuum source ( $P_{10}$ ) is locked after approximately 6600s. Limited vacuum is available in the prepreg after 7900s, corresponding to a window of 1.8-2.2 h available for air evacuation and impregnation during the cure cycle at 0.5 °C/min. The prepreg position further away

from the vacuum source for a part processed at 3 °C/min starts locks-up after approximately 1260s, while an earlier locking of the part takes place at approximately 1540s (20-26 min). It is obvious that the high heating rate limits significantly the time frame available for air evacuation and leads to a laminate with higher porosity content and reduced impregnation levels. Using a slow heating rate of 0.5 °C/min leads to a slower, but more efficient porosity reduction. Virtual processing with a slow heating rate leads to lower porosity levels in the MTM 44-1 prepreg within the first 8500s of the cure cycle, where no gelling is anticipated (see Tab. 3-14).

The beneficial effect of using a reduced heating rate during OoA processing in the residual porosity has been observed by Lucas et al. [46], after investigating laminates manufactured using the 5320 and 5320-1 Cycom prepreg with heating rates between 0.28-1.67 °C/min. During the investigations performed by Lucas et al. [46], the part produced at 1.67 °C/min was the only one that did not meet the 0.5% porosity target set for the study. Furthermore Agius et al. [238] investigated the influence of heating rates in the range of 1.5-10 °C/min on the porosity formation of laminates manufactured OoA at various stages of the cure cycle, using as a basis the 8552 Hexply prepreg. No influence is observed on the average prepreg porosity, though a slight increase is observed in the large voids (1000-15000 µm) when utilizing a faster heating rate [238].

Contrary to the experimental findings from Lucas et al. [46], Agius et al. [238] and the results of simulation summarized in this work, Centea et al. [18, 43, 57, 239] reports porosity reduction at increased heating rates identified via simulation [18, 57] and experiments [239]. Nevertheless, the author could not deduct an influence of the high heating rate on the intra-tow porosity reduction reported in the work by Centea et al. [239]. Limited influence appears in one of the investigated prepregs based on an 8HS textile, where a high porosity is measured after 28 days of prepreg ageing at room temperature. In the study by Centea et al. [239] dominating influence on the intra-tow porosity formation has the textile type and the dwell temperature selection. Centea et al. [57, 59] models the impregnation of OoA tows, considering an instantaneous and constant vacuum everywhere in the prepreg. The main influence captured by Centea's model [57] is that of a slower viscosity reduction rate on the tow impregnation rate, when a cycle with a slower heating rate is used. In the case of a very slow impregnation, resin gelation takes place before the tows are fully impregnated and may lead to intra-tow porosity formation [18]. Therefore, the faster impregnation of the prepreg close to the inlet cannot be captured in the model developed by Centea et al. and this may be the reason for the discrepancy observed [54, 57].

#### **4.2.4.4 The Influence of Temperature Gradients on the Impregnation of a Part Outside the Autoclave**

The challenges associated with the scalability of OoA processing and the influence of the inhomogeneous temperature distribution on the gas pressure and porosity develop-

ment are discussed in this Section based on two studies. The first demonstrates the influence of an imposed temperature gradient along the length of the part, on the air evacuation and vacuum distribution. The second presents the impact of temperature gradients through the thickness of a part produced on a single-sided heated tooling OoA.

### In-Plane Temperature Gradients

The domain depicted in Fig. 4-33(a) is used to evaluate the influence of temperature gradients on a part manufactured on a tool which consists of three heated zones. Three heating rates are applied on the three Zones, while six probes are located in the air and resin saturated domains of the prepreg (Fig. 4-33(a)). To accurately capture the position of the resin front, the tow is discretized with a high element density at the transition region between the heating zones and a total of 2100 elements, as shown in Fig. 4-33(b).

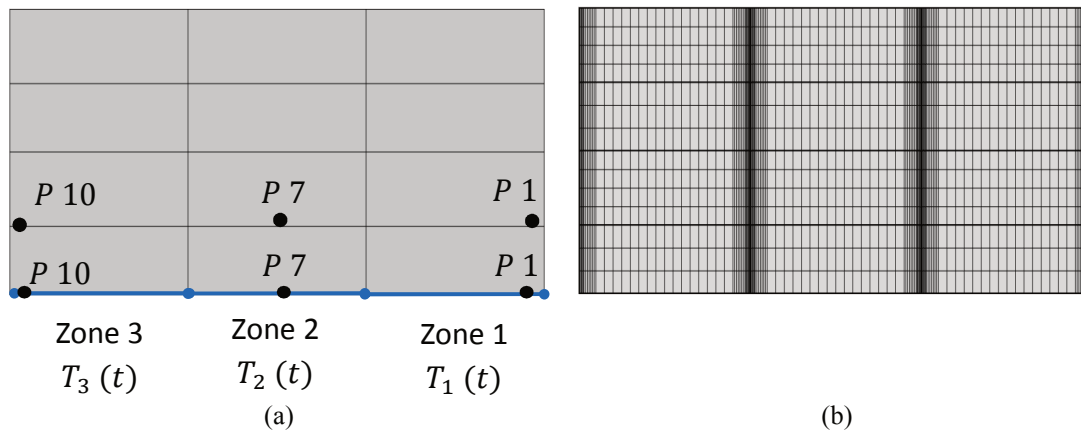


Fig. 4-33: (a) Domain and probe locations (b) spatial discretization (meshing)

The heating rates applied and the location of the probes are presented in Tab. 4-5.

Tab. 4-5: Temperature cycles applied in the three Zones of the part and probe locations

Zone	Ramp rate $^{\circ}\text{C}/\text{min}$	Dwell Temperature $^{\circ}\text{C}$	Probes	Location	Unit
1	0.5	130	<i>P 1 – Air</i>	$(0.58997, 0)$	<i>m</i>
			<i>P 1 – Resin</i>	$(0.58997, 2.35 \cdot 10^{-4})$	<i>m</i>
2	1.5	130	<i>P 7 – Air</i>	$(0.3, 0)$	<i>m</i>
			<i>P 7 – Resin</i>	$(0.3, 2.35 \cdot 10^{-4})$	<i>m</i>
3	3	130	<i>P 10 – Air</i>	$(1.719 \cdot 10^{-4}, 0)$	<i>m</i>
			<i>P 10 – Resin</i>	$(1.719 \cdot 10^{-4}, 2.35 \cdot 10^{-4})$	<i>m</i>

A slower heating-rate is applied close to the vacuum source, aiming to reduce the rate of gas pressure increase, caused by the temperature increase rate. The temperature and resin viscosity at the probe locations of Tab. 4-5 are shown in Fig. 4-34.

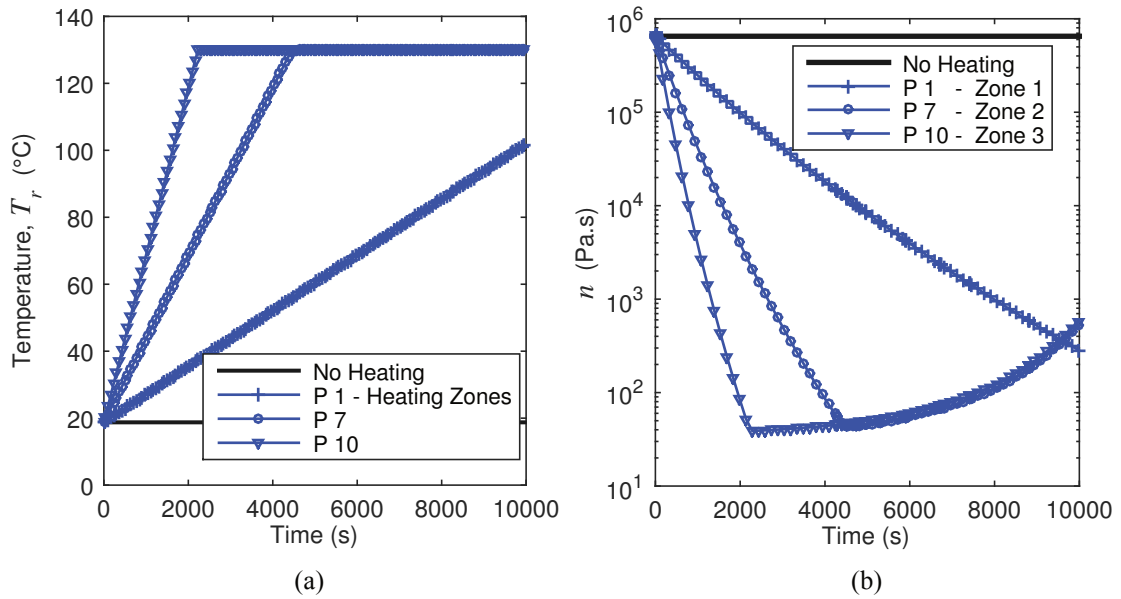


**Fig. 4-34:** (a) Temperature development inside the resin impregnated sub-domain of the prepreg (b) resin viscosity at P 1, P 7, P 10 for the cure cycles depicted in (a)

A reduced gas pressure is available away from the vacuum source (*Zones 2, 3*), even when the part is not heated, as shown Fig. 4-35.

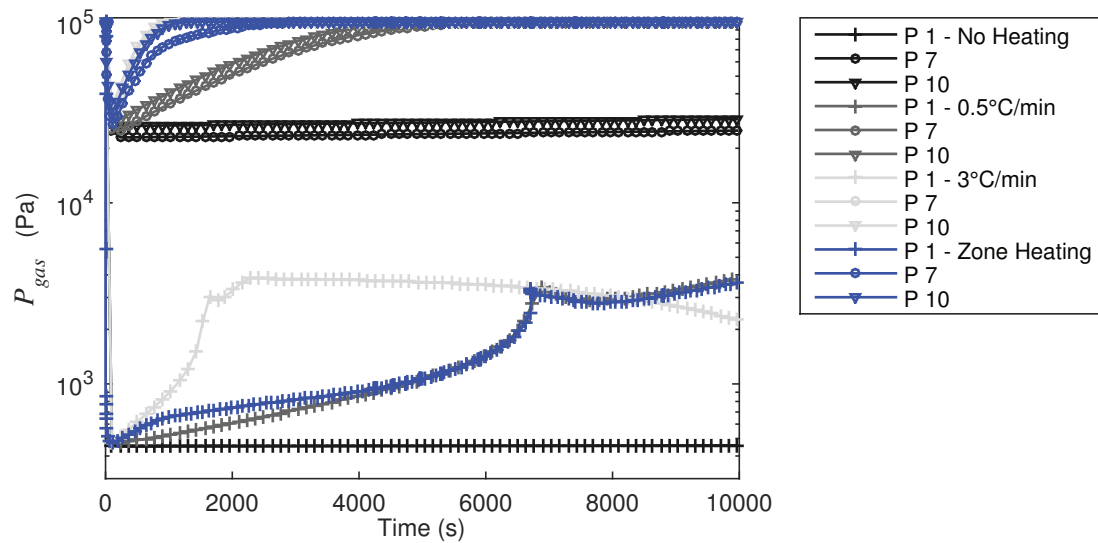


**Fig. 4-35:** Gas pressure at three positions along the length of the air-saturated sub-domain for the material of Case 1 (see Tab. 4-4) at room temperature (at 291.9K ~19°C) and for three cure cycles at 0.5, 3°C/min and with zone heating (see Tab. 4-5)

As the temperature raises faster in the tool section furthest from the vacuum source (*P10 – Zone 3*), the gas pressure raises to atmospheric pressure first. The middle section follows (*P 7 – Zone 2*), while the location close to the vacuum source (*P1 – Zone 1*) maintains access to vacuum throughout the cure cycle. When a higher heating rate is used as a basis for the temperature cycle, the resin viscosity decreases

faster and so does the prepreg impregnation rate. From the point the gas pressure reaches a plateau, no significant impregnation takes place in the respective section of the prepreg. This effect is shown in Fig. 4-36, where the temperature and gas pressure is presented at three characteristic times, selected to reflect the maximum impregnation state reached in each zone of the part a few seconds after a steady state is reached.

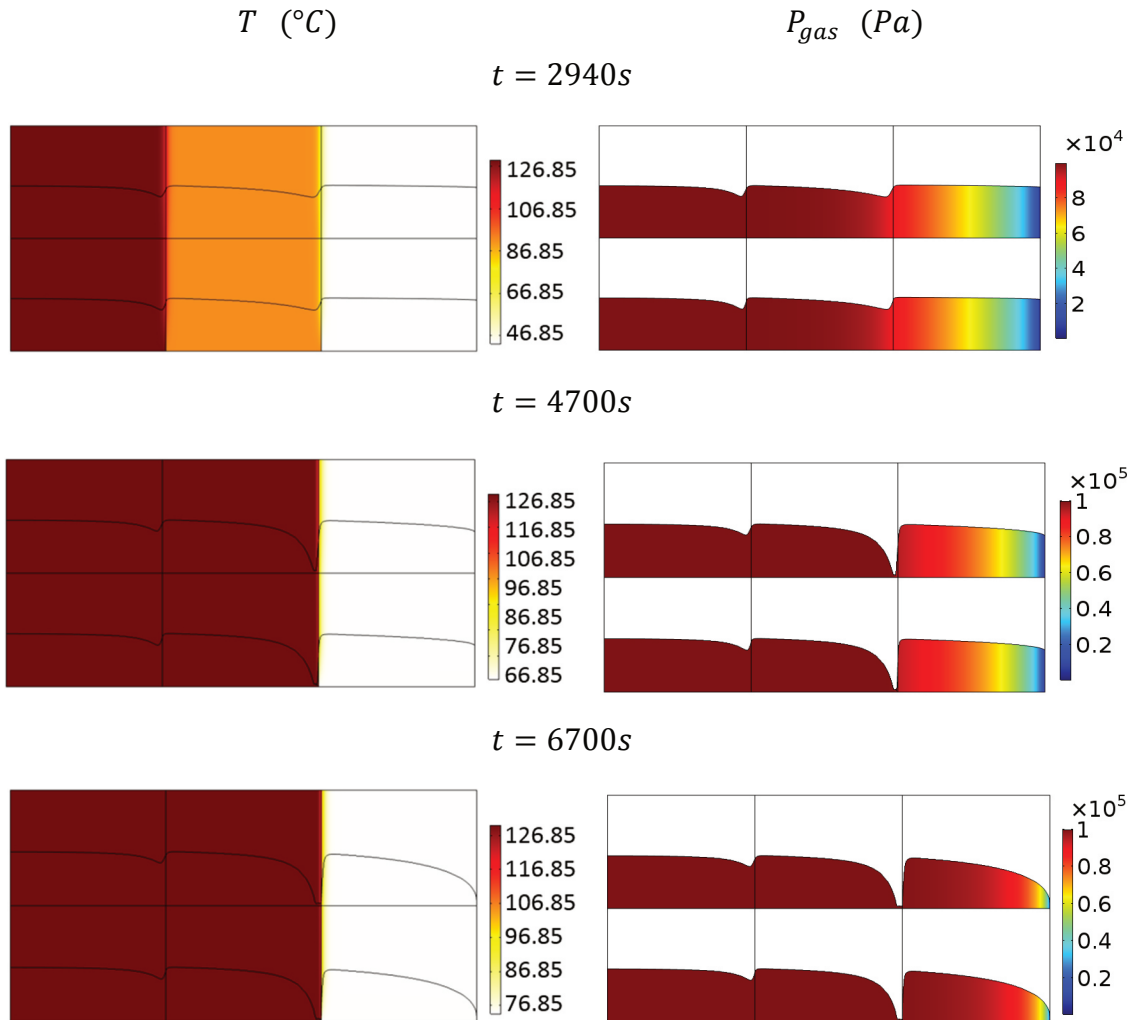


**Fig. 4-36: 2D Temperature and gas pressure development inside the domain of Fig. 4-33 at three selected times when the zone heating concept presented in Tab. 4-5 is utilized**

After approximately 2900s, no vacuum reaches *Zone 3*, while after 4700s the pressure access to *Zone 2*, is inhibited as well. The section close to the vacuum source (*Zone 3*) impregnates last. The influence of utilizing the zone-heating concept on the porosity, air permeability and the impregnation level is presented in Fig. 4-37(a)-(d). All graphs compare the evolution of the properties during the cure cycle on the heated tool, against the Cases where either no temperature or a homogeneous temperature is applied on the part (see Fig. 4-20).



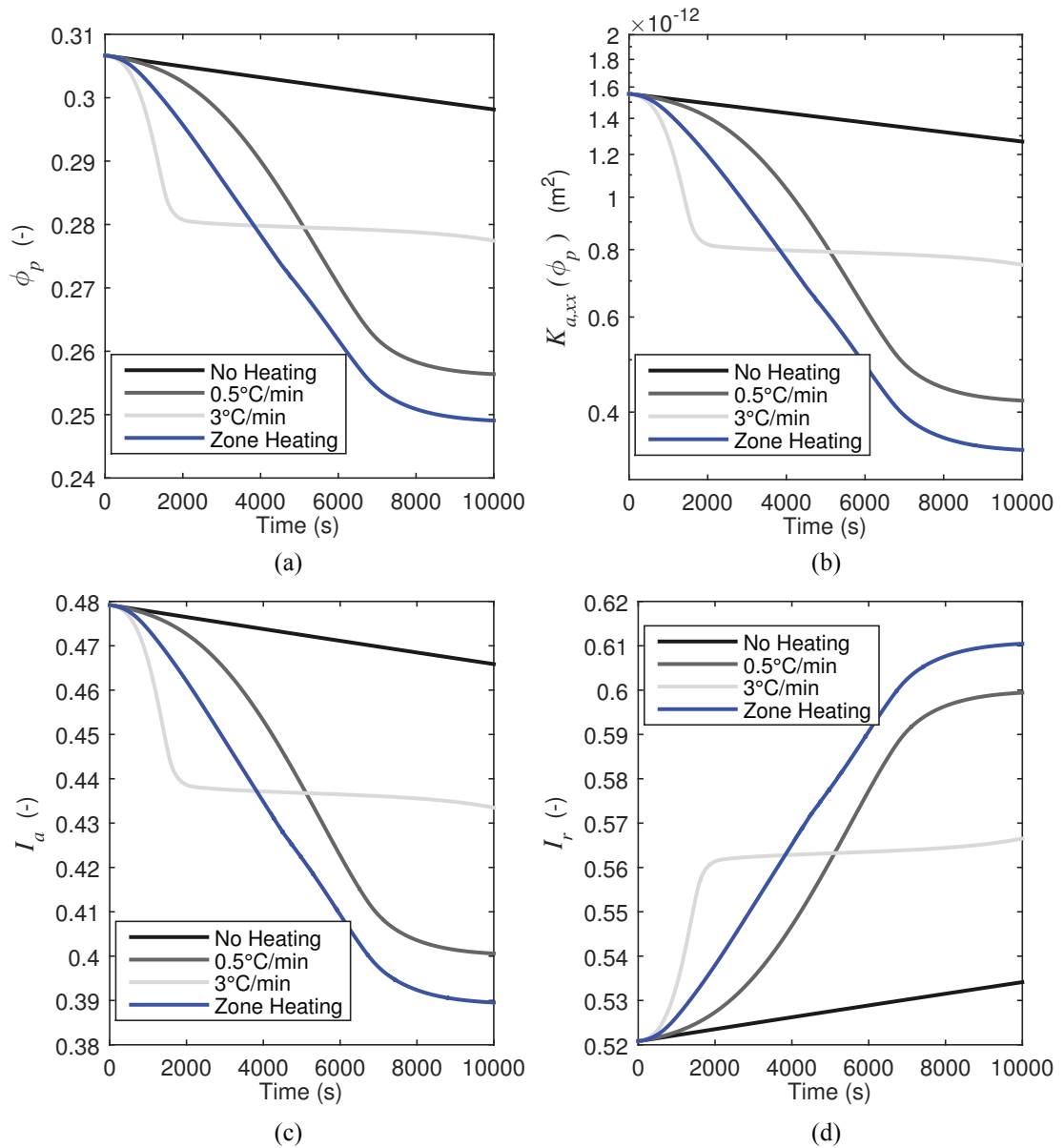


**Fig. 4-37:** (a) Porosity evolution in the prepreg of Case 1 processed at room temperature and three cure cycles at 0.5, 3°C/min and with zone heating (Tab. 4-5) (b) air permeability as a function of porosity (c) impregnation state - air (d) impregnation state - resin

As shown in Fig. 4-37, utilizing the zone-heating concept leads to the lowest residual porosity and thus the highest degree of impregnation of the prepreg with resin. The fast viscosity reduction at the early stages of the cure cycle far from the vacuum source, enables local impregnation of the zone before the gas pressure equilibrates with the atmospheric pressure. Though the impregnation rate is in between the rates attained when homogenous heating with heating rates of 0.5 and 3°C/min is considered, the shape of the curve and the time when the porosity/impregnation plateau is reached resembles closer the cycle with a heating rate of 0.5°C/min. The plateau is reached when the front part of the tow reaches the maximum impregnation level, obstructing the vacuum distribution in the remaining part.

### Out-of-Plane Temperature Gradients

The part depicted in Fig. 4-38 consists of twenty plies of the prepreg with properties of Case 1 stacked on top of each other and is used as a basis for this study. The part dimensions are summarized in Tab. 4-6.

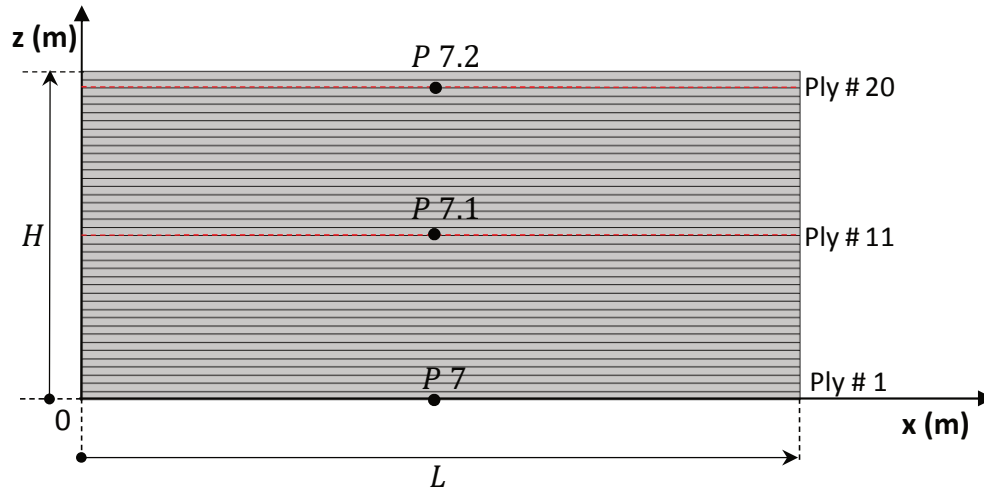


Fig. 4-38: Domain used as a basis for studying the effects of out-of-plane temperature gradients

A temperature profile  $T(t)$  with a heating rate of  $0.5^{\circ}\text{C}/\text{min}$  is applied on the bottom of the part, while its top and sides are insulated as shown in Fig. 4-39(a).

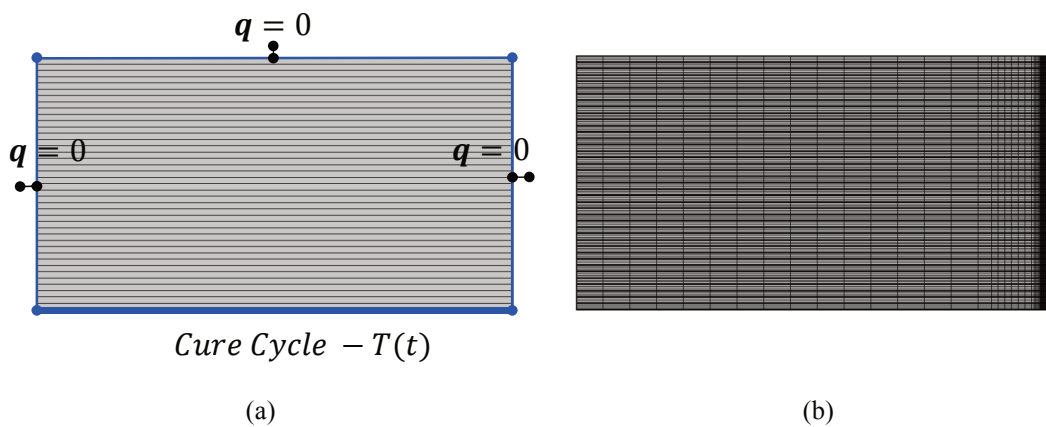
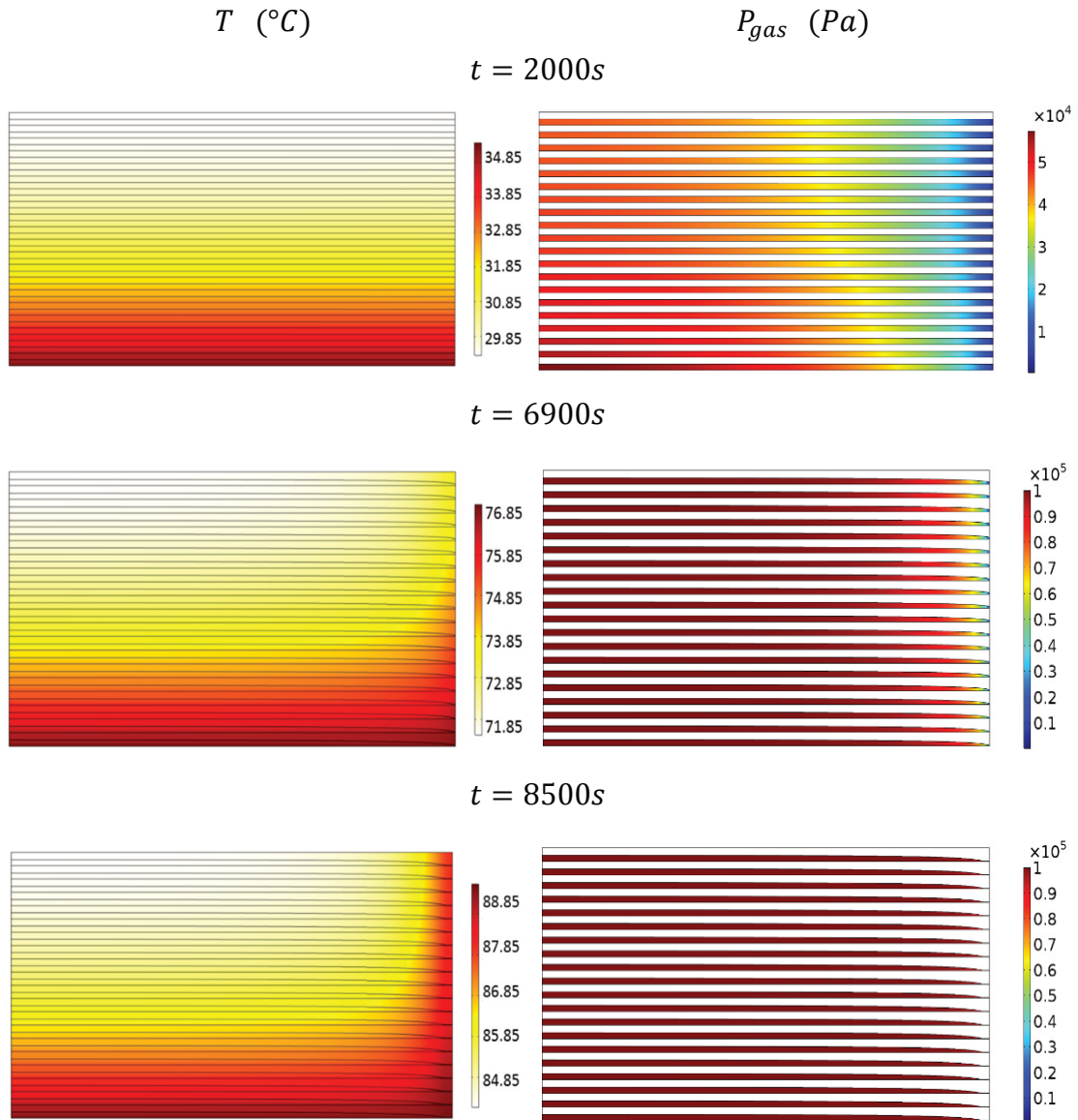


Fig. 4-39: (a) Temperature boundary conditions and (b) spatial discretization (meshing)

The part domain is discretized using a structured, non-homogeneous mesh consisting of 10080 elements. Eight elements are included through the thickness of each ply, with four elements included in each sub-domain. A dense discretization is used, with elements of increasing size close to the vacuum source ( $0.5\text{ m} < L < 0.59\text{ m}$ ) as shown in Fig. 4-39(b). A dense discretization of the whole part was not possible due to memory and computational power limitations imposed by the operating system available (16GB Ram, 2.4GHz Processor on an 8 Core Laptop PC) and the selected numerical scheme. The selected meshing strategy allows fine discretization of locations where the largest pressure gradients are present, enabling reduction of the running time to less than 20 h.

The temperature and gas pressure distribution is depicted in Fig. 4-40 at selected times. Focus is placed on capturing the temperature development and its influence on the gas pressure distribution through the part's thickness. Both phenomena have an effect on the impregnation and the porosity development inside the part during processing.



**Fig. 4-40:** Temperature and gas pressure distribution in the part of Fig. 4-38 at selected times

A temperature gradient of  $6^\circ\text{C}$  develops within the first 2000s through the thickness of the part. The part close to the tool is hotter, while the temperature distribution in-plane is rather homogeneous. The increased temperature contributes towards a faster increase of the gas pressure in the hotter regions. This results from the direct temperature effect on the gas pressure (ideal gas law) and the indirect effect of the increased heating rate on the resin viscosity. The faster heating of the resin leads to an accelerated impregnation, which inhibits the vacuum distribution in the prepreg. The air flow through the prepreg can be captured as a function of either the local porosity in each ply or the global

porosity of the part. The global porosity is used to capture the air flow in Fig. 4-40. The temperature evolution in three locations through the part thickness, at its mid-span is presented in Fig. 4-41(a), while the viscosity is captured in Fig. 4-41(b). The probe positions are given in Tab. 4-6. The heat transfer characteristics of the air saturated domain have and influence on the resin temperature, as the heat progresses from the bottom to the top of the part. Their development when local and global porosity is captured in Fig. 4-41.

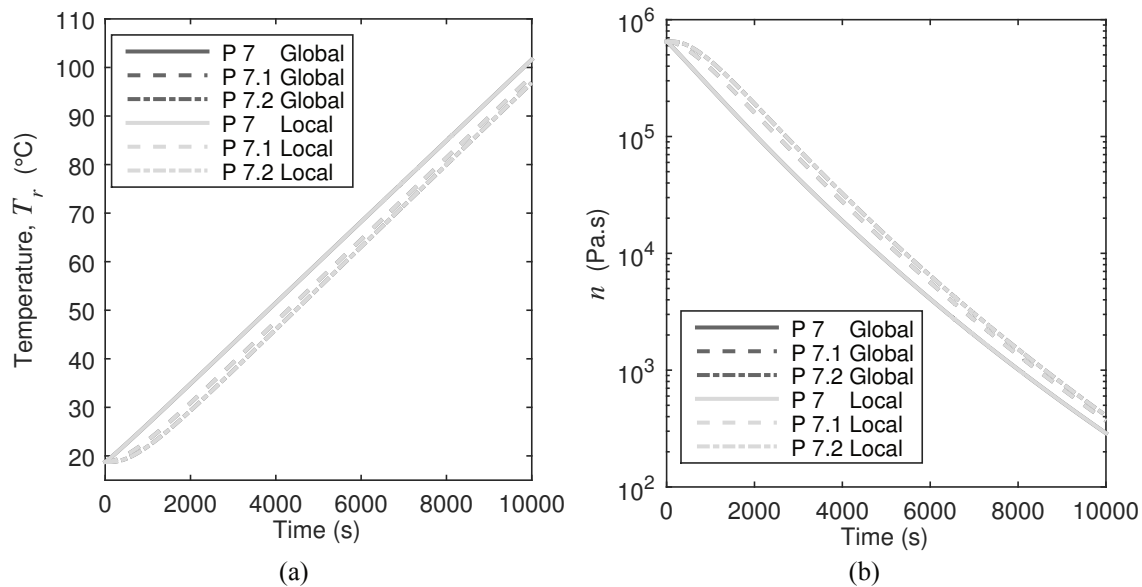


**Fig. 4-41:** (a) Resin temperature development utilizing the local and global porosity to describe the in-plane air evacuation (b) resin viscosity at three positions through the part thickness (P 7, P 7.1, P 7.2)

As shown in Fig. 4-41, utilizing the local (ply) or global (part) porosity as a basis for the air flow through the prepreg, has a negligible influence on the resin temperature development, dominated by temperature difference through the part thickness.

**Tab. 4-6:** Part dimensions and probe locations inside the part of Fig. 4-38

Symbol	Value	Unit
$H_p$	$0.45 \cdot 10^{-3}$	$m$
$H$	$9 \cdot 10^{-3}$	$m$
$L$	0.59	$m$
P 7 – Air	(0.3, 0)	$m$
P 7 – Resin	(0.3, $2.35 \cdot 10^{-4}$ )	$m$
P 7.1 – Air	(0.3, $4.5 \cdot 10^{-3}$ )	$m$
P 7.1 – Resin	(0.3, $4.49 \cdot 10^{-3}$ )	$m$
P 7.2 – Air	(0.3, $8.56 \cdot 10^{-3}$ )	$m$
P 7.2 – Resin	(0.3, $8.98 \cdot 10^{-3}$ )	$m$

The effect of temperature on the gas pressure developed in the mid-span of the part, at positions  $P 7$ ,  $P 7.1$ ,  $P 7.2$ , is depicted in Fig. 4-42.

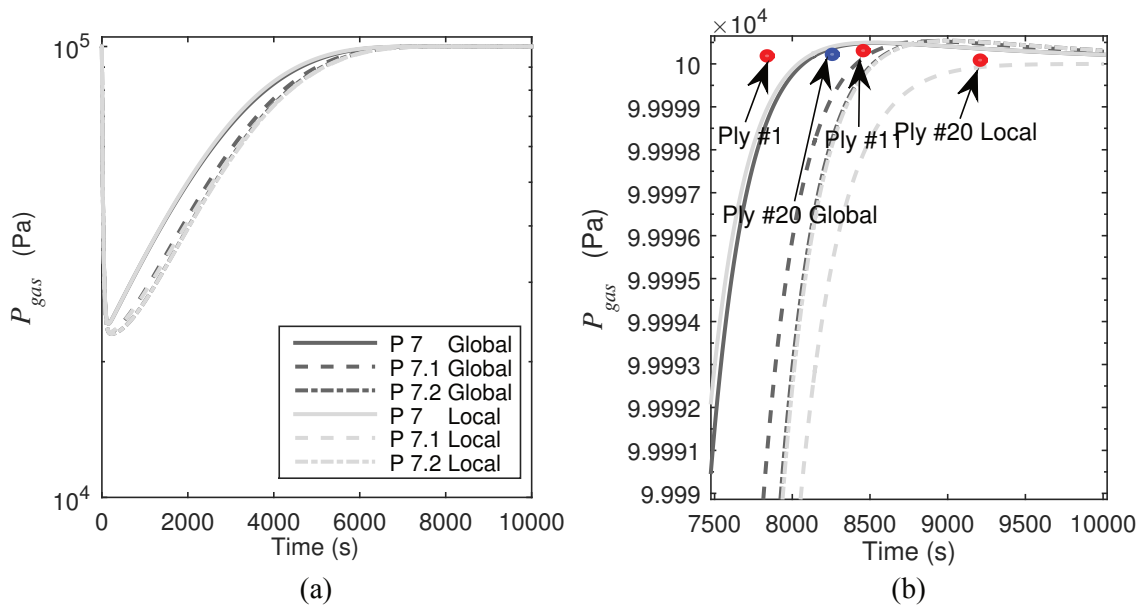


**Fig. 4-42:** (a) Gas pressure at three positions at the mid-span of the part, through its thickness (P 7, P 7.1, P 7.2) considering air evacuation based on the local and global porosity development and (b) zoom on the locking time of the three plies concerned (# 1, 11, 20)

Since the air is insulating and its content is unevenly distributed along the length and thickness of the part, it results in the development of a temperature gradient. The bottom-right side of the part depicted in Fig. 4-40 is hotter and as a result the gas pressure in this region equalizes faster with the atmospheric pressure.

The gas pressure in the mid-span of the bottom ply of the part (P 7) equalizes with the atmospheric pressure after approximately 8000s, while the top ply (P 7.2) after 8500s. Though capturing the air evacuation at a global or local level does not have a significant influence on the gas pressure development at the top and bottom ply (P 7, P 7.2), it does have an impact on the pressure developed in its mid-plane (P 7.1) as shown in Fig. 4-43(b). The pressure in the mid-plane (P 7.1) equalizes with atmospheric pressure after approximately 8400s (2.33hrs) when the global porosity is considered, while it is delayed by approximately 800s if the local porosity is considered instead.

The local porosity evolution in all three plies (Ply # 1, 11, 20) and the global and local average porosity are captured in Fig. 4-43(a). In Fig. 4-43(b) the influence of the porosity evolution over time on the evolution of the in-plane air permeability and the degree of impregnation of the prepreg is shown in Fig. 4-43(c) and (d) respectively.

Accurate prediction of the time at which the prepreg's access to vacuum is inhibited ( $P_{gas} \approx P_{atm}$ ) has a significant influence on the prediction of the residual porosity, since it occurs before resin gelation takes place. Therefore modeling the air permeability evolution taking into account the local porosity is more accurate and shall be preferred,

while it contributes to a substantial reduction of the computational time. In particular for the geometry, mesh and boundary conditions utilized here, the computational time when the local porosity is considered is reduced by approximately one tenth of the time compared to the calculation performed using the global porosity (reduced from 20hrs to approximately 3hrs).

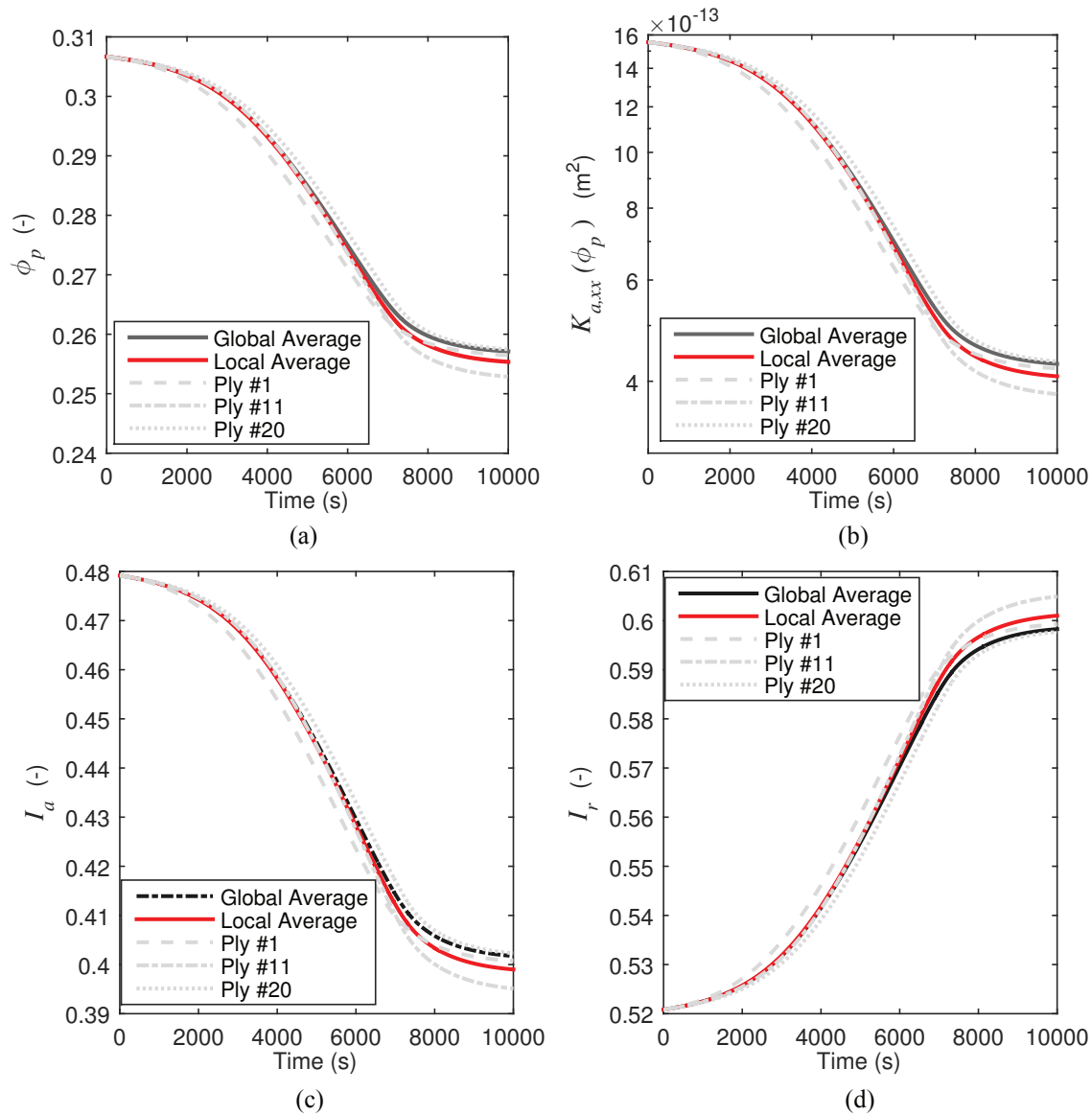


**Fig. 4-43:** Comparison of (a) the prepreg porosity of the material of Case 1 during processing with a rate of  $0.5^\circ\text{C}/\text{min}$  (Fig. 4-20) (b) the air permeability as a function of the prepreg porosity (c) the impregnation state - air (d) the impregnation state -resin

Utilizing the local porosity to describe the air flow through each ply leads to a faster porosity and in-plane permeability reduction at the top and bottom of the part as shown in Fig. 4-43(a) and (b) respectively. The highest percent of impregnation is achieved in the mid-plane of the part (*Ply #11*) as depicted in Fig. 4-43(d), as its impregnation rate becomes faster than that of the top and bottom plies as well as the average local and global impregnation after 7500s, while the resin has not gelled yet.

### 4.3 Summary and Discussion

The instantaneous air evacuation assumption used for modeling resin flow through textile preforms during liquid composite molding processes, typically underestimates the impregnation time of an Out-of-Autoclave prepreg away from the vacuum source as shown in Section 4.1. When vacuum is applied on one side of the part, the prepreg tows close to the vacuum source will impregnate first and will essentially cut-off the access of the remaining material from the applied vacuum. Since no pressure is available to further enable the tow saturation, the air becomes entrapped in the tows and once the resin gels, it transitions to residual porosity.

A debulking cycle typically takes place prior to OoA processing in order to establish a high and homogeneous vacuum and achieve the evacuation of unwanted gas and volatiles out of the part. To achieve this, material manufacturers kept part of the OoA tows intentionally dry. Nevertheless, to make use of the dry network as means for air evacuation, it shall be ensured that vacuum application does not cause ‘cold flow’ of resin in the air saturated domains, inhibiting the gas pressure distribution. To reduce the competition between the flow of the two fluids in the prepreg (air and resin) during room temperature debulking, the material shall ensure minimal resin flow, while maintaining a high, homogeneous rate of air evacuation.

The key properties enabling efficient air evacuation and homogeneous gas pressure distribution in the prepreg during debulking of a non-consolidating laminate are:

- The ratio of resin and air saturated permeability along the primary flow directions of the two prepreg domains ( $K_{r,zz} / K_{a,xx}$ )
- The ratio of in and out-of-plane permeability of the air saturated prepreg domain ( $K_{a,zz} / K_{a,xx}$ )
- The initial resin viscosity of the prepreg at room temperature ( $n_0$ )

Significantly reducing the out-of-plane permeability of the air saturated domain of the prepreg ( $K_{a,zz}$ ) contributes towards an intensification of the air flow in-plane, which subsequently leads to an improved gas pressure distribution along its length. This effect can be further enhanced through a simultaneous and more significant reduction of the out-of-plane permeability of its resin saturated domain ( $K_{r,zz}$ ), or an increase of the resin viscosity at room temperature ( $n_0$ ). Both modifications will reduce the speed of impregnation of the prepreg with resin and will provide more time for the gas to distribute along the part length. Nevertheless the main concern for significantly increasing viscosity of the resin at room temperature, is the potential of a parallel increase of the minimum viscosity attained during the cure cycle, which may lead to the development of inter-ply or inter-tow porosity.

When the air and resin permeability reduction out-of-plane is significant and the resin viscosity is increased, the interaction between the flows of the two fluids in the prepreg



is insignificant. A fast, homogeneous in-plane air evacuation takes place, which is independent of the part's length. The simplified 1.5D delayed air evacuation model of Section 4.1 could also describe the air distribution in this ideal case under isothermal conditions, while the ratio of out-of-plane resin versus in-plane air permeability is smaller than one ( $K_{r,zz}/K_{a,xx} \ll 1$ ) and the air resistance to filling significantly larger than one ( $AR_f \gg 1$ ). For all other cases where a strong interaction between the air and resin flow is present, the 2D, two-way coupled simulation implemented in COMSOL Multiphysics presented in Section 4.2 is the suggested tool for accurately simulating the OoA prepreg impregnation.

Regarding the actual design of the OoA cure cycle, faster heating leads to faster impregnation, which in combination with an intensified pressure differential close to the vacuum source results to an earlier 'locking' of the prepreg's access to vacuum. As a result, at higher heating rates the gas pressure in the material equalizes faster with the atmospheric pressure, while an increased volume of gas cannot be evacuated out of the tows and remains entrapped as porosity. Therefore, a reduced heating ramp-rate promotes a slower tow impregnation, which allows more air to evacuate the tow before it locks-off. During the selection of a heating rate for an OoA cure cycle, a balance shall be struck between a slow heating which will enable air to evacuate the dry tows due to a slow raise of the gas pressure to atmospheric pressure and a fast enough heating rate, which will enable homogeneous temperature and gas pressure distribution and maximum impregnation before the resin gels. Generally, uncontrolled temperature gradients, particularly through the thickness of the part as shown in 4.2.4.4 may lead to significant differences in the impregnation time of the various prepreg plies, which may lead to porosity zoning once the resin gel-time is reached. Nevertheless, in Section 4.2.4.4 we show that a controlled in-plane temperature gradient may be beneficial for porosity reduction, with the right selection of the temperature ramp rates in the available heating zones of a self-heated tool. In the example selected, the fastest heating region is located far from the vacuum source, while the heating rate selected reduces, with the slowest heating rate applied close to the vacuum source. This selection enables the impregnation of the three zones to take place in three phases, as a result of the interaction of the temperature developed in each sub-domain with the viscosity evolution and the gas pressure. The high rate of resin viscosity evolution at the part section far from the vacuum initially exceeds the rate of gas pressure increase due to temperature and starts impregnating the material, until the gas pressure equalizes with the atmospheric pressure. The middle zone follows, while the zone close to the vacuum source impregnates last. Nevertheless, for this concept to be successful, maximum impregnation has to take place before the gel time of the resin.

Several researchers investigated the air evacuation of OoA prepregs decoupling the air from the resin flow, considering the amount of resin flow at room temperature insignificant [33, 54, 57, 132, 204]. In 4.2.4.2 it is shown that this is a very strong assumption. On the contrary it is demonstrated that there is a strong interaction between the air and



resin flow and the fibrous domain properties in both directions of a prepreg with the MTM 44-1 characteristics. To minimize the interaction between the air and resin flow, the prepreg shall become practically impermeable through thickness, or the resin viscosity shall be increases significantly beyond the standard viscosities of hot-melt epoxy systems at room temperature. Two-way coupling of the gas and resin pressure in 2D enables capturing the competition between the two flows as well as deviations from the anticipated in-plane air evacuation behavior. This is neither possible with the 1.5D model presented in 4.1, nor with other existing models developed in the literature to date [27, 28, 33, 54, 57, 132, 191, 204], to the best knowledge of the author. It shall be stretched that the compressibility of the prepreg has not been taken into account in this work, which may contribute to the overestimation of the predicted prepreg impregnation rate. The modeling tools developed and presented in this Chapter can be used in the design of new debulking or cure cycles, as well as in comparatively investigating textiles or resin systems, assisting in screening existing or designing an optimized OoA material. The non-isothermal model based on COMSOL Multiphysics can be used as a virtual cure cycle design tool, which will enable manufacturing of monolithic parts with reduced porosity, while reducing the amount of time and cost invested in trial and error approaches. It will be beneficial to further enhance the tool capabilities with the addition of the prepreg's compressibility and an indication of the gelation-time, which will enable an accurate prediction of residual porosity.



## 5 Validation of the OoA Simulation

In this Chapter, the evolution of properties measured during the manufacturing process of a monolithic CFRP part inside the oven are compared against the simulated properties using the OoA simulation framework developed in COMSOL Multiphysics and presented in Section 4.2. An instrumented test-bench was devised for this purpose [240], with the capability to simultaneously log the pressure, temperature, viscosity as well as the thickness evolution of the part during manufacturing. A comparison between the measured and simulated temperatures, viscosity and pressure, developed at the bottom of the laminate during processing is performed. The magnitude of the laminate's consolidation is recorded, though not included in the simulation. Finally, the residual porosity is quantified via microscopy at selected locations along the length of the part.

### 5.1 Experimental Test Bench

The test bench used for manufacturing the demonstrator consists of an aluminum tool supported on an aluminum framework placed on wheels, shown in Fig. 5-1(a). The tool can accommodate parts as large as 0.6m x 1.8m. To add flexibility in the positioning of the sensors and guide the cables, rails are included on the top of the tool. Manufacturing of the demonstrator OoA took place in a convection oven from Vötsch Industrietechnik (model VTLD 150/200/200), utilizing a dedicated vacuum pump.

Temperature, pressure, viscosity and displacement measurement sensors are instrumented either on the tool, inside or on top of the part being manufactured, in order to register the development of the properties of interest before and throughout the cure cycle. Due to the large amount of sensors and the variety of sensing principals, a synchronous acquisition of the input signals was developed using a cRIO-9074 platform from National Instruments.

The data logging and the HMI were realized in Lab-View [240]. The sensors were calibrated [240] and tested independently [S5], to ensure the anticipated range and accuracy is attainable before utilizing them for process monitoring purposes. The general scheme used for data-acquisition is shown in Fig. 5-1(b), while details about each sensor follow in Section 5.2. Wiring and set-up details and instructions can be found in the test-bench manual (SigCat Documentation) [240].

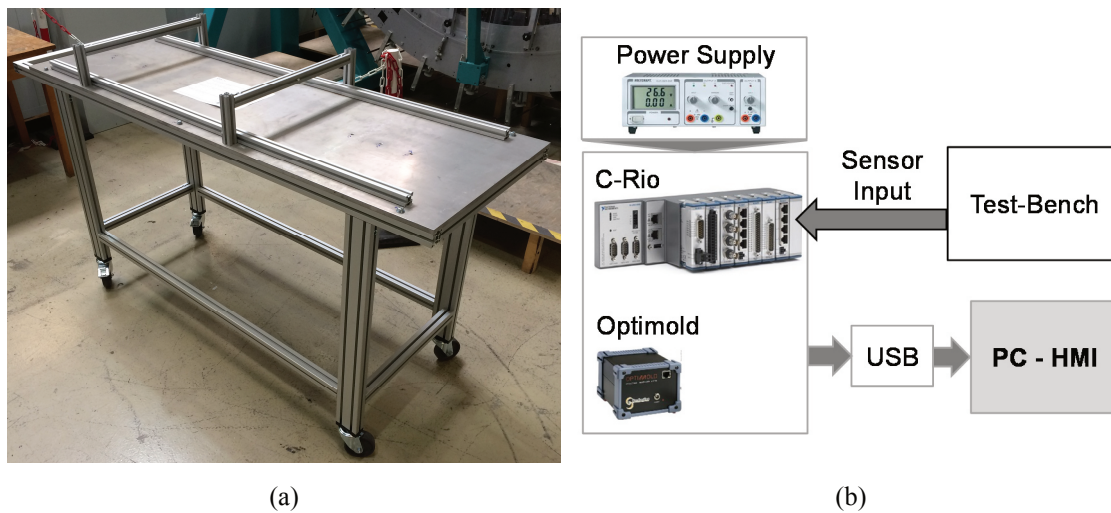


Fig. 5-1: (a) Aluminum tool used in the manufacturing of the CFRP demonstrator (b) data-acquisition scheme

## 5.2 Process Monitoring

A range of sensors are utilized during the OoA manufacturing process, in order to verify the results of the simulation developed in COMSOL Multiphysics, presented in Section 4.2. The main physical properties captured with the OoA simulation are the laminate temperature, gas pressure and resin viscosity. Therefore, sensors able to capture the evolution of these properties during the cure cycle are selected for instrumenting the part. The magnitude of consolidation taking place during the cure cycle is captured via a displacement sensor included in the process-monitoring scheme. The fully instrumented part placed on the tool before undergoing curing is shown in Fig. 5-2.

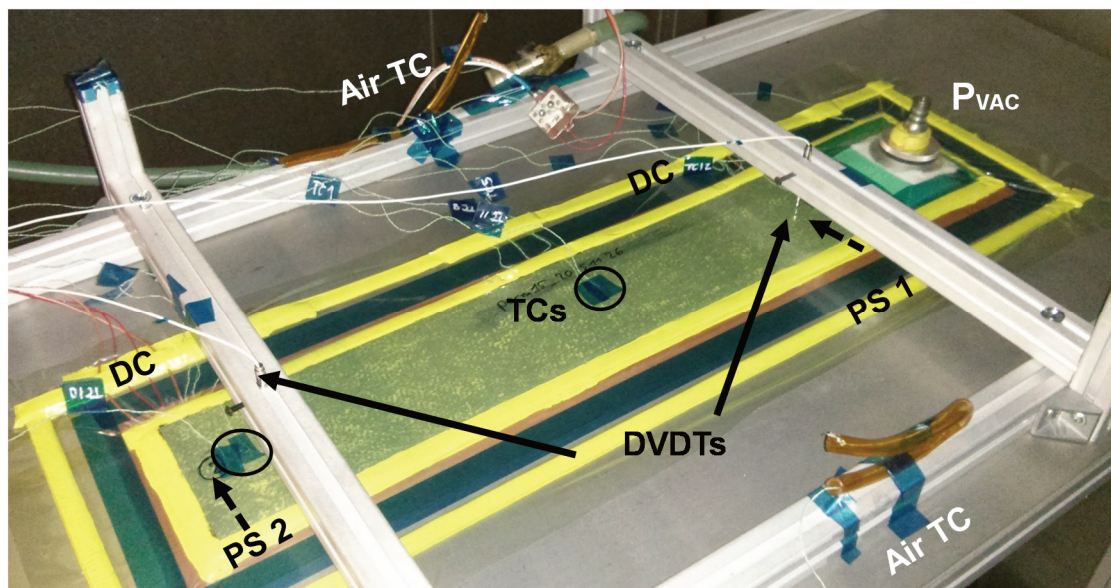


Fig. 5-2: Fully instrumented demonstrator part before undergoing OoA processing

## 5.2.1 Pressure Gauges

Accurately capturing the gas pressure development inside the laminate during processing outside the Autoclave plays a dominant role in this work. The main challenge with utilizing pressure sensors is the difficulty to integrate them into the laminate in order to directly measure the gas flow in the material, without obstructing the air flow nor affecting the laminate quality.

Miniaturized sensors can assist with these aspects, though any direct contact of the sensor with the liquid resin during processing shall be avoided, since it may impair the sensor's functionality and complicating the set-up further. Threaded miniaturized gauges (Kulite HKL-233C-375) shown in Fig. 5-3, linearly compensated and calibrated for operation up to  $150^{\circ}\text{C}$  were utilized to capture the gas pressure evolution in the laminate with a maximum absolute pressure rating of  $1.7 \cdot 10^5$  Pa (or 1.7 Bar). An NI 9237 bridge module is used for logging the signal of the pressure sensors via Ethernet using an NI 9949 Ethernet-to-lead adaptor [240]. The sensors are integrated inside the tool and are in direct contact with the bottom ply of the laminate as shown in Fig. 5-3. To avoid contamination of the sensor by the flowing resin during processing, a semi-permeable VAP membrane is placed on top of the sensor, between the laminate and the tool surface. The membrane enables vacuum to be distributed in the sensor while at the same time it acts as a resin-blocking medium. An O-ring and PVC tape is used to cover the thread of the pressure sensor, in order to prevent any leaks. An Oerlikon Leybold vacuum sensor (Cerovac CTR100) with a measurement range of  $1.3 \cdot 10^4$  Pa (or 0.13 Bar) is used to measure the vacuum level attained in the hose at the inlet of the bag outside the oven. Before each test all pressure sensors were calibrated using as a reference the pressure measured by the Oerlikon vacuum sensor in the hose close to the vacuum pump. The method utilized for this purpose is discussed in detail in the Term Project Report [S5].

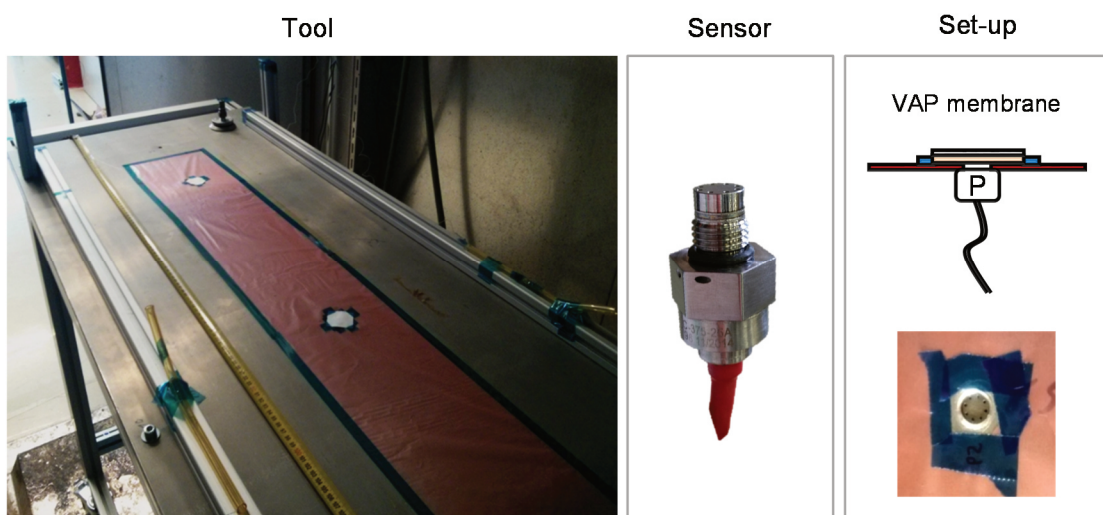


Fig. 5-3: Pressure sensor and tool-part integration



## 5.2.2 Temperature and Viscosity Sensors

Sixteen type-K thermocouples can be registered simultaneously using the NI 9213 module. None of the logging thermocouples in the c-RIO platform is able to control the cure cycle, which is programmed and control independently utilizing the integral sensing elements of the oven through a dedicated control panel. A DC based resistance monitoring system from Synthesites (Optimold) is used to monitor the viscosity evolution. The system can measure a material's resistivity and temperature using specialized sensors and suitable electronics, with the measured resistance varying from  $10^5$  Ohms up to  $5 \cdot 10^{13}$  Ohms [241]. As shown in several publications, the DC resistance can be directly correlated with the viscosity evolution of the resin up to the gelation point, where the viscosity becomes infinite, while the material resistance remains constant at constant temperature [168, 169, 174, 179]. Flexible DC sensors are integrated at selected locations inside the laminates manufactured Outside the Autoclave as shown in Fig. 5-4(b).

## 5.2.3 Displacement Sensors

Two sub-miniature displacement sensors (DVDT) with a demodulator and an 8mm stroke-length from MicroStrain (DEM0D-DVRT) are used to measure the laminate thickness change during manufacturing. This provides useful information on the magnitude and laminate consolidation time-frame during OoA processing. Since a significant amount of air is included at the initial state of the prepreg, it is expected to be evacuated during processing.

The two displacement sensors shown in Fig. 5-4(a) are guided in the selected location using an aluminum rail placed on the top of the tool. Once the bagging set-up is completed, the sensors are placed on top of the set-up and the spring is pushed down to reach its maximum stroke. While the vacuum is pulled, the stroke length of the sensor increases, with the magnitude of change showing the relative difference in mm between the initial and final set-up thickness, including the thickness of the backing paper and vacuum bag. The sensors are compensated up to  $175\text{ }^\circ\text{C}$ , nevertheless the sensor readings are further corrected to exclude the influence of the support-frame deformation [S5].

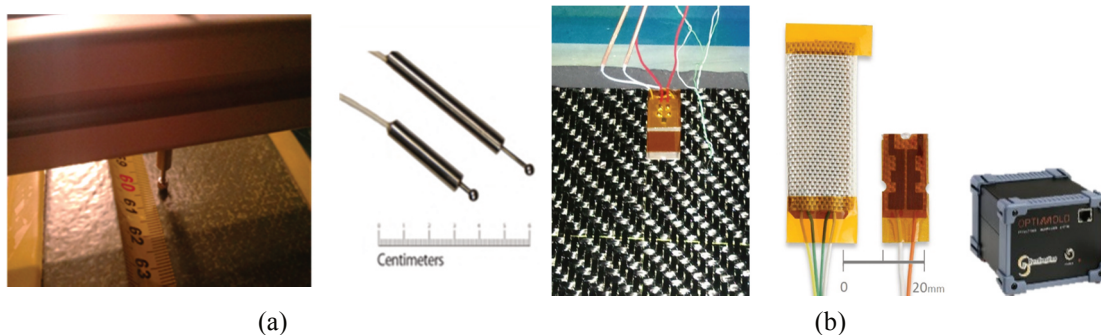


**Fig. 5-4:** (a) Displacement measurement sensors (DVDTs) (b) real-time viscosity measurement via a measurement of the DC Resistance – provided by Synthesites (Optimold)

### 5.3 Room Temperature Debulking

A debulking experiment revealed the interaction between the air and resin flow inside the prepreg. Seven MTM 44-1 prepreg plies with a length  $L = 0.6m$  and a width of  $w = 0.1m$  are stacked on top of each other, according to the set-up of Fig. 5-5.

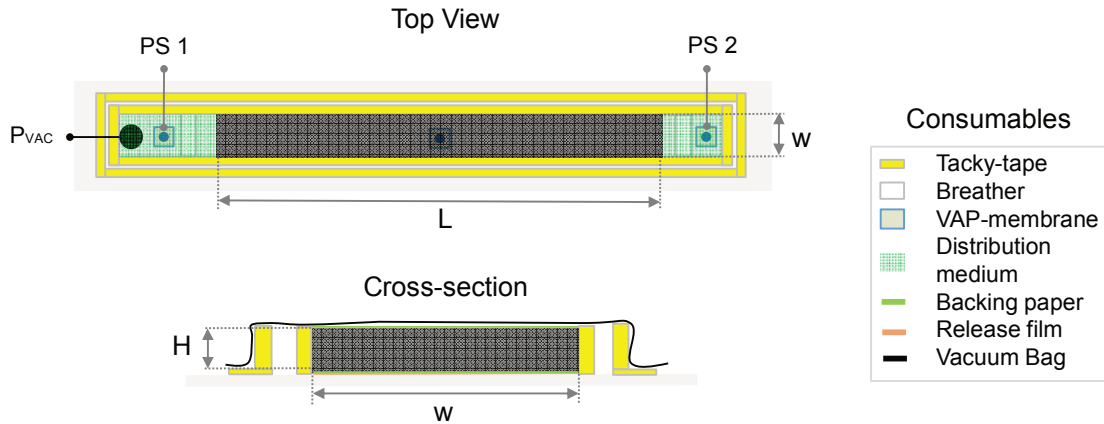


Fig. 5-5: Set-up used to perform debulking experiments at room temperature

The pressure sensor *PS 1* was placed just before the part, close to the inlet as shown in Fig. 5-5. The pressure sensor *PS 2* was placed at the other end of the part, with sole access to vacuum through the dry fibrous channels of the laminate. Pressure development at the two ends of the part during debulking is depicted in Fig. 5-6(a).

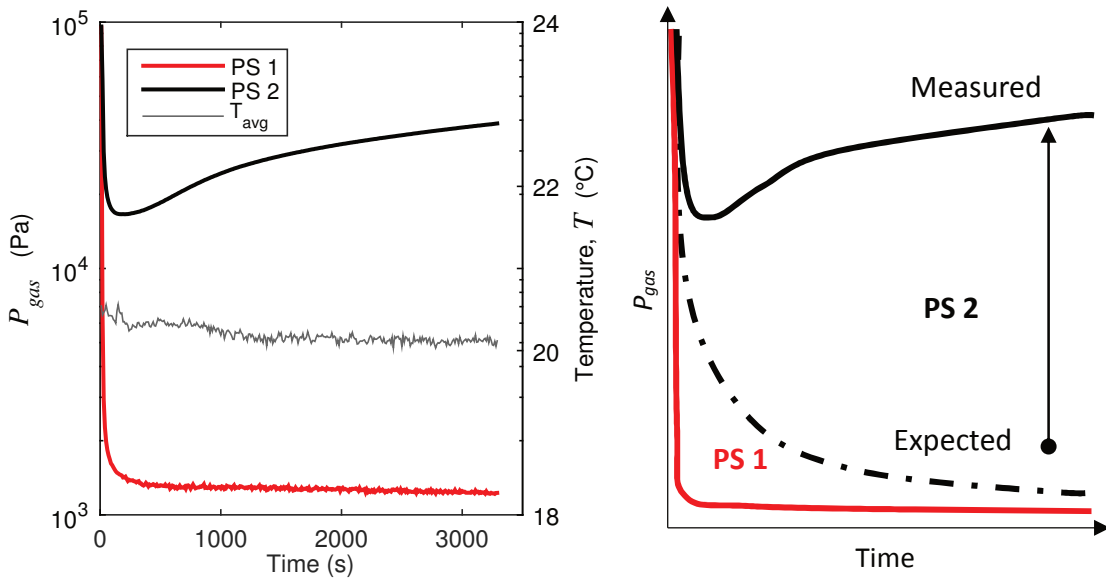


Fig. 5-6: (a) Measurement of the gas pressure at PS 1 and PS 2 during room temperature debulking ( $T_{avg}$ ) (b) sketch of the expected versus measured gas pressure at PS 2

As shown in Fig. 5-6(a), vacuum application during debulking leads to the obstruction of the air flow through the initially dry fibrous channels of the prepreg within the first

minutes of the debulking process at room temperature. This observation essentially confirms the competition between the time-frames for air and resin flow through the MTM 44-1 prepreg, even at short debulking cycles taking place at room temperature. If a limited interaction between the air and resin impregnated domains of the prepreg could be assumed, the expected gas pressure in the material would continuously reduce over time until it reached the imposed vacuum levels, as depicted in Fig. 5-6(b). It is obvious that considering a gas flow through the prepreg not inhibited by the resin flow, will lead to a homogeneous vacuum distribution everywhere inside the laminate.

As shown in Fig. 5-6(a) this is certainly not confirmed via experimental observations. Cold flow of resin and compaction of the fiber bed does take place during debulking and as the applied vacuum close to the vacuum pump is higher, the locations closer to the inlet 'lock-up' first and inhibit the distribution of vacuum further along the length of the part. This leads to an inhomogeneous gas pressure distribution along the part length and a gradual raise of the gas pressure towards atmospheric pressure inside the laminate. Therefore, for an accurate prediction of the vacuum state attained inside the laminate during OoA processing, the use of a two-way coupled air and resin flow model through the fibrous medium is required for an accurate physical description of the phenomena. Such a model was developed in the context of this work (see details in Section 4.2.4.2) and is utilized in the following sections to predict the pressure, temperature, viscosity and impregnation levels of the demonstrator part during OoA manufacturing, for model validation purposes.

## 5.4 Manufacturing a CFRP Demonstrator OoA

The manufacturing process utilized for the production of a monolithic CFRP demonstrator OoA based on the MTM 44-1 prepreg is presented here. As shown in Fig. 5-7, twenty plies of the prepreg are stacked on top of each other, constructing a part with a thickness  $H \approx 9 \cdot 10^{-3}m$ , length  $L = 0.59m$  and width  $w = 0.1m$  at its uncured state. The laminate is instrumented with a range of sensors able to measure pressure ( $PS$ ), temperature ( $T$ ), DC resistivity ( $R$ ) and thickness evolution ( $dH$ ) of during processing under vacuum in the convection oven, using the sensors and sensing principals summarized in Section 5.2. It shall be noted that in order to capture the influence of the part's length on the vacuum distribution, all edges including the top-surface of the laminate are sealed, apart from the vacuum inlet at the front of the part ( $x = L$ ). In this fashion the air evacuation and vacuum distribution is forced to take place primarily along the length of the part, mimicking the worst-case scenario as far as vacuum distribution is concerned.

The temperature cycle applied, is based on the cycle provided by Cytec [225], adjusted to enable heating at rates higher than  $1.3^{\circ}C/min$  and lower than  $2^{\circ}C/min$ . A dwell temperature of approximately  $130^{\circ}C$  is selected. The resulting heating profiles are presented in Section 5.5.



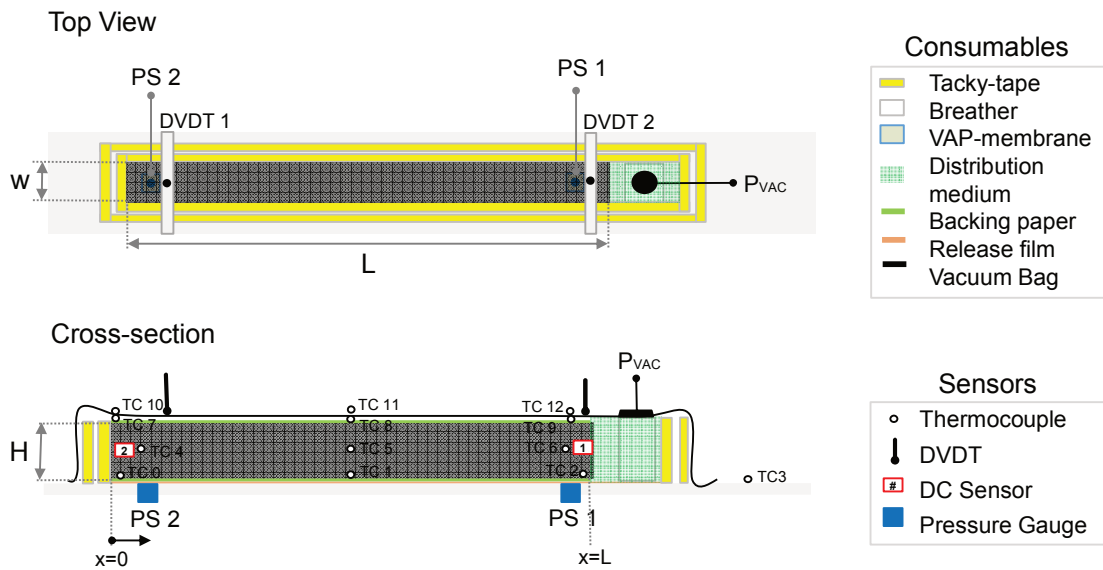


Fig. 5-7: Bagging and instrumentation scheme used for manufacturing of the demonstrator

## 5.5 Simulation and Experimental Verification

A comparison is performed in this Section between the simulated and experimentally measured gas pressure, temperature and viscosity fields developed in the demonstrator part. The experimental set-up utilized for this purpose and the manufacturing scheme were presented in Sections 5.1 and 5.4. The simulation domain, mesh and boundary conditions utilized for OoA process simulation are presented in Section 5.5.1, while the results of the comparison are presented in Sections 5.5.1-5.5.3. The experimentally measured part thickness change during consolidation is discussed in Section 5.5.4.

### 5.5.1 Simulation Domain and Assumptions

The length and thickness of the demonstrator part depicted in Fig. 5-7 is implemented in COMSOL Multiphysics as a 2D domain according to Fig. 5-8. The dimensions of the simulation domain are based on the part dimensions given in Section 5.4, considering they remain constant throughout the process (laminare compaction not considered). The part is discretized using a structured non-homogeneous mesh consisting of 11360 elements. Eight elements are included through the thickness of each ply, with four elements in each sub-domain. A dense discretization is selected close to the vacuum source ( $0.5 < L < 0.59 \text{ m}$ ), as shown in Fig. 5-8(b). The modeling approach utilized to simulate the Out-of-Autoclave process in COMSOL Multiphysics is presented in Sections 4.2.2 and 4.2.3. The temperature boundary conditions applied in the domain of Fig. 5-8 are presented in 5.5.2, while the flow boundary conditions are presented in Section 5.5.3. The air flow through each prepreg ply is influenced by the continuous reduction of the air permeability, as a function of the local porosity evolution according to Equation (3-23).

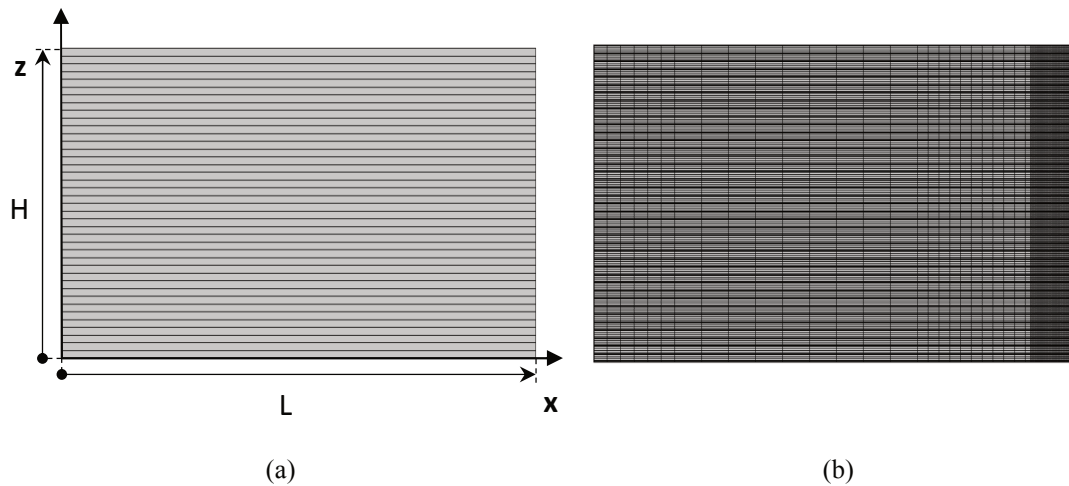


Fig. 5-8: (a) CFRP demonstrator geometry in COMSOL Multiphysics (b) spatial discretization

## 5.5.2 Temperature and Viscosity Evolution

Simulating the heat transferred in the CFRP demonstrator during OoA processing under vacuum in a convection oven is performed according to the methodology discussed in Section 4.2.2.2. The domain and boundary conditions are depicted in Fig. 5-9(a). The experimental and virtual sensors monitoring temperature and resin viscosity are shown in Fig. 5-9(b).

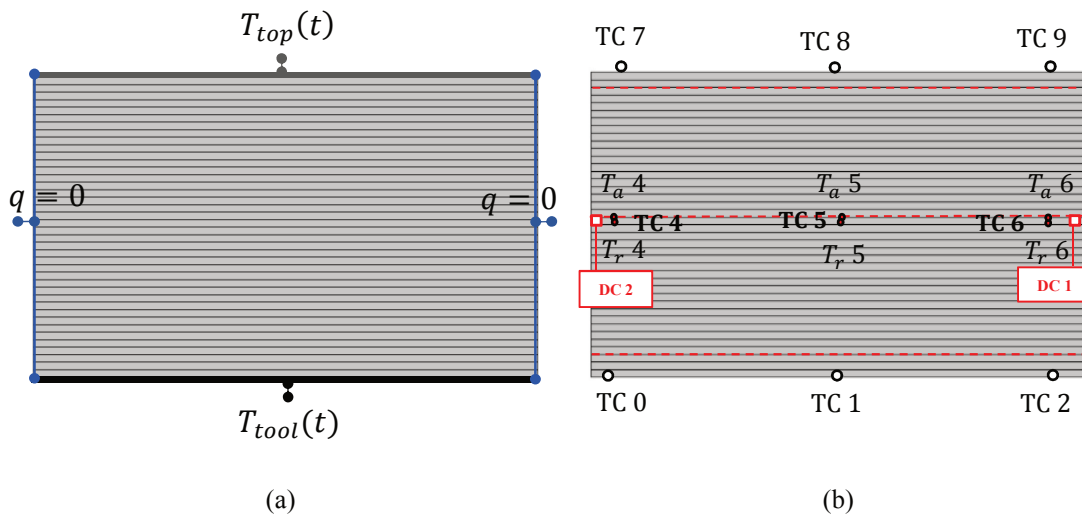
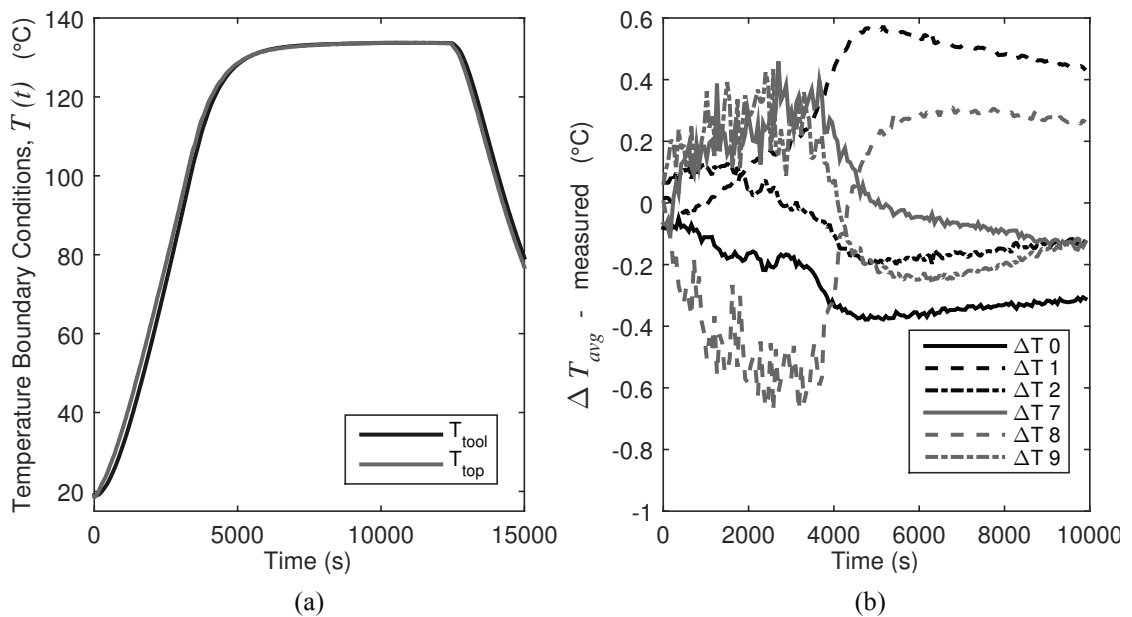


Fig. 5-9: (a) Temperature boundary conditions (b) experimental and virtual sensor positions

The temperatures at the top  $T_{top}(t)$  and bottom of the part  $T_{tool}(t)$ , are directly applied as boundary conditions on the simulated part. These profiles result from averaging the temperature of three thermocouples recorded at the bottom ( $TC\ 0, 1, 2$ ) and top of the part ( $TC\ 7, 8, 9$ ) under the vacuum bag (see Fig. 5-9(b)). As shown in Fig. 5-10(b) a temperature difference  $\Delta T_m$  smaller than  $1\ ^\circ\text{C}$  is measured between the average and the

local tool temperatures ( $\Delta T_m = TC_{avg,m} - TC$ ). Preliminary tests performed to determine the temperature homogeneity of the tool are presented in Appendix h.



**Fig. 5-10: (a) Temperature cycles applied at the top and bottom of the part (b) difference between the average and local temperatures, measured at the top and bottom plane**

Though experiments to determine the heat-flux at the top of the part were performed in the same oven and with the same tooling, they were not successful in determining an accurate thermal coefficient due to unsteady air flow and the significant thermal mass of the tool which prevented the establishment of a steady state. As demonstrated in Sections 4.2.4.3 and 4.2.4.4, accurately capturing the temperature evolution inside the part is crucial for an accurate prediction of the resin viscosity and air density, which both influence the establishment of the gas pressure inside the laminate. Preliminary simulations utilizing the over-estimated convection coefficient led to the development of a hotter part and therefore a significantly lower vacuum pressure established in the laminate. Therefore, the direct application of temperatures registered during the experiment was the most accurate method to capture the temperature state of the part in the simulation. For a generic application of the model in more complex part geometries, the convection coefficient and modeling the thermal behavior of the tool may be of interest.

The simulated temperature and viscosity development inside the part in COMSOL Multiphysics is shown in Fig. 5-11. A temperature gradient is present through the part thickness within the first 4000s. The top section is initially hotter, due to the hot air released parametrically from the sealing of the convection oven ( $t = 2000s$ ). After the vacuum is applied, the air evacuates the prepreg while the locations close to the vacuum source maintain the lowest gas pressure. This leads to a reduced air content close to the vacuum and since the air has an insulating effect, this region of the part is hotter therefore an in-plane temperature gradient develops.

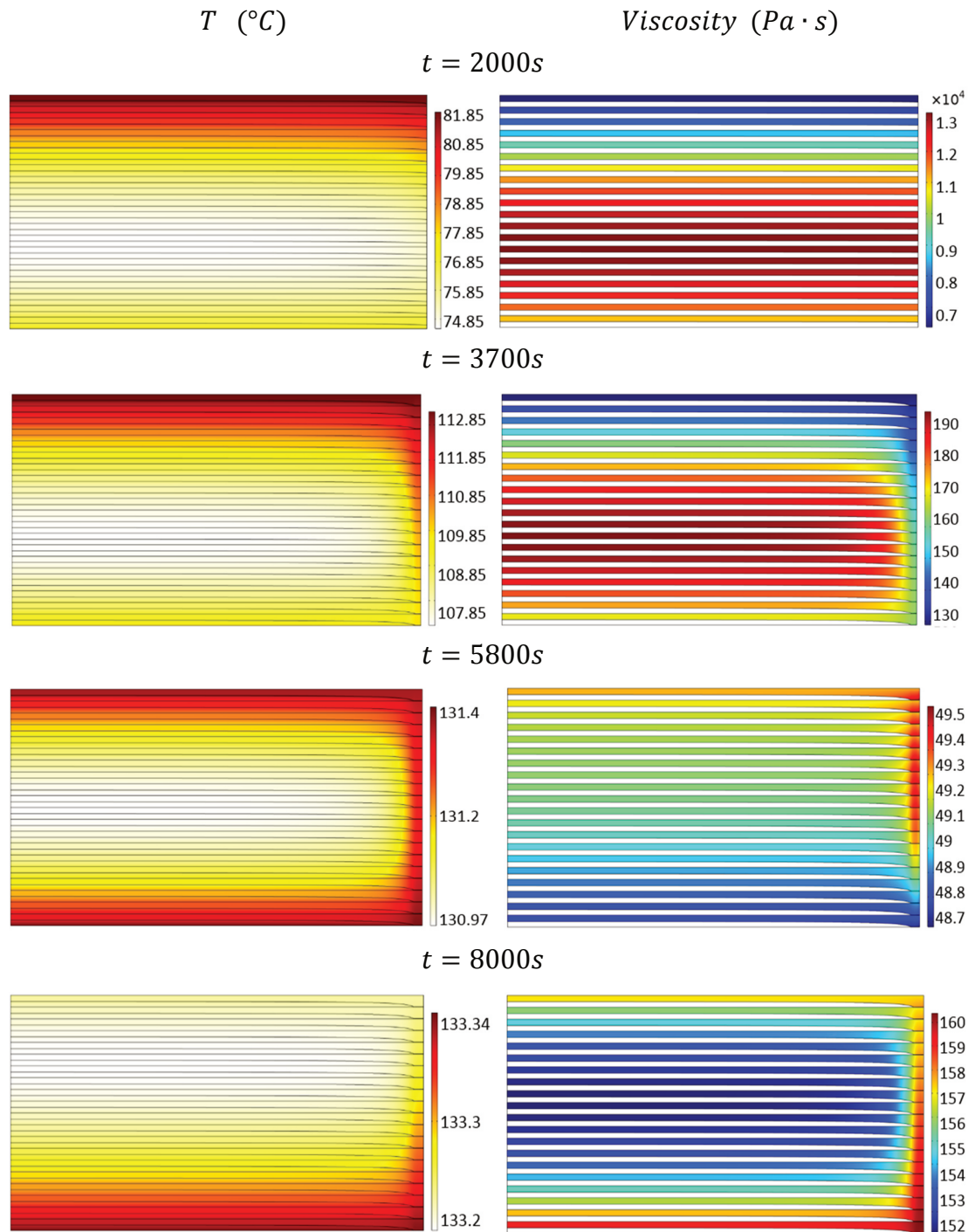


**Fig. 5-11: Simulated temperature and resin viscosity development in the demonstrator part**

The temperature gradient is particularly visible in the middle section of the part ( $t = 3700s$ ). As the cure cycle progresses, the air temperature stabilizes close to the dwell temperature ( $\sim 130^{\circ}C$ ), while the aluminum tool releases the residual heat stored. This leads to the development of a hotter zone at the bottom of the part towards the end of the cure cycle ( $t = 5800 - 8000s$ ). The equations utilized to model the thermal conductivity of the prepreg (see Section 4.2.2.2) are selected to attain a temperature state in

the simulated part, which will closely match the experimentally measured temperature, at the first seconds of the cure cycle. Since the top and bottom temperatures are imposed as boundary conditions, the temperatures at positions  $TC$  4, 5, 6 are used for comparison purposes in Fig. 5-12(a)-(c). The thermocouple readings ( $TC$ ) are compared against the temperature inside the air ( $T_a$ ) and resin saturated domain of the prepreg ( $T_r$ ).

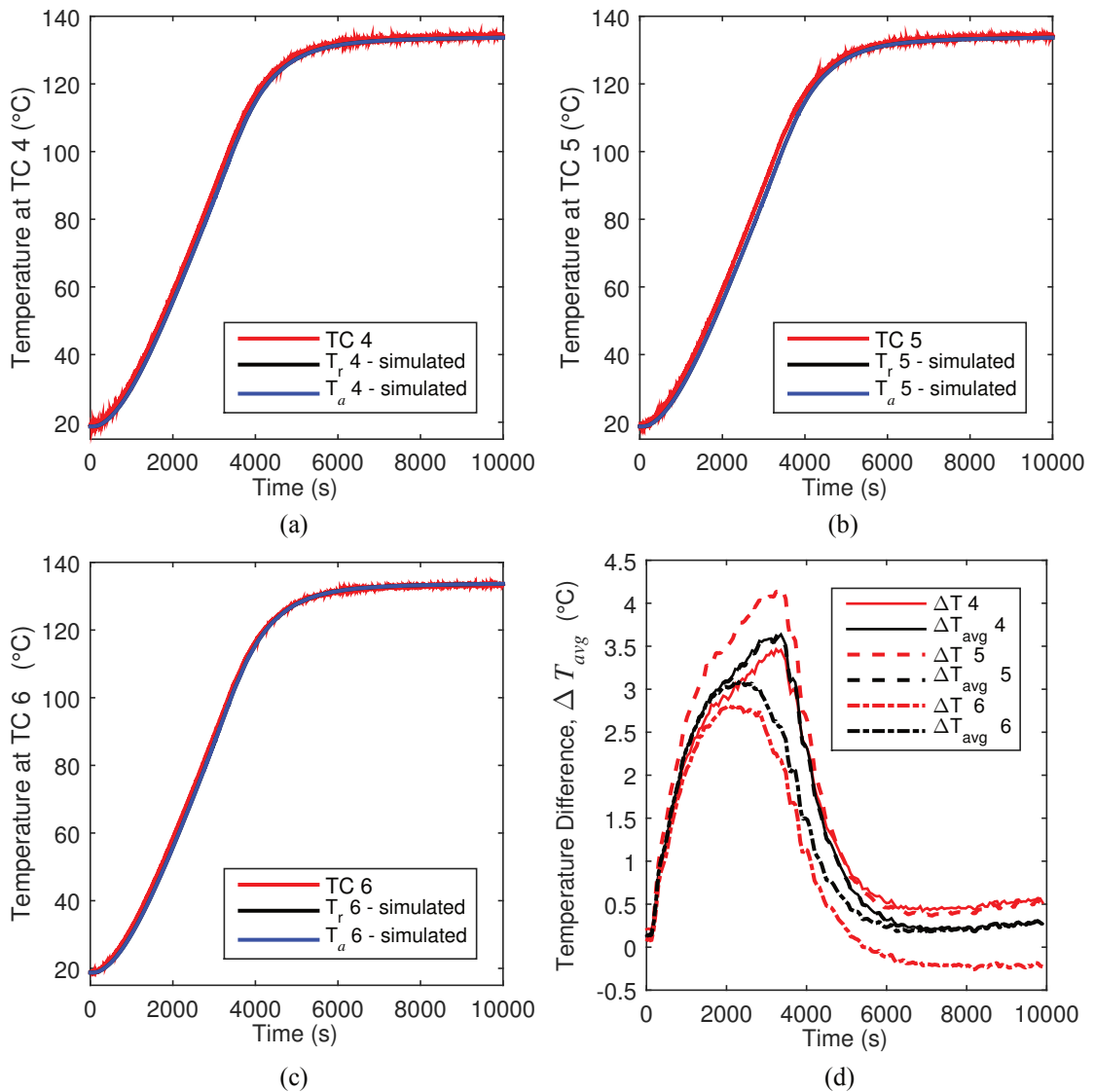


**Fig. 5-12: Comparison of experimentally measured and simulated temperatures at the mid-plane of the CFRP demonstrator (between the tenth and eleventh ply)**

(a) Temperature at the location furthest from the vacuum source – TC 4 (b) temperature at the mid-span – TC 5 (c) temperature measured close to the vacuum source – TC 6 (d) difference between the measured, local and the average, simulated temperature -  $\Delta T$  as well as the average experimental and simulated temperature -  $\Delta T_{avg}$ .

The thermocouples and simulation probes are placed between the tenth and eleventh ply of the laminate, as depicted in Fig. 5-9. The exact probe positions are summarized in Tab. A- 7, Appendix h. The difference between the local, measured ( $TC$   $i$ ) and the average, simulated temperature ( $(T_r + T_a)/2$ ), is calculated as  $\Delta T$   $i$  via Equation (5-1),

while  $\Delta T_{avg}$  is the difference between the average experimental temperature at the mid-plane of the part ( $TC_{avg\_m}$ ) and the average simulated temperature  $((T_r + T_a)/2)$  which is calculated in this case via Equation (5-2).

$$\Delta T_i = TC_i - \frac{(T_r + T_a)}{2} \quad (5-1)$$

$$\Delta T_{avg} = TC_{avg\_m} - \frac{(T_r + T_a)}{2} \quad (5-2)$$

Since the resin saturated domain at the top of the tenth ply and the air saturated domain at the bottom of the eleventh ply are modeled as separate domains, the average temperature is utilized instead for comparison against the thermocouple readings.

In Fig. 5-12(d) the temperature difference is smaller than 0.3°C within the first 150s, while from this point onwards it gradually raises to a maximum of 4°C, which is reached within 2000-4000s depending on the location of the sensor inside the part. The highest temperature difference of approximately 4°C is present in the middle of the part ( $TC 5$ ), while the smallest difference of approximately 2.5°C is measured close to the vacuum source ( $TC 6$ ). The simulated temperature is lower than the experimental temperature throughout the cure cycle and therefore a positive temperature difference is depicted, with the only exception of  $TC 6$  which measures an insignificantly lower temperature than the simulated one (by approximately 0.2°C). The temperature difference peaks at 4000s and starts reducing thereof to approximately 6000s, when the temperature difference stabilizes to less than 1°C. Though the temperature difference in the middle and far end of the part is not small, it can be justified by the assumption of a constant fiber volume fraction and part thickness utilized, which does not reflect reality as discussed in Section 5.5.4. It is evident that the underestimation of the evolving fiber volume fraction in reality, to a constant initial fiber volume content and ply thickness throughout the process in the simulation will lead to an underestimation of the heat transfer in the part, particularly within the time-scale where most of the compaction takes place. As shown in Fig. 5-20, capturing the thickness evolution of the part during processing, the time-frame within which maximum temperature difference occurs, coincides with the time-frame of maximum compaction due to the presence of a reducing pressure gradient in the part. This indicates that including the compaction physics in the OoA process simulation scheme developed will significantly enhance the current prediction capabilities.

Nevertheless, the temperature close to the vacuum source is depicted with a very good accuracy, considering the measurement error of the thermocouple and the error originating from the application of an average temperature boundary condition at the bottom and top of the part. Accurate prediction of the temperature close to the vacuum source influences significantly the impregnation and air evacuation process. As the resin velocity is higher close to the vacuum source throughout the process, this location impregnates or ‘locks’ first. The gas pressure development during processing is presented in

detail in Section 5.5.3. The influence of temperature on the resin viscosity and its impregnation velocity is evident. The viscosity evolution of the resin is experimentally captured using the Optimold and the flexible DC sensor, able to measure the electrical resistance of the material shown in Fig. 5-13(a).

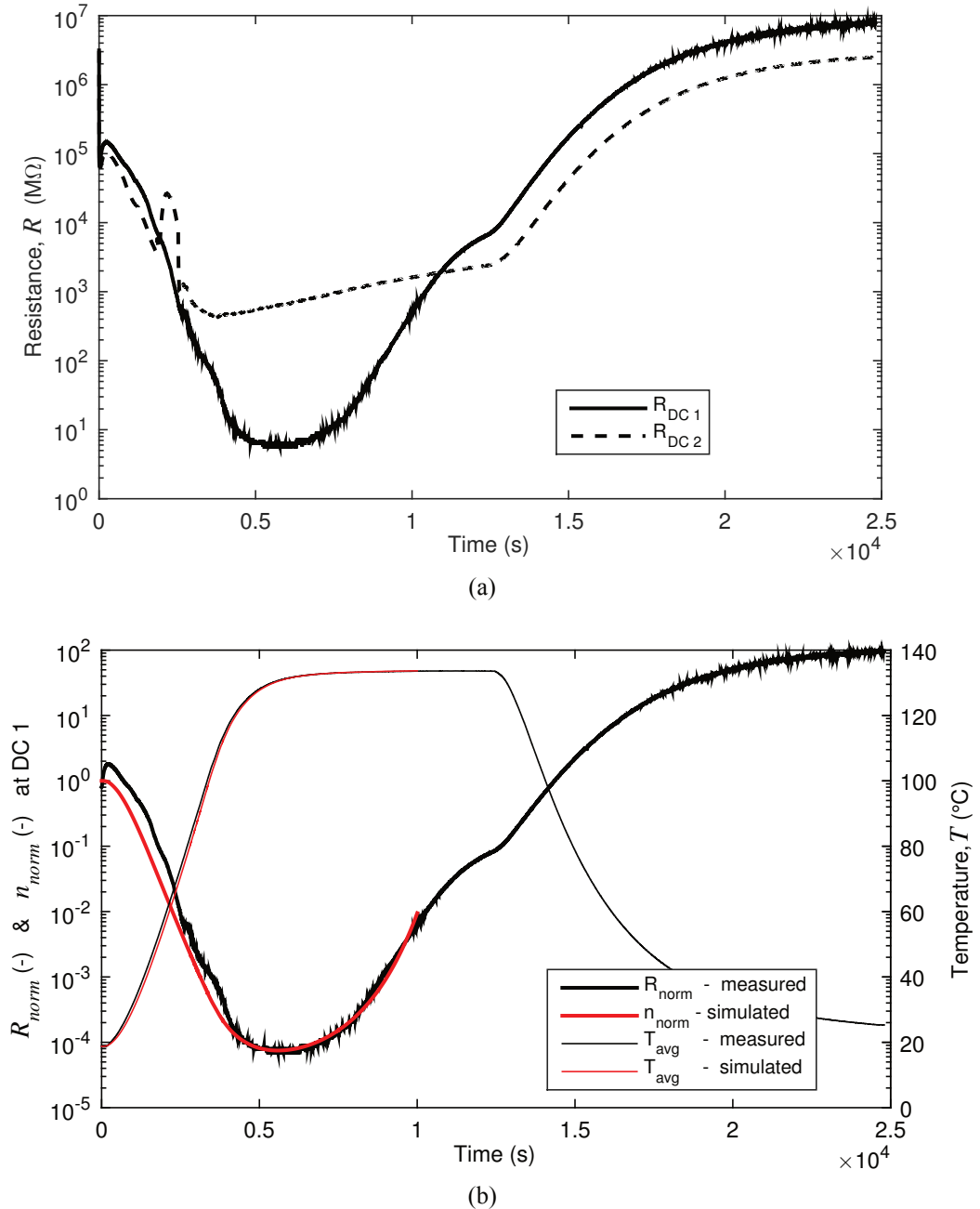


**Fig. 5-13:** (a) Resistance measured in the material at positions DC 1 and DC 2, in the mid-plane of the laminate (b) comparison of the measured and simulated temperatures as well as normalized viscosity and resistance signals at position DC 1 in the laminate

The electrical resistance of the uncured laminate reduces while the vacuum is distributed, due to the increasing laminate compaction. Once the resin comes in contact with the sensors at positions *DC 1* and *DC 2*, the resistance evolution depicted in Fig. 5-13(a)



reflects primarily the change in resin viscosity. The steep, linear drop of the resistance from  $10^7$  to approximately  $10^5$  M $\Omega$  takes place within the vacuum application time frame. By this time, a good contact between the sensor and the laminate is attained, which in the case of the *DC 1* sensor leads to capturing the viscosity evolution of the resin throughout the cure cycle. The minimum resistance measured at *DC 1* is approximately 6 M $\Omega$ . In the case of the sensor at *DC 2*, the signal becomes noisy at approximately 2000s, limiting the usability of the data for further analysis. This behavior was repeatedly observed at sensors placed far from the vacuum source, in a range of parts manufactured Outside the Autoclave [S5], using the same material and manufacturing set-up. Potential explanation for this behavior could be the insufficient consolidation of the laminate far from the vacuum source, which may subsequently lead to insufficient wetting of the sensor with resin. The signal of the *DC 2* sensor is not used for further analysis. The normalized resistance at *DC 1* is calculated according to Equation (5-4) is compared against the predicted viscosity at the same location, normalized and calculated by Equation (5-3) in Fig. 5-13(b).

$$n_{norm}(t) = \frac{n(t)}{n_{max}} \quad (5-3)$$

$$R_{norm}(t) = \underbrace{\left(100 \cdot \frac{n(t_1)}{n_{max}} - \frac{R(t_1)}{R_{max}}\right)}_{\text{constant at } t=t_1} \cdot \frac{R(t)}{R_{max}} \quad (5-4)$$

The time at  $t = t_1$  reflects the end of the linear resistance drop in the signal ( $10^7$ - $10^5$  M $\Omega$ ), depicted in Fig. 5-13(a).

The shape of the two normalized curves (viscosity and resistance at *DC 1*) matches closely throughout the duration of the cure cycle. A small difference is observable within the first 4000s, possibly due to the influence of the laminate compaction. Apart from the qualitative comparison of the shape of the curve, comparing the time when a viscosity minimum is attained in simulation, against the minimum measured resistance during processing, gives a quantitative indication of the prediction quality attained. A good match of the elapsed-time is obtained at the minimum of both curves, with a difference of less than 7min (460s) between the two, considering the variability of the resistance sensor (1 M $\Omega$ ), which makes the definition of an absolute minimum challenging.

**Tab. 5-1: Time at which the minimum DC Resistance and viscosity is measured**

Symbol	Unit	Time at minimum
$R_{min}$	s	5278-6000
$n_{min}$	s	5580

### 5.5.3 Gas Pressure Development

The most novel aspect of the Out-of-Autoclave simulation is the coupling of the air and resin pressures at the resin-front throughout the prepreg impregnation process, which takes place during the cure cycle. In this section, the measured gas pressure at two locations at the bottom ply of the part, along its length, is compared against the simulated pressure developed at the same locations. The gas pressure distribution is simulated in the complete part, while the influence of the temperature gradients on the impregnation levels attained in each ply are discussed below. The locations of the pressure sensors and virtual probes used for simulations are shown in Fig. 5-15, while the exact positions are summarized in Tab. A- 7 of Appendix h.

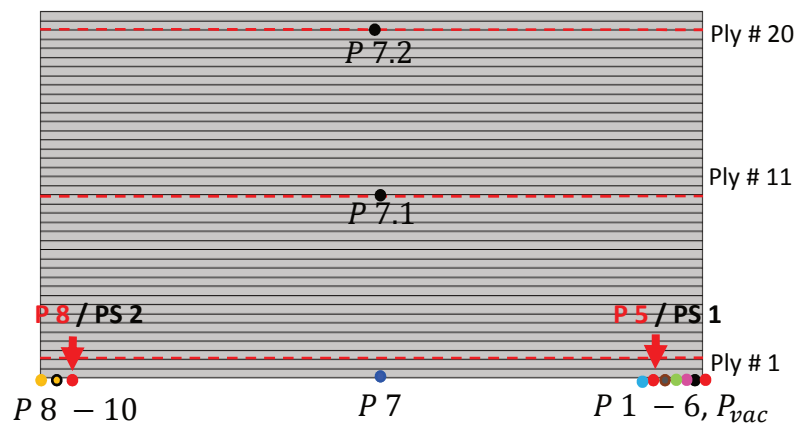
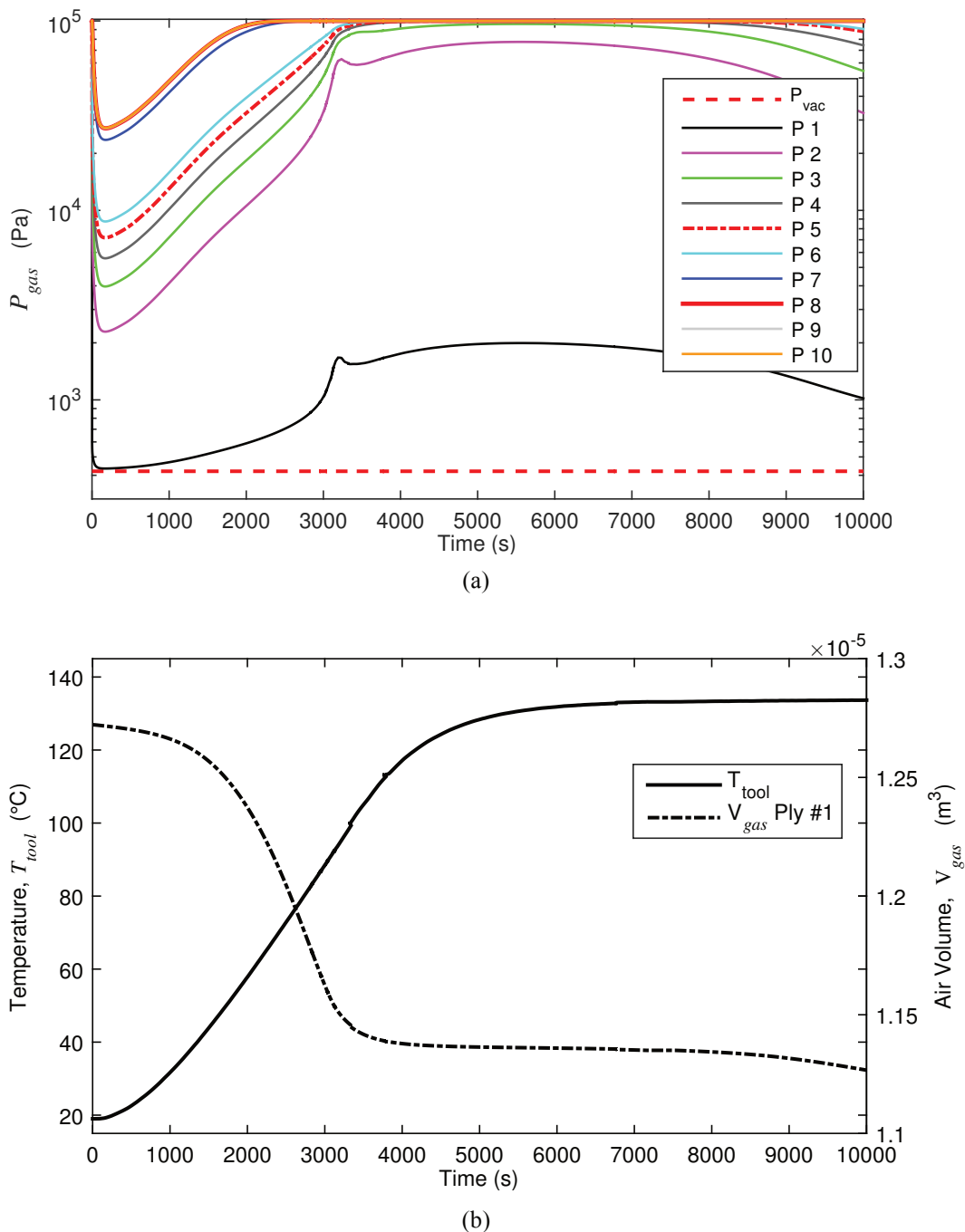


Fig. 5-14: Locations of the pressure sensors and simulation probes inside the demonstrator

The development of the gas pressure inside the MTM 44-1 prepreg is simulated in COM-SOL Multiphysics according to the coupling scheme presented in Section 4.2.3, while the part undergoes heating in a convection oven during the cure cycle of Section 5.5.2.

The domain of Fig. 5-15 consists of twenty MTM 44-1 plies stacked on top of each other. The initial ply thickness ( $H_p = 0.45 \cdot 10^{-3}\text{m}$ ) determined in Section 3.2 and an approximation of the volume fractions of air, resin and fibers in the MTM 44-1 prepreg are utilized in this simulation ( $V_{f,a} = V_{f,r} = V_{f,p} = 36\%$ ,  $V_{r,p} = 34\%$  and  $\phi_p(0) = 30\%$ ). The air and resin flow are coupled according to the methodology presented in Section 4.2.2.1, while the in-plane air permeability of the prepreg is considered as a function of the ply porosity according to Equation (3-23). The through thickness permeability of the prepreg remains constant throughout the cure cycle, since the fiber volume fraction and the thickness of the material remains constant. The through thickness permeability of both the air and resin saturated domains of the prepreg are equal, while the in-plane permeability of the resins saturated domain is high, to prevent the resin from flowing outside each ply (same as in Case 1 - Tab. 4-3). The vacuum pressure is applied with the use of a step function at position  $x = L$ , while no flux boundary condition ( $v_a = 0$ ) is applied on the other walls of the air saturated domain, as shown in Fig. 4-15.

The gas pressure established at the bottom ply of the demonstrator, at ten positions along its length ( $P 1 - P 10$ ) is depicted in Fig. 5-15(a). The red dashed line shows the inlet vacuum pressure  $P_{vac}$ , applied as a boundary condition in the simulation, while the solid red ( $P 8$ ) and the dotted red lines ( $P 5$ ) reflect the simulated pressures at the sensor positions. The average temperature at the tool surface ( $T_{tool}$ ) and the volume of gas in the bottom ply, in contact with all sensors ( $Ply \#1$ ) is depicted in Fig. 5-15(b).



**Fig. 5-15:** (a) Simulated gas pressures at the inlet and ten more locations along the length of the demonstrator (P 1-P 10, at positions depicted in Fig. 5-14) (b) tool temperature and the air volume evolution as depicted in the bottom ply of the part during the cycle

A direct comparison of the measured and simulated gas pressure at positions  $P 5$  and  $P 8$ , where sensors  $PS 1$  and  $PS 2$  are located is shown in Fig. 5-16.

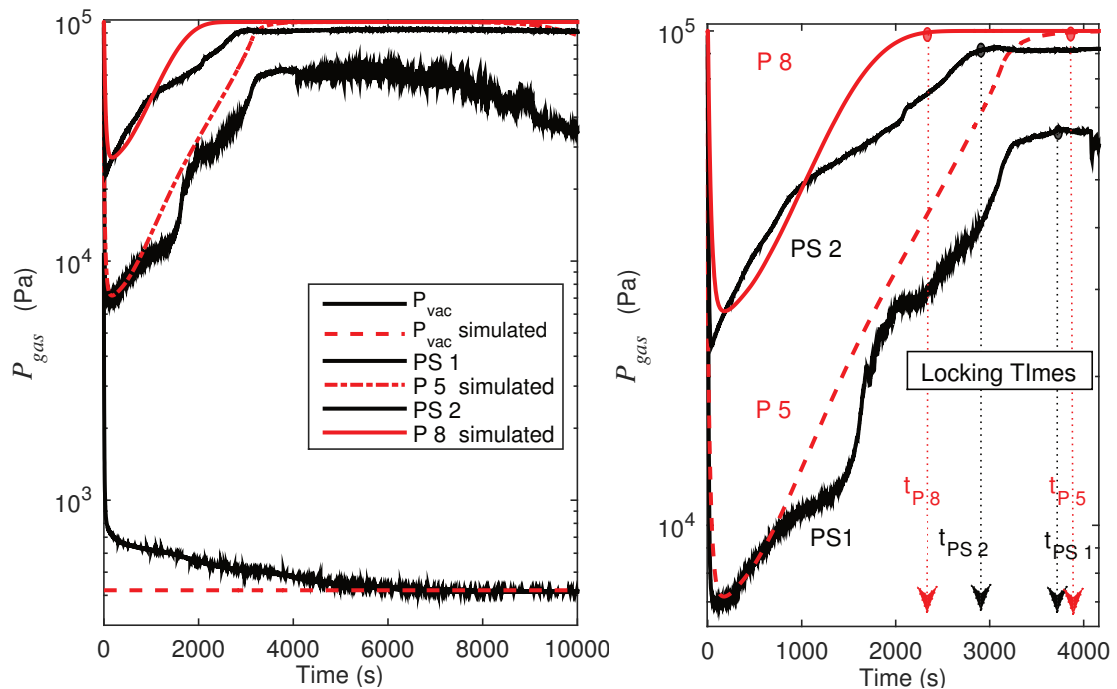


**Fig. 5-16: Comparison of the measured and simulated pressure at the inlet and at two positions along the part length ( $P 5/ PS 1$  and  $P 8/ PS 2$ , see Fig. 5-14 for sensor locations)**

A delay in attaining a constant pressure at the inlet of the vacuum bag can be observed in Fig. 5-16 ( $P_{vac}$  - simulated), most likely as a result of the interaction between the vacuum pump characteristics and the quality of vacuum attained under the vacuum bag. As the vacuum pressure is measured at the hose which connects the pump to the vacuum bag, the pressure registered lumps the contribution of the vacuum pump characteristics and the quality of vacuum established under the vacuum bag. The steady-state vacuum pressure established after approximately 5000s, is utilized as a boundary condition at position  $x = L$  for the OoA simulation. A very close match is attained between the minimum simulated and experimentally measured gas pressure. The minimum pressure predicted at position  $P 5$  close to the vacuum source (sensor  $PS 1$ ) is higher by 200 Pa than the measured, which is established with a delay of approximately 100s. The minimum gas pressure established at position  $P 8$  lags behind the measured gas pressure (sensor  $PS 1$ ) at the same position by approximately 150s, while the measured pressure is higher by 350 Pa. These differences are not significant, considering the duration of the cure cycle and the range of pressures concerned ( $10^2 - 10^5 Pa$ ). Shortly after a minimum pressure is reached, both the experimental and simulated pressures increase towards atmospheric pressure. This increase is the result of the interaction between the impregnation of the initially dry tows of the prepreg with resin and therefore locking-off the air-pathways, as well as the direct effect of temperature on the gas pressure through the air density. The interaction between the evolution of the local, simulated

temperature and pressure and the residual air volume within the first ply at positions  $P 1$ ,  $P 5$  and  $P 8$  as well as at the vacuum inlet is depicted in Fig. 5-17.

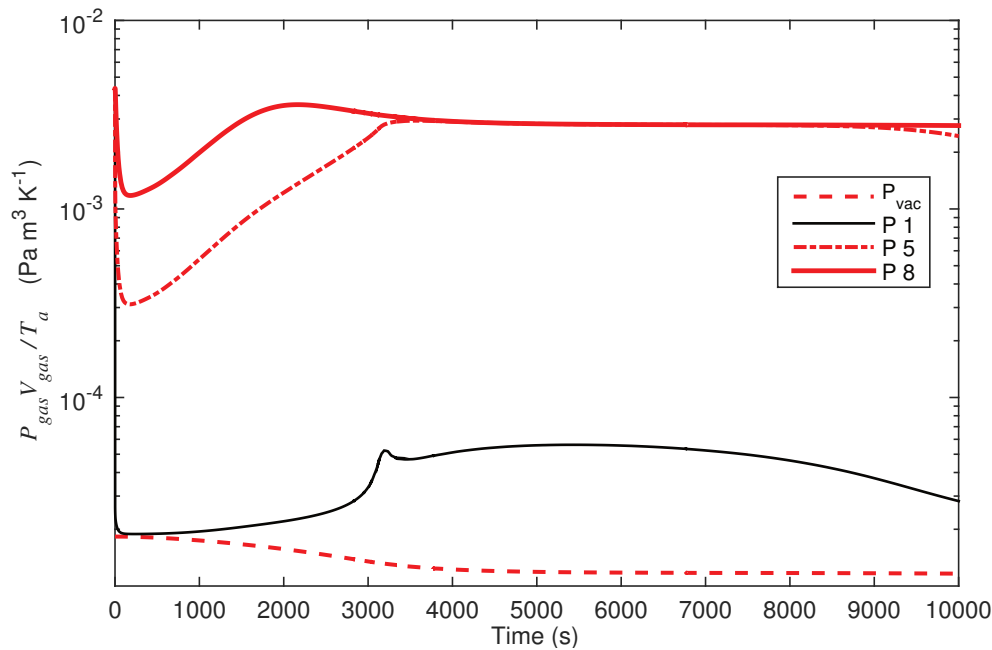


**Fig. 5-17: Interaction between the simulated temperature, pressure and air volume in the bottom ply of the demonstrator at the inlet and three locations along the part length**

The prepreg impregnates first close to the vacuum source, due to the presence of an increased local pressure difference ( $\Delta P = P_{atm} - P_{gas}$ ). This leads to a reduction of the available pressure and eventually a blockage of the part's access to vacuum.

It can therefore be deduced that limited impregnation will take place at  $t_{PS1} = 3800s$  (63min), since  $P_{gas} \approx P_{atm}$ . The back side of the part ( $P 8 / PS 2$ ) loses access to vacuum already after  $t_{PS2} = 3000s$  (50min) due to a reduced initial pressure. This time is referred to as prepreg 'locking time', implying locking of the prepreg's access to vacuum. This effect in combination with an advanced state of resin gelation define the time-frame available before an intra-tow porosity becomes entrapped. Though the slope of the experimental and simulated gas pressure is almost the same within the first 800s of the cycle, the experimental gas pressure significantly slows down compared to the simulated pressure, reaching a steady state at lower pressures than predicted. The discrepancy between experimental and simulated gas pressure increase may result from:

- The increased porosity and thickness of the resin saturated domain considered in the simulation, since the prepreg consolidation during processing is not modeled (see Section 5.5.4). This leads to a higher simulated resin velocity and therefore a faster raise of the gas pressure.
- The macroscopic definition of the flow front. For a more accurate localization of the resin front inside the woven textile, the definition of a mesoscopic reference volume element (RVE) shall be developed and coupled to the macroscopic front.

- Continuous air evacuation between the first ply and the tool interface may have been possible due to a potential leak through the bagging set-up utilized.

An accurate prediction of the material's 'locking time' is nevertheless possible with the current capabilities of the OoA simulation. As shown in Fig. 5-16, the pressure measured close to the vacuum source reaches a plateau only approximately *3min* before it does in the simulation ( $t_{p5} > t_{pS1}$ ), while the simulated gas pressure at *P 8* reaches a plateau first ( $t_{pS2} > t_{p8}$ ), with the measured pressure following after *7min*.

Although the dominating pressure gradient in the demonstrator develops in-plane, a small temperature difference developed during the cure cycle (see Fig. 5-11) leads to a gradual impregnation from the top towards the bottom of the part, as shown in Fig. 5-18.

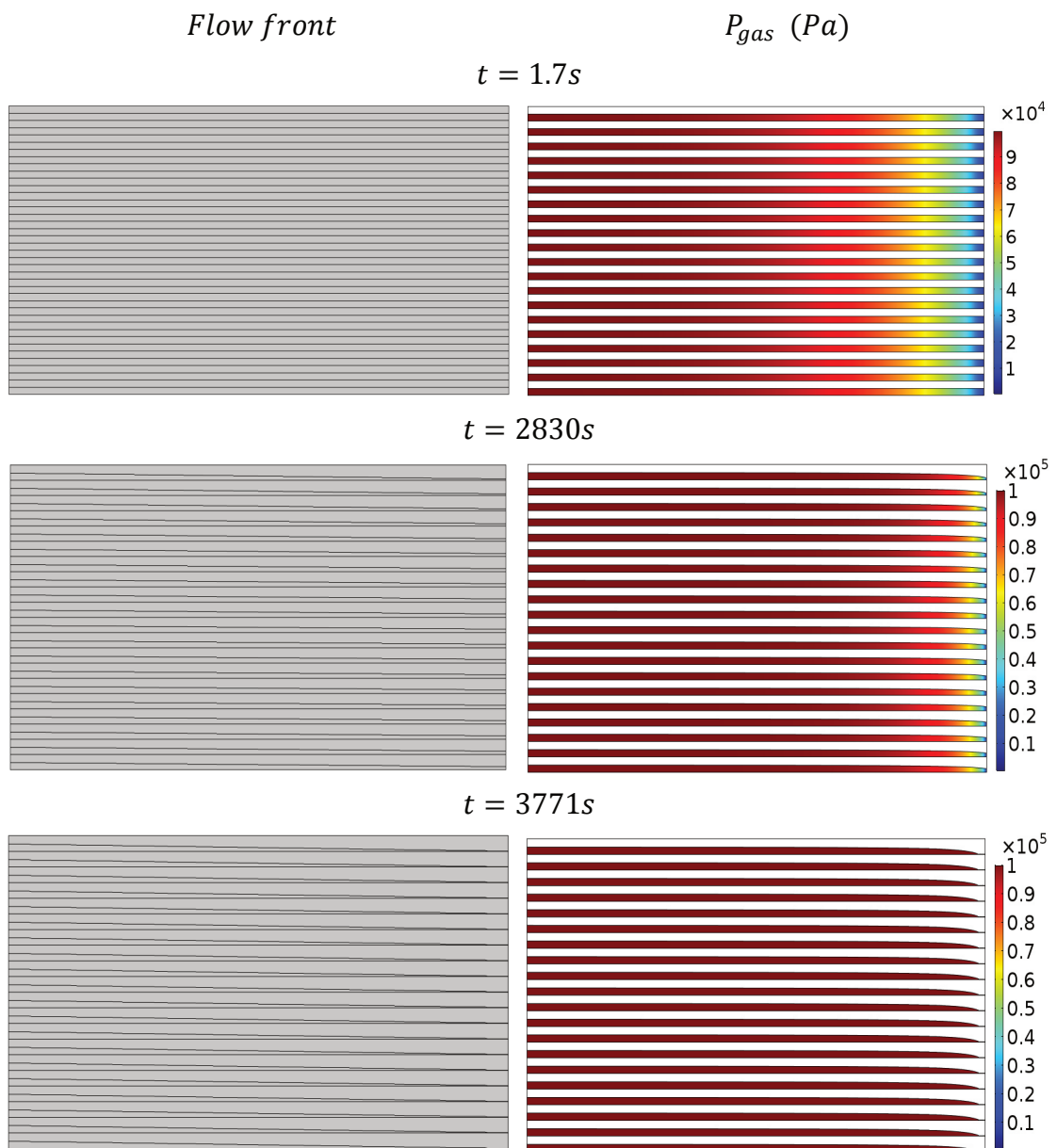
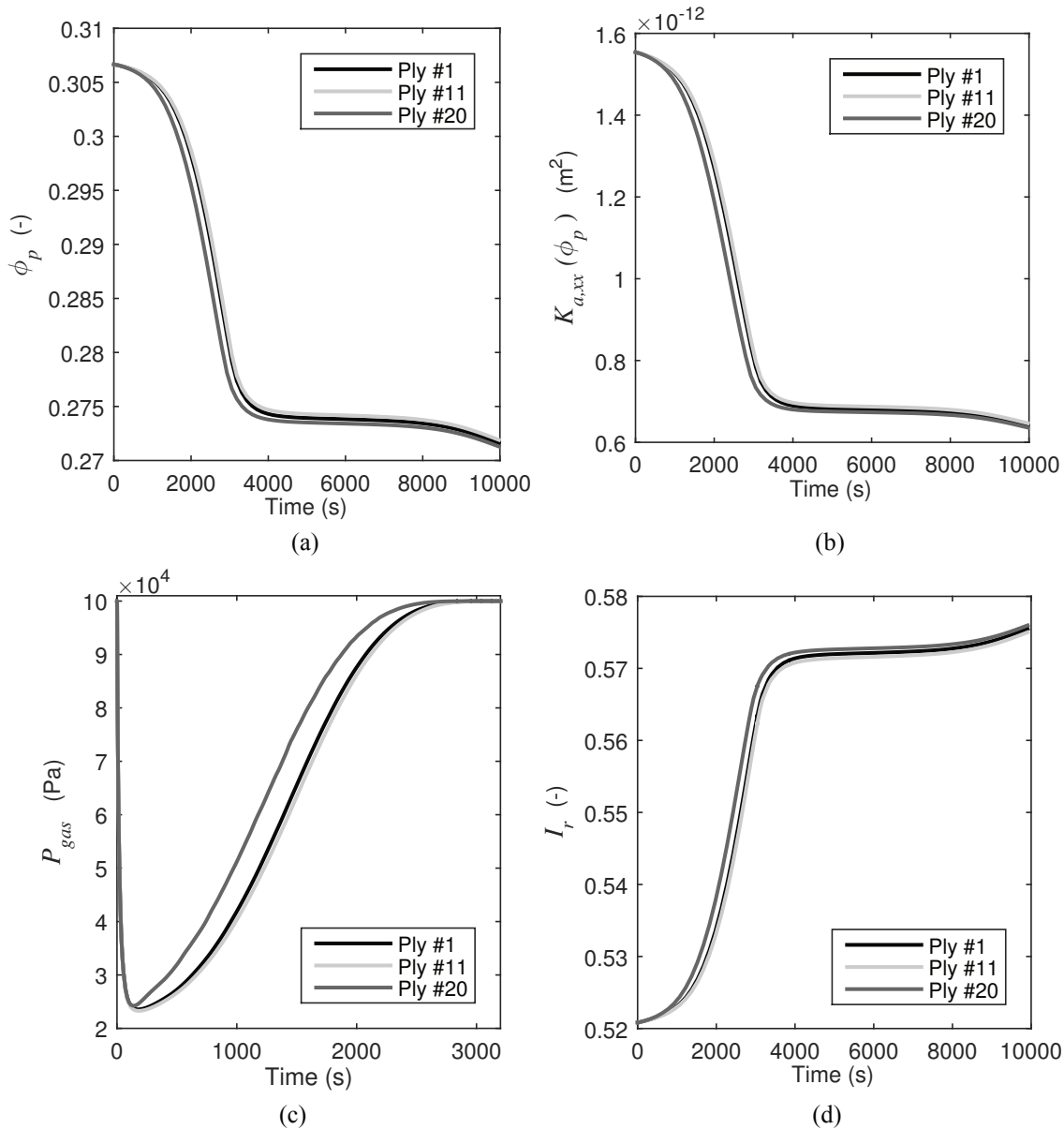


Fig. 5-18: Domain deformation and gas pressure development at three selected times

The porosity and resulting air permeability development of three plies located at the bottom (*Ply #1*), middle (*Ply #11*), and top of the part (*Ply #20*) during the cure cycle and the impact it has on the degree of impregnation is shown in Fig. 5-19.



**Fig. 5-19:** (a) Local porosity evolution in three plies located through the thickness of the part (ply #1,11, 20) (b) air permeability as a function of the local porosity evolution (c) gas pressure at the mid-span of the part (d) degree of impregnation - resin

It can be seen that the gas pressure at the top ply increases faster, due to a faster heating of the top-side of the laminate at the initial phase of the cure cycle. The ply porosity reduces faster inside *Ply #20*, as the resin flows faster, leading to a higher level of impregnation attained at the end of the 10000s. Nevertheless the final impregnation level attained in all three plies at the end of the cure cycle varies minimally, indicating limited intra-tow porosity zoning present through the thickness of the part.



### 5.5.4 Laminate Consolidation

The evolution of the part's thickness is measured experimentally at the two ends of the part with the use of two displacement sensors (see Section 5.2.3 for sensor details) during OoA processing. The thickness change is compensated to exclude tool deformations developed due to heating, while it is compared against the gas pressure (Fig. 5-20(a)) and the difference between measured and simulated temperatures at the two end of the part (Fig. 5-20(b)).

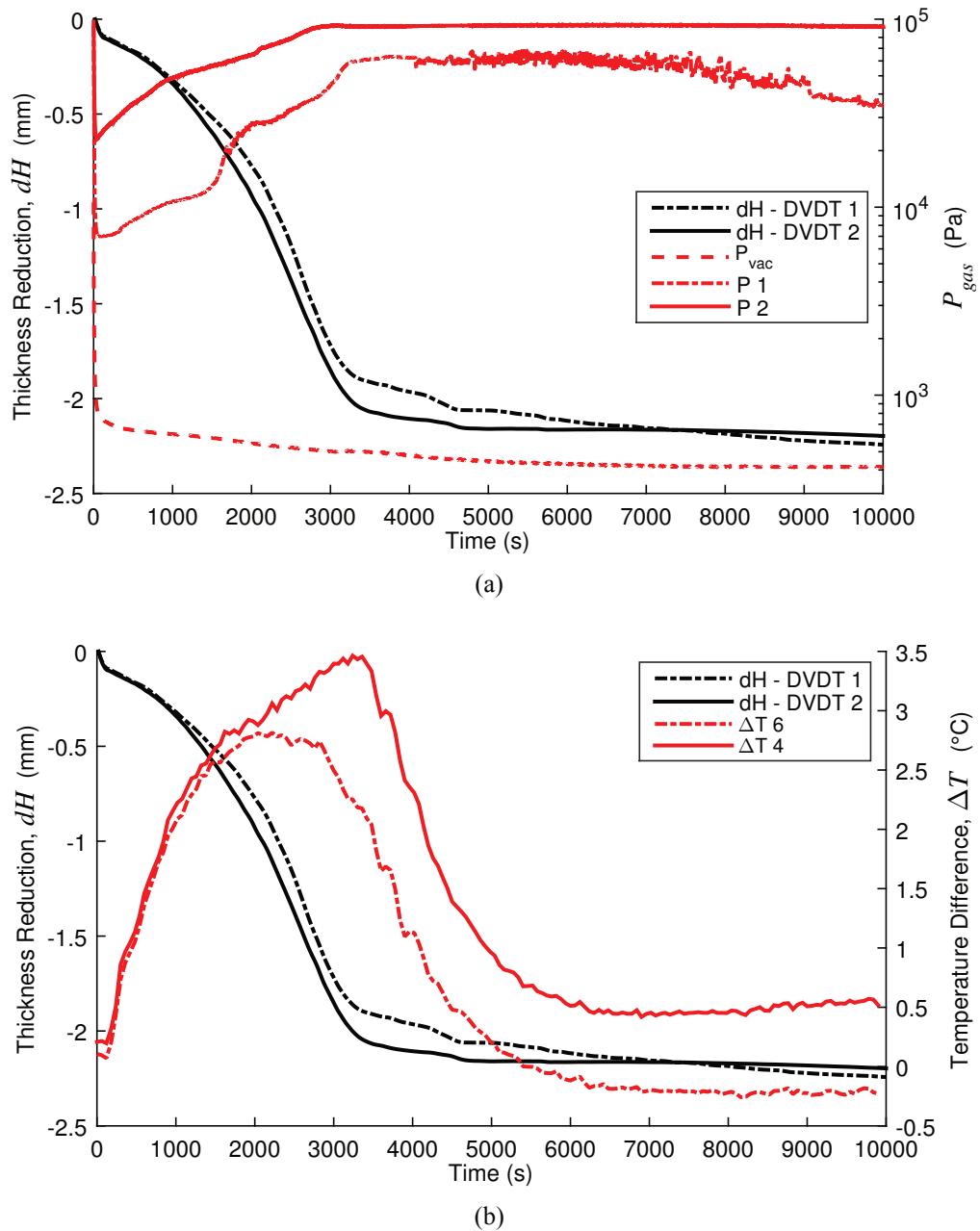


Fig. 5-20: Part thickness evolution during OoA processing plotted along (a) the pressure development and (b) the local difference between measured and simulated temperature

In Fig. 5-20 it can be seen that the maximum thickness change takes place within the first 3500-4000s, with the back side of the part (*DVDT 2*) reaching steady state first. This time closely coincides with the time the gas pressure reaches steady state in the laminate, at a pressure close to atmospheric. The most significant porosity reduction has already taken place within this time frame, as shown in Fig. 5-19 (a), where the simulated porosity evolution is depicted throughout the cure cycle. Therefore the thickness change of the laminate is reflected in the OoA simulation as the increasing difficulty of air evacuation out of the part, as shown in Fig. 5-19 (b), also confirmed by the close match of the steady state of gas pressure established at the two ends of the demonstrator within the same time. The laminate thickness reduces after processing to approximately 75% of the initial thickness of the part.

Though the part thickness reduction is initially caused by porosity reduction due to air evacuation, as the cure cycle proceeds the pressure difference applied is also born by the fibers, which leads to an increase in the fiber volume fraction. This effect has not been captured in the simulation, since the initial fiber volume fraction of both the resin and air saturated domains remains constant throughout the OoA process. This difference leads in simulating a higher resin impregnation rate than realistic, which causes a discrepancy between the simulated and measured rate of gas pressure increase, as discussed in Section 5.5.3. Furthermore the underestimation of the ply thickness and fiber volume content leads to a reduced heat transfer both in-plane, as well as through the thickness of the part, which explains the temperature difference between the measured and simulated temperatures depicted in Fig. 5-20. An exact match of the experimentally determined porosity is therefore not possible yet, due to the overestimation of the ply thickness by approximately 25 % over the course of the cure cycle and the underestimation of the fiber volume content, since the laminate consolidation is not taken into account. Though a direct comparison of the experimentally measured and simulated porosity is quantitatively not possible yet, the model can be used to determine areas of the part more prone to porosity formation due to the development of pressure and temperature gradients as well as to compare materials and cure cycles against each other.

The consolidation behavior of Out-of-Autoclave prepregs is complex, since the prepregs consist of dry and resin saturated regions which cannot be easily distinguished, particularly in the case of prepregs based on a woven fabric. To characterize the consolidation behavior of the MTM 44-1 fiber volume fraction evolution, a pressure of 1Bar ( $10^5$  Pa) is applied at different displacement rates and temperatures in a stack of 18 plies of the material. The resulting curves of the fiber volume fraction of the material as a function of the applied pressure, were utilized as a basis for the development of a phenomenological model at isothermal and non-isothermal conditions without capturing the relaxation phase, in the context of Desiree Grießl's Term Project [S3]. The model has not been implemented in the OoA simulation tool due to insufficient time after the completion of the experimental work.

## 5.6 Laminate Quality Evaluation

As a final step in the evaluation of the manufactured CFRP demonstrator, microscopic investigations are used to determine its residual porosity after cure. To investigate the impact of scaling-up the part's length on the porosity development, a 1.2m long part is manufactured with the MTM 44-1 prepreg, using the same number of plies and OoA manufacturing scheme. The global and intra-tow porosity is determined using microscopy and image analysis, while the resulting porosity at the front, middle and the back-side of both parts is compared in Fig. 5-21 and Fig. 5-22.

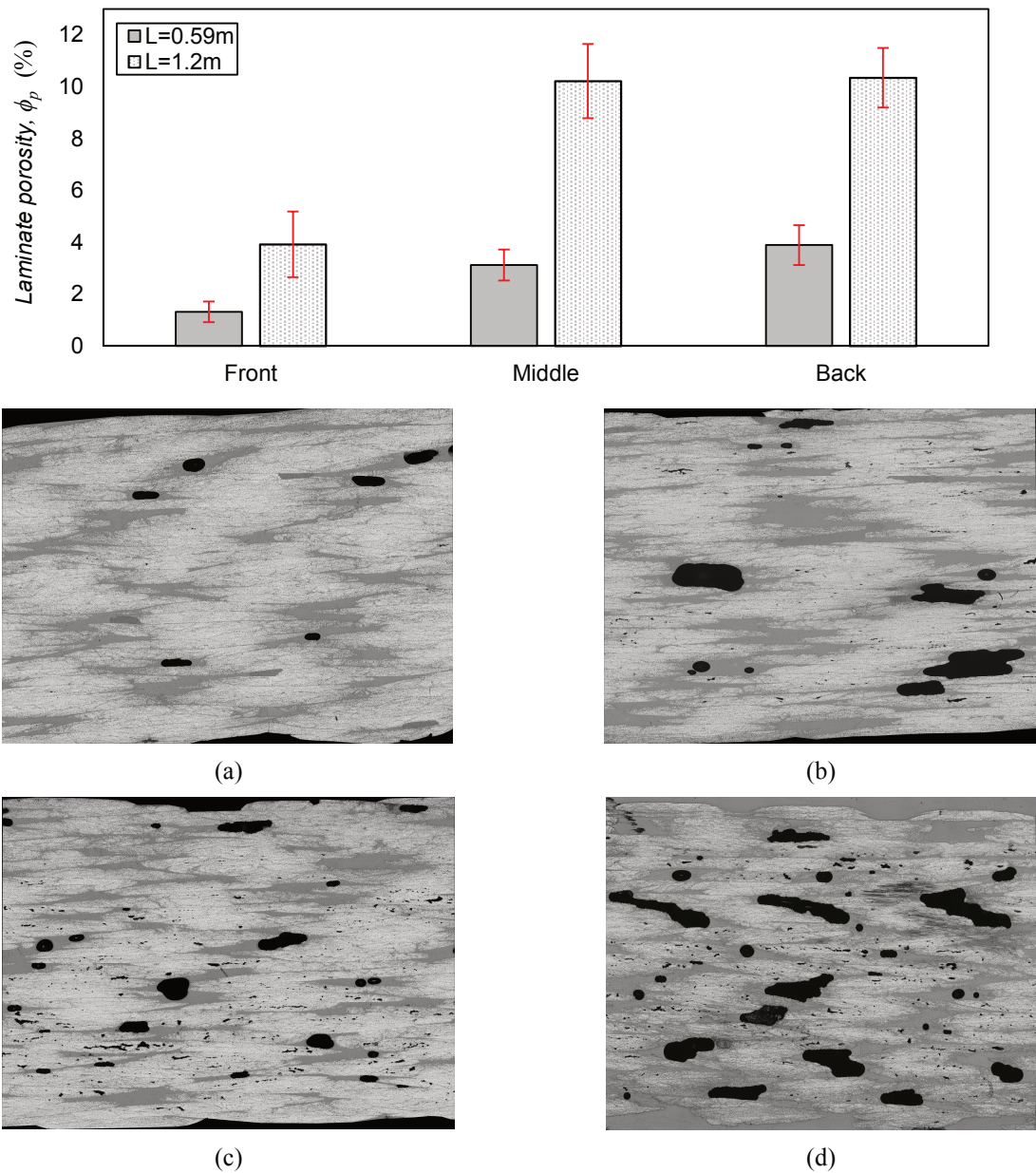
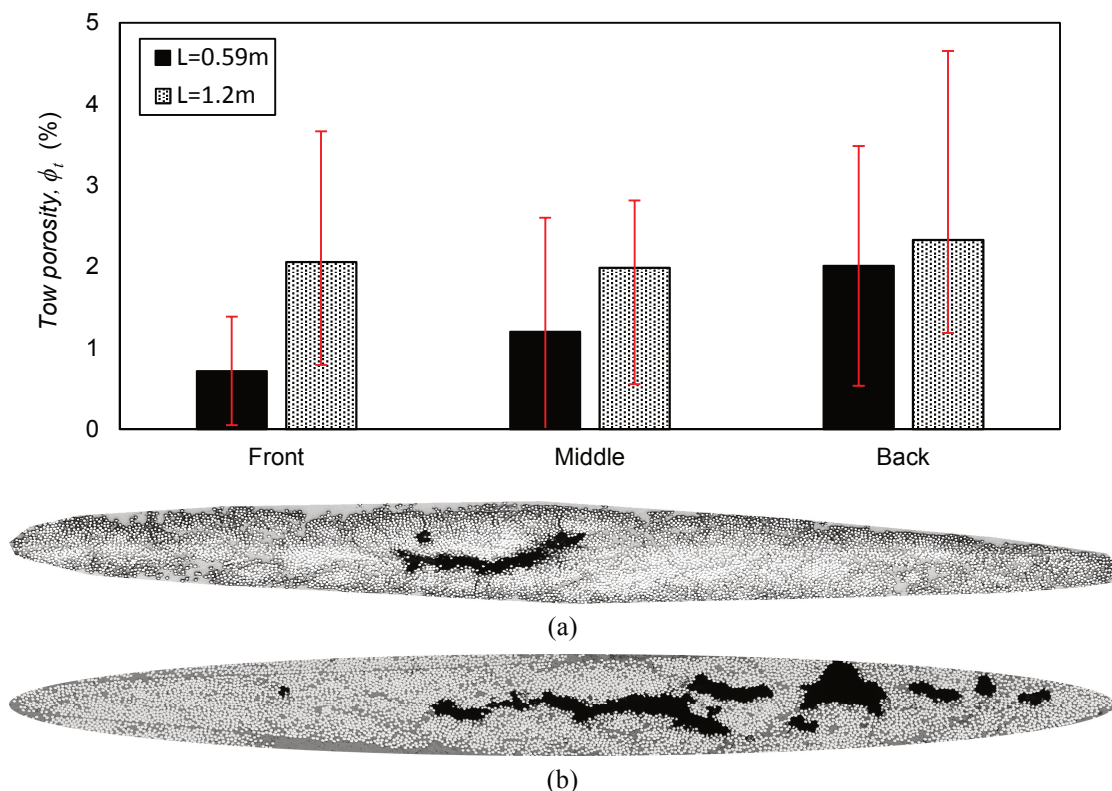


Fig. 5-21: Porosity of parts with 0.59 and 1.2m length at three locations along the part length and pictures depicting (a) front side of part with L=0.59m (b) back side of part with L=0.59m (c) front side of part with L=1.2m (d) back side of part with L=1.2m [S5]

Sections of 30mm x 30mm are cut out of the center of the part, at three locations along the length, close to the vacuum source, which are depicted in Fig. 5-21(a) and (c), at its mid-span and at the end of the part, depicted in Fig. 5-21(b) and (d). As shown in Fig. 5-21, the porosity of both parts is lower close to the vacuum source, while it increases gradually towards the back side, due to the reduced vacuum pressure measured and predicted by the OoA simulation in 5.5.4. It is also shown that doubling the part's length, leads to a non-linear increase of the porosity along the part's length since the porosity at the back side of the 1.2m long part is 2.5 times higher than that the porosity of the demonstrator part with almost half the length.

The pictures included in Fig. 5-21(a)-(d) were taken using the Olympus BX41M Reflected light microscope, using a 10x magnification at  $\pm 45^\circ$  to the fibers [S5]. The images were analyzed using image segmentation and particularly two thresholding algorithms in Image J (Fiji), after adjusting the brightness and contrast while considering their average. The total porosity is determined as the percentage of the black area in each sample, analyzed at  $\pm 45^\circ$  and  $0/90^\circ$  to the fibers. The intra-tow porosity is defined as the percentage of black area inside each tow, for three tows selected at each location. As shown in Fig. 5-22, the average and maximum intra-tow porosity increases far from the vacuum source and with increasing part length, similarly to the global porosity, although some variability is present due to the reduced measurement area of the tows.



**Fig. 5-22: Intra-tow porosity summary and indicative worst-case porosities observed at the back side of each part for (a) 0.59m long part (b) 1.2m long part**

## 5.7 Summary and Discussion

The experimentally measured temperature, gas pressure and viscosity evolution during OoA manufacturing of a monolithic demonstrator part were compared against the properties simulated in COMSOL Multiphysics. The consolidation of the laminate is not included in the simulation. The results of the prepreg domain characterization, its constituent volume fractions, the air permeability and resin viscosity (Chapter 3) are utilized as input.

As shown in Chapters 4 and 5, the temperature development inside the part during the cure cycle plays a dominating role in the distribution of the vacuum pressure as it has an influence on both the resin viscosity, the impregnation velocity of the prepreg with resin and the air density. Since OoA processing takes place solely under vacuum pressure, a close match between the measured and simulated gas pressure distribution in the material during processing is a prerequisite for an accurate depiction of the OoA physics. To achieve a close match of the real boundary conditions and the simulation, the average temperature measured via thermocouples placed at the top and bottom of the part is used as a boundary condition to model the heat transfer in the demonstrator. The temperature predicted in the mid-plane of the part is generally lower than the measured one, with an increasing difference of up to a maximum of 2.5-4°C captured at different locations during the air evacuation phase. Within this period, a significant amount of part thickness reduction is encountered, reaching up to 20% reduction of the initial thickness. The simulated temperature is underestimated since the initial thickness and fiber volume fraction of the part are maintained constant throughout the process. Once the laminate pressure reaches steady state, the difference between measured and predicted temperature is less than 1°C and therefore the temperature match attained is satisfactory. The shape of the viscosity curve and the time at minimum viscosity matches closely the shape and global minimum of the DC resistance measured up until the end of the cycle.

A very close match between the minimum simulated and the experimentally measured gas pressure is attained, considering the cycle duration and involved pressures. Shortly after a minimum pressure is reached, both the experimental and simulated pressures increase towards atmospheric pressure. This increase is the result of the interaction between the impregnation rate of the dry tow with resin and therefore locking-off the air-pathways and the direct effect of temperature on the air density and therefore the gas pressure. An accurate prediction of the material's locking-time, where no significant flow takes place, is therefore possible with the current OoA simulation capabilities. Apart from the physical properties, qualitative evaluation of the degree of impregnation and the residual porosity in the part is possible and can be used to virtually down-select materials or cure cycle. Implementing the consolidation behavior of the prepreg and incorporating the textile mesoscopic structure would assist in improving the temperature and pressure accuracy, providing a more realistic prediction of the residual porosity.





## 6 Conclusions and Outlook

Primary aim of the research presented in this thesis was the development of a virtual testing platform, which will assist in the down-selection of OoA material systems and optimum cure cycle parameters, with the ultimate goal being to enable the production of parts with minimum porosity outside the Autoclave. The simulation primarily addressed aspects related to the influence of the air evacuation and heat transfer, on the intra-tow/intra-ply porosity formation during Out-of-Autoclave manufacturing.

The contributions and most significant results of the thesis in the context of OoA simulation developments, material characterization as input for the simulation and process monitoring for model validation purposes, are highlighted in the following Sections (6.1 and 6.2). Limitations and possibilities for future work are outlined in each individual Section below. Emphasis is placed on understanding the drivers, which enable manufacturing of a porosity free monolithic part outside the Autoclave via sensitivity studies, which resulted in formulating recommendations for the improvement of the process, summarized in Section 6.3.

### 6.1 OoA Process Simulation

A toolkit of models has been developed with the aim to capture the evacuation process of air through the initially dry tows of an OoA prepreg and the influence it has on the prepreg's impregnation quality. Emphasis was placed on capturing the local gas pressure evolution in the tows and the influence it may have on the local tow impregnation with resin, at both isothermal and non-isothermal conditions. The simulation development focused on coupling the physics of transient air flow through the prepreg, on the resin flow progression at isothermal and non-isothermal conditions.

The transient air flow through the tows was explicitly modeled, with the aim to capture the instantaneous, delayed air evacuation or compromised connection to vacuum and the influence it has on the gas pressure development during OoA processing. This methodology comes as an improvement of the state-of-the-art expression developed by Arafath et al. [35], which only provides information on the lumped mass of air evacuated out of the laminate and thus cannot capture the local evolution of vacuum pressure in the tows. The impregnation state of the tows was predicted via setting the local gas pressure developed at the dry tow domain as a boundary condition for the resin flow through its thickness.

Two modeling approaches were developed in the context of this work. Initially a simplified 1.5D model was developed to predict the impregnation time of an initially dry



OoA tow at isothermal conditions. The model was implemented in Matlab using a numerical scheme with the air and resin flow weakly coupled during the air evacuation period. This model can capture the impact of the air evacuation on the resin flow (one-way coupling) via predicting the local filling time of the tow at any location, without taking into account the laminate consolidation nor the viscosity evolution due to curing. The predicted tow impregnation times were in good agreement with the analytically determined times for the instantaneous air evacuation and compromised vacuum connection. Sensitivity studies demonstrated the robustness of the proposed scheme for a wide range of time scales. A new metric, the air resistance to filling  $AR_f$  which correlates the time-scale of the tow impregnation with resin, with the characteristic time for air flow through the same tow, was proposed. This approximate relationship correlates all parameters which have an influence on the gas pressure development in the prepreg, since no analytical solution of the coupled problem is available. It can also be used in identifying the interaction potential between the air and resin flow within the tows of a prepreg, before utilizing a more complex simulation approach.

If the interaction between the flows of the two fluids (air and resin) in the prepreg is insignificant, homogeneous and fast in-plane air evacuation takes place. In this case the tow impregnation time is independent of the part's length within the range of lengths considered in this study (up to 20m). The air distribution under isothermal conditions can be described using the simplified 1.5D delayed air evacuation model, presented in Section 4.1. If there is a strong interaction between the air and resin flow time-scales, the 2D simulation developed using COMSOL Multiphysics shall be used to accurately capture the impregnation process outside the Autoclave. In this case the following features enable depicting the influence of resin flow on the gas distribution inside the material: a two-way coupling between air and resin flow, the development of a relationship which correlates the in-plane air permeability with the porosity development in the prepreg or ply (global or local) and the use of a moving front to capture the resin front propagation in each ply. Local temperature or pressure gradients may lead to a faster impregnation of the tows with resin ('locking-off'), obstructing the vacuum distribution in the material and leading to residual porosity development once gelling of the resin takes place.

A monolithic CFRP demonstrator was manufactured outside the Autoclave, as a basis for comparison between the measured and predicted temperature, pressure and viscosity development inside the part. The MTM 44-1 prepreg and properties resulting from its characterization (Chapter 3) were used in the simulation.

The temperature predicted in the mid-plane of the demonstrator during the air evacuation phase was lower than the temperature measured, by a maximum of 4°C, which was measured away from the vacuum source. Though this temperature difference is not small, it can be justified by the assumption of a constant fiber volume fraction and a part of constant thickness utilized in the simulation, since the consolidation of the material has not been captured. Within this period, a thickness reduction of up to 20% of the

initial thickness takes place, which has not been depicted in the simulation. Once the temperature and pressure reached steady state, this difference reduced to less than 1°C, providing a very good match between experimental and simulated temperatures. The shape of the viscosity curve and the time at minimum viscosity matches closely the shape and global minimum of the measured DC resistance.

The minimum gas pressure obtained via simulation shows a very good agreement with the corresponding experimental pressure along the length of the demonstrator. Shortly after the minimum pressure is reached, gradual locking of the air-pathways and the influence of the increasing temperature on the air density, lead to a raise of the gas pressure towards atmospheric pressure and therefore a ‘locking’ of the air channels. This behavior is successfully depicted in the simulation, with the predicted ply locking-time being approximately seven minutes faster than the measured time. The rate of gas pressure increase simulated is overestimated, predicting a higher gas pressure established in the laminate than the one measured. Although the initial reduction of the laminate’s thickness is assumed to be the result of porosity reduction in the air saturated domain due to air evacuation, influencing directly in the in-plane air evacuation ( $K_{a,xx}(\phi_p)$ ), as the cure cycle proceeds the pressure difference applied is also borne by the fibers. This will lead to an increase of the fiber volume fraction and therefore a slow-down of the prepreg’s impregnation velocity. This effect was obvious in the experimental measurements of the gas pressure but has not been captured in the simulation, where the initial fiber volume fraction of both the resin and air saturated domains and the ply thickness remain constant throughout the OoA process. This difference is the cause for the overestimation of the prepreg’s impregnation rate during the simulation. A good correlation between the experimentally determined and predicted porosity is not possible yet since the laminate consolidation is not taken into account, for the above-mentioned reasons. Comparative evaluation of the degree of impregnation and the residual porosity to virtually down-select materials or cure cycle parameters is nevertheless possible at this stage.

Implementing the consolidation behavior of the prepreg in the simulation will improve the accuracy of the gas pressure and temperature distribution in the part and will lead to a more realistic prediction of the residual porosity. An initial approach may involve the depiction of the compaction behavior of the prepreg as a whole, without separating the consolidation behavior of the two domains saturated with two fluids (air and resin) according to the phenomenological model developed in [S3]. Furthermore incorporating mesoscopic information of the textile structure used as a basis for the prepreg may further enhance the porosity prediction capabilities and increase the applicability of the simulation to a wider range of material systems.

Tab. 6-1 provides an overview of the quality of validation of the developed OoA simulation proposed in the context of this work.

**Tab. 6-1: OoA process simulation tool and quality of predicted outputs**

Predicted Quantities	Ranking	Prediction Quality
Gas pressure distribution at RT	+++	Close match
Min gas pressure during cure cycle	+++	Close match
Residual gas pressure far from vacuum	++	Overestimated
Temperature	++	Underestimated during heat-up
Viscosity evolution	+++	Close match
Tow locking time	+++	Close match
Porosity	+	Overestimated

## 6.2 Material Characterization, Process Monitoring and Quality Evaluation

The viscosity and cure kinetics of the MTM 44-1 resin film and the air permeability of the prepreg were characterized as input for the OoA simulation developed in the context of this work. Neither the rheokinetic properties of the resin, nor the air permeability of the MTM 44-1 prepreg have been previously characterized in the literature. All characterization methods were based on well-established techniques, adapted to the specific needs of the OoA prepreg characteristics and allowing implementation in the simulation framework. Microscopic characterization of the prepreg's structure was imperative for the development of a geometrically representative domain used as a basis for the simulation. The initial volume fractions of prepreg constituents, the mesoscopic structure of the prepreg and tow shapes and local volume fractions have been extensively characterized using optical (microscopy and  $\mu$ CT) as well as mercury porosimetry. Image segmentation was used to determine the degree of impregnation, the porosity and fiber volume fraction of the prepreg at its initial stages. The  $\mu$ CT image resolution was only sufficient to determine its porosity, while microscopy could also be used for fiber volume fraction determination. The information of the microstructure may be used to expand the simulation capabilities towards a mesoscopic fabric representation.

The transient in-plane permeability of the MTM 44-1 prepreg to air ( $K_{a,xx}$ ) was characterized for a range of porosities. Correlating a prepreg's permeability with its porosity provided the means to capture the permeability evolution of a prepreg during OoA processing, decoupling it from temperature and time evolution. The direct correlation of the air permeability with the part porosity enabled a convenient implementation of the air flow physics in the OoA simulation via decoupling the air flow from and laminate compaction. While no in-plane air permeability measurements of the MTM44-1 prepreg are available in the literature, the permeability determined in this work agrees with the permeabilities reported by Hickey et al. [37], Cender et al. [39], Arafath et al. [35] for other OoA prepreg systems. Future work shall enable a more detailed study of the MTM44-1

prepreg at high (< 30%) and low porosity contents (0-6%) to increase the confidence of the developed model in these regions. Furthermore the implementation of the effective instead of the viscous permeability including the Klinkenberg sliding effect will be beneficial at low porosity and low gas pressure levels, accompanied by a detailed quantification of the material microstructure to quantify the dimensions of the mean free path of the gas molecules in the prepreg (Klinkenberg factor – b). During OoA processing, most of the air evacuation and transient heating takes place within the first minutes of the cycle. The quality of fit between experimental and modeled resin viscosities achieved within this period and for heating rates in the range of 1-2°C/min is very good. Nevertheless, the development of a model with broader applicability and the identification of the chemical interactions responsible for the atypical, non-exponential viscosity development towards gelling will be beneficial. This will provide insights for further improvement of the fitting quality of the experimental viscosity curves for a wider range of times and heating rates. A summary of the physics and constitutive laws incorporated in the simulation are given in Tab. 6-2.

**Tab. 6-2: Review of the governing physics and constitutive laws implemented in COMSOL Multiphysics, used as a basis for the OoA simulation and suggestions for future work**

Physics	Spatial Resolution	Model	Limitation	Future work
Air flow in porous medium	1D, 2D	Darcy $K_{a,xx}(\phi_p)$	Macroscopic Accuracy at low porosity	Mesosopic
Air permeability	1D	Fifth order polynomial	Limited to $\phi_p > 6\%$	Extend applicability to $\phi_p < 6\%$
Resin flow in porous medium	1D	Darcy $K_r = \text{constant}$	Macroscopic $K_r = \text{constant}$	Mesosopic $K_{r,zz}(V_{f,p})$
Rheology	-	Kiuna et al. and Keller et al. modified for MTM 44-1	Optimized up to the gel-point and 1-2°C/min	Improve fitting quality between $n_{min}$ and $n_{gel}$
Moving resin flow-front	1D	Deformed Geometry	Movement based on $u_{rf,zz}$	Movement to be based on $\mathbf{u}_{rf}$
Heat transfer in porous medium	2D	Equilibrium model for saturated porous medium	Homogeneous fiber conductivity $k_{f,xx} = k_{f,zz}$	Inhomogeneous fiber conductivity $k_{f,xx} > k_{f,zz}$
Compaction	-	-	-	Implementation

A significant portion of this work dealt with the identification and development of methods, which enabled quantification of the impregnation state of the prepreg, either indirectly via capturing physical properties inside the laminate during processing or via imaging of the impregnation state of the material itself. The integration of pressure sensors at the bottom of the laminate, embedding thermocouples and DC resistance sensors at selected locations inside the part and measurement of the part's thickness development during manufacturing, enabled the validation of the most significant physical parameters simulated in the context of this thesis. Microscopy was used to quantify the residual porosity at the end of the cure cycle, at selected locations along the demonstrator's length. Capturing the impregnation state of the prepreg during processing was not possible using advanced imaging methods, such as  $\mu$ CT or MR, due to the large part dimensions and the resolution required to image pores in the size of a few mm down to  $\mu$ m. A common method encountered in the literature to image prepregs is the interruption of an experiment at selected times and the extraction of smaller specimens for further detailed analysis [53, 55, 58]. Though utilizing this approach would require manufacturing of several parts potentially at a range of attained vacuum levels, which adds significant variability to the process and can make direct correlation of the predicted and actual flow-front progression challenging. Cender et al. [27, 39] depicts the planar evolution of a prepreg's impregnation at the bottom of the laminate during OoA processing, which cannot capture the through thickness impregnation of the tows. Although several imaging approaches can be used to evaluate the microstructure of the part at selected times and locations of an interrupted process and quantify the residual porosity after processing, they cannot be used to validate the flow-front evolution and porosity development real-time. Therefore future work on identifying and developing methods which can depict the impregnation of large parts real-time would significantly assist the research in the field of Out-of-Autoclave processing.

### **6.3 Recommendations for Manufacturing Monolithic Parts Out-of-Autoclave**

A typical Out-of-Autoclave manufacturing cycle consists of the debulking cycle, which typically takes place at room temperature and the cure cycle, which takes place in an oven or heated tooling, under vacuum pressure. The debulking cycle is used to enable evacuation of unwanted gas and volatiles out of the prepreg, while it shall also enable the vacuum to be evenly distributed along the length of the part. To achieve this material manufacturers kept part of the OoA tows intentionally dry, nevertheless to make use of the dry network vacuum application shall not lead to 'cold flow' of resin inhibiting the gas pressure distribution. To reduce the competition between the air and resin flow through the prepreg during debulking, the material shall ensure a minimal flow of resin and a high, homogeneous air evacuation rate.

The key properties enabling efficient air evacuation and homogeneous gas pressure distribution in the prepreg are, the ratio of resin and air saturated permeability along the primary flow directions of the prepreg ( $K_{r,zz}/K_{a,xx}$ ), the ratio of in and out-of-plane permeability of the air saturated domain ( $K_{a,zz}/K_{a,xx}$ ) and the resin viscosity at debulking temperature ( $n_0$ ). Significant reduction of the out-of-plane permeability of the air saturated domain ( $K_{a,zz}$ ) leads to an in-plane air flow intensification, which subsequently enhances the distribution of gas along the part length. This effect can be further enhanced when combined with a simultaneous reduction of the out-of-plane permeability of the resin saturated domain ( $K_{r,zz}$ ), or an increase of the resin viscosity. All mentioned modifications result in reducing the impregnation speed of the prepreg with resin and provide more time for the gas distribution in the material. Nevertheless significantly increasing the resin's viscosity at room temperature, may lead to a simultaneous increase of the minimum viscosity attained during the cure cycle and therefore cause the development of inter-ply or inter-tow porosity. This should be factored-in during the development of resin systems for OoA prepregs.

Regarding the design of an OoA cure cycle, faster heating generally leads to a faster prepreg impregnation, which in combination with an intensified pressure differential close to the vacuum source results in an earlier 'locking' of the part access to vacuum. As a result the gas pressure in the material reaches atmospheric pressure, while an increased amount of air is entrapped inside the prepreg since it cannot be evacuated. A reduced heating rate promotes slower impregnation, which allows for more air to evacuate the prepreg, before it locks-off. To select the ideal heating rate for an OoA cure cycle, a balance shall be struck between a slow heating rate which will enable air to evacuate the dry tows and a fast enough heating rate, which will enable maximum impregnation before resin gelation. Uncontrolled temperature gradients may cause significant differences in the impregnation time of the various prepreg plies and develop into porosity. Nevertheless, in Section 4.2.4.4 we showed that a controlled in-plane temperature gradient on a self-heated tool with several zones, may be beneficial for porosity reduction, if the appropriate tool design and temperature heating rates are used. Positioning a colder zone close to the vacuum source is beneficial for the vacuum distribution along the part's length, though not sufficient to guarantee a porosity free part. Due to the strong interdependency between the local temperature and gas pressure development as well as the part geometry, providing general guidelines on the design of self-heated tooling which can be used for OoA manufacturing is not straight-forward. This suggests that the bagging-scheme and cure cycle or tool design defined for a particular part and material system cannot be transferred directly for producing another part geometry or using a different material system. The OoA simulation package can be used to identify the best process design, select the optimum cure cycle or oven settings or down select the most-suited material for manufacturing a part with a specific geometry.





## References

- [1] M. Rössler. *Repairs of Aircraft Composite Structures*. 1st ed, Zofingen, CH, in *flugundform*, 2015.
- [2] F. C. Campbell. *Manufacturing Processes for Advanced Composites*, Oxford, UK, in *Elsevier Advanced Technology*, 2004.
- [3] R. Paton, “Forming technology for thermoset composites,” in *Composite forming technologies*, C. A. Long, Ed, Cambridge: Woodhead Publishing Ltd. and CRC Press LLC, 2007, pp. 239–255.
- [4] S. G. Advani and E. M. Sozer. *Process modeling in composites manufacturing*. 2nd ed, USA, in *CRC Press*, 2011.
- [5] S. Mazumdar. *Composites Manufacturing: Materials, Product and Process Engineering*, Boca Raton, USA, in *CRC Press*, 2002.
- [6] P. Hubert, G. Fernlund, and A. Poursartip, “Autoclave processing for composites,” in *Manufacturing Techniques for Polymer Matrix Composites (PMCs)*, S. G. Advani and K. T. Hsiao, Eds, Cambridge, UK: Woodhead Publishing Ltd, 2012, pp. 414–434.
- [7] H. M. Hsiao and M. I. Daniel, “Effect of fiber waviness on stiffness and strength reduction of unidirectional composites under compressive loading,” *Composites Science and Technology*, vol. 56, pp. 581–593, 1996.
- [8] H. J. Chun, J. Y. Shin, and M. I. Daniel, “Effects of material and geometric nonlinearities on the tensile and compressive behavior of composite materials with fiber waviness,” *Composites Science and Technology*, vol. 61, pp. 125–134, 2001.
- [9] C. Ridgard, “Out of Autoclave composite technology for aerospace, defense and space structures,” in *Spring Symp. Proc. SAMPE '09*, Baltimore, May, 2009.
- [10] M. Skea, “No Autoclave, No Oven, No Problem!,” *Composites World Magazine*, Sep. 2014. [Online]. Available: <http://compositesmanufacturingmagazine.com/2014/08/out-of-autoclave-solutions-expand-composite-opportunities-across-market-sectors/>.
- [11] G. Gardiner, “Out of Autoclave prepregs: Hype or revolution?,” *Composites World Magazine*, Jan. 2011. [Online]. Available: <http://www.compositesworld.com/articles/out-of-autoclave-prepregs-hype-or-revolution>.
- [12] T. Kourkoutsaki, S. Comas-Cardona, K. Masania, R. K. Upadhyay, and R. Hinterhoelzl, “A process modeling toolkit developed to address scale-up challenges of Out-of-Autoclave manufacturing,” in *Techn. Conf. Proc. CAMX 2015*, Dallas, October, 2015, pp. 1–15.

- [13] S. Mortimer and M. J. Smith, "Product development for Out-of-Autoclave (O.O.A.) manufacture of aerospace structures," in *Spring Symp. Proc. SAMPE '10*, Seattle, May, 2010.
- [14] J. Schlimbach and A. Ogale, "Out-of-Autoclave curing process in polymer matrix composites," in *Manufacturing Techniques for Polymer Matrix Composites (PMCs)*, S. G. Advani and K. T. Hsiao, Eds, Cambridge, UK: Woodhead Publishing Ltd, 2012, pp. 435–480.
- [15] J. L. Kardos, "Void Growth and Dissolution," in *Processing of Composites*, R. Dave and A. C. Loos, Eds, Munich, DE: Hanser Publishers, 2000, pp. 183–206.
- [16] J. L. Kardos, M. P. Dudukovic, and R. Dave, "Void growth and resin transport during processing of thermosetting — matrix composites," in *Epoxy Resins and Composites IV*, C. Dusek, Ed, Berlin, DE: Advances in Polymer Science, Springer, 1986, pp. 101–123.
- [17] T. Centea and P. Hubert, "Measuring the impregnation of an Out-of-Autoclave prepreg by micro-CT," *Composites Science and Technology*, vol. 71, no. 5, pp. 593–599, 2011.
- [18] T. Centea, L. K. Grunenfelder, and S. R. Nutt, "A review of Out-of-Autoclave prepregs – Material properties, process phenomena, and manufacturing considerations," *Composites Part A: Applied Science and Manufacturing*, vol. 70, pp. 132–154, 2015.
- [19] T. Kourkoutsaki, S. Comas-Cardona, C. Binetruy, R. K. Upadhyay, and R. Hinterhoelzl, "The impact of air evacuation on the impregnation time of Out-of-Autoclave prepregs," *Composites Part A: Applied Science and Manufacturing*, vol. 79, pp. 30–42, 2015.
- [20] G. M. Bader, "Selection of composite materials and manufacturing routes for cost-effective performance," *Composites Part A: Applied Science and Manufacturing*, vol. 33, pp. 913–934, 2002.
- [21] T. Gutowski *et al.*, "Development of a theoretical cost model for advanced composite fabrication," *Composites Part A: Applied Science and Manufacturing*, vol. 5, no. 4, pp. 231–239, 1994.
- [22] T. Centea and S. R. Nutt, "Manufacturing cost relationships for vacuum bag-only prepreg processing," *Journal of Composite Materials*, vol. 50, no. 17, pp. 2305–2321, 2015.
- [23] S.G. Advani and K.T. Hsiao, Eds. *Manufacturing Techniques for Polymer Matrix Composites (PMCs)*, Cambridge, UK, in *Woodhead Publishing Ltd*, 2012.
- [24] M. Beck, "Composites: The final frontier," *Composites Manufacturing Magazine*, Oct. 2014. [Online]. Available: <http://compositesmanufacturingmagazine.com/2014/10/composites-key-outer-space-applications-material/>.

- [25] G. G. Bond, J. M. Griffith and G. L. Hahn, "Non-autoclave (prepreg) manufacturing technology," Boeing, Sep. 2008. [Online]. Available: <http://www.dtic.mil/get-tr-doc/pdf?AD=ADA510683>.
- [26] J. Kratz and P. Hubert, "Anisotropic air permeability in Out-of-Autoclave prepregs: Effect on honeycomb panel evacuation prior to cure," *Composites Part A: Applied Science and Manufacturing*, vol. 49, pp. 179–191, 2013.
- [27] T. A. Cender, "Resin film impregnation in fabric prepregs with dual length scale permeability," *Composites Part A: Applied Science and Manufacturing*, vol. 53, pp. 118–128, 2013.
- [28] R. Helmus, R. Hinterhoelzl, and P. Hubert, "A stochastic approach to model material variation determining tow impregnation in Out-of-Autoclave prepreg consolidation," *Composites Part A: Applied Science and Manufacturing*, vol. 77, pp. 293–300, 2015.
- [29] S. S. Tavares, V. Michaud, and Månson J.-A.E, "Assessment of semi-impregnated fabrics in honeycomb sandwich structures," *Composites Part A: Applied Science and Manufacturing*, vol. 41, no. 1, pp. 8–15, 2010.
- [30] T. Kourkoutsaki, S. Comas-Cardona, C. Binetruy, R. K. Upadhyay, and R. Hinterhoelzl, "Impact of air evacuation in Out-of-Autoclave flow and compaction modeling," in *Conf. Proc. ECCM-16*, Seville, June, 2014, pp. 1–8.
- [31] S. B. Shim and J. C. Seferis, "Thermal and air permeation properties of a carbon fiber/toughened epoxy based prepreg system," *Journal of Applied Polymer Science*, vol. 65, no. 1, pp. 5–16, Jul. 1997.
- [32] J. D. Nam and J. C. Seferis, "Gas permeation and viscoelastic deformation of prepregs in composite manufacturing processes," *Polymer Composites*, vol. 16, no. 5, pp. 370–377, 1995.
- [33] S. S. Tavares, V. Michaud, and J.-A. Månson, "Through thickness air permeability of prepregs during cure," *Composites Part A: Applied Science and Manufacturing*, vol. 40, pp. 1587–1596, 2009.
- [34] S. S. Tavares, N. Caillet-Bois, V. Michaud, and J.-A. Månson, "Non-autoclave processing of honeycomb sandwich structures: Skin through thickness air permeability during cure," *Composites Part A: Applied Science and Manufacturing*, vol. 41, pp. 646–652, 2010.
- [35] A. Arafath, G. Fernlund, and A. Poursartip, "Gas transport in prepregs: Model and permeability experiments," in *Conf. Proc. ICCM-17*, Edinburgh, July, 2009, pp. 1–10.
- [36] Y. Hou, S. Comas-Cardona, C. Binetruy, and S. Drapier, "Gas transport in fibrous media: Application to in-plane permeability measurement using transient flow," *Journal of Composite Materials*, vol. 47, no. 18, pp. 22–37, 2013.

- [37] C. Hickey, J. G. Timms, and S. Bickerton, "Compaction response and air permeability characterization of Out-of-Autoclave prepreg materials," in *Conf. Proc. FPCM-11*, Auckland, July, 2012.
- [38] T. A. Cender, P. Simacek, and S. G. Advani, "A method to determine open pore volume with pulse decay," *Applied Physics Letters*, vol. 105, no. 13, pp. 134101-1:4, 2014.
- [39] T. A. Cender, P. Simacek, and S. G. Advani, "Gas permeability of partially saturated fabrics," in *Conf. Proc. ICCM-19*, Montreal, Canada, July, 2012, pp. 1–9.
- [40] T. Shad, "Vacuum-Bag-Only processing of composites," Doctor of Philosophy, University of Southern California, Southern California, USA, 2009.
- [41] Cytec. (2013). *Lay-up and Bagging Guidelines TDS1043\_04\_13\_Issue1a. MTM 44-1 and MTM45-1 Prepregs*.
- [42] M. Brilliant, "Out-of-Autoclave manufacturing of complex shape composite laminates," M.S. thesis, McGill University, Montreal, Canada, 2010.
- [43] T. Centea and P. Hubert, "Out-of-Autoclave prepreg consolidation under deficient pressure conditions," *Journal of Composite Materials*, vol. 48, no. 16, pp. 2033–2045, 2013.
- [44] L. W. Davies, R. J. Day, D. Bond, A. Nesbitt, J. Ellis, and E. Gardon, "Effect of cure cycle heat transfer rates on the physical and mechanical properties of an epoxy matrix composite," *Composites Science and Technology*, vol. 67, no. 9, pp. 1892–1899, 2007.
- [45] L. Repecka and J. Boyd, "Vacuum-Bag-Only curable prepregs that produce void-free parts," in *Conf. Proc. SAMPE '02*, Long Beach, CA, May, 2002.
- [46] S. Lucas, S. Howard, and J. Senger, "Vacuum bag only processing: Improving prepreg out-time and porosity for large composite structure," in *Spring Symp. Proc. SAMPE '10*, Seattle, May, 2010.
- [47] J. K. Sutter, W. S. Kenner, L. Pelham, S. G. Miller, D. L. Polis, C. Nailadi, T-H. Hou, D. J. Quade, B. A. Lerch R. D. Lort; T. J. Zimmerman, J. Walker and J. Fikes, "Comparison of Autoclave and Out-of-Autoclave composites," Oct. 2011. [Online] Available: <http://ntrs.nasa.gov/achive/nasa/casi.ntrs.nasa.gov>.
- [48] J. Kratz and P. Hubert, "Processing out-of-autoclave honeycomb structures: Internal core pressure measurements," *Composites Part A: Applied Science and Manufacturing*, vol. 42, no. 8, pp. 1060–1065, 2011.
- [49] J. Kratz and P. Hubert, "Vacuum bag only co-bonding prepreg skins to aramid honeycomb core. Part I. Model and material properties for core pressure during processing," *Composites Part A: Applied Science and Manufacturing*, vol. 72, pp. 228–238, 2015.

- [50] J. Kratz and P. Hubert, "Vacuum-bag-only co-bonding prepreg skins to aramid honeycomb core. Part II. In-situ core pressure response using embedded sensors," *Composites Part A: Applied Science and Manufacturing*, vol. 72, pp. 219–227, 2015.
- [51] T.-H. Hou, J. M. Baughman, T. J. Zimmerman, J. K. Sutter, and J. M. Gardner, "Evaluation of sandwich structure bonding in Out-of-Autoclave processing," in *Fall Techn. Conf. Proc. SAMPE '10*, Salt Lake City, October, 2010.
- [52] S. Anandan, S. Nagarjan, K. Bheemreddy, K. Chandrashekhara, D. Pfitzinger, and N. Phan, "Performance evaluation of Out-of-Autoclave sandwich structures with K-COR and Nomex core," *Journal of Multifunctional Composites*, vol. 2, no. 1, pp. 45–53, 2014.
- [53] L. Farhang and G. Fernlund, "Void evolution and gas transport during cure in Out-of-Autoclave prepreg laminates," in *Conf. Proc. SAMPE '11*, Long Beach, May, 2011, pp. 1153: 1–12.
- [54] L. K. Grunenfelder and S. R. Nutt, "Void formation in composite prepregs – Effect of dissolved moisture," *Composites Science and Technology*, vol. 70, no. 16, pp. 2304–2309, 2010.
- [55] J. Kay and G. Fernlund, "Processing conditions and voids in Out of Autoclave prepregs," in *Conf. Proc. SAMPE '12*, Baltimore, May, 2012.
- [56] L. K. Grunenfelder and S. R. Nutt, "Air removal in VBO prepreg laminates: Effects of breathe-out distance and direction," in *Conf. Proc. SAMPE Tech '43*, Fort Worth, TX, May, 2011.
- [57] T. Centea and P. Hubert, "Modelling the effect of material properties and process parameters on tow impregnation in Out-of-Autoclave prepregs," *Composites Part A: Applied Science and Manufacturing*, vol. 43, no. 9, pp. 1505–1513, 2012.
- [58] J. Kay, L. Farhang, K. Hsiao, and G. Fernlund, "Effect of process conditions on porosity in Out of Autoclave prepreg laminates," in *Conf. Proc. ICCM-18*, Jeju Island, August, 2011.
- [59] L. K. Grunenfelder, T. Centea, P. Hubert, and S. R. Nutt, "Effect of room-temperature out-time on tow impregnation in an Out-of-Autoclave prepreg," *Composites Part A: Applied Science and Manufacturing*, vol. 45, pp. 119–126, 2013.
- [60] S. Hernández, F. Sket, J. M. Molina-Aldareguia, C. González, and J. LLorca, "Effect of curing cycle on void distribution and interlaminar shear strength in polymer-matrix composites," *Composites Science and Technology*, vol. 71, no. 10, pp. 1331–1341, 2011.
- [61] S. Hernández, F. Sket, C. González, and J. LLorca, "Optimization of curing cycle in carbon fiber-reinforced laminates: Void distribution and mechanical properties," *Composites Science and Technology*, vol. 85, pp. 73–82, 2013.

- [62] B. W. Grimsley, J. K. Sutter, G. D. Dixon and S. S. Smeltzer, "Elevated temperature notched compression performance of Out of Autoclave processed composites," NASA Technical Reports, 2014. [Online]. Available: <http://ntrs.nasa.gov/20140003159.pdf>.
- [63] S. Kellas, B. A. Lerch and N. Wilmoth, "Mechanical characterization of in- and Out-of-Autoclave cured composite panels for large launch vehicles," NASA Technical Reports, Jun. 2012. [Online]. Available: <http://ntrs.nasa.gov/archive/nasa/casi.ntrs.nasa.gov/20120009342.pdf>.
- [64] P. Czarnocki and K. Czajkowska, "Delamination resistance of laminate made with VBO MTM46/HTS prepreg," *Acta Mechanica et Automatica*, vol. 9, no. 3, pp. 173–177, 2015.
- [65] M. Suhot and A. R. Chambers, "The effect of voids on the flexural fatigue performance of unidirectional carbon fibre composites," in *Conf. Proc. ICCM-16*, Kyoto, Japan, July, 2007, pp. 1–10.
- [66] V. Michaud and A. Mortensen, "Infiltration processing of fibre reinforced composites: governing phenomena," *Composites Part A: Applied Science and Manufacturing*, vol. 32, no. 8, pp. 981–996, 2001.
- [67] K. M. Pillai and S. G. Advani, "A model for unsaturated flow in woven fiber preforms during mold filling in resin transfer molding," *Journal of Composite Materials*, vol. 32, no. 19, pp. 1753–1783, 1998.
- [68] P. Simacek and S. G. Advani, "A numerical model to predict fiber tow saturation during liquid composite molding," *Composites Science and Technology*, vol. 63, no. 12, pp. 1725–1736, 2003.
- [69] J. M. Lawrence, V. Neacsu, and S. G. Advani, "Modeling the impact of capillary pressure and air entrapment on fiber tow saturation during resin infusion in LCM," *Composites Part A: Applied Science and Manufacturing*, vol. 40, no. 8, pp. 1053–1064, 2009.
- [70] B. Gourichon, C. Binetruy, and P. Krawczak, "A new numerical procedure to predict dynamic void content in liquid composite molding," *Composites Part A: Applied Science and Manufacturing*, vol. 37, no. 11, pp. 1961–1969, 2006.
- [71] B. Gourichon, M. Deléglise, C. Binetruy, and P. Krawczak, "Dynamic void content prediction during radial injection in liquid composite molding," *Composites Part A: Applied Science and Manufacturing*, vol. 39, no. 1, pp. 46–55, 2008.
- [72] J. Schell, M. Deleglise, C. Binetruy, P. Krawczak, and P. Ermanni, "Numerical prediction and experimental characterisation of meso-scale-voids in liquid composite moulding," *Composites Part A: Applied Science and Manufacturing*, vol. 38, no. 12, pp. 2460–2470, 2007.



- [73] P. Simacek, V. Neacsu, and S. G. Advani, "A phenomenological model for fiber tow saturation of dual scale fabrics in liquid composite molding," *Polymer Composites*, vol. 31, no. 11, pp. 1881–1889, 2010.
- [74] Y. Wang and S. M. Grove, "Modelling microscopic flow in woven fabric reinforcements and its application in dual-scale resin infusion modelling," *Composites Part A: Applied Science and Manufacturing*, vol. 39, no. 5, pp. 843–855, 2008.
- [75] Y. Wang, M. Moatamedi, and S. M. Grove, "Continuum dual-scale modeling of liquid composite molding processes," *Journal of Reinforced Plastics and Composites*, vol. 28, no. 12, pp. 1469–1484, 2009.
- [76] A. Babeau, S. Comas-Cardona, C. Binetruy, and G. Orange, "Modeling of heat transfer and unsaturated flow in woven fiber reinforcements during direct injection-pultrusion process of thermoplastic composites," *Composites Part A: Applied Science and Manufacturing*, vol. 77, pp. 310–318, 2015.
- [77] H. Tan and K. M. Pillai, "Fast liquid composite molding simulation of unsaturated flow in dual-scale fiber mats using the imbibition characteristics of a fabric-based unit cell," *Polym Compos*, vol. 31, no. 10, pp. 1790–1807, 2010.
- [78] H. Tan and K. M. Pillai, "Multiscale modeling of unsaturated flow in dual-scale fiber preforms of liquid composite molding III: Reactive Flows," *Composites Part A: Applied Science and Manufacturing*, vol. 43, no. 1, pp. 29–44, 2012.
- [79] H. Tan and K. M. Pillai, "Multiscale modeling of unsaturated flow in dual-scale fiber preforms of liquid composite molding I: Isothermal flows," *Composites Part A: Applied Science and Manufacturing*, vol. 43, no. 1, pp. 1–13, 2012.
- [80] H. Tan and K. M. Pillai, "Multiscale modeling of unsaturated flow of dual-scale fiber preform in liquid composite molding II: Non-isothermal flows," *Composites Part A: Applied Science and Manufacturing*, vol. 43, no. 1, pp. 14–28, 2012.
- [81] S.G. Advani, Ed. *Governing equations for flow through stationary fiber beds. Flow and Rheology in Polymeric Composites Manufacturing*, Amsterdam, NL, in Elsevier, 1994.
- [82] C. L. Tucker III and R. B. Dessenberger, "Governing equations for flow and heat transfer in stationary fibre beds," in *Governing equations for flow through stationary fiber beds. Flow and Rheology in Polymeric Composites Manufacturing*, S. G. Advani, Ed, Amsterdam, NL: Elsevier, 1994.
- [83] S. Whitaker, "Flow in porous media I: A theoretical derivation of Darcy's law," *Transport in Porous Media*, vol. 1, pp. 3–25, 1986.
- [84] H. Darcy. *Les Fontaines Publiques de la Ville de Dijon. Exposition et Application a Suivre et des Formules a Employer dans les Question de Distribution d'Eau*, Paris, FR, in Victor Dalmont, 1856.



- [85] M. V. Brusckhe and S. G. Advani, "A finite element/control volume approach to mold filling in anisotropic porous media," *Polymer Composites*, vol. 11, pp. 398–405, 1990.
- [86] P. Simacek and S. G. Advani, "Desirable features in mold filling simulations for liquid composite molding processes," *Polymer Composites*, vol. 25, no. 4, pp. 355–367, 2004.
- [87] A. W. Chan and R. J. Morgan, "Tow impregnation during resin transfer molding of bi-directional nonwoven fabrics," *Polymer Composites*, vol. 14, no. 4, pp. 335–340, 1993.
- [88] H. C. Stadtfeld, M. Erninger, S. Bickerton, and S. G. Advani, "An experimental method to continuously measure permeability of fiber preforms as function of fiber volume fraction," *Journal of Reinforced Plastics and Composites*, vol. 21, no. 10, pp. 879–899, 2002.
- [89] C. Binetruy, B. Hilaire, and J. Pabiot, "Tow impregnation model and void formation mechanisms during RTM," *Journal of Composite Materials*, vol. 32, no. 3, pp. 223–245, 1998.
- [90] S. G. Advani, M. V. Brusckhe, and R. S. Parnas, "Resin transfer molding flow phenomena in polymeric composites," in *Flow and Rheology in Polymer Composites Manufacturing*, S. G. Advani, Ed, Amsterdam, NL: Elsevier Science B.V, 1994.
- [91] C. Binetruy, B. Hilaire, and J. Pabiot, "The interactions between flows occurring inside and outside fabric tows during RTM," *Composites Science and Technology*, vol. 57, pp. 587–596, 1997.
- [92] K. M. Pillai and M. S. Munagavalasa, "Governing equations for unsaturated flow through woven fiber mats. Part 2. Non-isothermal reactive flows," *Composites Part A: Applied Science and Manufacturing*, vol. 35, no. 4, pp. 403–415, 2004.
- [93] R. S. Parnas, K. M. Fly, and Dal-Favero M.E, "A permeability database for composites manufacturing," *Polymer Composites*, vol. 18, no. 5, pp. 623–633, 1997.
- [94] T. Sadiq, S. G. Advani, and R. S. Parnas, "Experimental investigation of transverse flow through aligned cylinders," *International Journal of Multiphase Flow*, vol. 21, no. 5, pp. 755–774, 1995.
- [95] Y. de Parseval, K. M. Pillai, and S. G. Advani, "A simple model for the variation of permeability due to partial saturation in dual scale porous media," *Transport in Porous Media*, vol. 27, pp. 243–264, 1997.
- [96] H. Tan, T. Roy, and K. M. Pillai, "Variations in unsaturated flow with flow direction in resin transfer molding: An experimental investigation," *Composites Part A: Applied Science and Manufacturing*, vol. 38, no. 8, pp. 1872–1892, 2007.

- [97] R. Matsuzaki, D. Seto, A. Todoroki, and Y. Mizutani, "Void formation in geometry–anisotropic woven fabrics in resin transfer molding," *Advanced Composite Materials*, vol. 23, no. 2, pp. 99–114, 2013.
- [98] M. Nordlund and V. Michaud, "Dynamic saturation curve measurement for resin flow in glass fibre reinforcement," *Composites Part A: Applied Science and Manufacturing*, vol. 43, no. 3, pp. 333–343, 2012.
- [99] H. S. Sas, E. B. Wurtzel, P. Simacek, and S. G. Advani, "Effect of relative ply orientation on the through-thickness permeability of unidirectional fabrics," *Composites Science and Technology*, vol. 96, pp. 116–121, 2014.
- [100] P. Simacek and S. G. Advani, "Permeability model for a woven fabric," *Polymer Composites*, vol. 17, no. 6, 1996.
- [101] N. D. Ngo and K. K. Tamma, "Microscale permeability predictions of porous fibrous media," *International Journal of Heat and Mass Transfer*, vol. 44, no. 16, pp. 3135–3145, 2001.
- [102] J. Wolfrath, V. Michaud, A. Modaressi, and J.-A. Manson, "Unsaturated flow in compressible fibre preforms," *Composites Part A: Applied Science and Manufacturing*, vol. 37, no. 6, pp. 881–889, 2006.
- [103] J. Bréard, A. Saouab, and G. Bouquet, "Numerical simulation of void formation in LCM," *Composites Part A: Applied Science and Manufacturing*, vol. 34, no. 6, pp. 517–523, 2003.
- [104] T. G. Gutowski. *Advanced Composites Manufacturing*, New York, USA, in *John Wiley & Sons Inc*, 1997.
- [105] R. Dave, J. L. Kardos, and M. P. Dudukovic, "A model for resin flow during composite processing: Part 1 - General mathematical development," *Polymer Composites*, vol. 8, no. 1, pp. 29–38, 1997.
- [106] S. Comas-Cardona, P. Le Grogneq, C. Binetruy, and P. Krawczak, "Unidirectional compression of fibre reinforcements. Part 1: A non-linear elastic-plastic behaviour," *Composites Science and Technology*, vol. 67, no. 3-4, pp. 507–514, 2007.
- [107] M. A. Biot, "Theory of elasticity and consolidation for a porous anisotropic solid," *Journal of Applied Physics*, vol. 26, no. 2, pp. 182–185, 1955.
- [108] J. Bear. *Dynamics of Fluids in Porous Media*, New York, USA, in *Dover Publications Inc*, 1972.
- [109] B. Chen, E. J. Lang, and T.-W. Chou, "Experimental and theoretical studies of fabric compaction behavior in resin transfer molding," *Materials Science and Engineering: A*, vol. 317, no. 1-2, pp. 188–196, 2001.

- [110] Z.-R. Chen and L. Ye, "A micromechanical compaction model for woven fabric preforms. Part II: Multilayer," *Composites Science and Technology*, vol. 66, no. 16, pp. 3263–3272, 2006.
- [111] T. G. Gutowski and G. Dillon, "The elastic deformation of lubricated carbon fiber bundles: Comparison of theory and experiments," *Journal of Composite Materials*, vol. 26, no. 16, pp. 2330–2347, 1992.
- [112] R. Dave, J. L. Kardos, and M. P. Dudukovic, "A model for resin flow during composite processing: Part 2 - Numerical analysis for unidirectional graphite/epoxy laminates," *Polymer Composites*, vol. 8, no. 2, pp. 123–132, 1997.
- [113] R. Dave, "A unified approach to modeling resin flow during composite processing," *Journal of Composite Materials*, vol. 24, pp. 22–41, 1990.
- [114] W. A. Walbran, B. Verleye, S. Bickerton, and P. A. Kelly, "Prediction and experimental verification of normal stress distributions on mould tools during liquid composite moulding," *Composites Part A: Applied Science and Manufacturing*, vol. 43, no. 1, pp. 138–149, 2012.
- [115] Q. Govignon, S. Bickerton, and P. A. Kelly, "Simulation of the reinforcement compaction and resin flow during the complete resin infusion process," *Composites Part A: Applied Science and Manufacturing*, vol. 41, no. 1, pp. 45–57, 2010.
- [116] F. Robitaille and R. Govin, "Compaction of textile reinforcements for composites manufacturing. I: Review of experimental results," *Polymer Composites*, vol. 18, no. 2, pp. 198–216, 1998.
- [117] J. Merotte, P. Simacek, and S. G. Advani, "Flow analysis during compression of partially impregnated fiber preform under controlled force," *Composites Science and Technology*, vol. 70, no. 5, pp. 725–733, 2010.
- [118] S. Comas-Cardona, C. Binetruy, and P. Krawczak, "Unidirectional compression of fibre reinforcements. Part 2: A continuous permeability tensor measurement," *Composites Science and Technology*, vol. 67, no. 3-4, pp. 638–645, 2007.
- [119] N. Pearce and J. Summescales, "The compressibility of a reinforcement fabric," *Composites Manufacturing*, vol. 6, no. 1, pp. 15–21, 1995.
- [120] C. M. Hickey, "The influence of variation in process parameters on the manufacturing of advanced fibre composites," Doctor of Philosophy in Mechanical Engineering, Department of Mechanical Engineering, The University of Auckland, Auckland, New Zealand, 2014.
- [121] R. A. Saunders, C. Lekakou, and G. M. Bader, "Compression and microstructure of fibre plain woven cloths in the processing of polymer composites," *Composites Part A: Applied Science and Manufacturing*, vol. 29A, pp. 443–454, 1998.

- [122] D. J. Lukaszewicz and K. Potter, "Through-thickness compression response of uncured prepreg during manufacture by automated layup," *Proceedings of the Institution of Mechanical Engineers, Part B: Journal of Engineering Manufacture*, vol. 226, no. 2, pp. 193–202, 2012.
- [123] V. Michaud, R. Tornqvist, and J.-A. E. Månson, "Impregnation of compressible fiber mats with a thermoplastic resin. Part II: Experiments," *Journal of Composite Materials*, vol. 35, no. 13, pp. 1174–1200, 2001.
- [124] P. Hubert and A. Poursartip, "A method for the direct measurement of the fibre bed compaction curve of composite prepreps," *Composites Part A: Applied Science and Manufacturing*, vol. 32, no. 2, pp. 179–187, 2001.
- [125] A. C. Loos and G. S. Springer, "Curing of epoxy matrix composites," *Journal of Composite Materials*, vol. 17, no. 2, pp. 135–169, 1983.
- [126] P. Hubert, R. Vaziri, and A. Poursartip, "A two-dimensional flow model for the process simulation of complex shape composite laminates," *International Journal for Numerical Methods in Engineering*, vol. 44, pp. 1–26, 1999.
- [127] P. Hubert and A. Poursartip, "A review of flow and compaction modelling relevant to thermoset matrix laminate processing," *Journal of Reinforced Plastics and Composites*, vol. 17, no. 4, pp. 286–318, 1998.
- [128] N. Correia, F. Robitaille, A. C. Long, C. D. Rudd, P. Simacek, and S. G. Advani, "Analysis of the vacuum infusion moulding process: I. Analytical formulation," *Composites Part A: Applied Science and Manufacturing*, vol. 36, pp. 1645–1656, 2005.
- [129] F. Klunker, Aranda S.; Ziegmann G.; Fideu P.; Baisch P, "Permeability and compaction models for non-crimp fabrics to perform 3D filling simulations of vacuum assisted resin infusion," in *Conf. Proc. FPCM-9*, Montreal, Canada, July, 2008.
- [130] V. Michaud and J.-A. Månson, "Impregnation of compressible fiber mats with a thermoplastic resin. Part I: Theory," *Journal of Composite Materials*, vol. 35, no. 13, pp. 1150–1173, 2001.
- [131] J. Sommer and A. Mortensen, "Forced unidirectional infiltration of deformable porous media," *Journal of Fluid Mechanics*, vol. 311, pp. 193–217, 1996.
- [132] R. Helmus, T. Centea, P. Hubert, and R. Hinterhoelzl, "Out-of-autoclave prepreg consolidation: Coupled air evacuation and prepreg impregnation modeling," *Journal of Composite Materials*, pp. 1–11, 2015.
- [133] J. Wolfrath, V. Michaud, and J.-A. Månson, "Deconsolidation in glass mat thermoplastic composites: Analysis of the mechanisms," *Composites Part A: Applied Science and Manufacturing*, vol. 36, no. 12, pp. 1608–1616, 2005.

- [134] R. Larsson, M. Rouhi, and M. Wysocki, “Free surface flow and preform deformation in composites manufacturing based on porous media theory,” *European Journal of Mechanics - A/Solids*, vol. 31, no. 1, pp. 1–12, 2012.
- [135] M. Wysocki and R. Larsson, “Modelling multiple scales in composites manufacturing,” in *Conf. Proc. FPCM-10*, Ascona, CH, July, 2014.
- [136] M. S. Rouhi, M. Wysocki, and R. Larsson, “Modeling of coupled dual-scale flow–deformation processes in composites manufacturing,” *Composites Part A: Applied Science and Manufacturing*, vol. 46, pp. 108–116, 2013.
- [137] R. Larsson, M. Wysocki, and S. Toll, “Process-modeling of composites using two-phase porous media theory,” *European Journal of Mechanics - A/Solids*, vol. 23, no. 1, pp. 15–36, 2004.
- [138] P. C. Carman, “Fluid flow through granular beds,” *Transactions of the Institution of Chemical Engineers*, vol. 15, pp. 155–166, 1937.
- [139] S. Sharma and A. D. Siginer, “Permeability measurement methods in porous media of fiber reinforced composites,” *Applied Mechanics Reviews*, vol. 63, pp. 020802-1:19, 2010.
- [140] B. R. Gebart, “Permeability of unidirectional reinforcements for RTM,” *Journal of Composite Materials*, vol. 26, no. 8, pp. 1100–1133, 1992.
- [141] H. L. Liu and W. R. Hwang, “Permeability prediction of fibrous porous media with complex 3D architectures,” *Composites Part A: Applied Science and Manufacturing*, vol. 43, no. 11, pp. 2030–2038, 2012.
- [142] X. Zeng, A. Endruweit, L. P. Brown, and A. C. Long, “Numerical prediction of in-plane permeability for multilayer woven fabrics with manufacture-induced deformation,” *Composites Part A: Applied Science and Manufacturing*, vol. 77, pp. 266–274, 2015.
- [143] E. E. Swery, “Numerical predictions of fibre preform permeability for enhanced process modelling of advanced composite Structures,” Doctor of Philosophy, Centre for Advanced Composite Materials, The University of Auckland, New Zealand, 2015.
- [144] N. Vernet *et al.*, “Experimental determination of the permeability of engineering textiles: Benchmark II,” *Composites Part A: Applied Science and Manufacturing*, vol. 61, pp. 172–184, 2014.
- [145] P. Ouagne and J. Bréard, “Continuous transverse permeability of fibrous media,” *Composites Part A: Applied Science and Manufacturing*, vol. 41, no. 1, pp. 22–28, 2010.

- [146] M. J. Buntain and S. Bickerton, "Compression flow permeability measurement: a continuous technique," *Composites Part A: Applied Science and Manufacturing*, vol. 34, no. 5, pp. 445–457, 2003.
- [147] E. E. Swery *et al.*, "Efficient experimental characterisation of the permeability of fibrous textiles," *Journal of Composite Materials*, vol. 50, no. 28, pp. 4023–4038, 2016.
- [148] V. Calado and S. G. Advani, "Thermoset resin cure and rheology," in *Processing of Composites*, R. Dave and A. C. Loos, Eds, Munich, DE: Hanser Publishers, 2000, pp. 32–107.
- [149] S. Shim, W. Lee, and J. Jang, "DSC cure studies of high performance epoxy resins II. The reaction with HPT curing agent from isothermal experiment," *Polymer Journal*, vol. 21, no. 7, pp. 911–916, 1991.
- [150] S. Shim, W. Lee, and J. Jang, "DSC cure studies of high performance epoxy resins I. The reaction with 4,4'-Diaminodiphenyl Sulfone (DDS)," *Polymer Journal*, vol. 23, no. 7, pp. 903–910, 1991.
- [151] T. Hatakeyama and F. X. Quinn. *Thermal Analysis*, Northampton, UK, in *John Wiley & Sons Inc*, 1994.
- [152] T. A. Osswald and N. Rudolph. *Polymer Rheology: Fundamentals and Applications*, Munich, DE, in *Hanser Publications*, 2015.
- [153] J. M. Kenny, "Application of modeling to the control and optimization of composites processing," *Composite Structures*, vol. 27, no. 1-2, pp. 129–139, 1994.
- [154] T. Kourkoutsaki, E. Logakis, I. Kroutilova, L. Matejka, J. Nedbal, and P. Pissis, "Polymer dynamics in rubbery epoxy networks/polyhedral oligomeric silsesquioxanes nanocomposites," *Journal of Applied Polymer Science*, vol. 113, no. 4, pp. 2569–2582, 2009.
- [155] M. L. Williams, R. F. Landel, and J. D. Ferry, "The temperature dependence of relaxation mechanisms in amorphous polymers and other glass-forming liquids," *Journal of the American Chemical Society*, vol. 77, pp. 3701–3707, 1955.
- [156] P. I. Karkanias and I. K. Partridge, "Cure modeling and monitoring of epoxy/amine resin systems II. Network formation and chemoviscosity modeling," *Journal of Applied Polymer Science*, vol. 77, no. 10, pp. 2178–2188, 2000.
- [157] J. M. Castro and C. W. Macosko, "Kinetics and rheology of typical polyurethane reaction molding systems," *Society of Plastics Engineering Tech. Papers*, vol. 26, p. 434, 1980.
- [158] L. Khoun, T. Centea, and P. Hubert, "Characterization methodology thermoset resins for the processing of composite materials - Case study: CYCOM 890RTM



- epoxy resin,” *Journal of Composite Materials*, vol. 44, no. 11, pp. 1397–1415, 2010.
- [159] J. Kratz, K. Hsiao, G. Fernlund, and P. Hubert, “Thermal models for MTM45-1 and Cycom 5320 out-of-autoclave prepreg resins,” *Journal of Composite Materials*, vol. 47, no. 3, pp. 341–352, 2013.
- [160] M. A. Stolin, A. Malkin, and A. G. Merzhanov, “Non isothermal phenomena in polymer engineering and science: A Review. Part II: Non isothermal phenomena in polymer deformation,” *Polymer Engineering and Science*, vol. 19, no. 15, pp. 1074–1080, 1979.
- [161] C. A. May, M. R. Dusi, J. S. Fritzen, D. K. Hadad, M. G. Maximovich, and Thrasher, K.G. and Wereta, A. Jr, “Process Automation: A rheological and chemical overview of thermoset curing,” in *ACS Symposium Series, Chemorheology of Thermosetting Polymers*, C. A. May, Ed, Washington, DC, USA: American Chemical Society, 1983, pp. 1–24.
- [162] M. B. Roller, “Characterization of the time-temperature-viscosity behavior of curing b-staged epoxy resin,” *Polymer Engineering and Science*, vol. 15, no. 6, pp. 406–414, 1975.
- [163] Q. Fontana, “Viscosity: thermal history treatment in resin transfer moulding process modelling,” *Composites Part A: Applied Science and Manufacturing*, vol. 29, no. 1-2, pp. 153–158, 1998.
- [164] N. Kiuna, C. Lawrence, Q. Fontana, P. D. Lee, T. Selerland, and P. Spelta, “A model for resin viscosity during cure in the resin transfer moulding process,” *Composites Part A: Applied Science and Manufacturing*, vol. 33, pp. 1497–1503, 2002.
- [165] A. Keller, K. Masania, A. C. Taylor, and C. Dransfeld, “Fast-curing epoxy polymers with silica nanoparticles: Properties and rheo-kinetic modelling,” *J Mater Sci*, vol. 51, no. 1, pp. 236–251, 2016.
- [166] M. R. Dusi, C. A. May, and J. C. Seferis, “Predictive models as aids to thermoset resin processing,” in *ACS Symposium Series, Chemorheology of Thermosetting Polymers*, C. A. May, Ed, Washington, DC, USA: American Chemical Society, 1983, pp. 301–318.
- [167] A. Shahkarami and D. Van Ee, “Material characterization for processing: ACG MTM45-1,” Convergent Manufacturing Technologies and National Center for Advanced Materials Performance, Nov. 2009. [Online]. Available: [http://www.niar.wichita.edu/coe/ncamp\\_documents/ACG%20MTM45-1/AC-GMTM45-1-ProcessingCharacterizationV1-0.pdf](http://www.niar.wichita.edu/coe/ncamp_documents/ACG%20MTM45-1/AC-GMTM45-1-ProcessingCharacterizationV1-0.pdf).
- [168] C. Garschke, P. P. Parlevliet, C. Weimer, and B. L. Fox, “Cure kinetics and viscosity modelling of a high-performance epoxy resin film,” *Polymer Testing*, vol. 32, no. 1, pp. 150–157, 2013.



- [169] Y. A. Tajima, "Monitoring cure viscosity of epoxy composites," *Polymer Composites*, vol. 3, no. 3, pp. 162–169, 1982.
- [170] C.A. May, Ed. *Chemorheology of Thermosetting Polymers*, Washington, DC, USA, in *American Chemical Society*, 1983.
- [171] D. R. Day and D. D. Shepard, "Effect of advancement on epoxy prepreg processing - A dielectric analysis," *Polymer Composites*, vol. 12, no. 2, pp. 87–90, 1991.
- [172] Y. Yu, H. Su, and W. Gan, "Effects of storage aging on the properties of epoxy prepregs," *Industrial & Engineering Chemistry Research*, vol. 48, no. 9, pp. 4340–4345, 2009.
- [173] *Thermosetting resin systems - Test method - Determination of gel time and viscosity*, EN6043, 1996.
- [174] P. J. Halley and M. E. Mackay, "Chemorheology of thermosets - An overview," *Polymer Engineering and Science*, vol. 35, no. 5, pp. 593–609, 1996.
- [175] W. X. Zukas, W. J. MacKnight, and N. S. Schneider, "An epoxy resin during cure," in *ACS Symposium Series, Chemorheology of Thermosetting Polymers*, C. A. May, Ed, Washington, DC, USA: American Chemical Society, 1983, pp. 223–248.
- [176] S. Comas-Cardona, S. Ziaee, and S. G. Advani, "Spatially homogeneous gelation in liquid composite molding," *Polymer Engineering and Science*, vol. 42, no. 8, pp. 1667–1673, 2002.
- [177] C.-Y. M. Tung and P. J. Dynes, "Relationship between viscoelastic properties and gelation in thermosetting systems," *Journal of Applied Polymer Science*, vol. 27, pp. 569–574, 1982.
- [178] H. H. Winter, "Can the gel point of a cross-linking polymer be detected by the  $G'$  -  $G''$  crossover?," *Polymer Engineering and Science*, vol. 27, no. 22, pp. 1698–1702, 1987.
- [179] P. J. Halley, M. E. Mackay, and G. A. George, "Determining the gel point of an epoxy resin by various rheological methods," *High Performance Polymers*, vol. 6, no. 4, pp. 405–414, 1994.
- [180] E. A. Mason and A. P. Maulinauskas. *Gas Transport in Porous Media: The Dusty-Gas Model*, Amsterdam, NL, in *Elsevier Scientific*, 1983.
- [181] J. R. Wood and G. M. Bader, "Void control for polymer-matrix composites (1): Theoretical and experimental methods for determining the growth and collapse of gas bubbles," *Composites Manufacturing*, vol. 5, no. 3, pp. 139–147, 1994.
- [182] R. K. Upadhyay and E. W. Liang, "Consolidation of advanced composites having volatile generation," *Polymer Composites*, vol. 16, no. 1, pp. 96–108, 1995.

- [183] S. T. Lundström, V. Frishfelds, and A. Jakovics, "Bubble formation and motion in non-crimp fabrics with perturbed bundle geometry," *Composites Part A: Applied Science and Manufacturing*, vol. 41, no. 1, pp. 83–92, 2010.
- [184] R. Helmus, "Out-of-Autoclave prepregs: Stochastic modelling of void formation," Ph.D. dissertation, Institute for Carbon Composites, Technische Universität München, Munich, DE, 2015.
- [185] M. Knudsen. *The kinetic theory of gases*, London, UK, in *Methuen and Co. Ltd*, 1934.
- [186] F. H. Newman and V. Searle. *The General Properties of Matter*. 5th ed, London, UK, in *Edward Arnold Publishers Ltd*, 1957.
- [187] A. S. Ziarani and R. Aguilera, "Knudsen's permeability correction for tight porous media," *Transport in Porous Media*, vol. 91, no. 1, pp. 239–260, 2012.
- [188] Y.-S. Wu, K. Pruess, and P. Persoff, "Gas flow in porous media with klinkenberg effects," *Transport in Porous Media*, vol. 32, pp. 117–137, 1998.
- [189] L. Klinkenberg, "The permeability of porous media to liquids and gases," *Drilling and production practice, American Petroleum Institute*, pp. 200–213, 1941.
- [190] S. K. Kim and I. M. Daniel, "Transient gas flow technique for inspection of fiber preforms in resin transfer molding," *Composites Part A: Applied Science and Manufacturing*, vol. 36, pp. 1694–1699, 2005.
- [191] A. Levy, J. Kratz, and P. Hubert, "Air evacuation during vacuum bag only prepreg processing of honeycomb sandwich structures: In-plane air extraction prior to cure," *Composites Part A: Applied Science and Manufacturing*, vol. 68, pp. 365–376, 2015.
- [192] T. Kourkoutsaki, R. K. Upadhyay, R. Hinterhoelzl, S. Comas-Cardona, and C. Binetruy, "Air evacuation in consolidation modeling of Out-of-Autoclave prepregs," in *Conf. Proc. FPCM-12*, Enschede, Netherlands, July, 2014.
- [193] R. B. Montgomery, "Viscosity and thermal conductivity of air and diffusivity of water vapor in air," *Journal of Meteorology*, vol. 4, pp. 193–196, 1947.
- [194] K. J. Ahn and J. C. Seferis, "Simultaneous measurements of permeability and capillary pressure of thermosetting matrices in woven fabric reinforcements," *Polymer Composites*, vol. 12, no. 3, pp. 146–152, Jun. 1991.
- [195] B. M. Louis, K. Hsiao, and G. Fernlund, "Gas permeability measurements of Out of Autoclave prepreg MTM45-1/CF2426A," in *Spring Symp. Proc. SAMPE '10*, Seattle, May, 2010.
- [196] K. J. Ahn and J. C. Seferis, "Prepreg processing science and engineering," *Polymer Engineering and Science*, vol. 33, no. 18, pp. 1177–1188, 1993.

- [197] C.-H. Park and L. Woo, "Modeling void formation and unsaturated flow in liquid composite molding processes: A survey and review," *Journal of Reinforced Plastics and Composites*, vol. 30, no. 11, pp. 957–977, 2011.
- [198] J. A. Garcia, L. Gascón, and F. Chinesta, "A fixed mesh numerical method for modelling the flow in liquid composites moulding processes using a volume of fluid technique," *Computer Methods in Applied Mechanics and Engineering*, vol. 192, no. 7-8, pp. 877–893, 2003.
- [199] J. A. García, L. Gascón, and F. Chinesta, "A flux limiter strategy for solving the saturation equation in RTM process simulation," *Composites Part A: Applied Science and Manufacturing*, vol. 41, no. 1, pp. 78–82, 2010.
- [200] L. Gascón, J. A. García, F. LeBel, E. Ruiz, and F. Trochu, "A two-phase flow model to simulate mold filling and saturation in resin transfer molding," *International Journal of Material Forming*, vol. 9, no. 2, pp. 229–239, 2016.
- [201] J. A. Acheson, P. Simacek, and S. G. Advani, "The implications of fiber compaction and saturation on fully coupled VARTM simulation," *Composites Part A: Applied Science and Manufacturing*, vol. 35, no. 2, pp. 159–169, 2004.
- [202] M. K. Kang and W. I. Lee, "A dual-scale analysis of macroscopic resin flow in vacuum assisted resin transfer molding," *Polymer Composites*, vol. 25, no. 5, pp. 510–520, 2004.
- [203] A. C. Loos and J. MacRae, "A process simulation model for the manufacture of a blade-stiffened panel by the resin film infusion process," *Composites Science and Technology*, vol. 56, pp. 273–289, 1996.
- [204] R. Helmus, T. Centea, P. Hubert, and R. Hinterhoelzl, "An integrated process model for air evacuation and tow impregnation in Out-of-Autoclave prepreg consolidation," in *28th Techn. Conf. Proc. of the American Society for Composites*, Pennsylvania, September, 2013.
- [205] C. A. Fracchia, J. Castro, and C. L. Tucker, "A finite element/control volume simulation of resin transfer mold filling," in *4th Tech. Conf. American Soc. Composites*, Lancaster, October, 1989.
- [206] F. Trochu, R. Gauvin, and D. M. Gao, "Numerical analysis of the resin transfer molding process by the finite element method," *Advances in Polymer Technology*, vol. 12, pp. 329–342, 1993.
- [207] S. Li and R. Govin, "Numerical analysis of the resin flow in resin transfer molding," *Journal of Reinforced Plastics and Composites*, vol. 10, pp. 314–327, 1991.
- [208] P. Celle, S. Drapier, and J. M. Bergheau, "Numerical modelling of liquid infusion into fibrous media undergoing compaction," *European Journal of Mechanics - A/Solids*, vol. 27, no. 4, pp. 647–661, 2008.

- [209] D. A. Nield and A. Bejan, "Convection in porous media," in *Convection Heat Transfer*, A. Bejan, Ed, Hoboken, NJ, USA: John Wiley & Sons Inc, 2013.
- [210] A. Bejan, Ed. *Convection Heat Transfer*, Hoboken, NJ, USA, in *John Wiley & Sons Inc*, 2013.
- [211] R. C. Progelhof, J. L. Throne, and R. R. Ruetsch, "Methods for predicting the thermal conductivity of composite systems: A Review," *Polymer Engineering and Science*, vol. 16, p. 615, 1976.
- [212] D. A. Nield, "Estimation of the stagnant thermal conductivity of saturated porous media," *International Journal of Heat and Mass Transfer*, vol. 34, no. 6, pp. 1575–1576, 1991.
- [213] S. Bories and M. Prat, "Transferts de chaleur dans les milieux poreux," *Dossier Techniques de L'Ingenieur, Genie energetique*, no. B 8 250, pp. 1–33, 1995.
- [214] A. Johnston, "An integrated model of the development of process-induced deformation in Autoclave processing of composite structures," Ph.D. dissertation, University of British Columbia, British Columbia, 1997.
- [215] K. Chawla. *Fibrous Materials*, Cambridge, UK, in *Cambridge University Press*, 2016.
- [216] K. Drechsler and E. Ladstätter, "Lecture on production technologies for composite parts," Materials and Process Technologies for Carbon Composites, Institute for Carbon Composites, TUM in WS2015/16.
- [217] P. Bankhead, "Image J User Guide," [Online]. Available: [http://imagej.net/User\\_Guides](http://imagej.net/User_Guides).
- [218] N. Otsu, "A threshold selection method from gray-level histograms," *IEEE Trans Systems Man and Cybernetics*, vol. 9 (No.1), pp. 62–66, 1979.
- [219] T. W. Ridler and S. Calvard, "Picture thresholding using an iterative selection method," *IEEE Trans. Systems Man and Cybernetics*, vol. 8, no. 8, pp. 630–632, 1978.
- [220] B. Thorfinnson and T.F. Biermann, "Degree of impregnation of prepregs - Effects on porosity," in *Conf. Proc. Intl. SAMPE Symp. '32*, Anaheim, California, April, 1987, pp. 1500–1509.
- [221] H. Giesche, "Mercury porosimetry: A General (practical) overview," *Part. Part. Syst. Charact*, vol. 23, no. 1, pp. 9–19, 2006.
- [222] P. A. Webb, "Volume and density determinations for particle technologists," Georgia, Micromeritics Instrument Corp, 2001. [Online]. Available: [http://www.particletesting.com/Repository/Files/density\\_determinations.pdf](http://www.particletesting.com/Repository/Files/density_determinations.pdf).

- [223] J. Rouquerol *et al.*, “The characterization of macroporous solids: An overview of the methodology,” *Microporous and Mesoporous Materials*, vol. 154, pp. 2–6, 2012.
- [224] Toho Tenax Europe GmbH. (2011). *Technical Data Sheet. Filament Yarn Tenax HTA*.
- [225] Cytec. (2013). *Product Data Sheet PDS1189\_09.13\_Issue8a. MTM 44-1 Prepreg*.
- [226] Cytec. (2014). *Safety Data Sheet. MTM44-1 Unsupported Resin Film*.
- [227] L. C. Thomas, “Making accurate DSC and MDSC specific heat capacity: measurements with the Q1000 Tzero DSC,” TA Instruments. [Online]. Available: [www.tainstruments.com/pdf/literature/TA310.pdf](http://www.tainstruments.com/pdf/literature/TA310.pdf).
- [228] J. D. Menczel and R. B. Prime. *Thermal Analysis of Polymers: Fundamentals and Applications*, Hoboken, NJ, USA, in *John Wiley & Sons Inc*, 2009.
- [229] D. Dykeman, “Minimizing uncertainty in cure modeling for composites manufacturing,” Doctor of Philosophy, Materials Engineering, University of British Columbia, Vancouver, Canada, 2008.
- [230] L. C. Thomas, “Chapter 3: Modulated DSC basics, optimization of MDSC experimental conditions,” in *Modulated DSC Technology Manual*, L. C. Thomas, Ed.: TA Instruments, 2005.
- [231] S. Sourour and M. R. Kamal, “Differential scanning calorimetry of epoxy cure: Isothermal cure kinetics,” *Thermochimica Acta*, vol. 14, pp. 41–59, 1976.
- [232] K. C. Cole, J.-J. Hechler, and D. Noel, “A new approach to modeling the cure kinetics of epoxy amine thermosetting resins. 2. Application to a typical system based on Bis[4-(diglycidylamino)phenyl]methane and Bis(4-aminophenyl) Sulfone,” *Macromolecules*, vol. 24, pp. 3096–3110, 1991.
- [233] C.-S. Chern and G. W. Poehlein, “A kinetic model for curing reactions of epoxides with amines,” *Polymer Engineering and Science*, vol. 27, no. 11, pp. 788–795, 1997.
- [234] COMSOL Multiphysics. (2015). *Multiphysics Reference Manual v5.2*.
- [235] A. Dimopoulos, “Effect of carbon nanoparticle addition on epoxy cure,” Ph.D. dissertation, School of Applied Sciences, Cranfield University, Cranfield, UK, 2007.
- [236] COMSOL Multiphysics. (2015). *Heat Transfer Module User's Guide v5.2*.
- [237] K. Zimmermann and Van Den Broucke, B, “Assessment of process-induced deformations and stresses in ultra thick laminates using isoparametric 3D elements,” *Journal of Reinforced Plastics and Composites*, vol. 31, pp. 163–178, 2012.

- [238] S. L. Agius, K. Magniez, and B. L. Fox, "Cure behaviour and void development within rapidly cured out-of-autoclave composites," *Composites Part B: Engineering*, vol. 47, pp. 230–237, 2013.
- [239] T. Centea, J. Kratz, and P. Hubert, "The effect of out-time and cure cycle on the consolidation of Out-of-Autoclave prepregs," in *Conf. Proc. FPCM-9*, Auckland, NZ, July, 2012.
- [240] T. Glockner, "SigCat Documentation - NI Test Bench Development," Lehrstuhl für Carbon Composites, Munich, DE, Aug. 2015.
- [241] N. G. Pantelelis and E. Bistekos, "Real-time process control applied in liquid composite moulding," in *Conf. Proc. FPCM-8*, Douai, France, July, 2006.
- [242] K. Mason, "Autoclave quality outside the Autoclave? Pioneers of out-of-autoclave processing in aerospace applications answer a qualified but enthusiastic yes!," *Composites World Magazine*, Mar. 2006. [Online]. Available: <http://www.compositesworld.com/articles/autoclave-quality-outside-the-autoclave>.
- [243] J. Sloan, "VBO prepregs: The Vision SF50 - OOA vacuum-bag-only process makes carbon fiber structures a reality for a unique personal jet," *Composites Manufacturing Magazine*, Feb. 2016. [Online]. Available: <http://cw.epubxp.com/i/630867-autoclave-2016>.
- [244] C. J. Wade and J. R. Savage, "The development and application of an out-of-autoclave prepreg solution for airbus A350XWB wing fixwd trailing edge," in *Conf. Proc. SAMPE '11*, Long Beach, CA, May, 2011.
- [245] *Composites World Magazine - Industrial News*, "Lockheed Martin unveils Orion composite heat shield," Jan. 2010. [Online]. Available: <http://www.compositesworld.com/news/lockheed-martin-unveils-orion-composite-heat-shield>.
- [246] G. Marsh, "De-autoclaving prepreg processing (Part 1)," *Materials Today - Reinforced Plastics*, Sep. 2012. [Online]. Available: <http://www.materialstoday.com/composite-processing/features/de-autoclaving-prepreg-processing-part-1/>.
- [247] Advanced Composites Group. (2009). *Technology Centre Report, Vol. 17, No. 2*.
- [248] G. Marsh, "De-autoclaving prepreg processing (Part 2)," *Materials Today - Reinforced Plastics*, Oct. 2012. [Online]. Available: <http://www.materialstoday.com/composite-applications/features/de-autoclaving-prepreg-processing-part-2/>.
- [249] T.G. Mezger. *Das Rheologie Handbuch*. 4th ed, Hannover, in *Vincentz Network*, 2012.



# A Appendix

## a OoA Applications and a Review of Commercially Available Prepregs (Chapter 1)

Tab. A- 1: A list of commercial products manufactured Out-of-Autoclave

Applications	Part Type	OoA Material
Meridian and Malibu aircraft Piper Aircraft Inc.'s [242]	Exterior fairings	LTM 24ST carbon/epoxy prepreg Toray T-300 carbon 2x2 TW fabric (Solvay)
Vision SF50 Cirrus Aircraft [243]	5+ passenger Aircraft	Carbon/epoxy prepreg by TenCate Advanced Compo- sites
Next Generation Heavy Launch Vehicles NASA/Boeing [24]	Cryogenic Tanks	Carbon/BMI OoA prepreg Carbon/Epoxy Cycom 5320-1 (Solvay)
Airbus A350 XWB GE Aviation Systems [244]	Trailing Edge Secondary Wing Structures	MTM 44-1 carbon/epoxy prepreg based on 2x2 TW fabric (Solvay)
Denver Orion Lockheed Martin [245]	Heat shield	TC420 carbon/cynate ester by TenCate Advanced Composites
Virgin Galactic - Scaled Compo- sites Spaceship 2 & White Knight 2 [246]	Aircraft	MTM 45-1 carbon/epoxy prepreg (Solvay)
X-55A Advanced Composite Cargo Aircraft Lockheed Martin [10]	Modification of Dornier fuselage	-
Radar antenna Norma MPM [247]	Complex modules for Antennas	VTM 240 prepreg with addition of fire retardants (Solvay)
ABN AMRO Volvo 70 Round the World Race boats [247]	Boat hull	VTM prepreg (Solvay)
Mercedes Benz SLR McLaren Hamble/GE Aviation Systems [244]	Chassis structures	OoA semi-pregs based on NCF
Tidal turbine rotor Marine Technology Seagen [248]	Thick structural carbon spars	VTM 260 prepreg (Solvay)

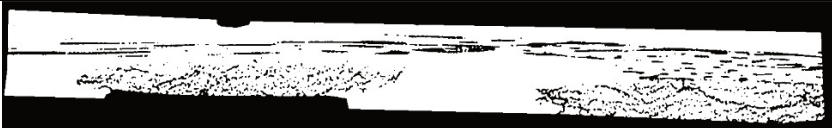









**Tab. A-2: A review of available commercial OoA prepregs, key features and their applications**

<b>Prepreg</b>	<b>Manufacturer</b>	<b>Application</b>	<b>Fabric</b>	<b>Resin</b>	<b>Impregnation</b>
MTM 44-1	Solvay (ACG)	Aerospace Secondary structures	UD woven	Toughened Epoxy	single-sided partial
MTM 45-1 MTM 57-1	Solvay (ACG)	Aerospace	woven fabrics	Epoxy	double-sided partial
MTM 47-1	Solvay (ACG)	-	UD slit tape woven	Toughened Epoxy	-
LTM 24ST	Solvay (ACG)	Automotive Tooling	-	Epoxy	single-sided partial
Cycom 5215 5320/-1	Solvay (Cytec)	Aerospace Primary structures	UD woven	Epoxy	various partial
Cycom 754	Solvay (Cytec)	Marine	-	Epoxy	-
HexPly M56	Hexcel	Aerospace	UD woven	Epoxy	-
HexPly M9	Hexcel	Wind Marine	-	Epoxy	- Information
SparPreg	Gurit	Spars	UD	Epoxy	-
Single Sprint ST94	Gurit	Industrial	woven multiaxial	Epoxy	single-sided or sandwiched
ZPreg	Solvay (ACG)	Industrial Marine Tooling	UD multiaxial	Epoxy	selective resin stripes
BT 250E-1 250E-6	TenCate	Rotor blade	-	Epoxy	-
TC 250 TC 275/-1 TC 350-1	TenCate	Aerospace	-	Epoxy	-
TC 420	TenCate	Very High Temperature (321°C)	-	Cyanate Ester	-
TC 800 BMI+	Ten Cate	High Temperature (236°C)	-	Toughened BMI	-
2510	Toray	Aerospace Primary structures	--	Epoxy	-
Loctite BZ	Henkel	-	-	Benzoxazine	-
E752	Park Electro-chemical	Aerospace	woven fabrics	Epoxy/ Benzoxazine	selective double-sided

## b Image Analysis of the MTM 44-1 Prepreg (Section 3.2.1.2)

Tab. A- 3: Global Porosity Determination via image segmentation of  $\mu$ CT images of single plies

Sample #	Prepreg Cross - Sections	$\phi_{p0}$
1		0.39
2		0.36
3		0.26
4		0.32
5		0.32
6		0.35
7		0.35
8		0.31
$\overline{\phi_{p0}} \pm d_{\phi_{p0}}$		$0.33 \pm 0.04$

## c Raw Data from the Air Permeability Measurements of the MTM 44-1 Prepreg (Section 3.3.1)

Tab. A- 4: List of measurement points used to define the in-plane air permeability of the MTM 44-1 prepreg as a function of its porosity (see Chapter 3, Section 3.3)

Sample #	$\phi_p$ (-)	$K_{a_{xx}}$ (m <sup>2</sup> )	$e_{K_{a_{xx}}}$ (%)
1	0.30	1.86e-12	248.92
2	0.25	4.08e-13	63.73
3	0.22	2.43e-13	13.99
4	0.20	1.58e-13	16.46
5	0.20	1.91e-13	16.22
6	0.18	1.12e-13	28.34
7	0.17	1.31e-13	22.03
8	0.16	9.39e-14	14.03
9	0.14	8.56e-14	22.08
10	0.14	1.00e-13	28.35
11	0.13	8.48e-14	22.29
12	0.12	4.62e-14	45.45
13	0.11	6.89e-14	12.51
14	0.11	5.18e-14	10.04
15	0.06	3.91e-14	22.22
16	0.06	4.50e-14	22.82
17	0.05	3.87e-14	13.55
18	0.00	6.00e-15	6.00

## d Dynamic Oscillatory Testing of Resins using Parallel Plate Rheometry (Section 3.4.2)

### Dynamic Oscillatory Testing

The elastic shear stress and strain during an oscillatory test are in phase for fully elastic materials, while the elastic modulus can be determined according to Equation (A-1).

$$\sigma_{s0} = G \gamma_{s0} \quad (\text{A-1})$$

On the other hand, pure viscous liquids demonstrate a time dependent response, when subjected to an oscillatory strain. The stress response is in this case proportional to the strain rate, which results into a lag of  $\pi/2$  radians behind the strain input. In this case the material behaves as a Newtonian fluid and the relationship of the viscous shear stress versus the strain rate is given in Equation (A-2).

$$\sigma_{s0} = n \dot{\gamma}_{s0} \quad (\text{A-2})$$

In this case the transient effects cancel each other out, resulting in a constant viscosity. Therefore in Newtonian fluids, viscosity is a material constant independent of the deformation rate, while in fully elastic materials the strain is directly proportional to the stress. Polymers, as viscoelastic materials exhibit a time dependent behavior, in between that encountered in perfectly elastic and viscous fluids. In this case the stress response (Equation (A-4)) lags  $\delta$  radians behind the strain (Equation (A-3)), as shown in Fig. A- 1.

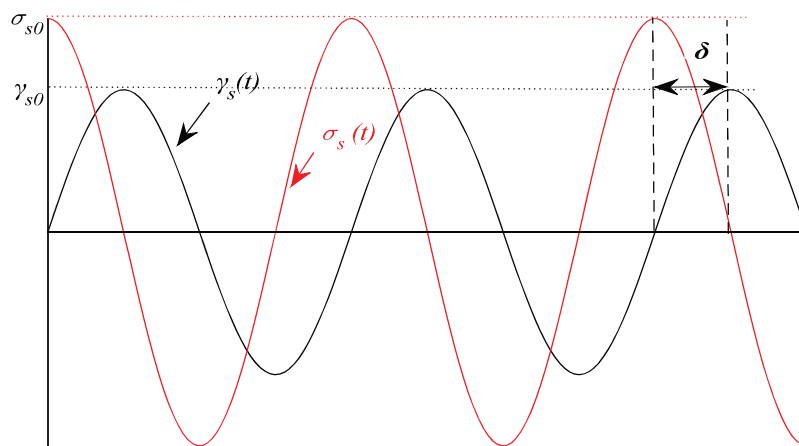


Fig. A- 1: Shear stress and strain of a viscoelastic fluid during an oscillatory test ( $0 < \delta < \pi/2$ )

$$\gamma_s(t) = \gamma_{s0} \sin(\omega t) \quad (\text{A-3})$$

$$\sigma_s(t) = \sigma_{s0} \sin(\omega t - \delta) \quad (\text{A-4})$$

In this case the complex form of the shear modulus is given by Equation (A-5). The complex shear modulus  $G^*$  is a sum of the storage  $G'$ , and the loss modulus  $G''$ . The ratio of loss to storage modulus is referred to as loss factor  $\tan \delta$ , which is a positive number for viscoelastic materials is given in Equation (A-6).

$$G^* = \frac{\sigma_s(t)}{\gamma_s(t)} = \frac{\sigma_{s0}}{\gamma_{s0}} e^{i\delta} = \frac{\sigma_{s0}}{\gamma_{s0}} (\cos \delta + i \sin \delta) = G' + iG'' \quad (\text{A-5})$$

$$\tan \delta = \frac{G''}{G'} \rightarrow 0 \leq \tan \delta \leq \infty \quad (\text{A-6})$$

Where the symbols  $\sigma_{s0}$ ,  $\gamma_{s0}$  stand for the stress and strain amplitude respectively.

From a rheological point of view, the complex viscosity of the viscoelastic material  $n^*$  is related to the shear modulus  $G^*$  according to Equation (A-7). Similarly the complex viscosity can be described by the elastic and viscous contributions according to Equation (A-9), where  $\omega$  is the angular frequency related to the frequency  $f$  via Equation (A-8), while the  $n'$  is the viscous and  $n''$  the elastic component of the complex viscosity.

$$G^* = (i\omega) n^* \quad (\text{A-7})$$

$$\omega = 2\pi f \quad (\text{A-8})$$

$$n^* = \frac{\sigma_s(t)}{\dot{\gamma}_s(t)} = n' - in'' \quad (\text{A-9})$$

### Parallel Plate Rheometry

The parallel plate or plate-plate rheometer consists of two plates, one stationary and one rotatory. The Anton Paar MCR 302 Rheometer and a schematic of the parallel plate measurement system used in this work are given Fig. A- 2.

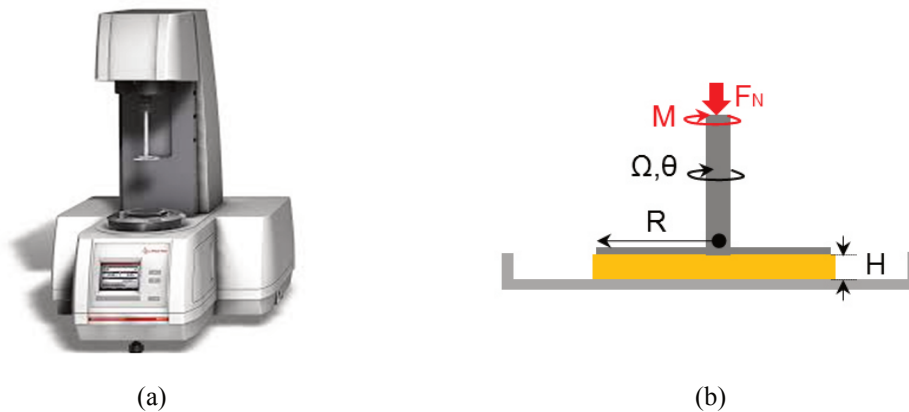


Fig. A- 2: (a) The Anton Paar MCR 302 Rheometer and (b) schematic of the parallel plate set-up utilized for testing the MTM 44-1 resin film

To ensure homogenous flow during the test, the distance between the plates ( $H$ ) shall be smaller than the radius of the plates used ( $R_p$ ). In the parallel plate set-up, the shear rate  $\dot{\gamma}_{sr}$  increases with increasing distance from the rotational axis, while the maximum shear rate is encountered at a distance of  $r = R$ , defined according to Equation (A-10). The shear rate can be varied by adjusting the angular velocity and the distance between the plates.

$$\dot{\gamma}_{sr} = \frac{v}{H} = \frac{R_p \cdot \Omega}{H} \quad (\text{A-10})$$

The shear stress is calculated according to Equation (A-11), where  $M$  is the torque of the shaft and the radius of the plates used ( $R_p$ ). In the parallel plate set-up.

$$\sigma_s = \frac{2M}{\pi R_p^3} \quad (\text{A-11})$$

## e Linear Visco-Elastic Domain Definition (LVE) of the MTM 44-1 Resin (Section 3.4.2)

Small amplitude oscillatory shear tests can be used to characterize the linear viscoelastic properties of polymers at small deformations. At large deformations, material properties such as storage and loss shear modulus exhibit a deformation dependent behavior, due to molecular disentanglement and orientation during the test [152].

A sweep within the small strain amplitude range, at a low constant frequency shall be performed, in order to identify the domain within which the storage modulus (as a parameter of the material structure) remains linear and unchanged. This region marks the linear viscoelastic domain, within which the viscosity measured is independent of the magnitude of the deformations during the measurement [249]. In the case of the MTM44-1 resin, a sweep within 0.01-10% deformation is performed at the frequency of 1Hz and at four temperatures in the temperature range of interest. The storage modulus is recorded against the deformation in % and displayed in Fig. A- 3.

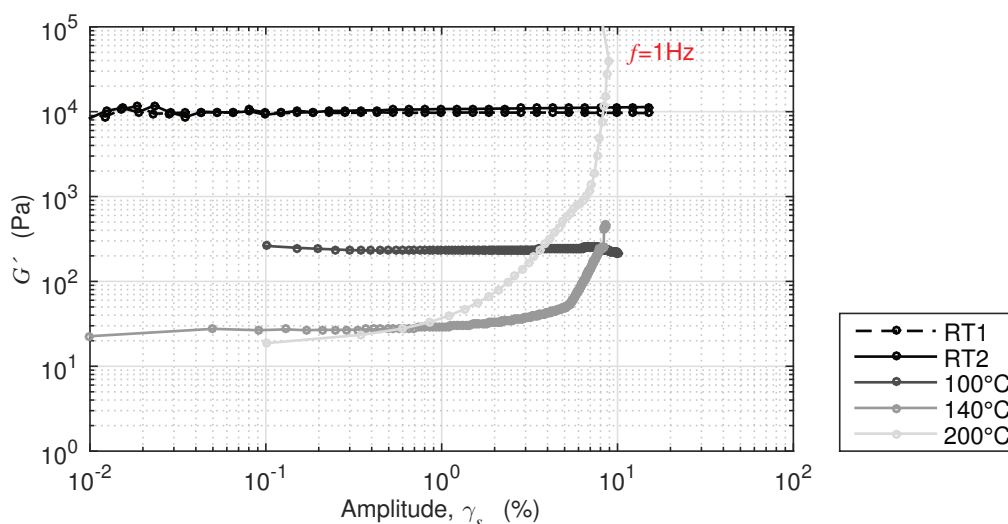


**Fig. A- 3: Amplitude sweep of the MTM 44-1 resin at 1Hz, for four isothermal temperatures**

As shown in Fig. A- 3, the MTM44-1 resin exhibits a linear viscoelastic behavior, nfor all temperatures in the range of 0.01-0.2% deformation. The increase of the storage modulus observed above 1% deformation at 140 and 200 °C, is caused by cure advancement of the resin, due to its extended exposure to high temperatures (see Fig. A- 4). When the material is tested at room temperature, it remains within the linear viscoelastic domain for the whole range of deformations tested. At 100 °C the storage modulus reduces approximately at 10% deformation. This is the critical strain of the resin at 100 °C, at which strain the polymer transitions from the linear to the non-linear viscoelastic domain. To ensure the resin remains in the LVE for an amount of time, at all temperatures of interest, a deformation of 0.1% is selected for all measurements of the MTM44-1 viscosity.



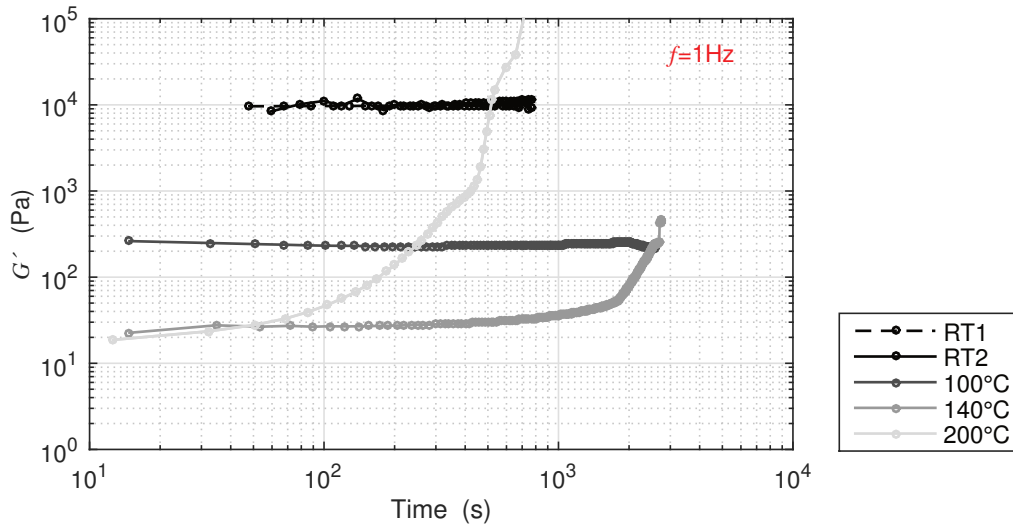


**Fig. A- 4: Evolution of the MTM 44-1 storage modulus during the isothermal amplitude sweep at 1Hz for a range of temperatures**

During the amplitude sweep, the sampling time is selected according to Equation (A-12) in order to avoid instability issues occurring during the measurement [249].

$$t_s \geq \frac{\omega}{2\pi} \quad (\text{A-12})$$

A frequency sweep at constant deformation (selected during the deformation sweep), shall enable the selection of a frequency, where the resin is at a liquid state. Particularly for the MTM 44-1 resin, the 0.1% deformation is selected for the test. The most critical temperatures (100-130 °C) for the viscosity model development are chosen to evaluate the state of the resin with a frequency sweep, between 0.1-100 Hz (see Fig. A- 5). Each test was repeated twice, one from low to high and one from high to low frequencies.

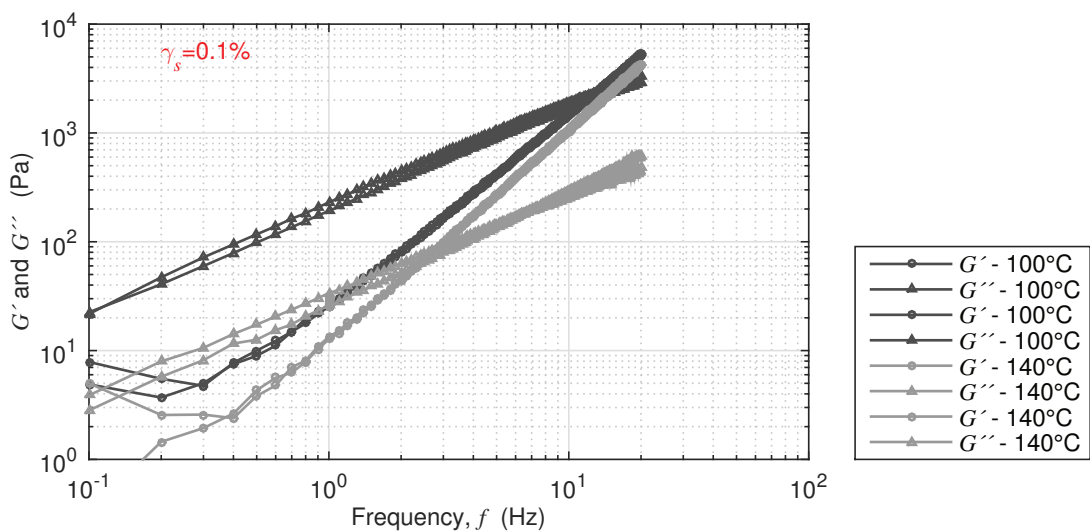


**Fig. A- 5: Evolution of the storage and loss modulus of the MTM 44-1 resin during a frequency sweep at 0.1% deformation, for a range of temperatures**

Typically in polymer melts, at low frequencies, the material responds as a perfect viscous fluid, while at high frequencies it behaves as a hookean solid [152]. At the frequencies shortly before the point where the storage and loss moduli cross each other (softening point), the material can be considered as a viscoelastic fluid and defines the frequency domain for these studies. The relative magnitude of the storage and loss modulus characterizes the properties of the material under test:

- If  $G' < G'' \rightarrow \tan \delta > 1$ , the material is at its liquid state.
- If  $G' > G'' \rightarrow \tan \delta < 1$ , the material is at a state after gelation.
- If  $G' = G'' \rightarrow \tan \delta = 1$ , is the material's gel transition point.

Therefore it is clear from Fig. A- 5 that the MTM44-1 resin is liquid at its initial state, while at frequencies close to 1Hz the resin can be considered a viscoelastic fluid below 140°C. Increasing temperature causes a shift of the softening point to lower frequencies. Therefore above 2.5Hz in the case of 140 °C and ~10Hz in the case of 100 °C, the resin transitions to a gel. A good repeatability of the softening time is observed when testing the material starting with high as well as low frequencies.

## f Inputs for the Isothermal Tow Impregnation Models (Section 4.1)

Tab. A- 5: Inputs used in the calculation of the tow impregnation times and pressure profiles at isothermal conditions during instantaneous air evacuation (Fig. 4-3), compromised vacuum connection (Fig. 4-4) and delayed air evacuation (Fig. 4-5)

Inputs	Units	Instantaneous air evacuation	Compromised vacuum connection	Delayed air evacuation
$H_t$	$m$	$0.5588 \cdot 10^{-3}$	$0.5588 \cdot 10^{-3}$	$0.5588 \cdot 10^{-3}$
$L$	$m$	Independent	Independent	5
$\phi_t$	–	0.5	0.5	0.5
$n$	$Pa \cdot s$	$10^4$	$10^4$	$10^4$
$\mu_a$	$Pa \cdot s$	Independent	Independent	$1.97 \cdot 10^{-5}$
$K_{r,zz}$	$m^2$	$4.68 \cdot 10^{-13}$	$4.68 \cdot 10^{-13}$	$4.68 \cdot 10^{-13}$
$K_{a,xx}$	$m^2$	Independent	Independent	$2.00 \cdot 10^{-17}$
$P_{vac}$	$Pa$	$2 \cdot 10^3$	$3 \cdot 10^3$	$2 \cdot 10^3$

**Tab. A- 6: Inputs used in sensitivity studies summarized in Section 4.1, Fig. 4-7 to Fig. 4-10**

Inputs	Units	Material 1	Material 2	Material 3
$H_t$	$m$	$0.44 \cdot 10^{-3}$	$0.44 \cdot 10^{-3}$	$0.44 \cdot 10^{-3}$
$L$	$m$	0.5	0.5	0.5
		1	1	1
		2	2	2
		5	5	5
		10	10	10
		20	20	20
$\phi_t$	—	0.59	0.3	0.1
$n$	$Pa \cdot s$	at 30°C $10^4$	at 30°C $10^4$	at 30°C $10^4$
		at 130°C 10.5	at 130°C $10.5^5$	at 130°C 10.5
$\mu_a$	$Pa \cdot s$	at 30°C $1.97 \cdot 10^{-5}$	at 30°C $1.97 \cdot 10^{-5}$	at 30°C $1.97 \cdot 10^{-5}$
		at 130°C $2.43 \cdot 10^{-5}$	at 130°C $2.43 \cdot 10^{-5}$	at 130°C $2.43 \cdot 10^{-5}$
$K_{r,zz}$	$m^2$	$4.68 \cdot 10^{-13}^*$	$4.14 \cdot 10^{-15}^*$	$2.16 \cdot 10^{-18}^*$
$K_{a,xx}$	$m^2$	$2.26 \cdot 10^{-12}^*$	$2.26 \cdot 10^{-12}^*$	$2.26 \cdot 10^{-12}^*$
		$1.91 \cdot 10^{-13}^{**}$	$1.91 \cdot 10^{-13}^{**}$	$1.91 \cdot 10^{-13}^{**}$
		$5.69 \cdot 10^{-14}^{**}$	$5.69 \cdot 10^{-14}^{**}$	$5.69 \cdot 10^{-14}^{**}$
		$9.60 \cdot 10^{-15}^{***}$	$9.60 \cdot 10^{-15}^{***}$	$9.60 \cdot 10^{-15}^{***}$
		$5.69 \cdot 10^{-16}^{****}$	$5.69 \cdot 10^{-16}^{****}$	$5.69 \cdot 10^{-16}^{****}$
		$2.0 \cdot 10^{-17}$	$2.0 \cdot 10^{-17}$	$2.0 \cdot 10^{-17}$
		$2.26 \cdot 10^{-18}$	$2.26 \cdot 10^{-18}$	$2.26 \cdot 10^{-18}$
$P_{vac}$	$Pa$	$2 \cdot 10^3$	$2 \cdot 10^3$	$2 \cdot 10^3$

\*Gebart [19, 140]

\*\* MTM 44-1 [19]

\*\*\* Fernlund et al. [19, 35]

\*\*\*\* Hickey et al. [19, 120]

## g Sensor and Probe Locations in the CFRP Demonstrator used for Validation (Chapter 5)

Tab. A- 7: Sensors (experimental) and probe (simulation) locations in the CFRP demonstrator part presented in Chapter 5

Property	Sensor	Probe	$x_{probe}$ (m)	$y_{probe}$ (m)	Ply #
Pressure	$P_{vac}$	$P_{vac}$	0.59	-	BC
	PS 1	P 5	0.56-0.57	0	tool/1
	PS 2	P 8	0.05-0.06	0	tool/1
Displacement	DVDT 1		0.065		20 +
	DVDT 2		0.525		20+
Resistance Viscosity	DC 1		0.55	$4.5 \cdot 10^{-3}$	10-11
	DC 2		0.01	$4.5 \cdot 10^{-3}$	10-11
Temperature	TC 0	-	0.03	-	tool/1
	TC 1	$T_a$ 1 $T_r$ 1	0.29	0 $2.35 \cdot 10^{-4}$	tool/1
	TC 2	-	0.52	-	tool/1
	TC 0 – 2	$T_{bottom}(t)$	Average		
	TC 3	Not used			
	TC 4	$T_a$ 4 $T_r$ 4	0.035	$4.5 \cdot 10^{-3}$	10/11
	TC 5	$T_a$ 5 $T_r$ 5	0.295	$4.5 \cdot 10^{-3}$	10/11
	TC 6	$T_a$ 6 $T_r$ 6	0.525	$4.5 \cdot 10^{-3}$	10/11
	TC 7	-	0.035	-	20
	TC 8	$T_a$ 8 $T_r$ 8	0.28	$8.56 \cdot 10^{-3}$ $8.98 \cdot 10^{-3}$	20
	TC 9	-	0.54	-	20
	TC 10	-	0.025	$9 \cdot 10^{-3}$	20+bag
	TC 11	-	0.27	$9 \cdot 10^{-3}$	20+bag
	TC 12	-	0.55	$9 \cdot 10^{-3}$	20+bag
	TC 10 – 12	$T_{top}(t)$	Average		
TC 14	-	0.3	-	oven/air	
TC 15	-	0.44	-	oven/air	

## h Temperature Homogeneity Measurements on the Tool used for Validation (Chapter 5)

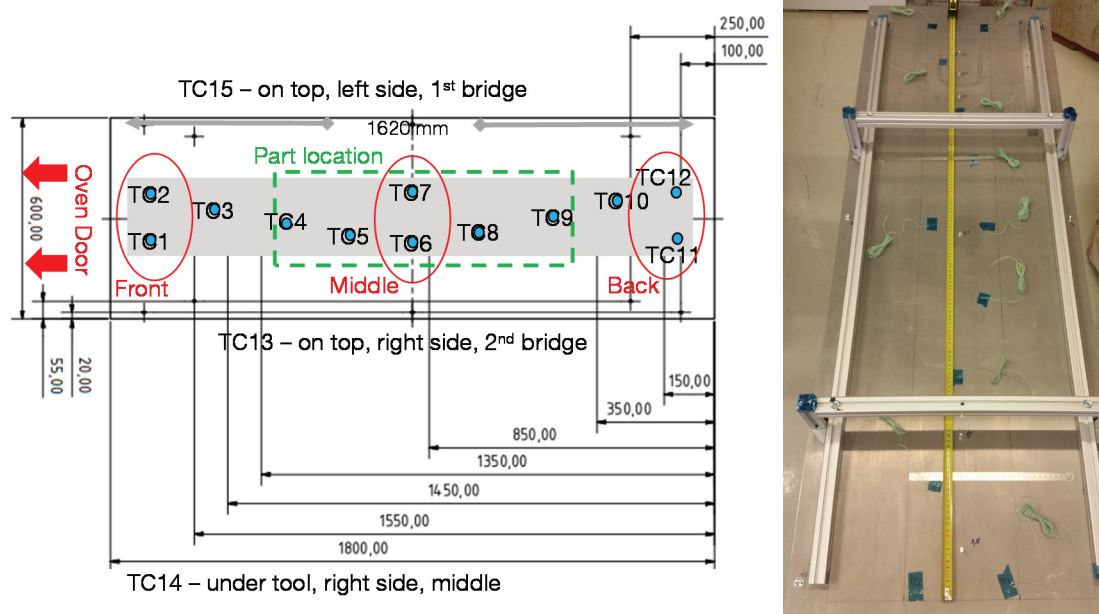


Fig. A- 6: Position and installation of thermocouples used to evaluate tool homogeneity

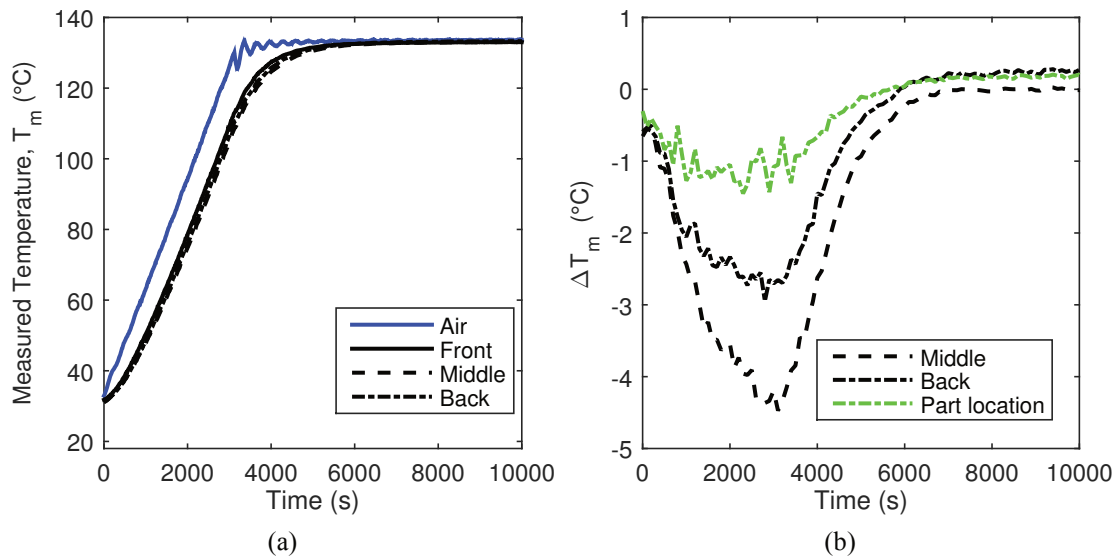
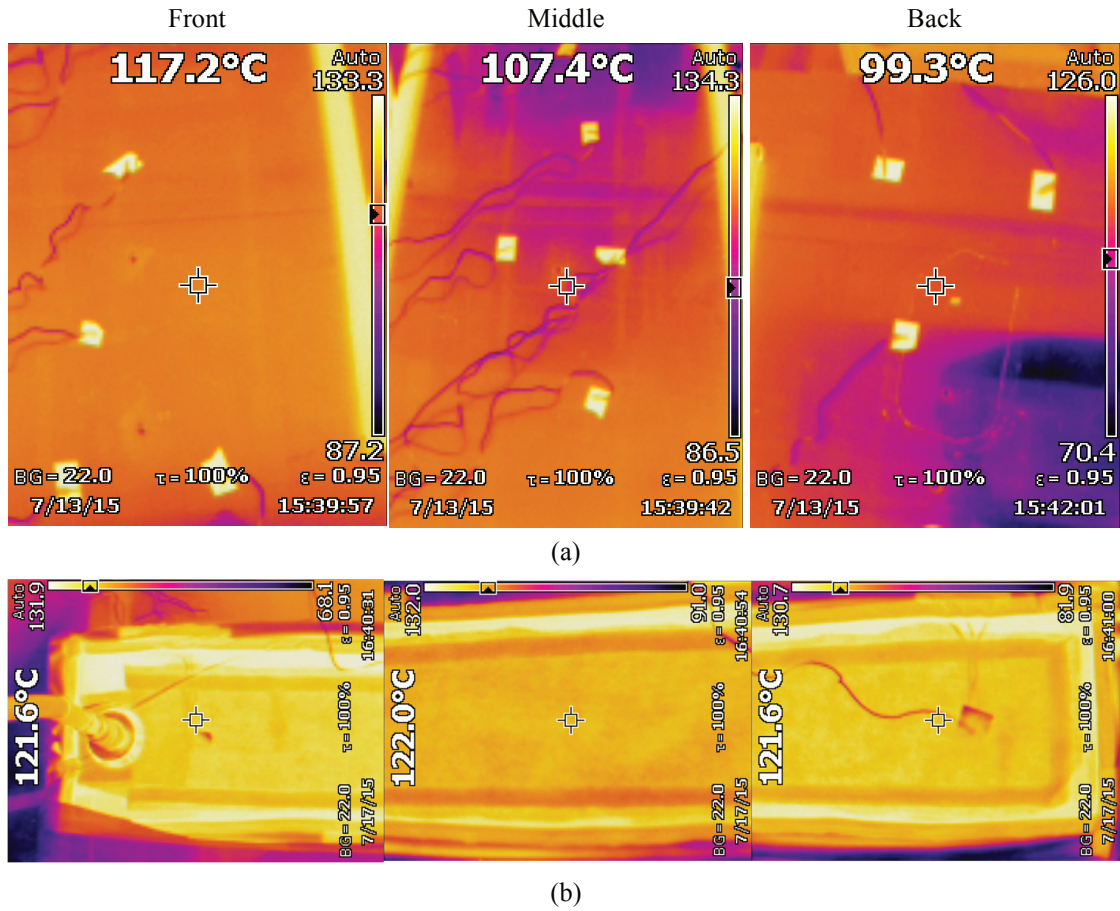


Fig. A- 7: (a) Tool and air temperature inside the oven ( $T_m$ ) versus time and (b) temperature difference between the front and middle/back of the tool and the two ends of the tool area where the validation parts are placed ( $\Delta T_m$ ) versus time, during the cure cycle

The temperature at the front (TC1,2), middle (TC 6,7) and back of the tool (TC 11,12) are calculated as an average of the two thermocouples at each position, placed according to the sketch of Fig. A- 6. The air temperature is reported as an average of TC 14 and 15. The difference between TC 4 and TC 9 depicts the difference between the two ends of the part.



**Fig. A- 8: Temperature homogeneity monitoring during cool-down, via an IR camera**  
 (a) Residual heat measured on the tool after the cure cycle, at three positions (front, middle, back) (b) residual heat measured on top of a part, at three positions along its length.





## B Publications

### Journal Papers

- [P1] T. Kourkoutsaki, S. Comas-Cardona, C. Binetruy, R. K. Upadhyay, and R. Hinterhoelzl, “The impact of air evacuation on the impregnation time of Out-of-Autoclave prepregs,” *Composites Part A: Applied Science and Manufacturing*, vol. 79, pp. 30–42, 2015.
- [P2] T. Kourkoutsaki, S. Comas-Cardona, K. Masania, and K. Drechsler, “A multiphysics simulation framework developed to address scale-up challenges of Out-of-Autoclave manufacturing: Model development and material characterization” to be submitted in *Journal of Composite Materials*.

### Conference Proceedings

- [C1] T. Kourkoutsaki, S. Comas-Cardona, C. Binetruy, R. K. Upadhyay, and R. Hinterhoelzl, “Impact of air evacuation in Out-of-Autoclave flow and compaction modeling,” in *Conf. Proc. ECCM-16*, Seville, June, 2014, pp. 1–8.
- [C2] T. Kourkoutsaki, S. Comas-Cardona, R. K. Upadhyay, R. Hinterhoelzl, and C. Binetruy, “Air evacuation in consolidation modeling of Out-of-Autoclave prepregs in *Conf. Proc. FPCM-12*, Enschede, Netherlands, July, 2014.
- [C3] T. Kourkoutsaki, S. Comas-Cardona, K. Masania, R. K. Upadhyay, and R. Hinterhoelzl, “A process modeling toolkit developed to address scale-up challenges of Out-of-Autoclave manufacturing,” in *Techn. Conf. Proc. CAMX 2015*, Dallas, October, 2015, pp. 1–15.



## C Supervised Student Theses

During my employment at the Chair of Carbon Composites - Lehrstuhl für Carbon Composites I have supervised the following student theses.

- [S1] S.S. Özer, Master Thesis, “Evaluation of Characterization Techniques for Out-of-Autoclave (OOA) prepregs in an uncured state”, Lehrstuhl für Carbon Composites, TUM, 2014. (Co-supervision with R. Helmus)
- [S2] T. Glockner, Term Project, “Characterization and Image Analysis of Out-of-Autoclave (OoA) prepregs in an Uncured State”, Lehrstuhl für Carbon Composites, TUM, 2014.
- [S3] D. Grießl, Term Project, “Charakterisierung – Kompaktierungsverhalten von Out-of-Autoclave (OoA) prepregs”, Lehrstuhl für Carbon Composites, TUM, 2016.
- [S4] W. Tan, Bachelor Thesis, “Cure kinetics modelling of the Cytec MTM44-1 Out-of-Autoclave epoxy resin system”, Lehrstuhl für Carbon Composites, TUM, 2016.
- [S5] L. Heidemann, Term Project, “In-Line measurements and quality investigation of parts manufactured with prepreg Out-of-Autoclave”, Lehrstuhl für Carbon Composites, TUM, 2016.

Co-supervised student thesis at the Institute of Research Institute in Civil Engineering and Mechanics (GEM), UMR CNRS 6183, Ecole Centrale de Nantes.

- [SN1] M. Devisse, J. Hemmer, H. Tertrais, Term Project, “Study of air flow in carbon semi-prepregs. Permeability measurement”, Research Institute in Civil Engineering and Mechanics, Ecole Centrale de Nantes, 2015.

Parts of the following theses contributed to the underlying doctoral thesis: [S1], [S2], [S4], [S5], [SN1]. The specific contributions are also indicated within the text.